

2024-01

Development of visible-light-driven photocatalysts for the degradation of organic pollutants and the disinfection of microorga

Akintunde, Olufemi Oluseun

Akintunde, O. O. (2024). Development of visible-light-driven photocatalysts for the degradation of organic pollutants and the disinfection of microorganisms (Doctoral thesis, University of Calgary, Calgary, Canada). Retrieved from <https://prism.ucalgary.ca>.

<https://hdl.handle.net/1880/117886>

Downloaded from PRISM Repository, University of Calgary

UNIVERSITY OF CALGARY

Development of visible-light-driven photocatalysts for the degradation of organic pollutants and
the disinfection of microorganisms

by

Olufemi Oluseun Akintunde

A THESIS

SUBMITTED TO THE FACULTY OF GRADUATE STUDIES
IN PARTIAL FULFILMENT OF THE REQUIREMENTS FOR THE
DEGREE OF DOCTOR OF PHILOSOPHY

GRADUATE PROGRAM IN CIVIL ENGINEERING

CALGARY, ALBERTA

JANUARY, 2024

© Olufemi Oluseun Akintunde 2024

Abstract

In this research, several visible-light driven photocatalysts were developed and their photocatalytic activities were evaluated in the removal of organic pollutants. Wastewater containing pathogen carriers such as total coliforms, and *E. coli* was tested for disinfection using the synthesized visible-light photocatalysts.

Graphitic carbon nitride (GCN or $g\text{-C}_3\text{N}_4$), a visible-light driven photocatalyst, was synthesized from different precursors. Also, different composites of GCN such GCN/ Ag_2CrO_4 , and GCN/ ZnO-Cu were synthesized. The purpose of these GCN composites is to enhance the photocatalytic activity of the GCN. Several characterization techniques were used to understand the physicochemical properties of the photocatalysts.

The initial photocatalytic experiments, detailed in Chapter 3, were on degrading 4-CP under a royal blue LED (450 nm) using precursor-derived GCNs and GCN composites. The results show that the GCN/ $0.3\text{Ag}_2\text{CrO}_4$ performed well with over 95% degradation of 4-CP.

The second set of photocatalytic experiments, detailed in Chapter 4, were on investigating the degradation of 2,4-D and MCPP, BSA protein, SARS-CoV-2 (Covid-19) spike protein, cATP, and total coliforms/*E. coli* using the best performing GCN/ $0.3\text{Ag}_2\text{CrO}_4$ in the first photocatalytic experiments and royal blue LED. Over 85% of 2,4-D and MCPP were simultaneously degraded, 77.5% of Covid-19 spike protein was achieved, and over one log reduction of cATP, total coliforms/*E. coli* was achieved in wastewater treatment.

In Chapter 5 (third set of experiments), new sets of photocatalysts were synthesized. GCN/ 0.1ZnO-Cu 3% performed best with over 65% of 4-CP degradation under royal blue LED. A complete 5.5 log reduction of coliforms-containing wastewater primary influent was achieved with the same photocatalyst.

In Chapter 6, the best-performing GCN/ZnO-Cu nanocomposite in observed in chapter 5 was coated on a polyvinyl chloride (PVC) substrate and the performance was evaluated under a 5000K LED (400 – 700 nm). The result shows a 2-log reduction of the coliform-containing wastewater treatment on the self-disinfecting coated surface.

To the best of our knowledge, this is the first research to investigate the comprehensive use and practical application of self-disinfecting coated surfaces under commercial and industrial light (5000K LED) irradiation.

All our results demonstrate that compositing GCN with metals can degrade pollutants and disinfect wastewater under visible light irradiation.

Preface

The University of Calgary offers the option to use published manuscripts authored or co-authored as part of a thesis. This thesis was prepared as such, following the guidelines of the faculty of graduate studies:

<https://grad.ucalgary.ca/current-students/thesis-based-students/thesis/building-thesis>.

Published and submitted papers

These chapters constitute papers that have either been published or submitted for publication after a review by my supervisor, Prof. Gopal Achari, and other co-authors:

Chapter 3: O.O. Akintunde, L. Yu, J. Hu, M.G. Kibria, G. Achari, Visible-Light Driven Photocatalytic Degradation of 4-Chlorophenol Using Graphitic Carbon Nitride-Based Nanocomposites, Catalysts. 12 (2022) 281. <https://doi.org/10.3390/catal12030281>.

Chapter 4: O.O. Akintunde, L. Yu, J. Hu, M.G. Kibria, C.R.J. Hubert, S. Pogolian, G. Achari, Disinfection and Photocatalytic Degradation of Organic Contaminants Using Visible Light-Activated GCN/Ag₂CrO₄ Nanocomposites, Catalysts. 12 (2022) 943. <https://doi.org/10.3390/catal12090943>.

Chapter 5: O.O. Akintunde, J. Hu, M.G. Kibria, S. Pogolian, G. Achari, A facile synthesis process of GCN/ZnO-Cu nanocomposite and the evaluation of the performance for the photocatalytic degradation of organic pollutants and the disinfection of wastewater under visible light, Chemosphere. 344 (2023) 140287. <https://doi.org/10.1016/j.chemosphere.2023.140287>.

Chapter 6: O.O. Akintunde, J. Hu, M.G. Kibria, S. Pogolian, G. Achari, Evaluation of the performance of self-disinfecting coated surface with GCN/ZnO-Cu nanocomposite under 5000K LED visible light. It is submitted to Chemosphere.

All research work was performed by the author of this thesis. Research supervision and advice were given by the supervisor.

Acknowledgments

This Ph.D. journey which started three years ago has finally come to an end. It was indeed a pleasant and memorable experience. This could not have been successfully completed without the support, contributions, and advice of many individuals met in this course of this journey.

To start with, I would like to express sincere and deep gratitude to my supervisor, Dr. Gopal Achari, Professor and Head of the Department of Civil Engineering, and immediate past Associate Dean of Graduate Studies and Research in the Schulich School of Engineering. I am very fortunate to have you as my supervisor and grateful for your support and guidance that ensured that this Ph.D. journey was smooth sailing. Your exceptional qualities of patience, understanding, and belief instilled the confidence in me to see this program through to a logical and meaningful conclusion.

A special thanks to members of my supervisory committee, Dr. Jinguang Hu and Dr. Md Golam Kibria for providing support and feedback that positively impacted the research and published manuscripts. My appreciation goes to the candidacy examiners, Dr. Hemanta Sarma and Dr. Susana Kimura-Hara for providing valuable feedback that contributed to the improvement of this research and the neutral chair, Dr. Merkebe Demissie. My appreciation also goes to the examiners at my PhD thesis final defense, Dr. Brij Maini and Dr. Ed McBean (external examiner from the University of Guelph), and the neutral chair, Dr. Muntasir Billah for finding time to be part of this momentous, memorable, and exciting time.

My sincere thanks go to Dr. Abraham Fapojuwo and Dr. Ayodeji Jeje. During this research, your support, guidance, and encouragement were a soothing balm.

This journey would not have been fun without the support of my friends and colleagues namely Saheli Rao, Fatemeh Hashemzadeh, Nasim Zare, Dr. Ron Thiessen, Dr. Ben Edafiaga, and Dr. Stanley Okonji. Our

conversations and your assistance made this research enjoyable. My sincere appreciation goes to Dr. Linlong Yu for his support and guidance in ensuring that this research started on a good note.

This journey would not have been possible without the belief and unwavering support of my family. Many thanks to my beautiful wife, Olufunke (Funke), and our lovely children Oludamilola (Dami), Oludemilade (Demi), and Oludasimi (Dara) for your sacrifices, encouragement, patience, understanding, prayers, and unconditional love during this Ph.D. study. We all carried this Ph.D. like a pregnancy and now, the pregnancy has been successfully birthed. I want to tell you, my dear family, “We made it to the end!”. Congratulations!!! My deep appreciation to my loving parents, Mr. & Mrs. Oluwale Akintunde, and siblings – thank you for the prayers and encouragement throughout this journey. To my parents and family, “I am here because you were there”.

Finally, I would like to thank the funders of this research, the Natural Sciences and Engineering Research Council of Canada (NSERC) and the Alberta Innovates CASBE program. I would like to thank the government of Alberta for finding me worthy and giving me the award, “Alberta Graduate Excellence Scholarship (AGES) – Doctoral Research”. A special appreciation to the industry partner, Nimalux Industrial through Samuel Pogorian, and Jode Himann for providing additional tools for this research. The funds, tools, and advice were valuable for the successful conclusion of this research.

Dedication

This thesis is dedicated to:

- The creator of heavens and the earth, and the giver of life, the ALMIGHTY GOD
- My beautiful wife, Funke, and our lovely children, Dami, Demi, and Dara
- My loving parents, Mr. & Mrs. Oluwole Akintunde

Table of Contents

Table of Contents

Abstract.....	i
Preface	iv
Acknowledgments.....	v
Dedication	vii
List of Tables	xv
List of Figures and Schemes	xvii
List of symbols, abbreviations, and nomenclature	xxii
Chapter 1: Introduction	1
1.1 Background	1
1.2 Knowledge gaps	4
1.3 Research goals and objectives	5
1.4 Thesis overview.....	6
Chapter 2: Literature Review	8
2.1 Photocatalysis	8
2.1.1 Photocatalytic mechanism.....	8
2.1.2 Photocatalytic application	12
2.2 Modification of semiconductor photocatalysts.....	14
2.2.1 Metal doping	14

2.2.2 Non-metal doping	16
2.2.3 Co-doping.....	17
2.2.4 Heterojunction	17
2.3 Visible light photocatalysis.....	19
2.3.1 Visible light photocatalysis and the degradation of organic pollutants	20
2.3.2 Visible light photocatalysis and the disinfection of microorganisms	24
2.4 Light sources and intensities.....	30
Chapter 3: Visible-Light-Driven Photocatalytic Degradation of 4-Chlorophenol Using Graphitic Carbon Nitride Based Nanocomposites.....	33
3.1 Highlights	33
3.2 Graphical abstract.....	34
3.3 Abstract.....	34
3.4 Introduction	35
3.5 Materials and Methods.....	37
3.5.1. Chemicals	37
3.5.2 Synthesis of Graphitic Carbon Nitride (GCNs) and GCN Composites.....	37
3.5.3. Characterization.....	39
3.5.4. Photocatalytic Experiments	40
3.5.5 Analysis	41
3.5.6 Actinometry	41
3.6 Results and Discussions	41

3.6.1 Physical and Chemical Properties of GCN and GCN Composites	41
3.6.2 Photocatalytic Degradation of 4-CP Using GCNs and GCN-Based Nanocomposites	47
3.6.3 Photocatalytic Degradation of 4-CP by U-GCN/0.3Ag ₂ CrO ₄ in Different Photoreactors	50
3.6.4 Proposed Photocatalytic Mechanism	53
3.7 Conclusions	55
Chapter 4: Disinfection and Photocatalytic Degradation of Organic Contaminants Using Visible Light-activated GCN/Ag ₂ CrO ₄ Nanocomposites.....	56
4.1 Highlights	56
4.2 Graphical abstract	57
4.3 Abstract	57
4.4 Introduction	58
4.5 Materials and Methods.....	62
4.5.1 Chemicals	62
4.5.2 Preparation of GCN, Ag ₂ CrO ₄ , and GCN/Ag ₂ CrO ₄ nanocomposite.....	62
4.5.3 Experimental set-up	63
4.6 Chemical analysis	65
4.6.1 Herbicide analysis	65
4.6.2 Protein analysis	65
4.6.3 ATP analysis.....	66
4.6.4 Total coliform/E. coli analysis	67
4.7 Results and discussions.....	68

4.7.1 Photocatalytic degradation of Killex ^R	68
4.7.2 Photocatalytic degradation of BSA protein and SARS-CoV-2 spike protein	72
4.7.3 Photocatalytic disinfection of wastewater secondary effluent	78
4.8 Conclusions	83
Chapter 5: A facile synthesis process of GCN/ZnO-Cu nanocomposite and the evaluation of the performance for the photocatalytic degradation of organic pollutants and the disinfection of wastewater under visible light.....	85
5.1 Highlights	85
5.2 Graphical abstract	86
5.3 Abstract	86
5.4 Introduction	87
5.5 Materials and Methods.....	90
5.5.1 Chemicals	90
5.5.2 Synthesis of GCN	91
5.5.3 Synthesis of ZnO nanoparticles and ZnO-Cu nanoparticles.....	91
5.5.4 Synthesis of GCN/ZnO-Cu nanocomposites.....	92
5.5.5 Characterization	92
5.5.6 Photoreactor	94
5.5.7 Photocatalytic degradation of 4-chlorophenol.....	95
5.5.8 Photocatalytic disinfection of total coliforms in wastewater primary influent.....	96
5.5.9 ROS identification	98

5.5.10 Particle size distribution.....	98
5.6 Results and discussions.....	98
5.6.1 XRD and Mean Crystallize Size (MCS)	98
5.6.2 Average Particle Size (APS)	101
5.6.3 FT-IR	102
5.6.4 SEM, TEM, and EDS	103
5.6.5 BET surface area, BJH pore volume, and BJH average pore size	107
5.6.6 PL spectra.....	108
5.6.7 UV-Vis DRS and Bandgap estimation	109
5.6.8 Photocatalytic degradation of 4-Chlorophenol	112
5.6.9 Reactive Oxidation Species (ROS) trapping experiment	115
5.6.10 Reusability experiment and stability test	116
5.6.11 Photocatalytic disinfection of wastewater primary influent	117
5.6.12 Proposed photocatalytic mechanism	119
5.7 Conclusions	121
Chapter 6: Evaluation of the performance of self-disinfecting coated surface with GCN/ZnO-Cu nanocomposite under 5000K LED visible light.....	123
6.1 Highlights	123
6.2 Graphical abstract.....	124
6.3 Abstract.....	124
6.4 Introduction	125

6.5 Materials and Methods.....	127
6.5.1 Chemicals	127
6.5.2 Synthesis of GCN	128
6.5.3 Synthesis of GCN/ZnO-Cu nanocomposites.....	128
6.5.4 Fabrication of PVC coatings	129
6.5.5 Characterization	129
6.5.6 Photocatalytic self-disinfecting experiments of coated PVC	130
6.5.7 ROS identification	132
6.6 Results and discussions.....	133
6.6.1 XRD	133
6.6.2 FT-IR	134
6.6.3 SEM, EDS, and AFM.....	135
6.6.4 UV-Vis DRS and Bandgap estimation	141
6.6.5 PL spectra	142
6.6.6 Photocatalytic disinfection of coated PVC.....	144
6.6.7 Reactive Oxidation Species (ROS) trapping experiment	147
6.6.8 Reusability experiment and stability test	148
6.6.9 Proposed photocatalytic mechanism	150
6.7 Conclusions	152
Chapter 7: Conclusions and Recommendations	153

7.1 Conclusions	153
7.2 Recommendations	155
References	157
Appendices.....	204
Appendix A: Copyright Form.....	204
Appendix B: Copyright Form	205
Appendix C: Copyright Form	206
Appendix D: Copyright Form.....	207
Appendix E: Supplementary materials for Chapter 3 (Paper 1).....	208

List of Tables

Table 2. 1 Photonic energy of different wavelengths of the electromagnetic spectrum [45].....	12
Table 2. 2 Visible-light active photocatalysts and the degradation of organic pollutants	23
Table 2. 3 Visible-light active photocatalysts and the disinfection of microorganisms.....	30
Table 2. 4 Characteristics of light sources	31
Table 2. 5 Estimate light intensities of polychromatic LED lights with different color temperatures	32
Table 2. 6 Estimated light intensities of polychromatic 5000K LED light at a varying distance to an object	32
Table 3. 1 BET surface area, BJH pore volume, and BJH average pore size.	43
Table 3. 2 Band gaps and the corresponding wavelengths of the synthesized photocatalysts.....	47
Table 3. 3 Comparison of 4-CP photocatalytic degradation with the results of previously published articles.	50
Table 3. 4 The photo energy (E_{photon}) required to achieve a log reduction of 4-CP.	52
Table 4. 1 Summary of first-order photocatalytic degradation rate constants.	70
Table 4. 2 Bond energies at 273K adapted from Ref. [219].	71
Table 4. 3 Comparison of 2,4-D and Mecoprop-P degradation with the results of previously published articles.....	72
Table 4. 4 Comparison of microorganism disinfection with the results of previously published articles. .	83
Table 5. 1 Mean Crystallite Size (MCS) of GCN, ZnO and ZnO-Cu3% nanoparticles, and GCN/0.1ZnO-Cu3% nanocomposite.	100
Table 5. 2 Average Particle Size (APS) of GCN, ZnO and ZnO-Cu3% nanoparticles, and GCN/0.1ZnO-Cu3% nanocomposite	102

Table 5. 3 BET surface area, BJH pore volume, and BJH average pore size.	108
Table 5. 4 Bandgaps and the corresponding wavelengths of GCN nanosheets, ZnO and ZnO-Cu3% nanoparticles, and GCN/0.1ZnO-Cu3% nanocomposite	111
Table 6. 1 BET surface area of powder GCN and GCN/ZnO-Cu3%	140
Table 6. 2 Bandgaps and the corresponding wavelengths of Uncoated PVC, Coated PVC (PU), Coated PVC (GCN), and Coated PVC (GCN/ZnO-Cu3%).....	142

List of Figures and Schemes

Figure 3. 1 Characterization of GCN and GCN-based nanocomposites: (a) XRD, (b) SEM for U-GCN/0.3Ag ₂ CrO ₄ , (c) EDS, and (d) DRS.	45
Figure 3. 2 Photocatalytic degradation of 4-CP using GCNs derived from different precursors and GCN/silver compounds-based nanocomposites under royal blue LED (450 nm) irradiation.	49
Figure 3. 3 Photocatalytic degradation of 4-CP using different photoreactors ($C_o = 20$ mg/L, $C_{U-GCN/0.3Ag_2CrO_4} = 1000$ mg/L).	52
Figure 4. 1 The dark experiment of Killex ^R : (a) 2,4-D and (b) Mecoprop-P.	69
Figure 4. 2 Photocatalytic degradation (royal blue LED irradiation) of Killex ^R : (a) 2,4-D and (b) Mecoprop-P.	69
Figure 4. 3 Change in BSA concentration with time: (a) Dark experiment and (b) Royal blue LED irradiation.	73
Figure 4. 4 UV-vis absorption spectra of BSA: Dark experiment (a and b) and Royal blue LED irradiation (c and d).	77
Figure 4. 5 Photocatalytic degradation of SARS-CoV-2 (Coronavirus) spike protein using GCN/Ag ₂ CrO ₄ . Under royal blue LED irradiation.	77
Figure 4. 6 The change of ATP in wastewater secondary effluent in the presence of GCN/Ag ₂ CrO ₄ with and without royal blue LED irradiation.	78
Figure 4. 7 Coliforms in wastewater secondary effluent: (a) total coliforms and (b) <i>E. coli</i>	81
Figure 5. 1 XRD spectra patterns of GCN nanosheet, ZnO and ZnO-Cu3% nanoparticles, and GCN/0.1ZnO-Cu3% nanocomposite	100

Figure 5. 2 Particle Size Distribution (PSD) of GCN nanosheet, ZnO and ZnO-Cu3% nanoparticles, and GCN/0.1ZnO-Cu3% nanocomposite.	101
Figure 5. 3 FT-IR spectra patterns of GCN nanosheet, ZnO and ZnO-Cu3% nanoparticles, and GCN/0.1ZnO-Cu3% nanocomposite	103
Figure 5. 4 SEM images: (a) GCN nanosheet, (b) ZnO nanoparticles, (c) ZnO-Cu3% nanoparticles, and (d) GCN/0.1ZnO-Cu3% nanocomposite	104
Figure 5. 5 TEM images: (a) GCN nanosheet, (b) ZnO nanoparticles, (c) ZnO-Cu3% nanoparticles, and (d) GCN/0.1ZnO-Cu3% nanocomposite	105
Figure 5. 6 EDS images: (a) GCN nanosheet, (b) ZnO nanoparticle, (c) ZnO-Cu3% nanoparticle, and (d) GCN/0.1ZnO-Cu3% nanocomposite.	106
Figure 5. 7 (a) BET surface area and (b) BJH pore size distribution, of GCN nanosheet, ZnO and ZnO-Cu3% nanoparticles, and GCN/0.1ZnO-Cu3% nanocomposites.....	108
Figure 5. 8 PL spectra patterns of GCN nanosheets, ZnO and ZnO-Cu3% nanoparticles, and GCN/0.1ZnO-Cu3% nanocomposite.	109
Figure 5. 9 (a) UV-Vis DRS and (b) Band gap, of GCN nanosheet, ZnO and ZnO-Cu3% nanoparticles, and GCN/0.1ZnO-Cu3% nanocomposite	111
Figure 5. 10 (a) Photocatalytic degradation performance of ZnO and ZnO-Cu composites, (b) Photocatalytic degradation performance of GCN nanosheet, ZnO and ZnO-Cu nanoparticles, and GCN/ZnO-Cu nanocomposite, (c) Rate constant of all the synthesized photocatalysts, and (d) Comparison between photocatalytic degradation and adsorption (in the dark) performances of the synthesized photocatalysts.	114
Figure 5. 11 ROS Experiment for the active species for the photocatalytic degradation of 4-CP by GCN/0.1ZnO-Cu nanocomposite.....	115
Figure 5. 12 (a) Reusability experiment and (b) Stability test (XRD analysis), of GCN/0.1ZnO-Cu3% after the 4 th cycle.	116

Figure 5. 13 (a) Disinfection of wastewater primary influent by the synthesized photocatalysts in the dark, (b) Photocatalytic disinfection of wastewater primary influent by the synthesized photocatalysts under visible light irradiation (Royal blue LED).	118
Figure 6. 1 XRD spectra patterns of Uncoated PVC, Coated PVC (PU), Coated PVC (GCN), and Coated PVC (GCN/ZnO-Cu3%).....	134
Figure 6. 2 FTIR spectra patterns of Uncoated PVC, Coated PVC (PU), Coated PVC (GCN), and Coated PVC (GCN/ZnO-Cu3%).....	135
Figure 6. 3 SEM: (a) Uncoated PVC, (b) Coated PVC (PU), (c) Coated PVC (GCN), and (d) Coated PVC (GCN/ZnO-Cu3%).....	138
Figure 6. 4 EDS: (a) Uncoated PVC, (b) Coated PVC (PU), (c) Coated PVC (GCN), and (d) Coated PVC (GCN/ZnO-Cu3%).....	139
Figure 6. 5 AFM: (a) Uncoated PVC, (b) Coated PVC (PU), (c) Coated PVC (GCN), and (d) Coated PVC (GCN/ZnO-Cu3%).....	140
Figure 6. 6 (a) UV-Vis DRS and (b) Bandgap, of Uncoated PVC, Coated PVC (PU), Coated PVC (GCN), and Coated PVC (GCN/ZnO-Cu3%).....	142
Figure 6. 7 PL spectral of Uncoated PVC, Coated PVC (PU), Coated PVC (GCN), and Coated PVC (GCN/ZnO-Cu3%).....	144
Figure 6. 8 Effect of coat layer on the self-disinfection performance of Coated PVC (GCN/ZnO-Cu3%) under 5000K LED (10 cm and 16,800 Lux).	146
Figure 6. 9 Self-disinfecting experiments of Uncoated PVC, Coated PVC (PU), Coated PVC (GCN), and Coated PVC (GCN/ZnO-Cu3%), (a) in the dark and (b) under 5000K LED (10 cm and 16,800 Lux). ..	146
Figure 6. 10 Effect of light intensity on the self-disinfection performance of Coated PVC (GCN/ZnO- Cu3%) under 5000K LED.	147

Figure 6. 11 ROS Experiment for the active species for the disinfection of Coated PVC (GCN/ZnO-Cu3%) under 5000K LED (10 cm and 16,800 Lux).	148
Figure 6. 12 Reusability experiment (a) and Stability tests for XRD pattern (b) and SEM image (c and d), of Coated PVC (GCN/ZnO-Cu3%) after the 4 th cycle under 5000K LED (10 cm and 16,800 Lux).	149
Figure S3. 1 N ₂ adsorption-desorption isotherms and their corresponding pore size distribution.....	208
Figure S3. 2 N ₂ adsorption-desorption isotherms and their corresponding pore size distribution.....	209
Figure S3. 3 XRD patterns for the photocatalysts: U-GCN/silver-based composites and U-GCN/silver chromate composites.....	210
Figure S3. 4 SEM images for the photocatalysts: (a) D-GCN, (b) U-GCN, (c) M-GCN, (d) Ag ₂ CrO ₄ , (e) U-GCN/0.1Ag ₂ CrO ₄ , (f) U-GCN/0.5Ag ₂ CrO ₄ , (g) U-GCN/0.3Ag, (h) U-GCN/0.3AgBr, and.....	211
Figure S3. 5 EDS images for the photocatalysts: (a) D-GCN, (b) U-GCN, (c) M-GCN, (d) Ag ₂ CrO ₄ , (e) U-GCN/0.1Ag ₂ CrO ₄ , (f) U-GCN/0.5Ag ₂ CrO ₄ , (g) U-GCN/0.3Ag, (h) U-GCN/0.3AgBr, and.....	212
Figure S3. 6 UV-Vis DRS for the photocatalysts: U-GCN/silver-based composites and U-GCN/silver chromate composites.....	213
Figure S3. 7 Bandgap energies of the photocatalysts: (a) GCNs derived from different precursors of dicyandiamide (D), urea (U), and melamine (M), (b) U-GCN/silver-based compounds, all in the same ratio of 1:0.3 and (c) U-GCN/xAg ₂ CrO ₄ where x = 0.1, 0.3 and 0.5.	214
Figure S3. 8 Adsorption performance of the synthesized photocatalysts on 4-CP in dark condition.....	215
Figure S3. 9 XRD pattern for Ag ₂ CrO ₄	215
Figure S3. 10 High-resolution SEM image of U-GCN/Ag ₂ CrO ₄	216
Scheme 2. 1 Schematic diagram of photocatalysis mechanism [44]	10
Scheme 2. 2 Schematic diagram of the physicochemical properties and the multi-functional application of g-C ₃ N ₄ [56].	14

Scheme 2. 3 Doping as an electron trapping site for TiO ₂ photocatalyst [66].	16
Scheme 2. 4 Schematic diagram representation of heterojunction semiconductor photocatalysts [78].	19
Scheme 2. 5 Photocatalytic degradation pathways for 4-chlorophenol [88].	24
Scheme 2. 6 Schematic diagram of the antimicrobial mechanisms of (a) Silver nanoparticles [99], (b) Zinc Oxide nanoparticles [114], and (c) Copper nanoparticles [102].	28
Scheme 3. 1 Synthesis procedures of GCN and GCN-based composites.	38
Scheme 5. 1 Synthesis process for GCN, ZnO-Cu nanoparticles, and GCN/ZnO-Cu nanocomposites.	94
Scheme 5. 2 Royal blue LED photoreactor.	95
Scheme 5. 3 Schematic representation of the proposed mechanism for the photocatalytic degradation of 4-CP and the photocatalytic disinfection of total coliforms in wastewater primary influent.	121
Scheme 6. 1 (a) Uncoated PVC and Coated PVC (GCN/ZnO-Cu) and (b) Schematic representation of the experimental setup.	132
Scheme 6. 2 Schematic representation of the proposed self-disinfecting mechanism of coliforms by Coated PVC (GCN/ZnO-Cu3%) under 5000K LED.	151

List of symbols, abbreviations, and nomenclature

Symbol	Definition
C_o	Concentration at time $t = 0$, mg/L or MPN/100 mL.
C_t	Concentration at time t , mg/L or MPN/100 mL
E_{CB}	Conduction band potential, eV
E_{VB}	Valence band potential, eV
E_g	Bandgap energy, eV
E^e	Free electron energy on the hydrogen scale, eV
E_{photon}	Photon energy, J
I_e	Light intensity, J/s
K	(pseudo) first-order rate constant, min^{-1}
t	time, min
X	Absolute electronegativity of the semiconductor, eV
λ	Wavelength, nm

Abbreviation	Definition
APS	Average Particle Size
AOPs	Advanced Oxidative Processes
BSA	Bovine Serum Albumin
BET	Brunauer-Emmett-Teller
BJH	Barret-Joyner-Halenda
cATP	Cellular Adenosine Triphosphate
EDS	Electron Dispersive X-ray Spectroscopy
eV	Electron-Volt

FT-IR	Fourier Transform Infrared Spectroscopy
GCN	Graphitic Carbon Nitride
HPLC	High Performance (or Pressure) Liquid Chromatography
LED	Light Emitting Diode
MPN	Most Probable Number
MCS	Mean Crystallite Size
Mecoprop-P or MCPP	Methyl Phenoxy Propionic acid
PL	Photoluminescence
PU	Polyurethane
PVC	Polyvinyl Chloride
PSD	Particle Size Distribution
ROS	Reactive Oxygen Species
RLU	Relative Light Unit
SARS-CoV-2 (Covid-19)	Severe Acute Respiratory Syndrome Coronavirus 2
SEM	Scanning Electron Microscopy
TEM	Transmission Electron Microscopy
UV-Vis DRS	Ultraviolet-Visible Diffuse reflectance Spectroscopy
UV-A	Ultraviolet A
WW	Wastewater
XRD	X-ray Diffraction
4-CP	4-Chlorophenol
2,4-D	2,4-Dichlorophenoxyacetic acid

Chapter 1: Introduction

1.1 Background

The process of industrialization and civilization over several decades have been identified as major indicators of development and urbanization in any society. With the benefits of industrialization and civilization come the negative consequences of the release of toxic chemicals such as gases, solid waste, as well as microorganisms into the environment (land, air, and water). Of interest is water pollution, which is increasingly becoming a global challenge[1–3]. Water pollution negatively affects our health as it kills more people in the world than war. Less than one percent of the earth’s freshwater is accessible for drinking. Without action, it is reported that the challenge of water pollution will increase by 2050 when global demand for freshwater is expected to be one-third more than it is now [4]. Water pollution is when hazardous substances such as chemicals and microorganisms contaminate surface waters (oceans, rivers, lakes, streams), groundwater, or other water bodies, degrading the quality of water and rendering it toxic to humans and the environment [5]. The United Nations’ World Water Development document in 2020, reported that changes to the water cycle will pose risks to food security, energy production, human health, economic development, and poverty reduction and therefore threaten the achievements of sustainable development goals [6]. Therefore, it is important to develop an advanced, eco-friendly, low-cost, and efficient wastewater treatment technology.

There are many conventional technologies used in the application of wastewater treatment in addressing water pollution, however, they have their limitations. For example, the use of chlorine in disinfecting microorganisms can react with organic compounds, generating chloro-organic compounds that are carcinogenic [7,8], such as the chlorination of phenolic compounds to produce chlorophenols. In addition, some pathogens such as viruses and bacteria (legionella) are known to be resistant to chlorine disinfection [9]. Ozonation and irradiation (use of germicidal lamps at 256 nm) have their limitations like the generation

of toxic disinfection by-products during ozonation [10], and the lack of residual effects during irradiation [11]. Other treatment methods such as adsorption [12], precipitation [13], and membrane filtration [14] while being effective, transfer the pollutants from one matrix to another [15]. Biological treatment of wastewater-containing chemical compounds is another effective way, but the chemicals can be toxic to microorganisms [16].

Advanced oxidative processes (AOPs), such as ozone photolysis (UV/O₃), hydrogen peroxide photolysis (UV/H₂O₂), Fenton's reagent (H₂O₂/Ferrous iron, e.g., FeSO₄), and photocatalysis, have shown effectiveness in the degradation of organic pollutants and the disinfection of microorganisms. The objective of these AOPs is to address some of the limitations associated with conventional treatment processes. AOPs are the collection of processes that can treat organic pollutants through the generation of reactive oxidative species [17,18]. Jing et al. removed atrazine from wastewater using UV/O₃ and reported 95% degradation in 3h [19]. Yu et al. studied the effect of UV/H₂O₂ on the degradation of sulfolane at different concentrations in water [20]. It was reported that 84% and 95% degradation of sulfolane were achieved after 8h. Yu et al achieved more than 95% degradation in 3h for sulfolane using Fenton-like reactions [21]. The difference between these AOPs is that the oxidant/photolysis processes such as UV/H₂O₂ and UV/O₃, and Fenton-like reactions are homogeneous catalytic processes in which the catalyst, the oxidant, and the contaminant are all in the same aqueous phase. Photocatalysis is a heterogeneous AOP in which the photocatalyst is in the solid phase while the contaminant is dissolved in the water. Direct photolysis is a photochemical process widely used in inactivating pathogens in wastewater. Photolysis can excite contaminants to a highly reactive state leading to degradation [22,23]. However, homogenous AOPs including direct photolysis require high-energy irradiation using UV-C lamps with a wavelength range of 200 – 280 nm (see Table 1) which is ideal for pathogen removal [24]. Photolysis occurs when a contaminant is irradiated at a wavelength that it can absorb causing excitation of the contaminant [22]. In addition to the need for high-energy radiation, they can also form harmful by-products. Some homogeneous AOP such as UV/O₃ can lead to the generation of toxic by-products when excess oxidant, O₃ is present in the solution. Excess O₃ in the solution can cause a

reaction with bromine ions in the water leading to the production of bromate. Bromate has been listed as a possible carcinogen by various environmental agencies such as the Environmental Protection Agency (EPA) and the International Agency for Cancer Research [25]. The maximum allowable bromate concentration in drinking water set by the World Health Organization is 10 µg/L. Therefore, when the concentration of bromine ion in raw water is below 20 µg/L then the concentration of bromate will remain within the guideline value. However, when bromine ion exceeds 20 µg/L, the formation of bromate tends to exceed guidelines and becomes a challenge. The limitations in the application of Fenton's process are the need to remove iron after treatment and the low pH requirement to maintain Fe (III) species in the solution. Fenton process depends on a cycle that regenerates Fe (II) [26].

Unlike other AOPs, photocatalysis does not require the use of chemical oxidants, strict control of environmental factors such as temperature and pH, and high-energy irradiation using UV-C lamps (200 – 280 nm) thereby reducing the cost of energy and chemicals [27]. Photocatalysis can take place in ambient conditions and under low to very low energy irradiation (UV-A to visible light) with a wavelength range (of 380 – 700 nm), and many recalcitrant organic compounds, metallic ions, and pathogens can be removed without the formation of toxic by-products [28].

1.2 Knowledge gaps

Visible-light-driven photocatalysis, is increasingly gaining a lot of attention because it is not energy-intensive, can utilize cheap, abundant, and renewable energy available from sunlight, has no harmful by-products, and completely mineralizes the pollutants to harmless products such as CO₂ and H₂O. The application of visible-light-sensitive photocatalysts in degrading pollutants and disinfecting microorganisms is widely reported. It is well known that light source and intensity play a significant role in photocatalytic degradation and disinfection kinetics. In published articles, the focus is commonly on the use of natural sunlight or solar simulator (xenon lamps) as the visible light source in the photocatalytic degradation of organic pollutants and the inactivation of microorganisms. Therefore, this serves as the starting point in understanding photocatalysis and more importantly the knowledge gaps in the synthesis and the application of visible-light-driven photocatalysis. Therefore, the following have been identified as knowledge gaps:

- Lack of research in the photocatalytic degradation of protein.
- Lack of research in the photocatalytic degradation of adenosine triphosphate (ATP). ATP is an organic compound that drives metabolic processes in living cells. It can be used as an indication of the biological activities of microorganisms.
- Limited research in the photocatalytic disinfection of total microbial population and total coliforms in real wastewater.
- Lack of research using a monochromatic visible light source in the photocatalytic degradation of organic pollutants and the disinfection of microorganisms.
- Limited research in self-disinfecting coated surfaces using a visible-light-driven photocatalyst and a visible light source.

1.3 Research goals and objectives

The goals of this research are (1) the development and synthesis of visible-light-driven photocatalysts that can degrade organic pollutants and disinfect wastewater and (2) the evaluation of the coating of a substrate with the developed visible-light-driven photocatalyst to act as a self-disinfecting surface under visible light irradiation. These goals are based on the identified knowledge gaps. These goals are geared towards full application in wastewater treatment and self-disinfecting coated surfaces. To this end, the following sub-objectives were identified to achieve these goals:

1. Synthesis and characterization of visible-light-driven photocatalysts based on graphitic carbon nitride (GCN) and GCN composites.
2. Evaluate the effect of using different precursors to synthesize GCN on degrading organic contaminant under visible light irradiation.
3. Evaluate the effect of synthesis of GCN composites such as GCN/Ag, GCN/AgBr, GCN/Ag₃PO₄, GCN/Ag₂CrO₄, GCN/ZnO-Cu in degrading organic contaminants (2,4-D, MCPP, 4-CP, BSA protein, and SARS-CoV-2 spike protein) and disinfecting wastewater.
4. Determine the photocatalytic efficiency of GCN composite in removing contaminants simultaneously.
5. Evaluate the effect of using different light sources such as single-wavelength visible light (royal blue LED, 450 nm), single-wavelength UV light (UV-A LED, 365 nm), Xenon lamp, and cool white, fluorescent lamps (400 – 700 nm) on the degradation of organic contaminant.
6. Investigate the reactive oxygen species (ROS) responsible for the degradation of organic contaminants and the disinfection of wastewater.
7. Develop self-disinfecting coated surfaces based on GCN composites of GCN/ZnO-Cu
8. Evaluate the disinfecting performance of the self-disinfecting coated surface in the dark and under multiple-wavelength visible light source (5000K LED, 400 – 700 nm).

9. Investigate the effects of multiple coats and light intensity on the performance of the self-disinfecting coated surface under 5000K LED.
10. Investigate the reactive oxygen species (ROS) responsible for the degradation of the self-disinfecting coated surface.
11. Investigate the reusability of the synthesized GCN composites for degrading organic contaminants, disinfecting wastewater, and self-disinfecting coated surfaces for practical application purposes.
12. Propose photocatalytic mechanisms for the degradation of organic contaminants, disinfection of wastewater, and self-disinfecting coated surfaces.

1.4 Thesis overview

The thesis is divided into seven chapters in a manuscript-based format. The description of the content of each chapter is outlined below.

Chapter 1 presents the background on water pollution, challenges with conventional water treatment methods and some advanced oxidative processes (AOPs), and photocatalysis. Also in this chapter are the research goals and objectives, and thesis overview.

Chapter 2 gives a literature review on photocatalysis, photocatalytic mechanism and application, modification of semiconductor photocatalysts, and visible light photocatalysis.

Chapter 3 is focused on the development of a visible-light-driven photocatalyst of GCN/Ag₂CrO₄ binary nanocomposite and the evaluation of its photocatalytic performance in degrading 4-chlorophenol under royal blue LED (450 nm). It also investigated other GCN composites such as GCN/Ag, GCN/AgBr, and GCN/Ag₃PO₄ by comparing their performances to GCN/Ag₂CrO₄. The effect of different light sources such as UV-A LED (365 nm), Xenon lamp, and cool white, fluorescent lamps (400 – 700 nm) in degrading 4-chlorophenol was investigated and their performances compared to royal blue LED (450 nm). This paper was peer-reviewed and published in the journal “Catalysts”.

Chapter 4 is focused on the degradation of multiple contaminants simultaneously. These include BSA protein, SARS-CoV-2 spike protein, and the disinfection of microorganisms, total coliforms, and *E. coli* in wastewater primary secondary effluent using the optimally performing GCN/Ag₂CrO₄ presented in chapter 3 and visible light, royal blue LED (450 nm). This paper was peer-reviewed and published in the journal “Catalysts”.

Chapter 5 presents the development of a visible-light-driven photocatalyst of GCN/ZnO-Cu ternary nanocomposite and the evaluation of the photocatalytic performance in the degradation of 4-chlorophenol and the disinfection of coliforms-containing wastewater primary influent under royal blue LED (450 nm). Investigations were also conducted to determine the reusability of the photocatalysts, and the dominant reactive oxidative species (ROS) involved in the photocatalytic reaction. A photocatalytic mechanism was also proposed based on the dominant ROS. This paper was peer-reviewed and published in the journal “Chemosphere”.

Chapter 6 focuses on self-disinfecting coated surfaces. Here, the synthesized visible-light photocatalysts in Chapter 5 (GCN/ZnO-Cu ternary nanocomposite) were coated on a polyvinyl chloride (PVC) substrate. The self-disinfecting performance of the coated PVC substrate denoted as coated PVC (GCN/ZnO-Cu) was investigated with a drop of coliforms-containing wastewater primary influent under a visible light source, 5000K LED (400 – 700 nm). The effects of coats and light intensity were investigated. The reusability of the coated PVC substrate and the dominant reactive oxygen species (ROS) involved in the self-disinfecting photocatalytic reaction were investigated. The self-disinfecting photocatalytic mechanism was proposed based on the dominant ROS. The manuscript is submitted to the journal “Chemosphere”.

Chapter 7 presents the conclusions of this research and recommendations for expanding on this work in the future.

Chapter 2: Literature Review

2.1 Photocatalysis

Photocatalysis was first discovered over 90 years ago [29,30]. However, it began receiving significant attention after the discovery of water splitting by Fujishima and Honda in 1971 [31]. Advanced Oxidative Process (AOP), including photocatalysis, was first proposed for the treatment of drinking water in 1980 and since then it has been studied for the treatment of different wastewater [32–34].

2.1.1 Photocatalytic mechanism

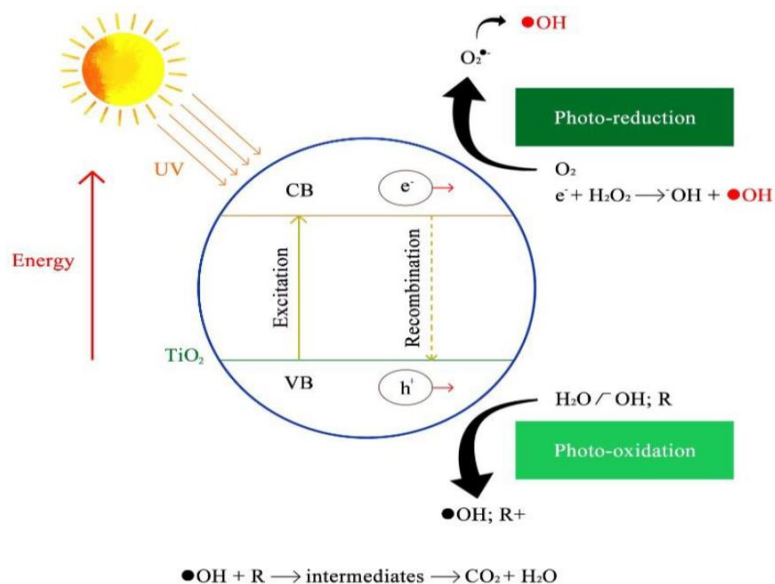
Photocatalysis is defined as the “acceleration of a photoreaction by the action of a catalyst” [35]. It is when light is used to initiate photocatalysis by bombarding the surface of the photocatalyst with photons [36,37]. For photocatalysis to take place, the light energy must be equal to or greater than the bandgap energy of the photocatalyst. The bandgap or energy gap is the difference in energy (in electron volts) between the top of the valence band and the bottom of the conduction band in insulators and semiconductors. It is the energy required to excite and eject an electron bound to a valence band to migrate to the conduction band and become a conducting electron that is free to move within the crystal lattice and serve as a charge carrier to conduct electric current. The energy required to cause this excitation comes from a light source that should be equal to or greater than the energy gap of the semiconductor photocatalysts. [Scheme 2.1](#) shows the movement of electrons to and from the conduction band. The irradiation from the light with greater photon energy than the bandgap energy of the photocatalyst causes the excitation of electrons (e^-). The electrons leave the valence band and migrate towards the conducting band leaving behind a hole (h^+) in the valence band. These electrons react with the dissolved oxygen (O_2) in water to form superoxide radicals ($\cdot O_2^-$) or hydroperoxide radicals ($\cdot HO_2$) and upon further reaction, the decomposition produces hydroxyl radicals ($HO\cdot$). The holes (h^+) can react with the hydroxyl ion (OH^-) or water molecule to form hydroxyl radicals ($HO\cdot$). These generated radicals are known as reactive oxygen species (ROS) or reactive species. The photogenerated electrons are considered reductant while the photogenerated holes also participate in the

oxidative decomposition due to their strong oxidizing power, which is the primary pathway for hydroxyl radical production. These photogenerated electrons, photogenerated holes, and the reactive oxygen species (ROS) participate in the degradation of organic pollutants or the disinfection of microorganisms. The photocatalytic mechanism is presented in equations (2.1) – (2.9) [38].

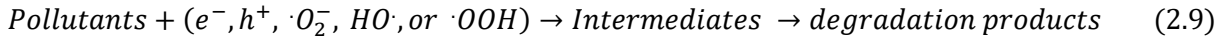
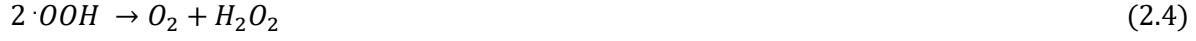
The photogenerated electrons can also lead to the evolution of hydrogen gas, a phenomenon known as photocatalytic water splitting, which is one of the applications of photocatalysis. In the overall water splitting mechanism, the photogenerated electrons react with the hydrogen ion in the water molecule to produce hydrogen gas (reduction reaction) and the photogenerated holes react with the water molecule to produce oxygen gas and hydrogen ion (oxidation reaction) as shown in equations (2.11) – (2.12) [39]. The produced oxygen gas can react with photogenerated electrons to form superoxide radicals ($\cdot\text{O}_2^-$) or hydroperoxide radicals ($\cdot\text{HO}_2$), and it further reacts with and degrades the organic pollutant causing complete mineralization (production of CO_2 and H_2O) and deactivate microorganisms. The photogenerated holes can also react with a water molecule to produce hydroxyl radicals and hydrogen ions (equation 2.7). With the hydrogen ion and the oxygen molecule present in the water, the oxygen molecule will more readily oxidize other molecules by accepting electrons. The oxidizing power of these oxidizing agents is reflected in their oxidation potential (OP) with O_2 having OP of 1.26 V [40] and hydrogen ion having OP of 0 V [41]. The OP of superoxide radical ($\cdot\text{O}_2^-$) is 0.34 V [42] and hydroxyl radical ($\text{HO}\cdot$) is 2.80 V, second only to fluorine which is 3.30 V [40]. This means that O_2 with a higher OP is a stronger oxidizing agent (oxidizer) than H^+ and has a stronger tendency (affinity) for electrons.

Table 2.1 shows the photonic energy of different wavelengths of the electromagnetic spectrum. The solar energy reaching the earth covers the entire electromagnetic spectrum, which is between 100 nm and 1,000,000 nm, corresponding to the photon energy between 12.4 eV and 1.24 meV. UV constitutes about 10% of the total electromagnetic radiation output from the sun. UV from sunlight, which can be divided into three parts, has 95% UV-A (longer wavelength range) and 5% of UV-B (median wavelength range)

reaching the earth. UV-C and most of UV-B do not reach the earth and are removed from extraterrestrial radiation by stratospheric ozone [43]. Therefore, approximately 5% of the UV component of solar radiation, which is largely UV-A reaches the earth. This indicates that a photocatalyst that essentially has a lower energy gap (band gap) can utilize the 5% UVA radiation from the sun to cause a photocatalytic reaction. Photocatalysis can only take place when the energy from the light is equal to or greater than the band gap of the photocatalyst. In this case, the energy of UV-A and UV-B regions of the solar spectrum is greater than any photocatalyst that has been reported, and therefore photocatalysis will take place. The UV region of the sunlight can be harnessed for photocatalysis by using visible light cut-off filters. The visible light cut-off filters will cut off radiation greater than 420 nm from the sun leaving only the UV radiation. Similarly, the visible light region of the sunlight can be harnessed for photocatalysis by using UV cut-off filters which cuts off radiation less than 420 nm. The 420 nm is mostly used as a cut-off limit in photocatalysis for both UV and visible light utilization in the solar spectrum to ensure that there is no adjacent visible light or UV interference or effect when using UV or visible light irradiation.



Scheme 2. 1 Schematic diagram of photocatalysis mechanism (Image cited under the Creative Commons Attribution license) [44]



The rate of photocatalytic degradation of organic pollutants or the photocatalytic disinfection of microorganisms can be represented by the pseudo-first-order kinetics at low substrate concentration as shown in equation (2.10):

$$\ln \left[\frac{C}{C_0} \right] = -kt \quad (2.10)$$

Where k = the apparent reaction rate constant

t = reaction time

C₀ = the initial concentration

C = the concentration of the pollutant at time t



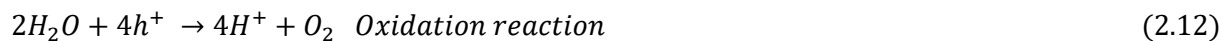


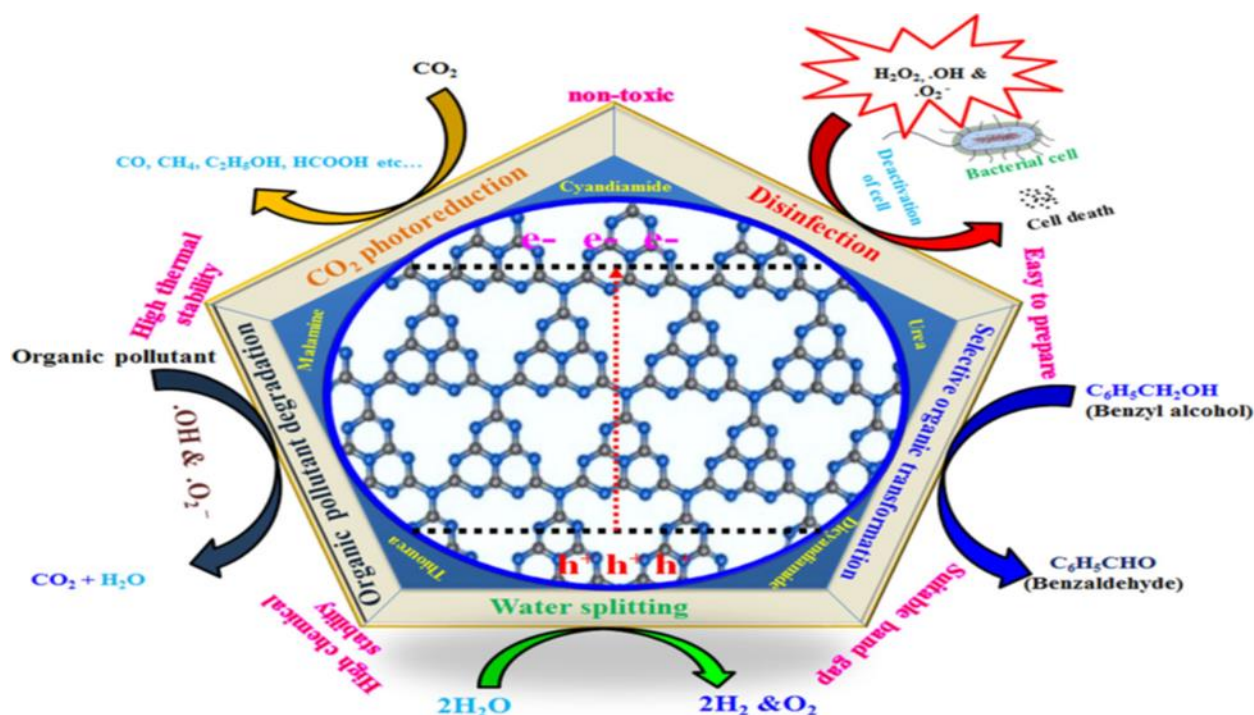
Table 2. 1 Photonic energy of different wavelengths of the electromagnetic spectrum [45].

S/N	Spectrum	Range	Abbreviation	Wavelength (nm)	Energy (eV)
1	Ultraviolet (UV)	Extreme UV	EUV	1 - 100	1240 – 12.4
		Far UV	UV-C	100 - 280	12.4 – 4.43
		Mid UV	UV-B	280 - 315	4.43 – 3.94
		Near UV	UV-A	315 - 380	3.94 – 3.26
2	Visible (Vis)	Violet		380 - 435	3.26 – 2.85
		Blue		435 - 500	2.85 – 2.48
		Cyan		500 - 520	2.48 – 2.38
		Green		520 - 565	2.38 – 2.19
		Yellow		565 - 590	2.19 – 2.10
		Orange		590 - 625	2.10 – 1.98
		Red		625 - 780	1.98 – 1.59
3	Infrared (IR)	Near Infrared	IR-A	780 - 1400	1.58 – 0.89
		Mid Infrared	IR-B	1400 - 3000	0.89 – 0.41
		Far Infrared	IR-C	3000 – 1000000	0.41 – 0.00124

2.1.2 Photocatalytic application

Photocatalysis has various applications - in disinfection and self-disinfection of microorganisms such as E. coli, degradation of organic pollutants to mineralized products of CO₂ and H₂O, water splitting to produce green hydrogen energy, and as a carbon capture and conversion mechanism in CO₂ reduction. The use of semiconductor catalysts in photocatalysis has been widely studied [46] due to their physicochemical properties such as bandgap energies charge transport characteristics, light absorption properties, and thermal and chemical stability [47]. The interest in semiconductor applications in photocatalysis is also because they are economical, harmless, large surface area-to-volume ratio, tunable bandgap (which can be modified by doping and size reduction), and broad absorption spectra [48]. However, the drawbacks of photocatalysis is that it is not specific to degradation of a contaminant or disinfection of microorganisms due to the physicochemical properties of the photocatalyst and the characteristics of the light source (visible or UV and intensity). The earliest and the most widely studied semiconductor photocatalyst is titanium dioxide (TiO₂), a metal-based semiconductor photocatalyst. It has been widely applied in organic pollutant

degradation, water splitting, and disinfection of wastewater. However, its wide bandgap (~ 3.2 eV) limits its utilization only to UV irradiation [49–51]. Metal-free semiconductor polymeric photocatalyst, such as graphitic carbon nitride (g-C₃N₄ or GCN) is increasingly gaining attention because of their narrow bandgap (2.7 eV – 2.80 eV) and the utilization of visible light irradiation [52–55], [Scheme 2.2](#) shows the structure of GCN, its physicochemical properties and its application in environmental remediation and chemical processes. Inside the pentagon is the structure of GCN which is the tri-s-heptazine ring. On the vertices are the physicochemical properties which are the ease of preparation from readily available and cheap precursors such as urea and melamine using a facile thermal polymerization process, stable bandgap, high chemical stability, and high thermal stability at very high temperatures of up to 600°C. On the edges are some of the applications including the degradation of organic pollutants to mineralized products of CO₂ and H₂O, and the disinfection of pathogens, by reacting with the photogenerated electrons, photogenerated holes, and reactive oxidative species (ROS). Other applications include water splitting to produce hydrogen, photocatalytic reduction of CO₂ and the breakdown of heavy molecular compounds such as benzyl alcohol.



Scheme 2. 2 Schematic diagram of the physicochemical properties and the multi-functional application of g-C₃N₄ (Picture cited with permission granted by Rightslink, Appendix A) [56].

2.2 Modification of semiconductor photocatalysts

Semiconductor photocatalysts are used to photocatalytically degrade organic pollutants and photocatalytically disinfect microorganisms. However, the use in bulk forms comes with the disadvantages of fast electron-hole recombination, poor charge transfer, and poor light utilization. To address these problems, the photocatalysts are modified to improve their photosensitive activity. Some of these modification techniques are doping with either metal, non-metal, or other semiconductor photocatalysts.

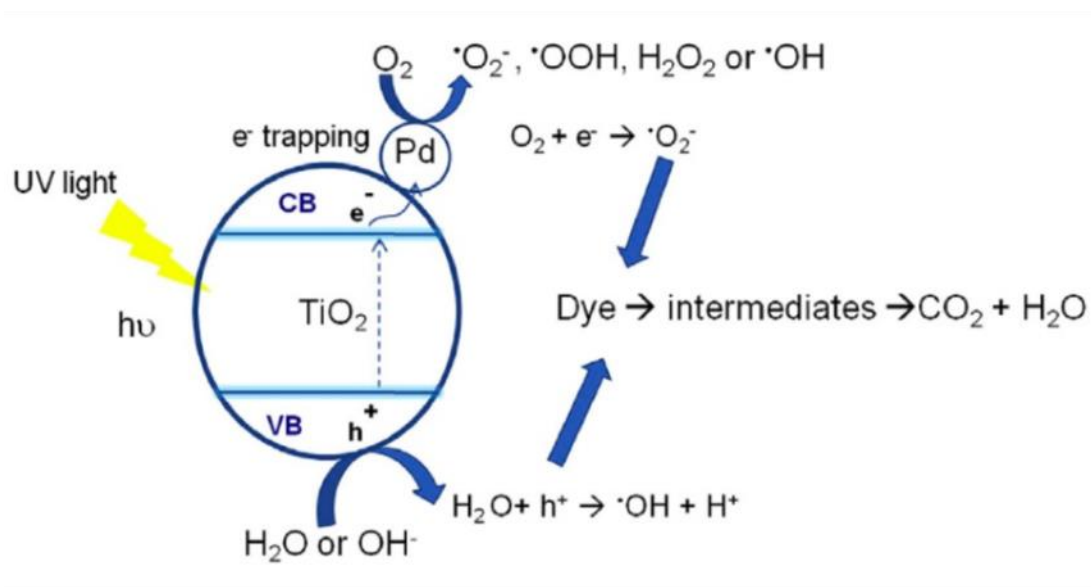
2.2.1 Metal doping

The addition of metallic compounds provides for improved photocatalytic activity such as reduction in bandgap energy and enhanced visible light absorption [57,58]. Doping is the introduction of a substance into an intrinsic semiconductor to modify its electrical, optical, and structural properties. An intrinsic semiconductor is an undoped semiconductor. The number of charge carriers is determined by the properties

of the material and not the dopant. When an intrinsic semiconductor is doped, it is referred to as an extrinsic semiconductor. The doping of a semiconductor with metal or non-metal can be achieved through several synthesis processes. Some of the widely used processes are thermal polymerization, hydrothermal, and precipitation. Some of these processes can also be combined to achieve better photocatalytic activity. Thermal polymerization is a process where the precursor of the dopant is mixed with the precursor of the semiconductor photocatalyst and heated in the muffle furnace at a certain temperature for a defined time to give a doped-semiconductor photocatalyst [59]. The hydrothermal process is heating the mixture of the solution of the synthesized semiconductor photocatalyst and the dopant precursor on a hot plate at a certain temperature for a defined duration in order to have the dopant precipitate into the structure of the photocatalysts [60]. The co-precipitation/hydrothermal process is the process of simply mixing the precursors of a semiconductor photocatalyst and the dopant on a hot plate at a certain temperature and defined time to achieve the precipitation of the semiconductor and the dopant [61,62]. Introduction of oxygen as a non-metal dopant into the semiconductor photocatalyst during thermal exfoliation [63]. The introduction of metal dopants creates a sub-energy level below the conducting band which facilitates reduced travel distance between the electrons and holes, a condition necessary for the enhanced photocatalytic activity of the semiconductor. The dopants also serve as trapping sites for the photogenerated electrons thereby delaying and reducing the rate of electron-hole recombination as seen in [Scheme 2.3](#). Some of the metals used for doping are potassium (K), sodium (Na), iron (Fe), manganese (Mn), Copper (Cu), Zinc (Zn), Molybdenum (Mo), Cobalt (Co), and others.

Wang et al. synthesized K-doped graphitic carbon nitride (GCN) by thermal polymerization of KBr and thiourea and reported the effect of potassium in GCN on the photocatalytic evolution of H₂ gas [59]. The report showed that the introduction of potassium in the GCN structure reduced the bandgap and the recombination rate of the electron-hole pair and enhanced the light absorption properties of the GCN. Tonda et al. prepared Fe-doped GCN by mixing the GCN with the mixture of ferric chloride and acetone and investigated the doping effect on the photocatalytic degradation of rhodamine B (RhB) [59]. They reported

a reduced bandgap which resulted in enhanced light absorption activity, and a faster degradation rate of RhB when compared to GCN. Le et al. prepared Cu-doped mesoporous GCN and reported a faster degradation rate of methyl orange (MO) than bulk GCN [64]. Oh et al. prepared Cu-doped, Fe-doped, and Co-doped GCN and investigated their photocatalytic performance in degrading sulfonamide antibiotic sulfathiazole (STZ) [65]. The order of photocatalytic activity is as follows: Co-doped GCN > Fe-doped GCN >> Cu-doped GCN. The result shows the superior stability and performance of Cobalt (Co).



Scheme 2. 3 Doping as an electron trapping site for TiO₂ photocatalyst (Picture cited with permission granted by Rightslink, Appendix B) [66].

2.2.2 Non-metal doping

Heteroatoms can adjust the bandgap of bulk GCN. The heteroatoms have high ionization energy and are strongly electronegative. They can form covalent bonds by accepting electrons when reacting with other compounds. Heteroatom is any atom that is not carbon or hydrogen which is in the ring of a cyclic compound. Examples of heteroatoms commonly used as dopants are nitrogen, oxygen, sulfur, chlorine, bromine, and iodine. Dong et al. synthesized carbon-doped GCN to improve the GCN bandgap and they reported a faster degradation of RhB when compared to bulk GCN [67]. She et al prepared oxygen-doped

GCN and reported improved band gap and enhanced light absorption which resulted in faster degradation of methyl orange (MO) [68]. Cao et al synthesized S-doped GCN and reported reduced band gap and enhanced photocatalytic activity [69]. This resulted in faster degradation of methylene blue (MB).

2.2.3 Co-doping

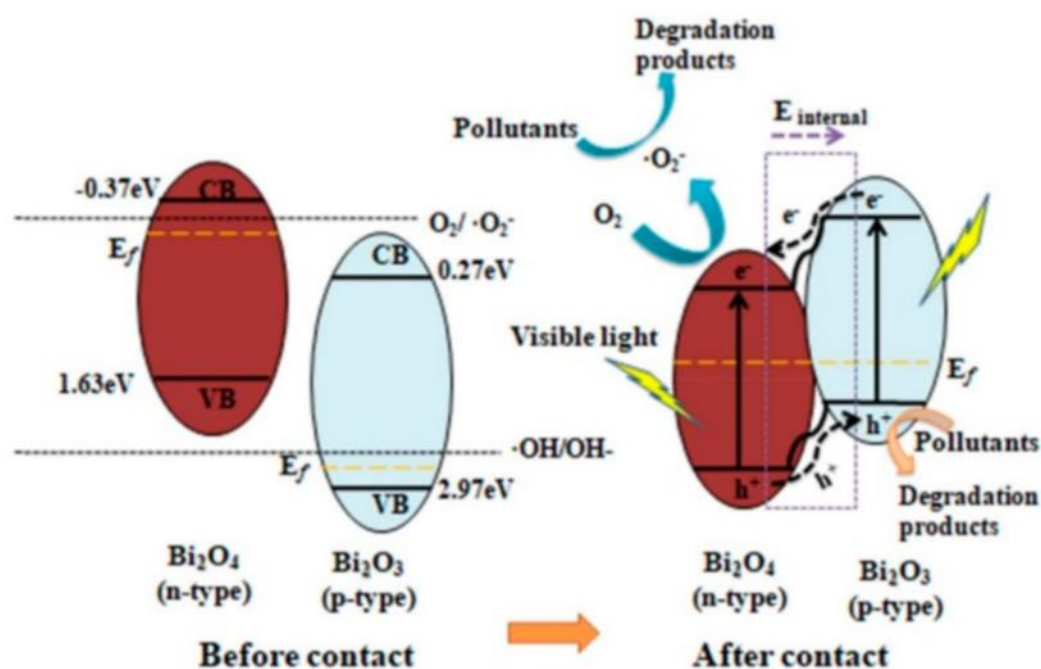
Co-doping, also known as tri-doping, is the combination of the benefits of these dopants which will lead to the enhanced photocatalytic performance of the semiconductor photocatalyst. Zhao et al prepared K-Na codoped GCN to tune the band structure of GCN by using KCl, NaCl, and melamine as precursors [70]. The photocatalytic degradation of RhB was significantly enhanced because of the enlarged surface area and reduced rate of electron-hole recombination. Hu et al codoped Fe and P on GCN and found that the intercalation of the metal (Fe) and non-metal (P) with the nitrogen in the GCN structure resulted in a synergistic effect by reducing the bandgap and improving charge separation [71]. This led to an enhanced photocatalytic performance in degrading RhB. Lin et al. codoped boron and fluorine on GCN by the polymerization of urea [72]. The X-ray photoelectron spectroscopy (XPS) revealed the interaction of the boron and fluorine heteroatoms in the GCN structure with B-N and F-N bond formation. This resulted in higher hydrogen evolution which is due to enhanced photocatalytic activity and improved charge separation.

2.2.4 Heterojunction

The heterojunction is an interface between two layers or regions of dissimilar coupled semiconductors. The coupling of these two or more dissimilar semiconductors is known as a composite. A semiconductor such as TiO₂ or GCN is known as a photocatalyst while a coupled semiconductor such as GCN/Ag₂CrO₄ with two different semiconductor parts (GCN and Ag₂CrO₄) is known as a semiconductor photocatalyst. Composite is when a material is made of various parts. These semiconductors have unequal band gaps. The heterojunction is used to improve the separation of photogenerated electrons and inhibit electron-hole pair

recombination [57,73,74]. Semiconductors can either be a negative type (n-type) or a positive type (p-type). The n-type plays a significant role in electron conduction because of the excess of electrons in the outer shell of the electrically neutral atoms while the p-type plays a significant role in hole conduction because it contains excess holes. Examples of n-type semiconductors are g-C₃N₄ (GCN) [75], Ag₂CrO₄ [76], TiO₂, ZnO, SnO₂, Bi₂O₄, and MoO₃ [77] while p-type semiconductors are GCN, NiO, Cu₂O, and Bi₂O₃ [77]. There are different types of semiconductor heterojunctions such as n-n, and p-n. These heterojunctions can be between wide and narrow bandgap semiconductors. TiO₂, NiO, and ZnO are UV-responsive semiconductor photocatalysts with wide band gaps (> 3.0 eV) while GCN is known to be a visible-light responsive semiconductor with a narrow bandgap (2.70 eV). The coupling of n-type GCN (2.70 eV) and another n-type semiconductor, such as TiO₂ (3.20 eV), ZnO (3.37 eV), or Ag₂CrO₄ (1.80 eV), to form n-n heterojunction expands the light absorption range and increases the specific surface area. Similarly, the coupling of n-type GCN with p-type semiconductors such as nickel oxide, and NiO (3.6 eV), to form p-n heterojunction also expands the light absorption range. [Scheme 2.4](#) shows the heterojunction of the p-n type semiconductors. In semiconductor/semiconductor heterojunction, the photogenerated electrons (e⁻) and the photogenerated holes (h⁺) flow towards the less negative potential and the less positive potential, respectively [78].

Adhikari et al. synthesized GCN/TiO₂ composites and reported enhanced photocatalytic performance in the degradation of RhB under natural sunlight [79]. Sundaram et al. synthesized GCN/ZnO composite by the calcination of melamine and sodium acetate [80]. The reduced electron-hole recombination resulted in the enhanced photocatalytic degradation of p-nitrophenol and MO. Tang et al. synthesized GCN/NiO which led to the suppression of electron-hole pair recombination and enhanced visible light absorption. This resulted in improved performance in CO₂ photocatalytic reduction [81].



Scheme 2. 4 Schematic diagram representation of heterojunction semiconductor photocatalysts (Image cited under the Creative Commons Attribution license) [78].

2.3 Visible light photocatalysis

The synthesis of visible-light-sensitive photocatalysts is becoming increasingly important because of its application in environmental remediation such as air purification and wastewater treatment [82]. Therefore, we plan to develop visible-light active photocatalysts that can achieve high degradation efficiency for organic pollutants while providing disinfection. This plan can be achieved by doping with metal, and non-metals or coupling two semiconductors together to form a heterojunction. This is to overcome the drawback of poor visible light utilization that is commonly associated with semiconductor photocatalysts. The poor visible light utilization is because of fast electron-hole recombination, poor charge separation, and transfer that are associated with the wide bandgap of semiconductors. The doping reduces the bandgap, increases the rate of charge transfer, improves charge separation between photogenerated electrons and photogenerated holes, and enhances visible light absorption and utilization. TiO_2 and ZnO which are wide band-gap semiconductors ($> 3.0\text{ eV}$) are very active under UV light and can be tuned to function under visible light by reducing the bandgap with metal or non-metal. Another option for improving the visible

light absorption range and reducing electron-hole recombination is by coupling two or more semiconductors to form a heterojunction. For example, TiO_2 and ZnO can be coupled with another semiconductor such as graphitic carbon nitride (2.7 eV, 459 nm) to form a GCN/ TiO_2 composite and GCN/ ZnO composite. The addition of GCN to TiO_2 (3.2 eV, 387 nm) and ZnO (3.37 eV, 368 nm) in the composite extends the light absorption from UV to the visible light region. This extension of light absorption is possible due to the formation of heterojunction between the semiconductor photocatalysts.

The heterojunction is the interface between two dissimilar semiconductors of unequal bandgaps. These combined bandgaps, especially between UV light-active photocatalysts such as TiO_2 and ZnO and visible-light-active photocatalyst such as GCN leads to enhanced light utilization from the UV region to the visible light (VL) region of the electromagnetic spectrum. This extended light absorption from the UV region to the VL region is of benefit in environmental remediation under natural sunlight and visible light applications since the two light sources have a visible light region and UV region which the composites like GCN/ TiO_2 and GCN/ ZnO can utilize for photocatalytic activities. In addition, a narrow bandgap semiconductor such as GCN (2.7 eV) can be coupled with another narrower bandgap semiconductor such as Ag_2CrO_4 (1.80 eV) to form GCN/ Ag_2CrO_4 heterojunction. The addition of Ag_2CrO_4 to GCN expands the visible light absorption from 460 nm to 688 nm. This is important when using light sources such as natural sunlight or visible light (400 nm – 700 nm).

2.3.1 Visible light photocatalysis and the degradation of organic pollutants

The organic compounds that can be degraded by photocatalysts under visible light irradiation are dyes, petroleum hydrocarbons, and phenolic compounds. Others are pharmaceuticals such as antibiotics and anti-inflammatories, and pesticides [83]. These organic compounds are chemically stable, toxic, and could be carcinogenic and recalcitrant [83–85]. Dyes such as Rhodamine B (RhB), Methyl Orange (MO), and Methyl Blue (MB) are non-biodegradable. Ni et al. synthesized $\text{SiO}_2/\text{MoS}_2$ composite and investigated the

photocatalytic performance in degrading MB and MO [86]. The result was that the high surface area and enhanced visible light absorption contributed to the faster degradation of the two dyes when compared to either SiO₂ or MoS₂.

Phenolic compounds in wastewater are the outcomes of industrial activities such as manufacturing, refining, pharmaceuticals, and petroleum production. Phenolic compounds are soluble in water, toxic, and non-biodegradable [87]. Phenols and their derivatives of chlorophenol and nitrophenol are broken down in the bulk liquid by hydroxyl radicals during the photocatalytic process to give intermediates such as hydroquinone, 4-chlorocatechol, pyrocatechol, and benzoquinone. These intermediates are eventually converted to mineralized products of CO₂ and H₂O. [Scheme 2.5](#) shows the photocatalytic degradation pathways for 4-chlorophenol (4-CP) [88], one of the contaminants of study in this Ph.D. program. In [Scheme 2.5](#), there are 2 competing primary intermediates in the degradation of 4-chlorophenol: through the formation of hydroquinone primary intermediate by substituting the chlorine ion with hydroxyl ion 2 and the formation of the 4-chlorocatechol primary intermediate by hydroxylation 3. Either of these 2 intermediates leads to the formation of another intermediate which is 1,2,4 benzenetriol 4, other intermediates, and then the mineralized products of CO₂ and H₂O. The ratio of these primary intermediates formed is determined by the experimental conditions and setup, such as the light source and the intensity, pH, temperature, and the quantity of reactive oxidative species (ROS) generated.

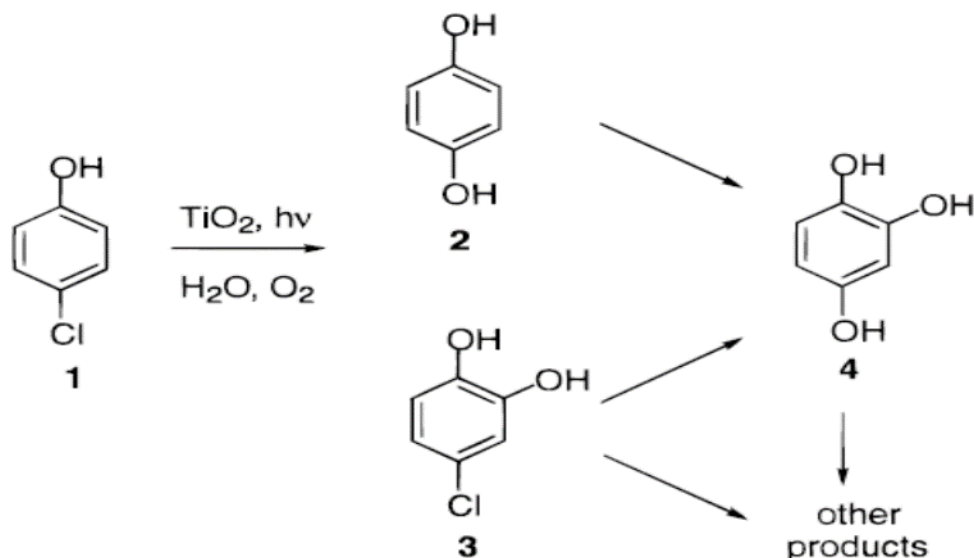
Pesticides are used as growth regulators, desiccants, ripening regulators, and to prevent damage during transportation or storage. However, pesticides are one of the primary sources of water pollution. All pesticides are toxic, non-biodegradable, and carcinogenic [89]. Domestic commercial brand herbicide, Killex^R consists of two organic compounds commonly used as herbicides, 2,4-Dichlorophenoxy acetic acid (2,4-D) and Methylchlorophenoxypropionic acid (Mecoprop-P or MCPP). These compounds are toxic, and recalcitrant, and have been designated as pollutants [90,91]. Heydari et al. used TiO₂ under natural sunlight to degrade the constituents of commercial brand herbicides, Killex^R which are 2,4-D and Mecoprop-P [92].

97% degradation of 2,4-D after 15 days and 100% degradation of Mecoprop-P after 22 days were reported.

Table 2.2 shows some visible light photocatalysts and their application in the degradation of organic pollutants and pesticides.

Table 2. 2 Visible-light active photocatalysts and the degradation of organic pollutants

S/N	Photocatalyst	Visible light source	Organic Pollutant	Conc (mg/L)	Degradation time (min)	Degradation efficiency (%)	Ref
1	SnO ₂ -MoS ₂	Visible light (200 W)	MB	20	120	96.4	[86]
2	TiO ₂	Natural sunlight	2,4-D and Mecoprop-P	49.4 and 27.3	15 days (21,600 min) and 22 days (31,680 min)	97 and 100	[92]
3	Ag/N-TiO ₂	Halogen Xenon lamp (1000W)	MO	10	120	54	[93]
4	ZnO/g-C ₃ N ₄ /Carbon xerogel	Simulated solar radiation (300W lamp), visible light (400W lamp)	4-CP	10	300	92	[94]
5	MoO ₃ /g-C ₃ N ₄	Natural sunlight	2,4-D	50	300	99	[95]
6	GCN	Xenon lamp (200 – 800 nm, 300W)	Mecoprop-P (MCP)	0.05	7	100	[96]



Scheme 2. 5 Photocatalytic degradation pathways for 4-chlorophenol. (Picture cited with permission granted by Rightslink, Appendix C) [88].

2.3.2 Visible light photocatalysis and the disinfection of microorganisms

Microorganisms are commonly found in wastewater, and they could be pathogenic leading to many infectious diseases. Some of these pathogenic microorganisms are enteroviruses that cause gastrointestinal diseases, *E. coli* strain that causes diarrhea, urinary tract infections, respiratory infection, and pneumonia, *S. aureus*, enterovirus and coronavirus that cause respiratory disease, skin infection, diarrhea and pneumonia, and salmonella that causes dysentery and meningitis. Matsunaga was the first to report the inactivation of bacteria using TiO_2 photocatalysis in 1985 [97]. The report shows the disinfection of bacteria in water provides a new path for the application of photocatalysis in the disinfection of microorganisms. Just like the degradation of organic pollutants, the reactive oxygen species (ROS) play an important role in the inactivation of microorganisms. The ROS destroys coenzyme A leading to the inhibition of respiratory activity and the oxidation of the nucleic acid, protein, and other macromolecules and eventually causing cell death [98]. Silver compounds, zinc compounds, and copper compounds have been known for a very long time to have antimicrobial properties. These unique properties have led to several studies on their

application for disinfecting water and wastewater, especially in photocatalysis. Several research and reviews reported the antimicrobial efficacy of silver nanoparticles (AgNP), silver ions (Ag^+) [99,100], ZnO [101], and copper nanoparticles [102]. These compounds can attach to the cell wall of microorganisms and the sulfide protein and then denature them, inhibiting the respiratory system and cell reproduction, and leading to the eventual cause of cell death. In addition, the production of ROS by these photocatalysts can lead to cell membrane disruption [99]. [Scheme 2.6](#) shows the antimicrobial mechanisms of silver nanoparticles (Ag NPs), ZnO nanoparticles (ZnO NPs), and copper nanoparticles (Cu NPs). In [Scheme 2.6 \(a\)](#), 7 different actions were proposed for the antimicrobial mechanism of Ag NPs as follows: the Ag^+ released by Ag NPs adhere to or pass through the cell wall or membrane, the interaction of the Ag^+ with the ribosomes leading to its denaturing, the interruption and the termination of adenosine triphosphate (ATP) production as a result of the deactivation of the respiratory enzyme by the Ag^+ , the disruption of the membrane by reactive oxygen species (ROS), interference of deoxyribonucleic acid (DNA) replication by Ag^+ and ROS which leads to DNA replication and cell multiplication, denaturing of the cell membrane by Ag NPs, and the perforation of the cell membrane by the Ag NPs leading to the leakage of organelles and nutrients from cells. In [Scheme 2.6 \(b\)](#), ZnO NPs show a similar mechanism to Ag NPs as follows: the Zn^{2+} released from the ZnO NPs adheres to and passes through the cell membrane and eventually attacks the cell structure, the ROS generated by the ZnO NPs interfere with the DNA and the cell structure and therefore inhibiting the DNA replication and cell multiplication, and the ZnO NPs disrupts the cell membrane, perforates it which eventually leads to the leakage of nutrients. In [Scheme 2.6 \(c\)](#), the antimicrobial mechanisms of Cu NPs are broken down for three microorganisms, bacteria, viruses, and yeast and fungi. For the anti-bacteria mechanism, again you see similar trends as compared to Ag NPs/ Ag^+ , ZnO NPs/ Zn^{2+} as follows: the Cu NPs adheres to, denatures, and perforates the cell membrane leading to leakage of nutrients, the interaction of the copper ions with protein leading to its damage and the generation of ROS by the Cu NPs leads to the interference of the DNA replication and thereby inhibiting the DNA replication and cell multiplication. While there are 3 steps involved in the disinfection process that are directly attached of the nanoparticles to the bacterial cell wall, the release of ions and the diffusion through the cell

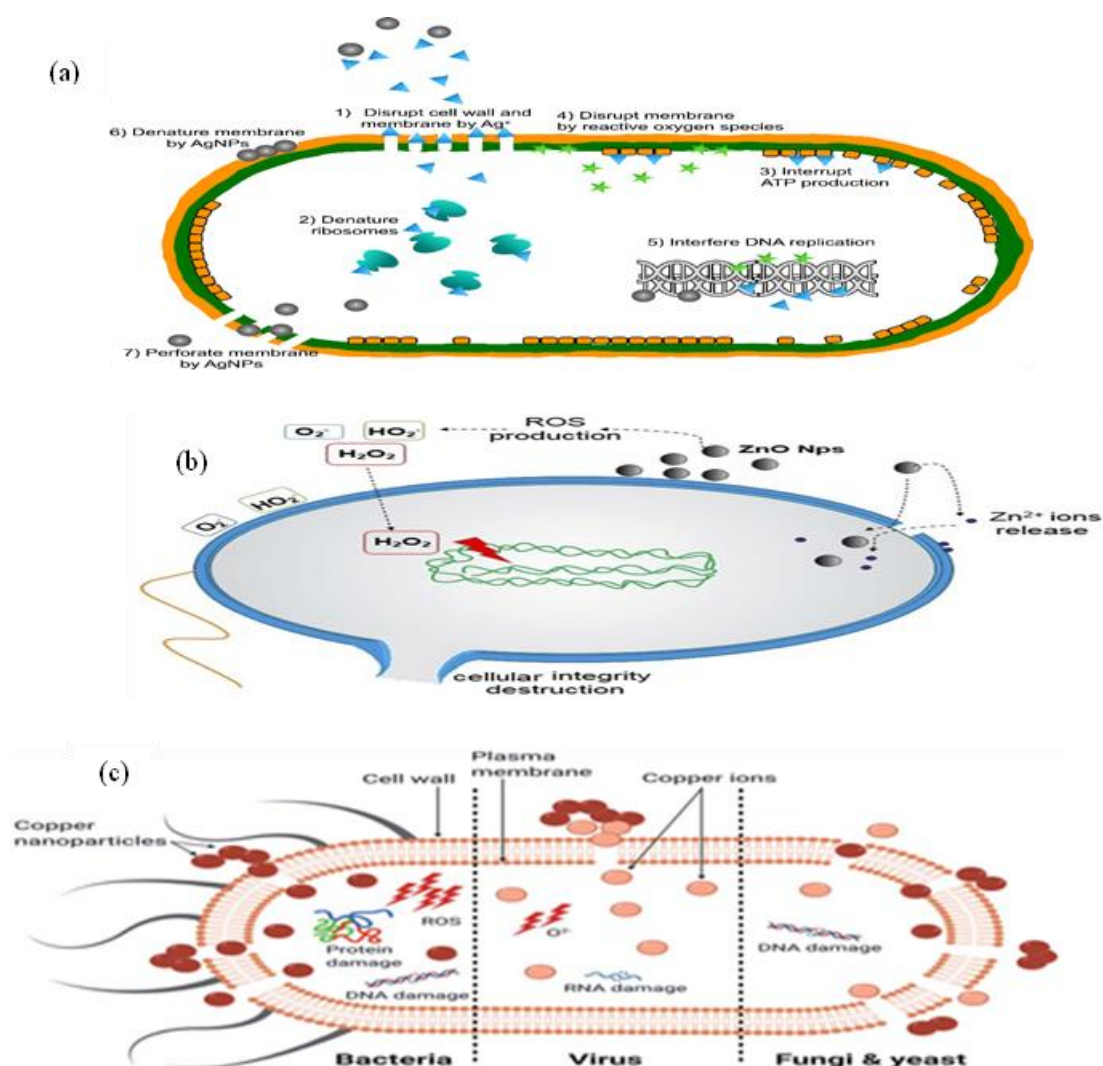
membrane, and the generation of ROS that disrupts the production of cellular functions, the photocatalytic disinfection mechanism remains elusive, complicated, varies across the board depending on the experimental conditions, and therefore controversial.

There are claims and counter-claims on which step is dominant when it comes to the ROS, ions, and charges responsible for the disinfection. However, there seems to be a general agreement that the ROS, charges, and ions all play a role to a varying degree in the photocatalytic disinfection mechanism. However, the closest and most simplified disinfection mechanism involving the irradiation of a semiconductor by light was proposed as seen in equations (2.13) – (2.23) showing the different targets in the bacteria by ROS, metal ions, and metal nanoparticles [103]. Equations (2.18) – (2.19) show that the released metal ions (oxidizing agents) from the photocatalyst can be reduced to metal nanoparticles (NP) and the metal NP (reducing agent) can be oxidized to generate ROS which attacks different parts of the bacteria [104]. The photocatalytic disinfection mechanism can also be used in apart, equations (2.21) – (2.23), for the photocatalytic degradation mechanism of protein. Ribosomes are a macromolecule found in the cells of microorganisms and are the site for protein synthesis and production of RNA.

Deng et al synthesized GCN/AgBr composite and used it to inactivate *E. coli* and *S. aureus* under visible light irradiation (Xenon lamp, 300W) [105]. The results show complete inactivation (6.5 log) of *E. coli* in 60 minutes and *S. aureus* in 150 minutes. The ROS of h^+ and $HO\cdot$ were reported to be dominant in the inactivation of the bacteria. Karunakaran et al. prepared a ZnO/TiO₂ composite and evaluated its photocatalytic performance in inactivating *E. coli* under two visible light sources, a 150 W tungsten lamp, and natural AM1 sunlight [106]. 9×10^{12} CFU/mL of *E. coli* was inactivated under the tungsten lamp irradiation in 30 minutes and 8×10^{14} CFU/mL of *E. coli* was inactivated under natural AM1 sunlight in 30 minutes. Zhang et al. synthesized a ternary composite of GCN/ZnO/Stellerite to inactivate *S. aureus* under visible light illumination [107]. Nearly 90% of inactivation was reached after 150 minutes. Ng et al. synthesized magnetic Fe₂O₃/AgBr to disinfect wastewater of *E. coli* and *S. aureus* under visible light

irradiation [108]. The disinfection of viruses has also been reported using visible light photocatalysis. Li et al. synthesized GCN and investigated its photocatalytic activity on MS2 under visible light irradiation (Xenon lamp, 300W) [109]. Bacteriophage MS2 is a commonly used surrogate for waterborne pathogenic viruses due to their similar size, structure, and surface properties [109,110]. The result showed complete inactivation (8 log) in 360 minutes with GCN at an optimal concentration of 150 mg/L.

Light-activated antimicrobial and antiviral coatings have been and are currently being studied for continuous disinfection of surfaces. The irradiation of photocatalysts with visible light results in the production of cytotoxic species such as photogenerated electrons, photogenerated holes, and reactive oxygen species such as singlet oxygen hydrogen peroxide and hydroxyl radicals. Kelly et al. synthesized Mo-doped titania photocatalysts and coated it on a stainless steel substrate to investigate their photocatalytic performance on *E. coli* under visible light [111]. Complete inactivation (7 log) was achieved in 24 hours. Khan et al. coated plastic Venetian blinds and glass substrates with the synthesized Ag-doped TiO₂ photocatalyst and investigated the photocatalyst activity of the coating in disinfecting *P. aeruginosa* and *B. subtilis* under visible light [112]. The coatings were carried out using two solvents, water, and ethanol. The water and ethanol coating methods were applied to the glass as well as the blinds. 90% disinfection of *P. aeruginosa* was achieved for the water-based coated glass in 120 minutes while 95% disinfection of *B. subtilis* was attained for water-based coated glass and water-based Venetian blinds in 120 minutes. The result shows that the water-based coating of Ag/TiO₂ on glass and Venetian blinds had optimal disinfection performance against the bacteria under visible light. Liu et al. coated Cu (II)-TiO₂ on a glass substrate and used it as a self-disinfecting coating to disinfect bacteriophage virus (1.2×10^{11} PFU/mL) [113]. The effect of pH was studied on the disinfection performance. Only 3 log reduction was achieved with a pH of 7 in 120 minutes while complete inactivation (log 8) was achieved with a pH of 12 in 120 minutes. [Table 2.3](#) shows the disinfection of microorganisms under visible light irradiation.



Scheme 2. 6 Schematic diagram of the antimicrobial mechanisms of (a) Silver nanoparticles (Image cited under the Creative Commons Attribution-NonCommercial License) [99], (b) Zinc Oxide nanoparticles (Image cited under the Creative Commons Attribution-NonCommercial License) [114], and (c) Copper nanoparticles (Picture cited with permission granted by Rightslink, Appendix D) [102].

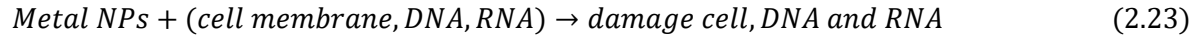
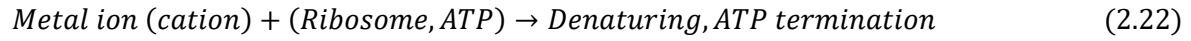
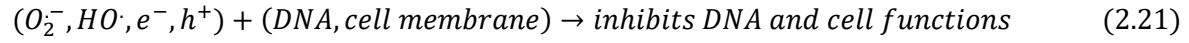
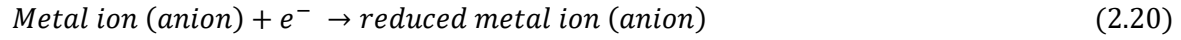
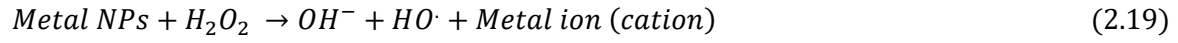


Table 2. 3 Visible-light active photocatalysts and the disinfection of microorganisms

S/N	Photocatalyst	Visible light source	Contaminant	Disinfection time (min)	Conc. (CFU/mL)	Disinfection efficiency	Ref
1	BiOBr/AgBr	Xenon lamp (1000 W/m ² , 300W)	E. coli	24	10 ⁷	Complete 7 log reduction	[115]
2	GCN/ZnO/Stel lerite	Visible light	S. aureus	120	10 ⁷	90%	[116]
3	Ag/BiOI	Iodide lamp (400W)	E. coli	20	10 ⁷	Complete 7 log reduction	[117]
4	Fe/ZnO	Solar irradiation (100,000 lux)	E. coli	90	10 ⁷	3log reduction	[61]
5	Ag/ZnO/GCN	Xenon lamp (300W)	E. coli	120	3.2 * 10 ⁷	Complete 7.5 log reduction	[118]
6	GCN/Mn-ZnO	Sunlight (68,000 – 73,000 lux)	E. coli, S. aureus, B. subtilis, and S. salivarius	-	-	High zone of inhibition	[119]
7	Alumina/ZnO	Yellow LED (65,000 lux, 160W)	E. coli	240	10 ⁶	Complete 6 log reduction	[62]

2.4 Light sources and intensities

There are three different types of light sources, and they are continuous polychromatic light (incandescent bulbs, halogen lamps, Xenon lamps, fluorescent lamps, and the sun), discrete polychromatic light (mercury-vapor lamps), and narrow-band monochromatic light (LEDs, OLEDs, and laser). Efficiencies of these light sources were reported based on their characteristics and reaction engineering perspective [120] which are tabulated below.

Table 2. 4 Characteristics of light sources

S/N	Characteristic	Polychromatic light	Monochromatic light
1	Filtering of the emission spectrum	Yes	No
2	Typical lifetime: For Example, 20,000h of operating time	No	Yes
3	Photon flux (mol/h)	Low (Xe and Hg-Vap)	Very high (Near UV and VL)
4	Cooling demand	High	Low

The table 2.4 shows that monochromatic light source such as blue LED has better practical application than polychromatic light source especially because of high photon flux, meaning that a large number of photons generated can be used to drive the photocatalytic reaction and long operating time. However, the practical limitation is the availability of monochromatic light for “all” required wavelength regions. Some LED-based light sources are also polychromatic with wavelengths ranging from 400 – 700 nm. These LED-based light sources are categorised based on the color temperature on a Kelvin scale which could be either warm or cool. For example, 3000K LED lights have a warm color (red) with peak intensity at wavelength > 600 nm, while 5000K LED lights have a cool color (blue) with peak intensity at wavelength 450 nm [121,122]. The 4000K LED light, which is between 3000K LED and 5000K LED, with amber color has a peak intensity at wavelength 550 nm. A relationship exists between the color temperature (degrees Kelvin) of LED lights when placed at the same distance of 10cm to an object and their light intensity (Lux) as estimated and observed using Nemalux Industrial Lights: 3000K LED, 4000K LED, and 5000K LED as seen in [Table 2.5](#). The table shows that the light intensity increases as the color temperature of the LED light increases. Reported articles validate this observation that low brightness (low light intensity) is associated with low and warmer color temperatures such as 3000K LED while high brightness (high light intensity) is associated with higher and cooler temperatures such as 5000K LED [123]. When a 5000K LED light (Nemalux Industrial) distance is varied to an object, different light intensities are estimated and observed as seen in [Table 2.6](#). It was observed that the light intensity decreases with the increasing distance to the object of

illumination. Overall, this indicates that the choice of color temperature for LED light and its distance to the object of illumination affect the light intensity. In this thesis, monochromatic LED light in the visible spectrum (450 nm) was used for chapters 3 to 5 in the photoreactor due to its directionality, high light intensity, and practical application while polychromatic LED light in the visible spectrum (400 – 700 nm) with the color temperature 5000K was used in chapter 6 which is about the self-disinfecting coated surfaces (see [Table 2.5](#)) due to its brightness and high light intensity. The 5000K LED as well as the 3000K LED and the 4000K LED can be deployed essentially for outdoor applications to simulate sunlight since sunlight is reported to have light intensities of 100,000 Lux (direct sunlight) and 3,000 – 18,000 Lux (diffuse sunlight) [124]. These LED lights can be used as task lights in workspaces that require high illumination such as construction sites at night time. The LED lights can also be used in residential rooms and commercial places that require light intensities between 100 – 800 Lux by placing them at a distance much further away from the object of illumination since light intensity is a function of the distance between the light source and the object of illumination (see [Table 2.6](#)).

Table 2. 5 Estimate light intensities of polychromatic LED lights (10 cm to object) with different color temperatures

Light source and type	3000K LED	4000K LED	5000K LED
Wavelength, nm	> 600	550	450
Light intensity (10cm distance to object), Lux	15,4000	15,610	16,800

Table 2. 6 Estimated light intensities of polychromatic 5000K LED light at a varying distance to an object

Distance to an object (cm)	Light intensity (Lux)
10	16,800
20	7,200
30	3,500

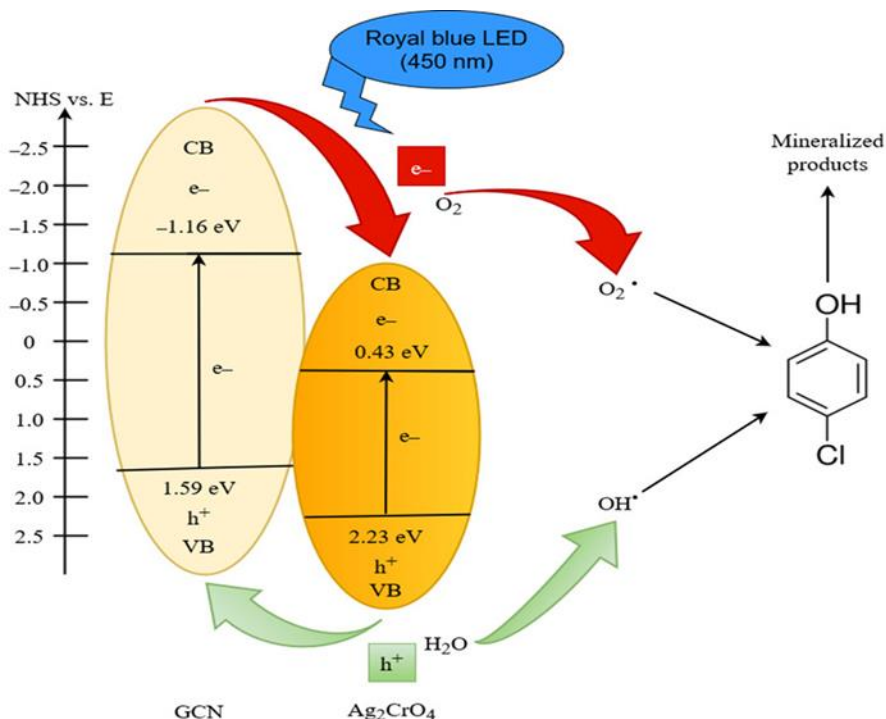
Chapter 3: Visible-Light-Driven Photocatalytic Degradation of 4-Chlorophenol Using Graphitic Carbon Nitride Based Nanocomposites¹

3.1 Highlights

- U-GCN showed the highest photocatalytic degradation activity.
- U-GCN/Ag₂CrO₄ nanocomposites showed superior photocatalytic degradation activity, among other U-GCN/silver-based nanocomposites.
- U-GCN/0.3Ag₂CrO₄ nanocomposite was photocatalytically activated by both royal blue LED and UV-A LED

¹ O.O. Akintunde, L. Yu, J. Hu, M.G. Kibria, G. Achari, Visible-Light Driven Photocatalytic Degradation of 4-Chlorophenol Using Graphitic Carbon Nitride-Based Nanocomposites, Catalysts. 12 (2022) 281. <https://doi.org/10.3390/catal12030281>.

3.2 Graphical abstract



3.3 Abstract

4-chlorophenol (4-CP), a hydroxylated aromatic compound (HAC), is a recalcitrant and toxic organic pollutant found in industrial wastewater and various environmental media. In this paper, visible-light-activated photocatalysis using graphitic carbon nitride (GCN) was used to treat 4-CP in an aqueous media. Graphitic carbon nitride from different precursors (dicyanamide, urea, and melamine), as well as GCN/silver nanocomposites (AgBr, Ag₃PO₄, Ag₂CrO₄, and Ag), were successfully synthesized and characterized by BET, XRD, SEM, EDS, and UV-Vis DRS. The band gaps of the photocatalysts were estimated using the UV-Vis DRS characterization results and Tauc plots. The evaluation of the efficacy of the GCN-based catalysts in degrading 4-CP was conducted with different photoreactors such as a royal blue light-emitting diode (LED), a UV-A LED, LUZCHEM cool white lamps, and a solar simulator. The results showed that GCNs with royal blue LED can effectively degrade 4-CP from aqueous media. Among the

different precursors, urea-derived GCN showed the best performance in degrading 4-CP due to its large surface area. GCN/0.3Ag₂CrO₄ nanocomposite showed a synergistic effect for the enhanced photocatalytic degradation of 4-CP. The degradation of 4-CP with a rate constant of $2.64 \times 10^{-2} \text{ min}^{-1}$ was achieved with a GCN/0.3Ag₂CrO₄ nanocomposite under royal blue LED irradiation.

3.4 Introduction

4-chlorophenol (4-CP), a hydroxylated aromatic compound (HAC), is a recalcitrant and toxic organic pollutant found in industrial wastewater and various environmental media. It is extensively used as an intermediate in the synthesis of pharmaceuticals, dye, wood preservatives, and agricultural products such as pesticides and herbicides [125,126]. The release of wastewater from industrial processes using 4-CP as an ingredient has been a major source of water pollution. Not only are chlorophenols found in industrial wastewater, but they can also be formed during the disinfection of municipal water upon chlorination of humic matter or natural carboxylic acid [127]. Physical adsorption and biological degradation have been reported to remove 4-CP in water [128]. However, physical adsorption only transfers 4-CP from the solution to the surface of the adsorbent. Adsorbents can be quickly exhausted when they are used to treat a high concentration of 4-CP. The high cost associated with the disposal and regeneration of exhausted adsorbent limits its use on a large scale [129,130]. The biodegradation of 4-CP usually requires a longer hydraulic retention time and produces a high microbial mass [128]. In addition, biodegradation performance is highly impacted by carbon source, oxygen level, nutrients, and temperature. Photocatalysis can address these limitations due to its high efficiency in the degradation and mineralization of organic pollutants to CO₂ and H₂O, and it is more eco-friendly as it will not release secondary pollutants into treated water and requires a lesser amount of chemical input [38,131]. Photocatalysis is a process in which a photocatalyst, such as TiO₂, is irradiated by photons with higher energy than its bandgap, leading to the generation of holes and electrons on its surface. Those photogenerated holes and electrons can react with electron donors and acceptors to form reactive oxidative species such as oxygen and hydroxyl radicals, which can degrade the

organic contaminants to less harmful by-products [132]. Photocatalysis has been widely used in the degradation of organic pollutants (dyes, phenolic compounds, and hydrocarbons), removal of heavy metals (mercury, arsenic, and cadmium), removal of pharmaceuticals (antibiotics), and inactivation of microorganisms [38]. Conventional photocatalysis has been focused on using titanium dioxide (TiO_2), which requires UV irradiation due to its large bandgap (3.2 eV). The high energy cost associated with UV irradiation puts a limitation on its practical application [133].

Over the last decade, visible-light-sensitive graphitic carbon nitride (GCN or $\text{g-C}_3\text{N}_4$), a metal-free photocatalyst, has gained a lot of attention in removing organic contaminants due to its narrow optical band gap (2.7 eV). It is readily synthesized from available precursors (dicyandiamide, urea, and melamine) and has a low cost of production [134–136]. GCN derived from different precursors has been successfully reported to remove nitrogen oxide, 4-nitrophenol, methyl orange, and rhodamine B under visible light [137–140]. The photocatalytic activity of GCNs can be further enhanced by doping with different organic and inorganic compounds to reduce the bandgap, increase visible-light utilization, decrease the recombination rate of e–h pairs, and improve the rate of charge transfer [141,142]. Silver-based inorganics are among the most promising compounds used to improve the properties of GCN because of their photosensitivity and photocatalytic activity. Ren et al. [143] observed that 4-CP degradation by GCN/ Ag_3PO_4 with a xenon lamp was 28 times faster than using pristine GCN. Deng et al. [105] enhanced visible-light-driven photocatalytic *E. coli* disinfection by using GCN/AgBr. A negligible inactivation of *E. coli* was obtained for pure GCN within one hour, while a 6.5 log reduction was achieved with GCN/AgBr. Faisal et al. [55] fabricated GCN/Ag nanoparticles to degrade methylene blue in water under a xenon lamp and found that the degradation rate with GCN/Ag is 1.9 times higher than pure GCN.

This research focuses on the synthesis and characterization of GCN and GCN/silver-based composites and their photocatalytic performance in degrading 4-CP under royal blue LED and other light sources. GCNs were prepared from different precursors, including dicyandiamide (D-GCN), urea (U-GCN), and melamine (M-GCN) through the direct pyrolysis method, while GCN/silver-based composites (U-GCN/Ag, U-GCN/ Ag_3PO_4 , U-GCN/AgBr, and U-GCN/ Ag_2CrO_4) were fabricated by a dark-induced/in-situ deposition

method. Different characterization techniques including BET, XRD, SEM, EDS, and UV-Vis DRS were used to study the composites' crystal structure, morphology, and optical and bandgap properties. The impact of GCN precursors, silver compounds, GCN/silver ratio, and light sources on the photocatalytic degradation of 4-CP has been fully investigated. A mechanism of the photocatalytic degradation of 4-CP by GCN/silver-based composites has been proposed.

3.5 Materials and Methods

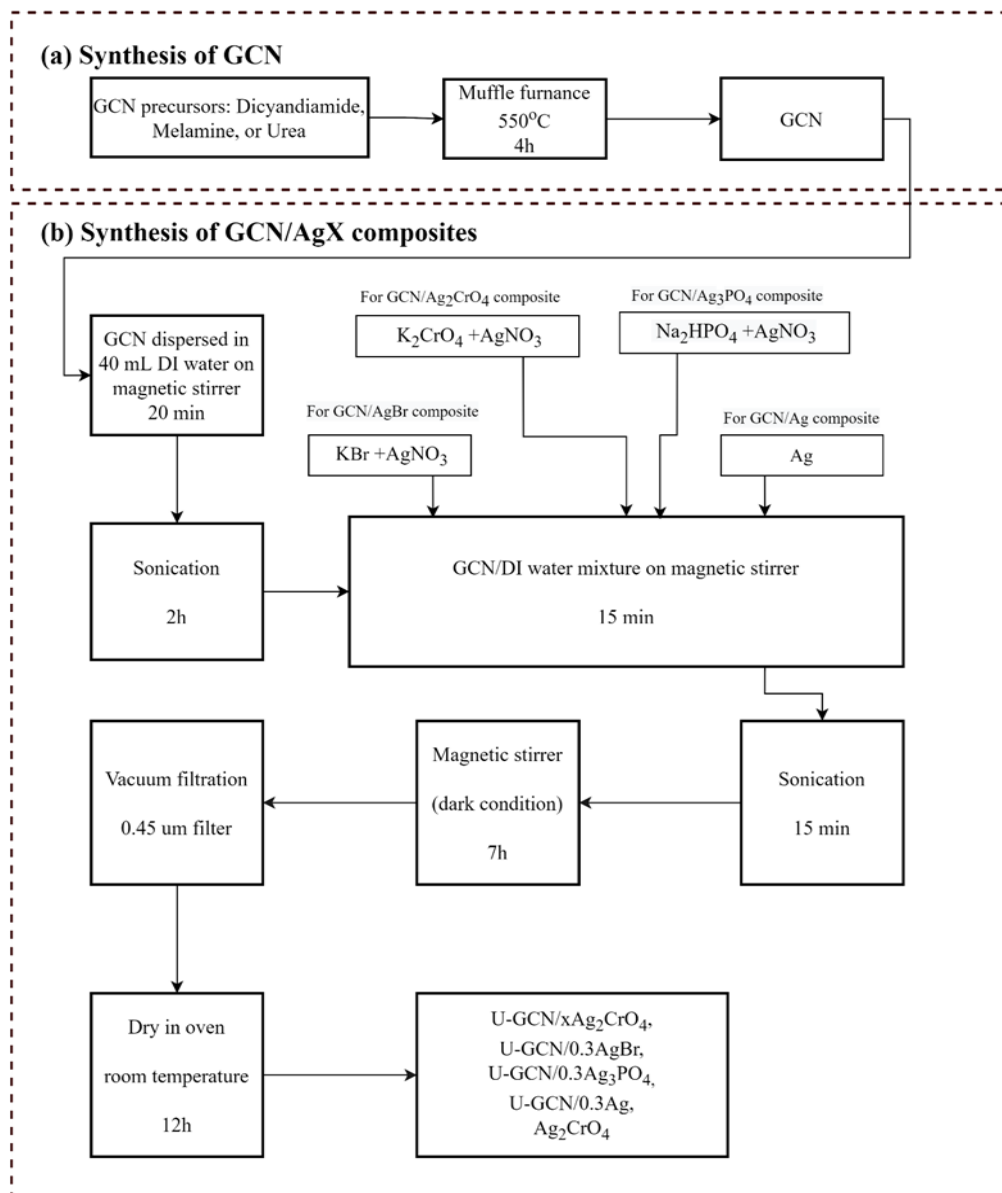
3.5.1. Chemicals

4-chlorophenol- $\text{ClC}_6\text{H}_4\text{OH}$ (99%), urea- $\text{CH}_4\text{N}_2\text{O}$ ($\geq 99.5\%$), silver nitrate- AgNO_3 ($\geq 99\%$), potassium chromate- K_2CrO_4 ($\geq 99\%$), potassium bromide-KBr ($\geq 99\%$), ethanol- $\text{C}_2\text{H}_5\text{OH}$ ($\geq 95\%$), 1-10 phenanthroline- $\text{C}_{12}\text{H}_8\text{N}_2$, iron III chloride- FeCl_3 , ammonium iron II sulfate hexahydrate (Mohr's salt, $\geq 98\%$) $-(\text{NH}_4)_2\text{Fe}(\text{O}_4)_2(\text{H}_2\text{O})_6$, and high-pressure liquid chromatography (HPLC) grade water were purchased from Sigma-Aldrich Co. (St. Louis, MO, USA). Melamine, $\text{C}_3\text{H}_6\text{N}_6$ ($\geq 99\%$), was purchased from Aldrich (St. Louis, MO, USA). Dicyandiamide- $\text{C}_2\text{H}_4\text{N}_4$ ($\geq 99\%$) and potassium trioxalatoferrate III trihydrate- $\text{K}_3\text{Fe}(\text{C}_2\text{O}_4)_3 \cdot 3\text{H}_2\text{O}$ were purchased from Alfar Aesar (Ottawa, ON, Canada). Nanosilver particles were purchased from Aldrich (Oakville, ON, Canada). HPLC grade acetonitrile, CH_3CN , was purchased from EMD (Gibbstown, NJ, USA). Sodium acetate- $\text{C}_2\text{H}_3\text{NaO}_2$ was purchased from Brady Canada. Aqueous solutions were prepared with deionized (DI) water. The disodium hydrogen phosphate, Na_2HPO_4 ($\geq 99\%$) was purchased from BDH (Toronto, ON, Canada). Phosphoric acid, H_3PO_4 (75%), was purchased from Chemco (Port Louis, Mauritius). All chemicals were used as received.

3.5.2 Synthesis of Graphitic Carbon Nitride (GCNs) and GCN Composites

In this study, GCNs were synthesized by direct pyrolysis from the different precursors' dicyandiamide, urea, and melamine [137,138,143,144], as shown in [Scheme 3.1a](#). Typically, 30 g of dicyandiamide, urea, or melamine was put in a partially closed alumina crucible and then placed in a muffle furnace (550-58, Fisher

Scientific, Waltham, MA, USA), set at 550 °C, for 4 h. After 4 h, the muffle furnace was turned off and the GCNs derived from these precursors were left to cool down to room temperature. The GCNs from dicyandiamide, urea, and melamine were ground to powder and labeled D-GCN, U-GCN, and M-GCN, respectively.



Scheme 3. 1 Synthesis procedures of GCN and GCN-based composites.

GCN/silver-based compound composites were synthesized by a dark-induced, in-situ deposition method (see [Scheme 3.1b](#)) [143,145]. A total of 1 g U-GCN was dispersed in 40 mL of deionized water, stirred on a magnetic stirrer for 20 min, and then placed in an ultrasonicator for 2 h. After that, the solution was placed on the magnetic stirrer and different amounts of K_2CrO_4 , KBr , Na_2HPO_4 , Ag , and AgNO_3 were added as follows: for U-GCN/0.3 Ag_2CrO_4 composites, 0.2774 g AgNO_3 and 40 mL K_2CrO_4 solution (4.83 g/L) were added; for U-GCN/0.3 AgBr , 0.277 g AgNO_3 and 40 mL KBr solution (4.85 g/L) was added; and for U-GCN/0.3 Ag_3PO_4 , 0.1386 g of AgNO_3 and 40 mL Na_2HPO_4 (2.42 g/L) were added, while for U-GCN/0.3 Ag , 0.3 g of Ag nanoparticle was added. The mixture of GCN/silver compounds was placed on the magnetic stirrer for 15 min and then transferred to the ultrasonicator for another 15 min. The solution was then placed on the magnetic stirrer in the dark for 7 h. The product was vacuum filtered using a 0.45 μm (nitrocellulose, Merck Millipore Ltd., Cork, Ireland), then washed with both DI water and ethanol at least five times. Finally, U-GCN/silver-based compound composites were obtained after drying in the oven (637 G, Fisher Scientific, Waltham, MA, USA) at room temperature for 12 h. Nanocomposites of U-GCN/ Ag_2CrO_4 with different mass ratios of Ag_2CrO_4 denoted as U-GCN- $x\text{Ag}_2\text{CrO}_4$, where $x = 0.1, 0.3$, and 0.5 , were synthesized using the same procedure above with different masses of AgNO_3 and K_2CrO_4 . Ag_2CrO_4 was synthesized following a similar procedure in Figure 5b above, but without U-GCN. Described briefly, 0.2774 g AgNO_3 was added to 0.1934 g of K_2CrO_4 40 mL solution, stirred for 20 min, sonicated for 2 h, stirred and sonicated for 15 min, and then stirred for 7 h in the dark. The product was vacuum filtered and washed with ethanol and water, then dried in the oven at room temperature for 12 h to obtain the Ag_2CrO_4 product.

3.5.3. Characterization

The crystal structure of the samples was studied using X-ray diffraction (XRD; Rigaku multiflex X-ray diffractometer) with $\text{Cu K}\alpha$ X-ray radiation, $\lambda = 1.5406 \text{ \AA}$. The morphology of the samples was examined by scanning electron microscope (SEM; Quanta FEG 250 FESEM). The elemental analysis of the samples was conducted using energy-dispersive X-ray spectroscopy (EDS; Bruker Quantum 5030 SDD X-ray

spectrometer) with SVE III pulse processing electronics. The surface areas and pore volumes were obtained from the N₂ sorption isotherm at 77 K using automatic adsorption equipment (Tristar II; Micrometrics). The UV-Visible (UV-VIS) diffuse reflectance spectroscopy (DRS) of the dry-pressed disk samples was measured using a spectrophotometer (UV-VIS DRS; UV-2600 Shimadzu spectrophotometer) with BaSO₄ as the reference sample. The UV-VIS DRS of the samples were used in estimating the Kubelka–Munk function $(F(R)E)^2$ using Equation (3.1), and then the band gap values of the samples were estimated from the Tauc plot of $(F(R)hv)^{1/Y}$ vs. hv , eV [146,147] as follows:

$$[F(R)hv]^{1/Y} = \left(\frac{(1-R)^2}{2R} * hv \right)^{1/Y} \quad (3.1)$$

$$K = (1 - R)^2; \quad S = 2R; \quad Y = \frac{1}{2} \text{ or } 2; \quad hv \equiv \text{eV}$$

where K is the molar absorption coefficient, S is the scattering factor, h is the Planck constant, ν is the photon's frequency, and Y is a factor dependent on the nature of the electron transition, which is either $\frac{1}{2}$ or 2 for the direct and indirect band gaps, respectively.

3.5.4. Photocatalytic Experiments

The photocatalytic performance of GCNs derived from different precursors (D-GCN, U-GCN, and M-GCN) was first evaluated by degradation of the 4-CP using a royal blue LED photoreactor (peak emission wavelength = 450 nm). In each experiment, 40 mg of the GCN was dispersed in a 40 mL solution containing 20 mg/L 4-CP in a 100 mL quartz beaker. Before LED irradiation, the water/catalyst mixture was stirred magnetically in the dark for 30 min to attain adsorption–desorption equilibrium. 3 mL of samples were collected at different irradiation intervals and filtered using a 0.45 μm syringe filter (PTFE, Chromatographic Specialities Inc., Brockville, ON, Canada) to remove the photocatalyst particles.

The GCN showing the best performance in degrading 4-CP was selected in synthesizing GCN/silver-based nanocomposites (Ag, AgBr, Ag₃PO₄, and Ag₂CrO₄), all at a fixed mass ratio of 1:0.3. The performance of the most promising photocatalyst, U-GCN/silver chromate composite, was further investigated using three different mass ratios ($x = 0.1, 0.3$, and 0.5). Furthermore, the performances of the UV-A LED (365 nm), Luzchem cool white light reactor (400–700 nm), and the solar simulator (350–1800 nm) using the optimal U-GCN/silver chromate composite were evaluated and then compared with royal blue LED photoreactor.

3.5.5 Analysis

The concentration of 4-CP was determined using high-performance liquid chromatography (HPLC; LC-2040C 3D Shimadzu Corporation, Kyoto, Japan) with UV absorbance detection at $\lambda = 280$ nm.

The mobile phases were 0.1% phosphoric acid in HPLC-grade water and 0.1% phosphoric acid in acetonitrile at a 50:50 mixture with a flow rate of 1 mL/min. The measurements were conducted in duplicate, and the detection limit was around 0.1 mg/L.

3.5.6 Actinometry

The radiation entering the reaction vessel was determined using ferrioxalate actinometry, which is based on the principle of the photoreduction of Fe³⁺ to Fe²⁺ [148,149]. This experiment was carried out for the royal blue LED, UV-A LED, cool white lights (LUZCHEM reactor), and solar simulator (HAL–320W). The analysis of the Fe²⁺ complex photoreduction was carried out using a spectrophotometer (UV-2600 Shimadzu Corp., Kyoto, Japan).

3.6 Results and Discussions

3.6.1 Physical and Chemical Properties of GCN and GCN Composites

The N₂ adsorption–desorption Brunauer–Emmett–Teller (BET) isotherms for the synthesized photocatalysts and their corresponding Barret–Joyner–Halenda (BJH) average pore size distribution curves are presented in [Figures S3.1 and S3.2](#). The N₂ adsorption–desorption for D-GCN, U-GCN, M-GCN, U-

GCN/0.3Ag₂CrO₄, U-GCN/0.1Ag₂CrO₄, U-GCN/0.5Ag₂CrO₄, U-GCN/0.3Ag, U-GCN/0.3AgBr, and U-GCN/0.3Ag₃PO₄ can be classified as a type IV isotherm with an H3-type hysteresis loop. This is an indication that those photocatalysts have mesoporous structures [150]. The N₂ adsorption–desorption for Ag₂CrO₄ follows the type III isotherm. This is due to the non-identifiable monolayer formation, weak adsorbent–adsorbate interactions, and the presence of macroporous structures that are typical of a type III isotherm [150]. The specific surface area, pore volume, and average pore size for GCN and GCN/silver-based composites are summarized in [Table 3.1](#). The specific surface area and pore volume of urea-derived GCN (57.68 m²/g, 0.30 cm³/g) are significantly larger than D-GCN (8.79 m²/g, 0.05 cm³/g) and M-GCN (2.95 m²/g, 0.02 cm³/g), which agrees with the published studies [137,138,151]. This can be attributed to the presence of heteroatoms of oxygen in the urea structure playing an important role in the increased surface area and enlarged pore volume during the process of condensation polymerization [138]. Oxygen is reported to be more efficient in increasing surface area and pore volume enlargement due to the increased formation of CO₂ and water vapor during polymerization [137,138,152]. U-GCN/silver-based composites have specific surface areas varying from 41.85 m²/g to 67.38 m²/g and pore volumes between 0.23 cm³/g and 0.39 cm³/g. All the U-GCN-based photocatalysts have a relatively large BET surface area (41.85 m²/g to 67.38 m²/g) and pore volume (0.23 cm³/g to 0.39 cm³/g) compared to M-GCN and D-GCN. This can be attributed to the heteroatoms of oxygen in the urea structure, which contributed to the large surface area and pore volume.

Table 3. 1 BET surface area, BJH pore volume, and BJH average pore size.

Photocatalyst	BET Surface Area (m ² /g)	BJH Pore Volume (cm ³ /g)	BJH Average Pore Size (nm)
M-GCN	2.95	0.02	25.92
D-GCN	8.79	0.05	20.76
U-GCN	57.68	0.30	23.78
Ag ₂ CrO ₄	1.32	0.01	97.96
U-GCN/0.1Ag ₂ CrO ₄	60.38	0.35	27.15
U-GCN/0.3Ag ₂ CrO ₄	42.68	0.23	26.78
U-GCN/0.5Ag ₂ CrO ₄	44.67	0.25	24.52
U-GCN/0.3Ag	41.85	0.21	23.87
U-GCN/0.3AgBr	48.02	0.24	23.70
U-GCN/0.3Ag ₃ PO ₄	67.38	0.39	30.29

The XRD patterns of GCN are presented in [Figure 3.1a](#). D-GCN, U-GCN, and M-GCN have dominant diffraction peaks at 27.72°, 27.9°, and 27.78°, respectively. According to Bragg's equation, the interplanar distance for D-GCN, U-GCN, and M-GCN was calculated to be 0.322 nm, 0.320 nm, and 0.321 nm, respectively. The dominant peaks at these degrees are indexed to the 002 plane. This is attributed to the strong interplanar packing of the aromatic conjugated structure of the GCN [137]. A weak peak at around 13.3° was also observed on the XRD spectrum of D-GCN, U-GCN, and M-GCN, which can be indexed to the 100 plane. This indicates the characteristics of the in-plane structural packing motif [153,154]. Both the 100 and 002 planes are associated with the hexagonal aromatic structure of GCN (JCPDS card number 87-1526) [155]. U-GCN has a broader and weaker diffraction peak than D-GCN and M-GCN, indicating its smaller crystallinity caused by the strong electronegative oxygen atom and strong C–O bond leading to low polymerization [137]. The Ag₂CrO₄, as seen in [Figures 3.1a and S3.9](#), showed several characteristic diffraction peaks, with the dominant peak at 31.68°, indexed at the 220 plane (JCPDS card number 26-0952) [156]. The shape of the peaks indicates that the prepared Ag₂CrO₄ was well crystallized and has the characteristic orthorhombic structure. [Figures 3.1a and S3.3](#) show the peaks of the as-synthesized U-GCN/silver-based nanocomposites. The main peak of Ag₂CrO₄ was not observed in the U-GCN/0.1Ag₂CrO₄ nanocomposite due to the low ratio of Ag₂CrO₄ in the nanocomposite. However, with an increasing ratio of Ag₂CrO₄, its main peak and other weak peaks were observed in U-GCN/0.3Ag₂CrO₄ and

U-GCN/0.5Ag₂CrO₄ composites with increasing intensity. This indicates the presence of the GCN hexagonal and the Ag₂CrO₄ orthorhombic structures. Moreover, the increasing intensity of Ag₂CrO₄ was accompanied by a corresponding decrease in the intensity of GCN as the ratio of Ag₂CrO₄ increased in the nanocomposites. The AgBr dominant peak at 31.10° was indexed to the 200 diffraction plane (JCPDS card number 79-0148) and the decreased GCN peak was observed in the U-GCN/0.3AgBr nanocomposite, indicating that the U-GCN acted as a support to the binding AgBr particles, while the Ag₃PO₄ peak was not observed in the U-GCN/0.3Ag₃PO₄ structure. The non-observable peak of Ag₃PO₄ could be due to the low ratio of Ag₃PO₄ in the nanocomposite. Though the dominant peak of Ag nanoparticles was not observed in the U-GCN/0.3Ag structure, other weak peaks were observed. This could be attributed to the low ratio of Ag particles in the nanocomposite.

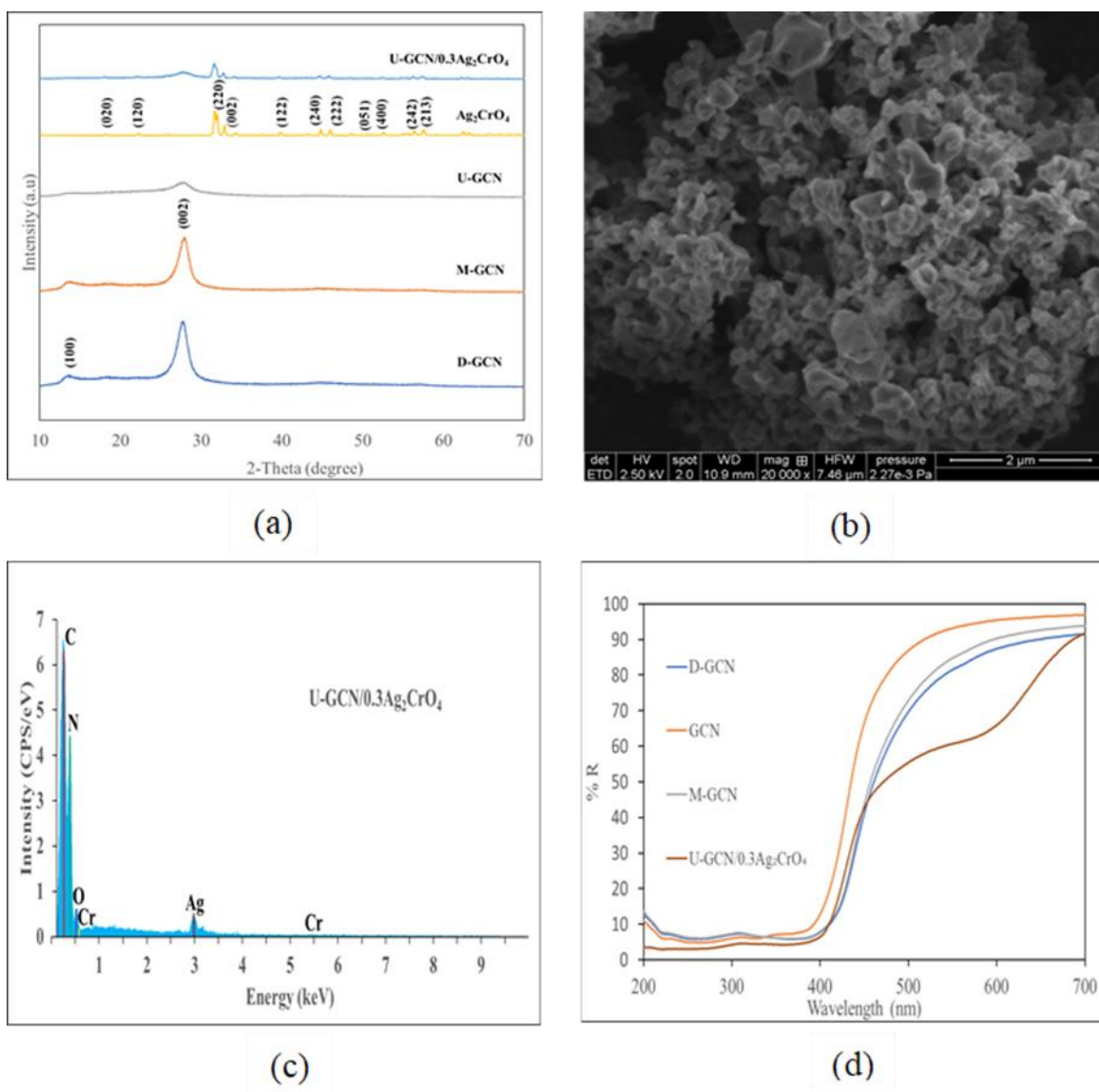


Figure 3. 1 Characterization of GCN and GCN-based nanocomposites: (a) XRD, (b) SEM for U-GCN/0.3Ag₂CrO₄, (c) EDS, and (d) DRS.

The SEM images of U-GCN/0.3Ag₂CrO₄ and other as-synthesized photocatalysts are shown in [Figures 3.1b, S3.4, and S3.10](#). In Figure S4a,c, the D-GCN, and the M-GCN show the characteristic stacked sheet-like morphologies [137,154,157], while in Figure S4b, the U-GCN shows the typical aggregated flake-like morphology [94]. In [Figure S3.4d](#), the Ag₂CrO₄ displays a spherical-like morphology which is typical of

Ag_2CrO_4 [158–160]. In Figures 3.1b, S3.4e–i, and S3.10, the U-GCN-based composites show a similar structure to U-GCN, though with more aggregated flake-like morphologies, indicating the presence of Ag_2CrO_4 , Ag, AgBr, and Ag_3PO_4 . The aggregated morphology exhibited by U-GCN and U-GCN-based composites is typical of GCN synthesized by the direct pyrolysis of urea [161]. The EDS in Figure S3.5 confirmed the formation of graphitic carbon nitride (GCN) with the presence of carbon and nitrogen peaks. For the nanocomposites, as seen in Figures 3.1c and S3.5, the presence of the silver compounds comprising the elements Ag, Cr, P, Br, and O was observed in the composite structures. The intensity of the energy peak for Ag increased with the increasing ratio of Ag_2CrO_4 in the U-GCN/silver chromate composite and was more pronounced with 0.5 wt% Ag_2CrO_4 .

The UV-Vis diffuse reflectance spectroscopy (UV-Vis DRS) of the synthesized graphitic carbon nitrides (GCNs) and U-GCN/ $0.3\text{Ag}_2\text{CrO}_4$ are shown in Figure 3.1d, and other nanocomposites are shown in Figure S3.6. The pristine GCNs show that the absorption edges shift to longer wavelengths from U-GCN to M-GCN and then to D-GCN. This indicates increasing light absorption in the visible light region and suggests that the GCNs can absorb photons with wavelengths lower than their absorption edges [138,146]. The difference in band gaps for D-GCN, U-GCN, and M-GCN is caused by the different degrees of condensation during GCN synthesis using different precursors [138]. The observed decrease in the reflectance (% R) of the composites means an increased absorbance of light, indicating the synergistic effect of coupling silver-based compounds (AgBr, Ag, Ag_3PO_4 , and Ag_2CrO_4) on the property of the light absorption characteristics of graphitic carbon nitride (GCN). This can be attributed to the silver compounds functioning as electron traps in the GCN bandgap [162]. The band gaps of those photocatalysts were estimated using a Tauc plot (Figure S3.7) derived from UV-Vis DRS and summarized in Table 3.2. Two band gaps appeared for U-GCN/ $0.3\text{Ag}_2\text{CrO}_4$ and U-GCN/ $0.5\text{Ag}_2\text{CrO}_4$. The first bandgaps (near 2.74 eV and 2.73 eV) are associated with GCN, while the second bandgaps (near 1.78 eV and 1.75 eV) are associated with Ag_2CrO_4 . This indicates that the nanocomposites can be activated by photons with energy larger than second bandgaps (1.78 eV and 1.75 eV). With these two band gaps, enhanced photocatalytic activity and

performance of U-GCN/0.3Ag₂CrO₄ and U-GCN/0.5Ag₂CrO₄ can be expected with the utilization of solar energy. The solar energy spectrum reaching the earth is between 100 nm and 1,000,000 nm, corresponding to the photon energy between 12.4 eV and 1.24 eV. This indicates that the as-synthesized photocatalysts with two band gaps can utilize a huge amount of energy from the sunlight up to the extreme ultraviolet region (12.4 eV) of the solar radiation spectrum.

Table 3. 2 Band gaps and the corresponding wavelengths of the synthesized photocatalysts.

Photocatalyst	Bandgap Energy (eV)	Wavelength (nm)
M-GCN	2.68	462
D-GCN	2.67	464
U-GCN	2.75	450
Ag ₂ CrO ₄	1.80	689
U-GCN/0.1Ag ₂ CrO ₄	2.75	450
U-GCN/0.3Ag ₂ CrO ₄	2.74, 1.78	452, 698
U-GCN/0.5Ag ₂ CrO ₄	2.73, 1.75	454, 708
U-GCN/0.3Ag	2.73	454
U-GCN/0.3AgBr	2.74	452
U-GCN/0.3Ag ₃ PO ₄	2.72	455

3.6.2 Photocatalytic Degradation of 4-CP Using GCNs and GCN-Based Nanocomposites

The photocatalytic degradation of 4-CP using GCNs and GCN-based nanocomposites with royal blue LED irradiation is summarized in [Figure 3.2](#). The concentration of 4-CP decreased along with irradiation time in the presence of GCNs or GCN-based nanocomposites. Royal blue LED irradiation only did not cause the direct photolysis of 4-CP, as 4-CP does not have significant light absorption in these wavelengths. The 60-minute adsorption experiments showed that 4-CP did not adsorb on the surface of GCN or GCN-based nanocomposites ([Figure S3.8](#)). Therefore, the decrease of 4-CP concentration in this study is due to the photocatalytic reaction initiated by the GCN or GCN composites activated by royal blue LED irradiation. The bandgap energy for the three pristine GCNs (U-GCN, D-GCN, and M-GCN) varied from 2.68–2.75 eV, which corresponds to 462–450 nm. The royal blue LED has its maximum emission at 450 nm, with a full width at half maximum equal to 20 nm. Most photons emitted from the investigated royal blue LED

have higher energy than the bandgap of the GCNs, which can be absorbed by the GCNs, leading to the photocatalytic degradation of 4-CP. Among the pristine GCNs, the highest 4-CP degradation rate ($0.05 \times 10^{-2} \text{ min}^{-1}$) was observed with U-GCN. U-GCN has been reported to have better performance than D-GCN and M-GCN in hydrogen production from water, nitrogen oxide (NO) removal in the gas phase, and dye removal in an aqueous medium due to its high surface area, large pore volume, and large pore size [137,138,151].

Higher 4-CP degradation rates were observed with all GCN nanocomposites, except GCN/0.3Ag. A negative impact of Ag nanoparticles inclusion in the GCN structure was observed with the k value of $0.02 \times 10^{-2} \text{ min}^{-1}$, which is 2.5 times lower than U-GCN. U-GCN/0.3Ag₂CrO₄ has the highest k value of $2.64 \times 10^{-2} \text{ min}^{-1}$, which was 52.8 times more than U-GCN. Further, U-GCN/0.3AgBr and U-GCN/0.3Ag₃PO₄ were 8.6 times and 4.2 times more than U-GCN, respectively. The enhanced photocatalytic performance of U-GCN/0.3Ag₂CrO₄, U-GCN/0.3Ag₃PO₄, and U-GCN/0.3AgBr over GCN can be attributed to the introduction of Ag₂CrO₄, Ag₃PO₄, and AgBr in the GCN structure. The bandgaps of Ag₂CrO₄ (1.78 eV), Ag₃PO₄ (2.45 eV) [163], and AgBr (2.65 eV) [164] are smaller than GCN (2.75 eV) and therefore are expected to enhance the photocatalytic activity of U-GCN. A synergistic effect was even observed for U-GCN/silver chromate nanocomposites. The degradation rates for U-GCN/silver chromate nanocomposites ($2.64 \times 10^{-2} \text{ min}^{-1}$) were larger than the sum of U-GCN alone ($0.05 \times 10^{-2} \text{ min}^{-1}$) and Ag₂CrO₄ alone ($0.14 \times 10^{-2} \text{ min}^{-1}$). This optimal performance by the U-GCN/silver chromate nanocomposite is due to the synergistic effect of coupling Ag₂CrO₄ with GCN. This resulted in reduced reflectance and, hence, increased absorption of light, reduced bandgap, and high photocatalytic activity, with the Ag₂CrO₄ serving as an electron trap by promoting charge carrier separation. Therefore, coupling GCN with silver-based photocatalysts can create a synergistic effect by inhibiting the e⁻-h⁺ pair recombination and improving the charge separation, thereby increasing the photocatalytic degradation of organic pollutants [143,146,162].

An optimal mass ratio between Ag_2CrO_4 and U-GCN was observed to be 0.3:1. The 4-CP degradation rate increased when the mass ratio was increased from 0.1:1 to 0.3:1. However, a further increase from 0.3:1 to 0.5:1 did not enhance the photocatalytic degradation of 4-CP. The excess Ag_2CrO_4 present in the nanocomposite could block the active sites on GCN, increase electron-hole (e-h) recombination, and inhibit the rate of transfer of photo-induced charges [165]. Table 3.3 shows the photocatalytic efficiency of U-GCN/0.3 Ag_2CrO_4 towards 4-CP degradation as compared with the results of other published articles. The mpg-GCN showed a very good performance at nearly 100% degradation of 4-CP compared to others on the table because of its very high surface area at $176 \text{ m}^2/\text{g}$. Up until now, the published articles on the photocatalytic degradation of organic pollutants, including 4-CP, involved the use of an Xe lamp as the light source for the solar simulator. The novelty of the royal blue LED as a light source is a potential application for indoor use in photocatalytic systems.

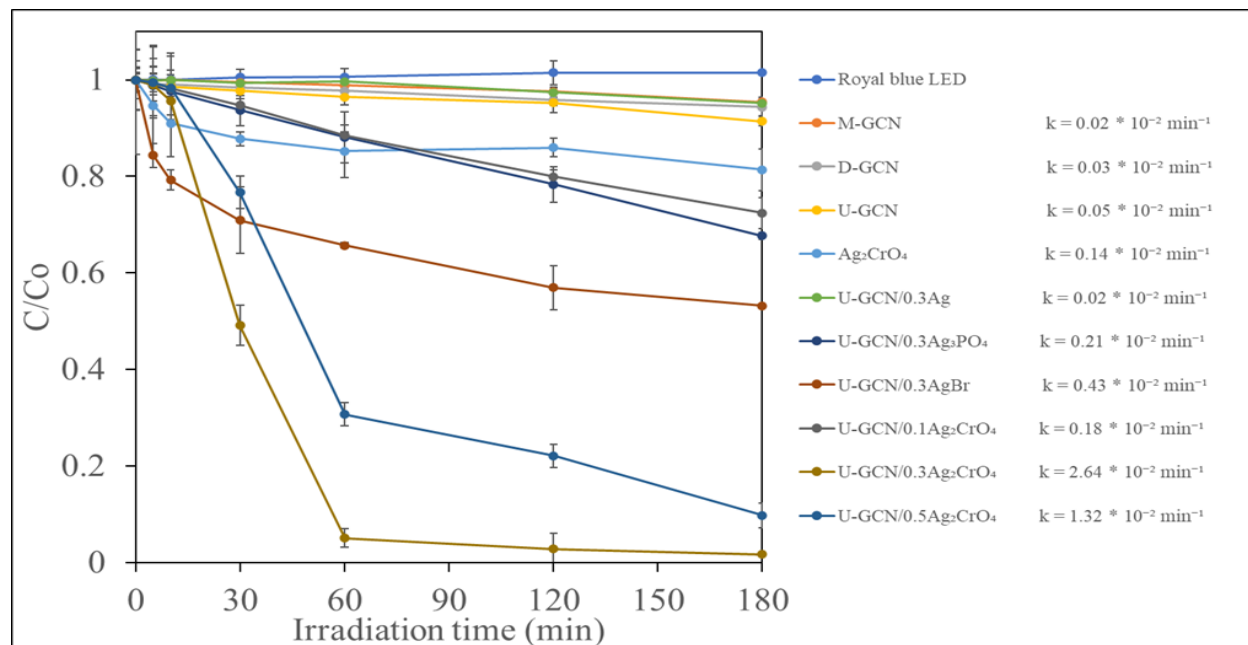


Figure 3. 2 Photocatalytic degradation of 4-CP using GCNs derived from different precursors and GCN/silver compounds-based nanocomposites under royal blue LED (450 nm) irradiation.

Table 3. 3 Comparison of 4-CP photocatalytic degradation with the results of previously published articles.

S/N	Photocatalyst	Synthesis Method	Light Source	Catalyst Amount (mg)	Conc. of 4-CP in Solution (mg/L)	Degradation Time (min)	Degradation Efficiency (%)	Rate Constant (min^{-1})	Ref
1	Mesoporous GCN (mpg-CN)	Template	300 W Xe lamp	40	15.4	60	~100	5.26×10^{-2}	[153]
2	CN/APO	Precipitation	500 W Xe lamp	50	20	180	96.5	1.80×10^{-2}	[143]
3	ZrO ₂ /g-C ₃ N ₄	Ultrasonication	300 W Xe lamp Solar simulator:	60	30	120	~90	1.73×10^{-2}	[166]
4	ZnO/g-C ₃ N ₄ /carbon xerogel	Precipitation	300 W lamp Visible light: 400 W lamp	100	10	300	92 72	1.20×10^{-2} 0.51×10^{-2}	[94]
5	Vc-GCN	Calcination	300 W Xe lamp 460 nm	50	10	120	60.8	0.79×10^{-2}	[167]
6	U-GCN/0.3Ag ₂ CrO ₄	Precipitation	Royal blue LED	40	20	180	98.26	2.64×10^{-2}	Current study

3.6.3 Photocatalytic Degradation of 4-CP by U-GCN/0.3Ag₂CrO₄ in Different Photoreactors

In addition to the royal blue LED reactor, the performance of the U-GCN/0.3Ag₂CrO₄ nanocomposite in the photocatalytic degradation of 4-CP was evaluated with three other photoreactors, including a UV-A LED (365 nm), a cool white lamp (400–700 nm), and a solar simulator (350–1800 nm, HAL-320W). The normalized concentration vs. irradiation time is presented in [Figure 3.3](#). The light intensities measured through ferrioxalate actinometry experiments for the solar simulator, cool white lamp, UV-A LED, and royal blue LED were 0.99×10^{17} photons/s, 0.61×10^{17} photons/s, 0.71×10^{17} photons/s, and 5.90×10^{17} photons/s, respectively. In order to compare the energy consumption for the different photoreactors, the photon energy (E_{photon}) required to achieve one log 4-CP reduction was estimated based on Equation (3.2) and is summarized in [Table 3.4](#).

$$E_{\text{photon}} = -\frac{\ln(0.1)}{k} * I_e \quad (3.2)$$

where k is the first-order degradation rate constant and I_e is light intensity in the form of J/s, which was estimated based on light intensity (photons per second) measured through ferrioxalate actinometry and the light emission spectrum for each reactor.

The results indicate that U-GCN/0.3Ag₂CrO₄, as a visible photocatalyst, can degrade organic contaminants under various lighting conditions. All evaluated photoreactors can emit photons with an energy larger than the bandgap of U-GCN, Ag₂CrO₄, and U-GCN/0.3Ag₂CrO₄ nanocomposite, and, therefore, can activate the photocatalyst to cause a series of photocatalytic reactions. The rate constants estimated for the solar simulator, cool white lamp, UV-A LED, and royal blue LED are $0.15 \times 10^{-2} \text{ min}^{-1}$, $0.34 \times 10^{-2} \text{ min}^{-1}$, $1.06 \times 10^{-2} \text{ min}^{-1}$, and $2.64 \times 10^{-2} \text{ min}^{-1}$, respectively. The royal blue LED had the highest k value of $2.64 \times 10^{-2} \text{ min}^{-1}$, which is 2.5 times that of UV-A LED, 7.8 times that of the cool white lamp, and 17.6 times that of the solar simulator. This high k value from the royal blue LED is due to its very high light intensity.

As shown in Table 3.4, the photon energy required to degrade 90% of 4-CP was 8960 J, 1366 J, 514 J, and 1364 J for the solar simulator, cool white light, UV-A LED, and royal blue LED, respectively. The lowest photon energy consumption was observed with the UV-A LED, as most of the photons emitted from the UV-A LED reactor can contribute to the photocatalytic reaction, while only a fraction of photons emitted from the royal blue LED reactor, solar simulator, and cool white lamps possess energy larger than the bandgap of U-GCN/0.3Ag₂CrO₄. The solar simulator emitted 10.8% of photons with a wavelength of < 452 nm (equivalent to the bandgap of U-GCN), and 35.3% of photons with a wavelength of < 689 nm (equivalent to the bandgap of Ag₂CrO₄). The percentage of photons (< 452 nm) in the emission spectrum of the cool white lamp and royal blue LED was 16.5% and 52.3%, while the percentage of photons (< 689 nm) emitted by the cool white lamp and royal blue LED was estimated to be 78.4%, and 61.6%, respectively. The photon energy consumptions are similar for royal blue LED and the cool white lamps,

although the fraction of photons less than 452 nm for royal blue LED is larger. This is because the cool white lamps emitted a large number of photons between 452 nm and 698 nm, which can also activate Ag_2CrO_4 . UV-A LED is efficient in terms of photon energy consumption, but its electricity-to-photon conversion efficiency is usually lower than visible LEDs and fluorescent lamps [168,169]. Although the solar simulator is not as effective in photocatalytically degrading the contaminant, the results indicate its huge potential for applying natural sunlight, free and clean energy in abundance, in photocatalytic treatment using $\text{GCN}/\text{Ag}_2\text{CrO}_4$ as a catalyst.

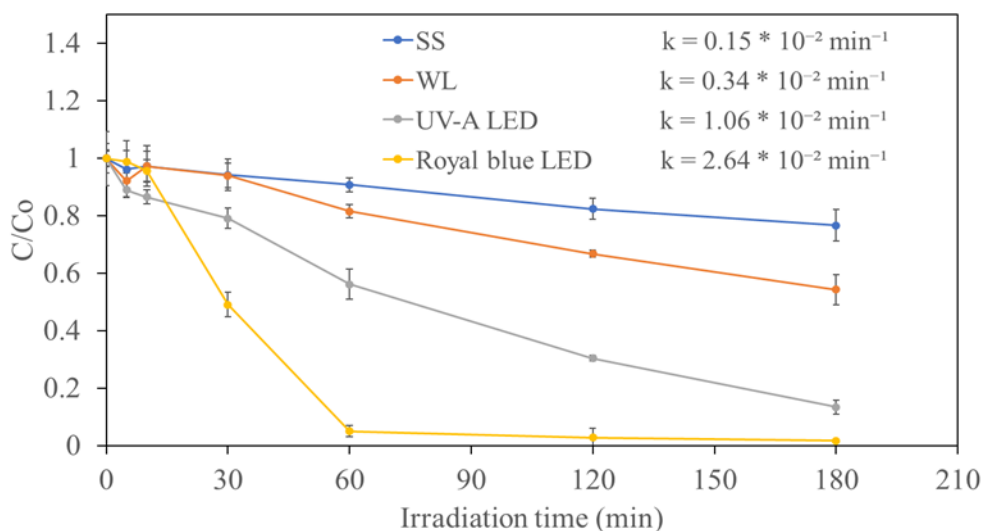


Figure 3. 3 Photocatalytic degradation of 4-CP using different photoreactors ($C_0 = 20 \text{ mg/L}$, C_U . $\text{GCN}/0.3\text{Ag}_2\text{CrO}_4 = 1000 \text{ mg/L}$).

Table 3. 4 The photo energy (E_{photon}) required to achieve a log reduction of 4-CP.

Photoreactor	E_{photon} (J)
Solar simulator	8960
Cool white light	1366
UV-A LED	514
Royal blue LED	1364

Therefore, the efficiency (or quantum efficiency) is defined as the actual amount electrons that reacted for every absorbed photons by the photocatalyst as shown in equation (3.3) [170]. The efficiency is determined based on the amount of H_2 gas released from the photoreduction of water. This is largely dependent on the type and physicochemical properties of the photocatalyst (bulk or composite photocatalyst) and characteristic of the light source (visible or UV and intensity).

$$\text{Quantum efficiency} = \left(\frac{H_2 \text{ gas production or evolution rate}}{\text{number of incident photon or photon flux}} \right) * \left(\frac{\text{number of moles of electrons}}{\text{number of moles of } H_2 \text{ gas}} \right) \quad (3.3)$$

3.6.4 Proposed Photocatalytic Mechanism

It was reported that GCN and modified GCN can produce reactive oxidative species (ROS) that can degrade organic pollutants under visible-light irradiation [143,153,154,162]. The results of the trapping experiments show that the active species, e^- , h^+ , $O_2^{\cdot-}$, and OH^{\cdot} were involved in the degradation of 4-CP and other chlorophenol compounds to the mineralized products CO_2 , H_2O , and HCl . Several by-products have been identified to have been formed in the course of the photocatalytic degradation of 4-CP to mineralized products, including hydroquinone, benzoquinone, phenol, and 4-chlorocatechol [88,171–173]. These by-products, which are hydroxylated intermediates, are formed during the oxidation of 4-CP.

Based on this, a possible photocatalytic degradation mechanism of 4-CP by U-GCN/ Ag_2CrO_4 is presented in Figure 4. The conduction band (CB) and the valence band (VB) potentials of GCN and Ag_2CrO_4 were calculated based on Equations (3.4) and (3.5) [158,174,175]:

$$E_{CB} = X - E^e - 0.5E_g \quad (3.4)$$

$$E_{VB} = E_{CB} + E_g \quad (3.5)$$

where E_{CB} and E_{VB} are conduction and valence band potentials, E^e is free electron energy on the hydrogen scale (~ 4.50 eV), E_g is the bandgap energy (Table 3.2), and X is the absolute electronegativity of the semiconductor, which is based on the geometric mean of the constituent atoms, which for GCN and

Ag_2CrO_4 is 4.72 eV and 5.83 eV, respectively [176]. Therefore, for GCN (based on the U-GCN estimated bandgap in Table 2) the E_{CB} and E_{VB} are -1.16 eV and 1.59 eV, while for Ag_2CrO_4 , the E_{CB} and E_{VB} are 0.43 eV and 2.23 eV, with the E_g of Ag_2CrO_4 as 1.80 eV.

In Figure 3.4, there is an excitation of electrons on the U-GCN and Ag_2CrO_4 upon irradiation from a visible-light source and the electrons move from their respective VB to CB. Due to potential differences, electrons migrate from the CB of GCN, and it is accepted on the CB of Ag_2CrO_4 , where the Ag^+ is reduced to Ag^0 , while holes in the VB of GCN move to the VB of Ag_2CrO_4 [143,177,178], leading to efficient charge separation. Subsequently, the accepted electrons by Ag_2CrO_4 react with the dissolved oxygen in the aqueous medium to produce superoxide radicals, while the holes on the surface of the GCN react with water molecules to produce hydroxyl radicals. The trapping of electrons and holes by the dissolved oxygen and water molecules will serve to limit the recombination, causing the formation of reactive oxidative species (O_2^\cdot And OH^\cdot) that will lead to the complete mineralization of 4-CP, producing CO_2 , H_2O , and HCl .

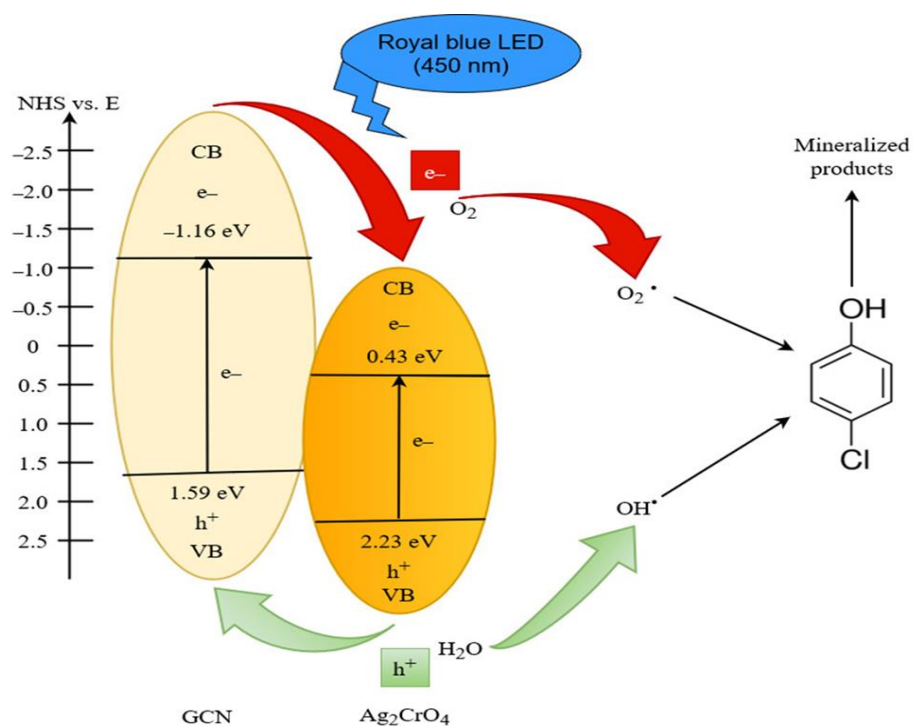


Figure 3. 4 Schematic representation of the proposed mechanism for 4-CP photocatalytic degradation using U-GCN/ Ag_2CrO_4 nanocomposite under royal blue LED irradiation.

3.7 Conclusions

In this study, GCNs derived from different precursors (dicyandiamide, melamine, and urea) were successfully synthesized through direct pyrolysis and GCN/silver-based nanocomposites were prepared through a dark-induced/in-situ deposition method. The prepared GCN and GCN/silver-based nanocomposites were characterized using UV-vis diffuse spectroscopy, XRD, SEM, and BET and evaluated for their photocatalytic degradation of 4-CP under royal blue LED irradiation. Among the different precursors, urea-derived GCN showed the best photocatalytic performance due to its large surface area and pore volume. The introduction of silver-based compounds such as AgBr, Ag₃PO₄, and Ag₂CrO₄ into urea-derived GCN enhanced its photocatalytic performance, as they increased visible light absorption, improved charge separation, enhanced charge transfer, and reduced the electron–hole pair recombination rate. The 4-CP degradation rate observed with U-GCN/Ag₂CrO₄ is 52 times higher than GCN alone and 18 times higher than Ag₂CrO₄ alone. The optimal mass ratio between U-GCN and silver chromate composites was determined to be 1:0.3. In addition to royal blue LED irradiation, U-GCN/Ag₂CrO₄ was found to be effective in degrading 4-CP under UVA-LED irradiation, cool white lamp irradiation, and solar irradiation. Though U-GCN/0.1Ag₂CrO₄ and U-GCN/0.3Ag₂CrO₄ have higher surface areas, pore volumes, and porosity, the possession of dual-band gaps and adsorption ability influenced and enhanced the photocatalytic performances of U-GCN/0.3Ag₂CrO₄ and U-GCN/0.5Ag₂CrO₄. The degradation rate of 4-CP for the optimal photocatalyst, U-GCN/0.3Ag₂CrO₄, was 15 times higher than for U-GCN/0.1Ag₂CrO₄ and 13 times higher than for U-GCN/0.3Ag₃PO₄. Therefore, for the GCN/silver -based composites, it was the band gap that determined the photocatalytic activity and not the surface area, especially for the composites with two band gaps.

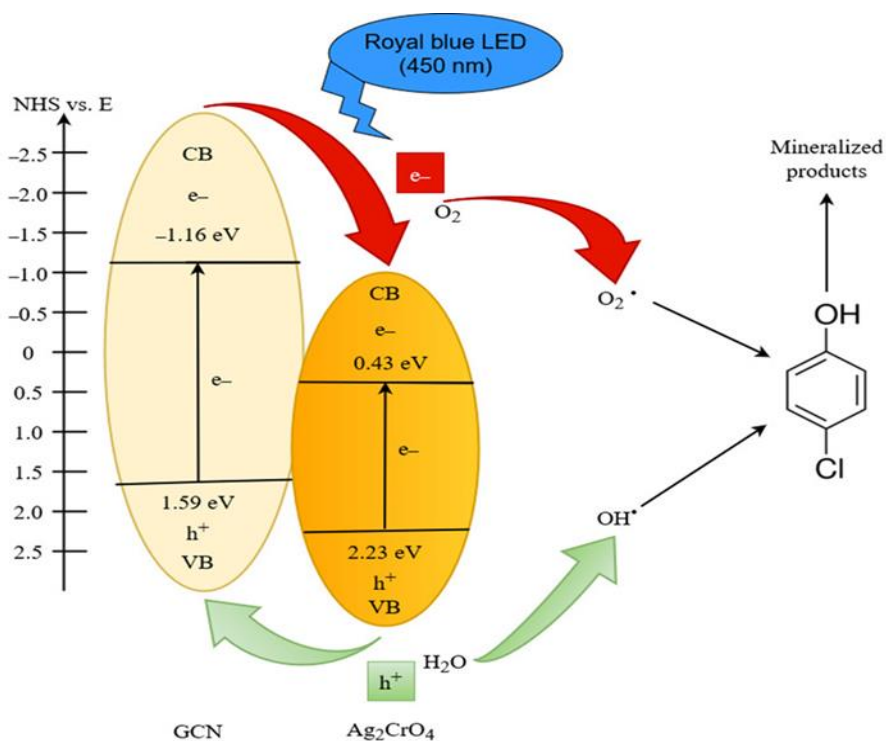
Chapter 4: Disinfection and Photocatalytic Degradation of Organic Contaminants Using Visible Light-activated GCN/Ag₂CrO₄ Nanocomposites²

4.1 Highlights

- GCN/Ag₂CrO₄ nanocomposite is highly photocatalytic and active under visible light irradiation.
- Degradation of commercial herbicide, Killex^R (2,4-D and Mecoprop-P) was achieved.
- Degradation of BSA protein and SARS-CoV-2 spike protein was achieved.
- Over one log reduction of microorganisms' cellular ATP, coliforms, and *E. coli* in wastewater was achieved in 60 minutes.

² O.O. Akintunde, L. Yu, J. Hu, M.G. Kibria, C.R.J. Hubert, S. Pogolian, G. Achari, Disinfection and Photocatalytic Degradation of Organic Contaminants Using Visible Light-Activated GCN/Ag₂CrO₄ Nanocomposites, *Catalysts*. 12 (2022) 943. <https://doi.org/10.3390/catal12090943>.

4.2 Graphical abstract



4.3 Abstract

Visible-light-driven photocatalysts have gained increasing attention in the past few decades in treating emerging contaminants in water and wastewater. In this work, the photocatalytic activity of the coupled graphitic carbon nitride (GCN) and silver chromate (Ag₂CrO₄), herein denoted as GCN/Ag₂CrO₄, nanocomposites were evaluated for degrading organic pollutants and inactivating microorganisms under visible light irradiation using a royal blue light-emitting diode (LED). The organic pollutants studied were 2,4-dichlorophenoxyacetic acid (2,4-D) and methyl chlorophenoxy propionic acid (MCP or Mecoprop-P) present in Killex^R, a commercially available herbicide, bovine serum albumin (BSA) protein, and SARS-CoV-2 spike protein. The disinfection experiments were conducted on wastewater secondary effluent. The results showed that over 85% degradation was achieved for both 2,4-D and Mecoprop-P in 120 minutes

while 100% of BSA protein and 77.5% of SARS-CoV-2 protein were degraded in 20 minutes and 30 minutes, respectively. Additionally, GCN/Ag₂CrO₄ nanocomposites led to over one log reduction of cellular ATP (cATP), total coliforms, and *E. coli* in wastewater treatment plant (WWTP) secondary effluent after 60 minutes of royal blue LED irradiation. It was observed that the degradation performance of a photocatalyst under light irradiation is contaminant-specific. The binding affinity of the released metal ions from GCN/Ag₂CrO₄ with protein and ATP functional groups was responsible for the degradation of proteins and the reduction of cATP, while the generated ROS was responsible for the disinfection of total coliforms and *E. coli*. Overall, the results indicate that GCN/Ag₂CrO₄ nanocomposite is a promising photocatalyst in degrading organic pollutants and disinfecting microorganisms under visible light irradiation within a reasonable time.

4.4 Introduction

Semiconductor photocatalysis is fast emerging as the advanced oxidation process to address environmental pollution and global warming such as organic pollutant removal, disinfection of microorganisms, hydrogen evolution, and CO₂ reduction [179–183]. In semiconductor photocatalysis, photoexcited electrons and holes are generated when the energy absorbed from light is greater than or equal to the bandgap energy of the photocatalysts. These electrons react with the dissolved oxygen in the solution while the holes react with water molecules to produce superoxide radicals (O₂^{•−}) and hydroxyl radicals (•OH), respectively. These radicals are referred to as reaction oxidative species (ROS) and they can oxidize organic pollutants, finally producing mineralized products such as CO₂ and H₂O. They can also be used for disinfection purposes. Titanium dioxide (TiO₂), a metal-based semiconductor, is the most widely studied photocatalyst, but it suffers from limited applications such as wide bandgap (3.2 eV), low visible light utilization, and high recombination rate of electron-hole pair [49–51,184]. Therefore, various semiconductor photocatalysts with narrow bandgap and visible-light activity were developed such as Bi₂WO₆ [185], CuO [186], and CdS [187]. To this end, modified and doped TiO₂ [188], photosensitizers [189], as well as the use of low-energy

systems such as light-emitting diodes [190,191] and “adsorb and shuttle” wherein adsorbent along with a photocatalyst [192] have also been investigated.

Graphitic carbon nitride (g-C₃N₄ or GCN) is a metal-free photocatalyst, with a bandgap of 2.7 eV that has gained a lot of attention in photocatalytic water splitting [52], photocatalytic degradation of organic pollutants [53], and disinfection of microorganisms [193] under visible light irradiation [194,195]. However, the major drawback of bulk GCN is its low surface area, high rate of electron-hole pair recombination, and low utilization of visible light up to only 460 nm (blue region) which limits its photocatalytic activity [55].

It is well known that silver-based photocatalysts such as silver halides [196,197], Ag₃PO₄ [198], and Ag₂CrO₄ [199] are potential catalysts because of their excellent light sensitivity and photocatalytic activity under visible light irradiation. Of note is Ag₂CrO₄ with its high visible-light absorption efficiency, and electronic and crystal structure [200]. However, Ag₂CrO₄, like other silver-based photocatalysts, has similar drawbacks which are aggregated particle size and ease of photocorrosion leading to poor stability and limited photocatalytic performance.

Coupling of GCN and the silver-based photocatalysts to form heterojunctions can address the individual shortcomings of GCN and silver-based photocatalysts by improving charge separation, reducing the rate of recombination of electron-hole pair, improving bandgap optical properties, and enhancing visible light absorption and utilization of GCN, as well as reducing the aggregation of silver-based photocatalysts. For example, GCN/Ag [55], GCN/AgBr [105], GCN/Ag₃PO₄ [143], and GCN/Ag₂CrO₄ [201] showed higher degradation of methylene blue (MB), *E. coli* disinfection, 4-chlorophenol (4-CP) degradation, and methyl orange (MO) degradation, respectively, under visible light when compared to GCN.

The purpose of this study is to investigate synthesized GCN/Ag₂CrO₄ to photocatalytically degrade organic pollutants as well as disinfect microorganisms. Kilex^R (2,4-D and Mecoprop-P), BSA, and SARS-CoV-2 spike protein were selected to study while WWTP secondary effluent was used to assess photocatalytic disinfection. The addition of Ag₂CrO₄ to GCN to form the GCN/Ag₂CrO₄ heterojunction enhances visible

light activity. Ag_2CrO_4 being a strong oxidizing agent serves as an electron trap by accepting photogenerated electrons from GCN thereby reducing electron-hole pair recombination rate and improving charge separation. The narrow band gap of Ag_2CrO_4 (1.80 eV) indicates strong absorption in the visible-light region which could enhance its photocatalytic activity. Both 2,4-D and certain microbial constituents in wastewater such as *E. coli* have known negative health and environmental impacts [91,202]. Moreover, 2,4-D and Mecoprop-P are common constituents of herbicides that can be found on the surface and in groundwater because of their use in lawns and agricultural lands [203]. A study in Alberta, Canada showed that 2,4-D is one of the most common pollutants in water and precipitate samples [204]. Mecoprop-P has been detected as a minor pollutant in U.S. and European soils, as well as in ground and surface waters, and it is the most often found herbicide in drinking waters [205,206]. Bovine serum albumin protein (BSA) is a commonly used standard for protein analysis selected for studying the interaction between proteins and other chemicals. SARS-CoV-2, the Coronavirus that causes COVID-19, has resulted in a worldwide pandemic with over 280 million infections and caused over 5 million deaths globally [207]. This viral disease continues to ravage the world with severe or mild variants. COVID-19 burden in communities has been monitored by testing wastewater to provide an early warning of a community spread [208]. Sources of coliforms can be humans, livestock, wildlife, and even pets. *E. coli* is considered a potential pathogen and its presence in the water body can indicate the presence of other waterborne pathogens such as bacteria, viruses, and parasites [209].

Photocatalytic degradation of 2,4-D and Killex using TiO_2 has been widely reported [148,210,211]. However, only a few studies focused on the photocatalytic degradation of 2,4-D using GCN. The degradation of 2,4-D using GCN-based composite under natural sunlight showed over 90% removal after 330 minutes [95]. About 100% degradation of a very small concentration (50 $\mu\text{g/L}$) of Mecoprop-P was achieved in 7 minutes using a GCN-based catalyst under simulated solar irradiation [96]. Heydari et al. degraded Killex^R (2,4-D and Mecoprop-P) using TiO_2 under natural sunlight exposure with 97% degradation of 2,4-D after 15 days and 100% degradation of Mecoprop-P after 22 days [92]. The

enhancement of the photocatalytic activity of GCN in degrading methylene blue (MB) was achieved with its combination with Co-NiS and sulfur to form 1D/2D Co-NiS/S-g-C₃N₄ heterojunction with 98% degradation in 32 minutes [212]. ZnFe₂O₄/S-g-C₃N₄ heterojunction was synthesized with varying wt% of S-g-C₃N₄. The ZnFe₂O₄/S-g-C₃N₄ (50%) showed maximum MB degradation under solar irradiation in 150 minutes [213]. The interaction between BSA and nanoparticles and the structural change to BSA have been investigated with nanoparticles such as MnO₂ [214], CuS [215], and silver nanoparticles (AgNP) [216,217] at different concentrations and compositions. The results show increasing interactions and structural changes to BSA with increasing concentration of the nanoparticles. The disinfection of *E. coli* using GCN-based composite under a xenon lamp as a solar simulator showed complete inactivation (6.5 log) after 60 minutes [105]. In the published literature, the focus was on either natural sunlight or solar simulator as broadband light sources for photocatalytic degradation and disinfection. To the best of our knowledge, the combination of a narrowband low-energy visible light source (in this case royal blue LED with a peak wavelength of 460 nm) and GCN-based nanocomposites has not been reported on degrading herbicides and protein and disinfecting WWTP secondary effluent. The benefits of narrowband light are its consistency, directionality (narrow and focused beam), and narrow frequency range [218]. The photons in narrowband light move at the same wavelength (consistency) and in the same direction (directionality) resulting in high light intensity.

This work aims to address the knowledge gaps in evaluating the photocatalytic performance of GCN/Ag₂CrO₄ nanocomposite under a narrowband low-energy visible light source (royal blue LED) in degrading different organic pollutants such as Killex^R (2,4-D and MCP), BSA protein, SARS-CoV-2 spike protein, and disinfecting WWTP secondary effluent. The reaction kinetics of 2,4-D, Mecoprop-P, and BSA protein were also investigated. The interaction between BSA and the photocatalysts, and the structural changes to BSA were studied using a UV-Vis spectrophotometer; log reduction of cellular ATP (cATP), total coliforms, and *E. coli* in WWTP secondary effluent was used to determine the efficiency of the catalyst in wastewater disinfection.

4.5 Materials and Methods

4.5.1 Chemicals

Killex^R, a known herbicide was purchased from a local store in Calgary, Alberta. Urea-CH₄N₂O (≥99.5%), silver nitrate-AgNO₃ (≥99%), potassium chromate-K₂CrO₄ (≥99%), 1-10 phenanthroline-C₁₂H₈N₂, iron III chloride-FeCl₃, ammonium iron II sulfate hexahydrate (Mohr's salt, ≥98%)—(NH₄)₂Fe(O₄)₂(H₂O)₆ and Bovine Serum Albumin (BSA) protein (hydrolyzed powder, crystallized ≥98.0%) were purchased from Sigma-Aldrich Co. (St. Louis, MO, USA). Luria broth, potassium trioxalatoferrate III trihydrate-K₃Fe(C₂O₄)₃·3H₂O (98%) was purchased from Alfa Aesar (St. Louis, MO, USA). Sodium acetate-C₂H₃NaO₂ (>99%) was purchased from Brady (Markham, ON, Canada). BSA Bradford assay protein test kit was purchased from BIORAD (Hercules, CA, USA). SARS-CoV-2 spike protein (SP), S-ECD (>95%) was purchased from Thermofisher Scientific (Ottawa, ON, Canada). ATP test kit was purchased from LuminUltra Technologies Ltd. (Fredericton, NB, Canada) while total coliforms/*E. coli* Colilert test kit was purchased from IDEXX laboratories Inc. (Westbrook, ME, USA). Secondary treated wastewater effluent was provided by Advancing Canadian Water Assets – ACWA (Calgary, AB, Canada), a full-scale testing facility embedded in a wastewater treatment plant in Calgary, Alberta.

4.5.2 Preparation of GCN, Ag₂CrO₄, and GCN/Ag₂CrO₄ nanocomposite

The GCN, Ag₂CrO₄, and GCN/Ag₂CrO₄ were synthesized based on a procedure described in detail elsewhere [194]. The GCN was synthesized using the direct pyrolysis method by heating urea at 550°C for 4h in a muffle furnace. The GCN/Ag₂CrO₄ composite was synthesized using the dark-induced/In-situ-deposition method by first sonicating one gram of GCN slurry. A known quantity of AgNO₃ and 4.83 g/L K₂CrO₄ were added to the GCN slurry under magnetic stirring. The mixture was then magnetically stirred in the dark for 7 h and after that, it was filtered using a 0.45 μm filter and washed about five times with water and alcohol. The residue was left to dry at room temperature and thereafter labeled as GCN/Ag₂CrO₄. The characterizations of these catalysts have been reported elsewhere [194].

4.5.3 Experimental set-up

4.5.3.1 Photocatalytic degradation of a commercial herbicide

Killex^R is a commercially-available herbicide that contains 95 g/L of 2,4-dichlorophenoxyacetic acid (2,4-D), 52.52 g/L of methyl phenoxy propionic acid (Mecoprop-P or MCP), and 9 g/L of Dicamba. A quantity of 0.8 mL of Killex^R was dissolved in 79.2 mL of distilled water (DI) which gave an 80 mL solution, resulting in the solution containing 12.1 mg/L of 2,4-D, 6.7 mg/L of Mecoprop-P, and 1.2 mg/L of Dicamba. In this experiment, 80 mg of the photocatalyst was dispersed in an 80 mL solution containing Killex^R in a 100 mL quartz beaker. The intensity of the royal blue LED (peak wavelength = 460 nm) entering the 80 mL solution was estimated to be 11.80×10^{17} photons/s using chemical ferrioxalate actinometry [148,149,219]. The same photoreactor was used for all experiments mentioned in this study. Before LED irradiation, the water/catalyst mixture was stirred magnetically in the dark for 30 minutes to attain adsorption-desorption equilibrium. Quantities of 5 mL of the samples were collected at different irradiation intervals and filtered using a 0.45 μ m syringe filter (PTFE, Chromatographic Specialties Inc., Brockville, ON, Canada) to remove the photocatalysts. Dark experiments with catalysts and light experiments without catalysts were also conducted as controls. HPLC was used to evaluate the concentration change of 2,4-D and Mecoprop-P.

4.5.3.2 Photocatalytic degradation of BSA protein and SARS-CoV-2 spike protein

In each experiment, 80 mg of the photocatalyst was dispersed in 80 mL of 100 mg/L BSA solution. During royal blue LED irradiation, 6 mL of sample was collected at different irradiation intervals and filtered using a 0.45 μ m syringe filter to remove the photocatalysts. The performance of GCN/Ag₂CrO₄ was also investigated on SARS-CoV-2 spike protein (SP) under royal blue LED. In the experiment, 40 mg of the GCN/Ag₂CrO₄ was dispersed in 40 mL of 10 mg/L SARS-CoV-2 SP, and 3 mL of the sample was collected at a different irradiation interval and filtered using a 0.45 μ m syringe filter to remove the photocatalysts. Bradford assay procedure was used to determine the concentration change for the BSA protein and SARS-

CoV-2 SP [220]. UV-Vis analysis was conducted for visible light and dark experiments to study the binding interaction between BSA and GCN/Ag₂CrO₄.

4.5.3.3 Photocatalytic disinfection of wastewater secondary effluent

Two sets of disinfection experiments were conducted. The first one was focused on the change of cATP level in the collected wastewater during the disinfection experiment, while the second one was aimed at quantifying the log reduction of total coliforms and *E. coli* by the catalyst under royal blue LED irradiation. For the cATP experiment, 80 mg of the photocatalyst was dispersed in 80 mL of wastewater secondary effluent and then irradiated with royal blue LED under continuous magnetic stirring. A total of 2.5 mL of the sample was taken at a different time interval and its cATP level was quantified using the LuminUltra test procedure for assay analysis [221]. Control experiments were carried out in the dark with the photocatalyst and under the light without the photocatalyst. Before the start of the disinfection experiment, the initial concentrations of total coliforms and *E. coli* were calculated using the tray count method [222]. A stock solution of 1L secondary treated wastewater effluent containing 50 mg of Luria broth nutrient was first prepared in a 1L jar and then incubated at 35°C ± 0.5°C for 24h. Then 1 mL of the 80 mL collected from the stock solution was serially diluted 40 times as follows: in the first mixture, 1 mL was added to 3 mL of deionized (DI) water. After mixing, 1 mL from the first mixture was added to 9 mL of DI water to give 40 times serial dilution, this gives the second mixture. Finally, using the tray count method, 1 mL of the second mixture was added to the mixture of 100 mL DI water and colilert reagent, giving the final dilution factor of 4000. The final mixed sample was poured in a quantitray, sealed with an IDEXX sealer, and incubated at 35°C ± 0.5°C for 24h. The tray, which has 49 large wells and 48 small wells, was used to estimate the most probable number (MPN) of coliforms and *E. coli* in a 100 mL wastewater sample. The actual MPN/100mL of total coliforms or *E. coli* present in the sample was calculated by multiplying the MPN by the dilution factor of 4000. The average initial concentrations of total coliforms and *E. coli* were calculated to be 5.2×10^6 MPN/100mL and 0.25×10^6 MPN/100mL respectively. Disinfection experiments were conducted and MPNs of total coliforms and *E. coli* were estimated and concentrations at different

time intervals were analyzed and calculated using the tray count method. Control experiments were also performed in the dark with photocatalysts and under the light without photocatalysts.

4.6 Chemical analysis

4.6.1 Herbicide analysis

The concentrations of 2,4-D and Mecoprop-P were determined using high-performance liquid chromatography (HPLC; LC-2040C 3D Shimadzu Corporation, Kyoto, Japan) with UV absorbance detection at $\lambda = 280$ nm. A kinetex 2.6 μm PFP column by Phenomenex (Torrance, CA, USA) was used to separate the target compounds and other interferences. The mobile phases were 0.1% phosphoric acid in HPLC-grade water and 0.1% phosphoric acid in acetonitrile at a 50:50 mixture with a flow rate of 1 mL/min. The measurements were conducted in duplicate, and the detection limit was around 0.1 mg/L.

4.6.2 Protein analysis

The concentration of BSA protein was determined using the Bradford protein assay procedure [220]. This procedure is based on the binding of Coomassie brilliant blue dye to protein. Briefly, the diluted dye was prepared by mixing concentrated Coomassie dye (80 mL) and deionized water (DI) of 240 mL and then filtered with 5 μm using vacuum filtration to remove dye particles. From the BSA stock solution (2000 mg/L), five standard dilute solutions were prepared (100 mg/L, 50 mg/L, 25 mg/L, 12.5 mg/L, and 6.25 mg/L). Then, 0.8 mL of each standard and photocatalytic degraded BSA sample was collected into the vial using a pipette, and 3.2 mL of diluted dye was added. The mixture was put on a rotary shaker and left to incubate for at least 5 minutes but not more than 60 minutes at room temperature. This incubation period allows for the colour change of the Coomassie dye from red to blue. This blue colour is an indication of the binding of the dye to the protein, which is detected at 595 nm. The spectrophotometer (UV-2600 Shimadzu Corp., Japan) was set at 595 nm to take the absorbance readings of BSA standards and the degraded samples using a disposable cuvette. The concentration of the degraded samples was calculated based on the known concentrations of the BSA standard.

This Bradford protein assay procedure was also used to determine the concentration of the SARS-CoV-2 SP. Five standard solutions of BSA of known concentrations (10 mg/L, 5 mg/L, 2.5 mg/L, and 0.625 mg/L) were prepared. Using the microassay plate, 800 µL of each standard and degraded SARS-CoV-2 SP sample was put in a vial and 200 µL of dye concentrate was added to have the protein-dye mixture. The same incubation period as described earlier was used for the spike protein and after that, the absorbance of the SP-dye complex was read at 595 nm using a spectrophotometer (UV-2600 Shimadzu Corp., Kyoto, Japan).

The UV-vis as an analytical technique was used to study the BSA and photocatalyst interaction and the structural changes to BSA. The UV-vis absorption spectra measurements were carried out for the dark as well as royal blue irradiation samples.

4.6.3 ATP analysis

The concentration of the microorganisms' cATP was determined using the LuminUltra test kit and assay procedure [221]. A total of 5 ml of the water sample was passed through a 0.45 µm syringe filter. The syringe filter containing microorganisms was re-attached to a clean syringe with the plunger removed, and then 1 mL of UltraLyse 7 was pipette into the syringe. The filtration was done slowly, and the sample was collected in a 9 mL UltraLute (dilution) tube. The purpose of the filtration using UltraLyse 7 is to be able to dissolve and remove the bound ATP (ATP in living microorganisms after disinfection) for analysis. A quantity of 100 µL of UltraLute (dilution) solution was pipette into a clean test tube and then 100 µL Luminase was added. The mixture was shaken about five times, and then the reading was taken within 10 seconds using a luminometer. The cellular ATP is calculated using equation (4.1) and the log reduction of the normalized concentration is evaluated using equation (4.2):

$$cATP \left(pg \frac{ATP}{mL} \right) = \frac{RLU_{cATP}}{RLU_{ATP1}} \times 10,000 \frac{pg \text{ ATP}}{V_{sample}(mL)} \quad (4.1)$$

$$Log \text{ reduction} = -\log \left(\frac{cATP_t}{cATP_o} \right) \quad (4.2)$$

where RLU is the unit of measurement as it is the relative light unit, pg is picogram, V_{sample} is the volume of the sample collected during the photocatalytic experiment, ATP is the calibrated ATP RLU value for the wastewater before the photocatalytic experiment, and $cATP_o$ and $cATP_t$ are the cellular ATP of the microorganisms at a time, $t = 0$ and $t = t$ min. Control experiments were conducted in the dark to determine the adsorption performance of the photocatalysts in disinfecting microorganisms and the corresponding estimation of ATP levels.

4.6.4 Total coliform/*E. coli* analysis

One mL sample was collected at different irradiation intervals and serially diluted using deionized water. This was aimed to (1) reduce the amount of catalysts and other water matrices present in the final tray so as to minimize their interferences on total coliform and *E. coli* measurement; (2) to ensure the concentration of total coliform and *E. coli* fall within the measurement range of the Colilert tray count procedure. The total coliforms and *E. coli* concentrations were determined using the tray count method [222] as described in section 4.5.3.3. The total coliform and *E. coli* disinfection efficiency were expressed in log form as shown in equation (4.3):

$$\text{Log reduction} = \log C_o - \log C_t \quad (4.3)$$

where C_o and C_t are the concentrations of total coliforms or *E. coli* before and after time t min, expressed as MPN/100 mL.

4.7 Results and discussions

4.7.1 Photocatalytic degradation of Killex^R

The dark adsorption of 2,4-D and Mecoprop-P on the synthesized photocatalyst are presented in [Figure 4.1](#). It is obvious that GCN alone did not adsorb and thus there was no decrease in the concentration of 2,4-D or Mecoprop-P during the dark experiment. Equilibrium was reached within 30 minutes for Ag₂CrO₄ and GCN/Ag₂CrO₄. A total of 8.06% of 2,4-D was adsorbed on Ag₂CrO₄ while 9.32% of Mecoprop-P was adsorbed on Ag₂CrO₄. A total of 6.24% of 2,4-D was adsorbed on GCN/Ag₂CrO₄ while 15.32% of Mecoprop-P was adsorbed on GCN/Ag₂CrO₄. The photocatalytic degradation of GCN/Ag₂CrO₄ on the 2,4-D and Mecoprop-P in Killex^R was investigated and the results are presented in [Figure 4.2](#). In the control experiment, 2,4-D and Mecoprop-P did not decrease with irradiation by a royal blue LED, indicating that the royal blue light (peak wavelength = 460 nm) did not degrade 2,4-D or Mecoprop-P. Using GCN, 16.85% of 2,4-D and 10.06% of Mecoprop-P degraded after 120 minutes. Ag₂CrO₄ remains largely unchanged under royal blue LED irradiation when compared to the dark experiment results. It was 7.05% for 2,4-D and 9.19% for Mecoprop-P. This is because silver-based photocatalysts are prone to photolysis and cannot stand the long-run duration of photocatalytic degradation [143], and the low surface area of Ag₂CrO₄ (1.32 m²/g) [194] available for the adsorption of 2,4-D and Mecoprop-P and the eventual photocatalytic activity. Silver-based particles have been reported to aggregate [223] while GCN in the GCN/Ag₂CrO₄ nanocomposite serves to prevent the aggregation of Ag₂CrO₄. GCN/Ag₂CrO₄ showed the highest percent degradation for both 2,4-D and Mecoprop-P at 86.32% and 86.39% in 120 minutes.

The first-order rate was calculated to evaluate the performance of the different photocatalysts. The rate constant (k) values are summarized in [Table 4.1](#). For 2,4-D, the k values of GCN and GCN/Ag₂CrO₄ were $0.16 \times 10^{-2} \text{ min}^{-1}$ and $1.59 \times 10^{-2} \text{ min}^{-1}$ respectively. The highest k value for degradation using GCN/Ag₂CrO₄ was 9.9 times that with GCN alone. For Mecoprop-P, the k values of GCN and GCN/Ag₂CrO₄ were $0.11 \times 10^{-2} \text{ min}^{-1}$ and $1.79 \times 10^{-2} \text{ min}^{-1}$ respectively. The highest k value for the

photocatalyst GCN/Ag₂CrO₄ was $1.79 \times 10^{-2} \text{ min}^{-1}$ which was 16.3 times that of GCN. This result shows that the deposition of Ag₂CrO₄ on GCN enhanced its photocatalytic activity by serving as an electron trap for photogenerated electrons in GCN.

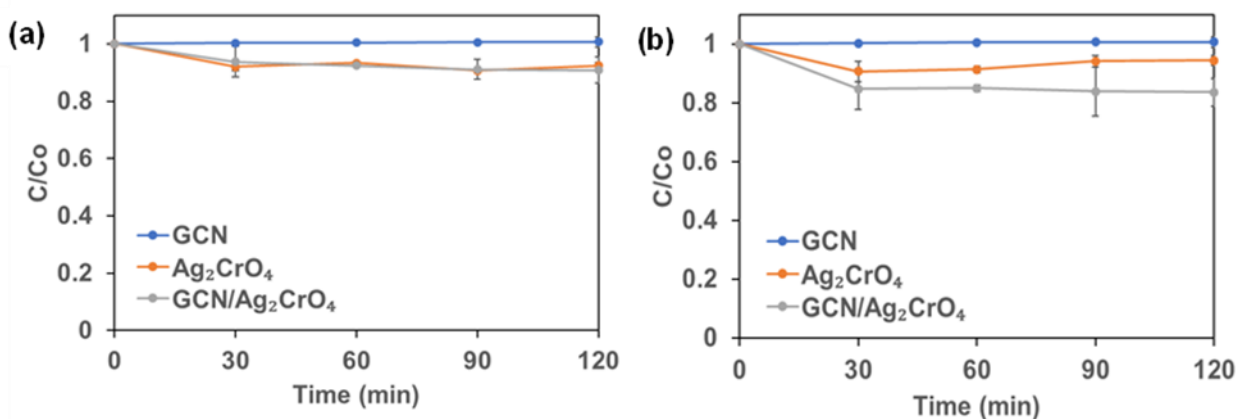


Figure 4. 1 The dark experiment of Killex^R: (a) 2,4-D and (b) Mecoprop-P.

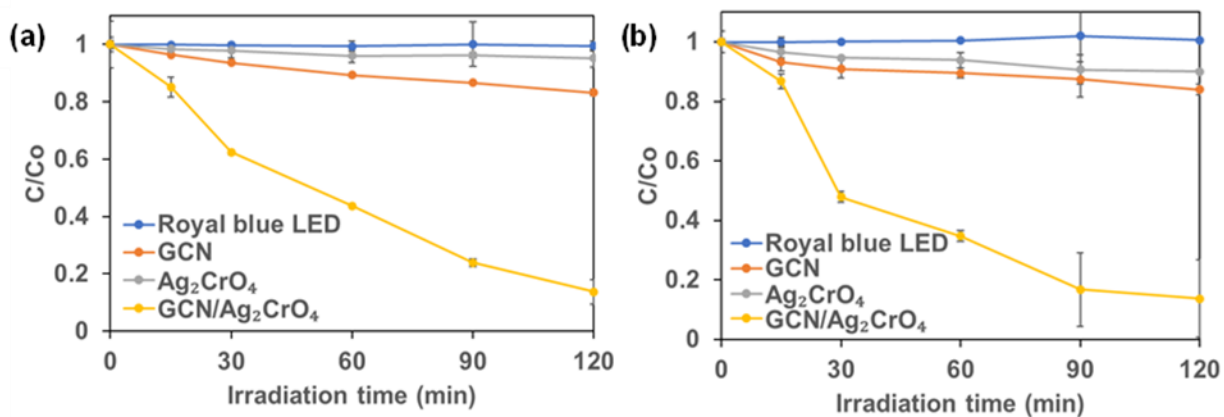


Figure 4. 2 Photocatalytic degradation (royal blue LED irradiation) of Killex^R: (a) 2,4-D and (b) Mecoprop-P.

Table 4. 1 Summary of first-order photocatalytic degradation rate constants.

Experimental Condition		GCN	Ag₂CrO₄	GCN/Ag₂CrO₄
2,4-D	Rate constant, $k (\times 10^{-2}) \text{ min}^{-1}$	0.16	1.20	1.59
	R^2	0.9891	0.6227	0.9959
Mecoprop-P	Rate constant, $k (\times 10^{-2}) \text{ min}^{-1}$	0.11	1.26	1.79
	R^2	0.8167	0.6377	0.9874

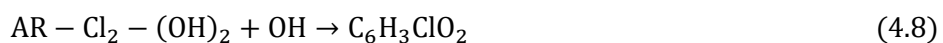
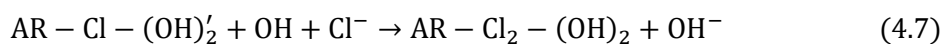
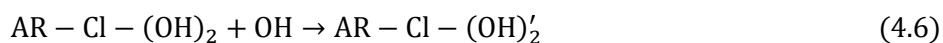
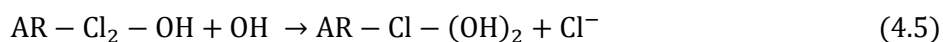
In our previous publication, we reported that the photocatalytic degradation of 4-CP by Ag₂CrO₄ was better than GCN [194], while in this study (Figure 4.2a and Figure 4.2b) we found a better performance was observed for GCN than Ag₂CrO₄ in the photocatalytic degradation of 2,4-D and Mecoprop-P. This indicates that the photocatalytic degradation performance of Ag₂CrO₄ is contaminant-specific. This can be attributed to the bond energies existing in the contaminants such as C-C, C=C, O-H, C=O, and C-Cl. Bond energy or bond dissociation energy is the measure of bond strength, and it is an indication of the easiness to break a chemical bond. The bond energies of bonds existing in 4-CP, 2,4-D, and Mecoprop-P are shown in Table 4.2.

There are fewer bonds in 4-CP than in 2,4-D and Mecoprop-P that need to be broken by ROS generated from Ag₂CrO₄. In 4-CP, apart from the aromatic ring, there are C-Cl, C-O, and O-H corresponding to 327 KJ/mol, 358 KJ/mol, and 459 KJ/mol, while 2,4-D and Mecoprop-P have all the bonds listed in Table 4.2 in addition to the aromatic ring. This means with 2,4-D and Mecoprop-P having more bonds and higher bond energies, they will be more difficult to break by the ROS generated from Ag₂CrO₄ and hence the observed low photocatalytic performance compared to 4-CP. The low surface area of Ag₂CrO₄, in addition to the bond energies of the contaminants, also would have contributed to the low performance. With a specific surface area of 1.32 m²/g [194], it means that less absorption of 2,4-D and Mecoprop-P would take place for sufficient photocatalytic activity compared to single contaminant absorption of 4-CP. Therefore, the combination of the low surface area of Ag₂CrO₄ for the absorption of the two contaminants and the several bonds and higher bond energies of 2,4-D and Mecoprop-P contributed to the observed low performance of Ag₂CrO₄.

Table 4. 2 Bond energies at 273K adapted from Ref. [224].

Bond	Bond energy (KJ/mol)
C-Cl	327
C-C	346
C-O	358
C-H	411
O-H	459
C=C	602
C=O	749

In the photocatalytic degradation of pollutants, the molecular structures could determine their susceptibility to ROS attack [96]. The compounds 2,4-D and Mecoprop-P are both chlorophenoxy herbicides (phenoxycarboxylic acid herbicides). These similar structures could explain their similar degradation rates under visible light. In the photocatalytic degradation of 2,4-D, the aromatic ring of 2,4-D is first hydroxylated to the main by-product, 2,4 dichlorophenol (2,4-DCP), followed by other by-products such as chlorohydroquinone, 4-chloropyrocatechol, 2,4-dichloropyrocatechol, and chlorobenzoquinone [225,226] as shown in equations (4.4) to (4.8), where AR is the aromatic ring.



In addition, in the photocatalytic degradation of Mecoprop-P, the aromatic ring is hydroxylated to the main by-product, 4-chloro-o-cresol, followed by other by-products such as 2-methyl hydroquinone, and 2-methyl-p-benzoquinone [206] as proposed in equations (4.9) to (4.11). The main reactive species involved in photocatalytic degradation is the $\cdot\text{OH}$ radical as reported for 2,4-D [95,227–229] and Mecoprop-P

[96,230]. Table 4.3 shows the photocatalytic degradation of 2,4-D and Mecoprop-P by different photocatalysts.

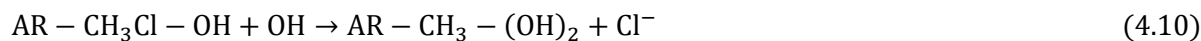
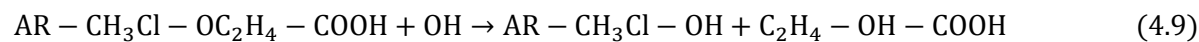


Table 4. 3 Comparison of 2,4-D and Mecoprop-P degradation with the results of previously published articles.

S/N	Photocatalyst	Visible Light Source	Organic Pollutant	Concentration (mg/L)	Degradation Time (min)	Degradation Efficiency (%)	Ref.
1	TiO ₂	Natural sunlight	2,4-D and Mecoprop-P	49.4 and 27.3	21,600 (15 days) and 31,680 (22 days)	97 and 100	[92]
2	MoO ₃ /g-C ₃ N ₄	Natural sunlight	2,4-D	50	300	99	[95]
3	GCN	Xenon lamp (200–800 nm, 300W)	Mecoprop-P	0.05	7	100	[96]
4	GCN/Ag ₂ CrO ₄	Royal blue LED (460 nm)	2,4-D and Mecoprop-P	12.1 and 6.7	120 and 120	86.32 and 86.39	Current study

4.7.2 Photocatalytic degradation of BSA protein and SARS-CoV-2 spike protein

The interaction between the synthesized photocatalysts and BSA in the absence of light (dark experiment) was investigated and the results are shown in Figure 4.3a. It was observed that the concentration of BSA did not change when GCN was present in the solution, indicating that the GCN had a negligible impact in the dark experiment. However, it was observed that the concentration of BSA decreased significantly by 93.1% in 30 minutes in the presence of GCN/Ag₂CrO₄. The photocatalytic degradation results of BSA are presented in Figure 4.3b. It shows that royal blue LED irradiation alone and GCN/royal blue LED irradiation could not degrade BSA. The royal blue LED with a peak wavelength of 460 nm and low energy

(2.7 eV) cannot alone degrade BSA with an absorption peak of 280 nm and high energy (4.4 eV) indicating that BSA requires high energy radiation greater than 4.4 eV for degradation to take place. The GCN/royal blue LED could not degrade BSA because of the high electron-hole pair recombination rate of GCN owing to its medium band gap (2.7 eV). However, more than 99.9% of BSA was degraded in 20 minutes in the presence of GCN/Ag₂CrO₄ under royal blue LED irradiation. The first-order rate constant (k) values of GCN and GCN/Ag₂CrO₄ were calculated, and they are $0.002 \times 10^{-1} \text{ min}^{-1}$ and $3.64 \times 10^{-1} \text{ min}^{-1}$ respectively.

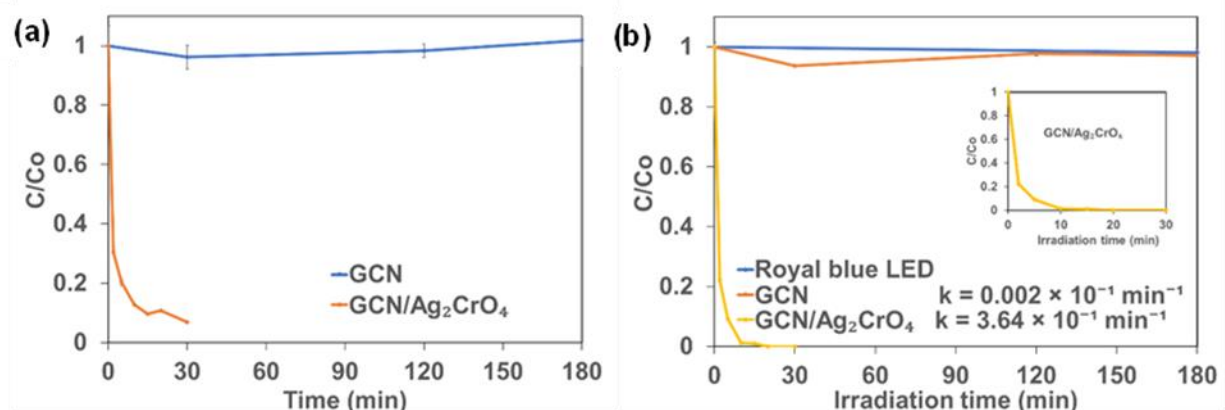


Figure 4. 3 Change in BSA concentration with time: (a) Dark experiment and (b) Royal blue LED irradiation.

In a recently published work, the photocatalytic degradation mechanism of protein using silver nanoparticles (AgNPs) was reported by investigating the effects of the following 3-step phenomenon; release of silver ions, generation of reactive oxidative species (ROS), and the light-induced protein oxidation through the bind-and-damage model [231]. It was postulated and concluded by asserting an alternate mechanism, which is that light-induced protein oxidation is responsible for the degradation rather than the popular notions that the mechanisms of Ag⁺ release from AgNPs and the generation of ROS are the driving forces for protein degradation and bacterial death. For the bind-and-damage model of the light-induced protein oxidation to take place, the AgNPs released the absorbed visible light energy in the form

of emission. This emission of light is then quenched by a protein which indicates that the absorbed light energy was transferred to the protein, causing structural damage to the proteins.

The assertions were applied to this work for verification by carrying out UV-vis absorption spectra measurements of BSA for GCN and GCN/Ag₂CrO₄ with and without royal blue LED irradiation to further understand the degradation profile and the change in concentration with time. UV-vis, as an analytical method, can be used in absorption spectra measurement in understanding structural changes in protein and the interaction between protein and nanoparticles [214,215,232,233]. The observation was that the phenomena: release of Ag⁺ from the Ag₂CrO₄, generation of ROS through photocatalytic reaction, and the bind-and-damage model of the light-induced protein oxidation, have varying degrees of contribution to the degradation of protein in the presence of GCN/Ag₂CrO₄ with and without blue LED irradiation. The roles these phenomena play in either protein degradation or bacterial death will depend on the type of photocatalyst, light intensity, radiation spectrum, and energy of the light source. In this work, two ions (Ag⁺ and CrO₄²⁻) were released against Ag⁺ of AgNPs since GCN/Ag₂CrO₄ composite was used, indicating the possibility of the impact of CrO₄²⁻ in the degradation mechanism as an electron scavenger during photocatalytic activity. The UV-vis absorption spectrum in Figure 4 shows the effect of GCN and GCN/Ag₂CrO₄ on BSA with and without royal blue LED irradiation. At time zero (Figure 4, a-d), BSA shows the typical absorption peaks at a lower wavelength of 200 nm and a higher wavelength of 280 nm. The absorption peak at 200 nm is attributed to the BSA's polypeptide backbone and the absorption peak at 280 nm is due to its aromatic amino acids (tryptophan, tyrosine, and phenylalanine). In Figure 4.4 (a and c), the GCN without and with royal blue LED irradiation revealed similar absorption spectra. In Figure 4.4a, without light (dark), the BSA peak did not change because the conditions required for protein damage which are light-induced protein oxidation and ROS generation are not present since photocatalytic activity did not take place. It also indicates no interaction between the BSA and GCN, hence no structural change to the protein. In Figure 4.4c, under royal blue LED irradiation, the bind-and-damage model of the light-induced protein oxidation and the generated ROS did not have an impact on the degradation of the protein.

This suggests that the emitted light from the absorbed light energy by the GCN was neither sufficient nor transferred to the protein for degradation, and the generated ROS was not sufficient to cause degradation because of the GCN's poor charge transfer and fast electron-hole recombination rate characteristics. In the presence of GCN/Ag₂CrO₄ (Figure 4.4 b and d), an absorption peak at 374 nm was observed. This peak is attributed to the presence of silver chromate in the BSA slurry. Silver compounds are known to have absorption peaks between 320 nm and 410 nm [216,217,234]. In Figure 4.4 (b and d), the GCN/Ag₂CrO₄ without and with royal blue LED irradiation show similar spectral patterns. In Figure 4.4b, without light (dark), Ag⁺ and CrO₄²⁻ were released by Ag₂CrO₄ in the GCN/Ag₂CrO₄ nanocomposite. The interactions of the Ag⁺ with BSA resulted in higher BSA absorption peaks compared to GCN without light (dark). In Figure 4d, under royal blue LED irradiation the bind-and-damage model light-induced protein oxidation and the ROS generation did not significantly contribute to the protein degradation since the peaks without light and with royal blue LED are similar. This is evident in the change in BSA concentration when exposed to GCN/Ag₂CrO₄ with and without royal blue LED irradiation (Figure 4.3 a and b), where the degradation is similar at 90% and 99% in 15 minutes respectively. Therefore, we can conclude the following: (1) the Ag⁺ released from GCN/Ag₂CrO₄ was largely responsible for BSA protein degradation with and without royal blue LED irradiation, and (2) the bind-and-damage model of light-induced protein oxidation and the generation of ROS did not significantly contribute to photocatalytic degradation of BSA protein, indicating that the light irradiation had less impact in the photocatalytic process. The less impact of light irradiation is expressed in the proximities of the degradation kinetics of GCN/Ag₂CrO₄ with royal blue irradiation ($3.64 \times 10^{-1} \text{ min}^{-1}$) which is less than two times without light, that is dark ($1.86 \times 10^{-1} \text{ min}^{-1}$). The reason for the dominance of these silver ions in the degradation of BSA protein could be attributed to their binding interactions with BSA. Previous studies show that silver ions and silver nanoparticles interact with protein functional groups, such as carboxylic groups (COOH), thiol groups (SH), and amino groups (NH) of protein, to form bonds resulting in protein inactivation [216,235–238]. Zaher et al. investigated the interaction between Ag⁺ and AgNPs with BSA protein and reported that Ag⁺ has stronger binding and quenching efficiency towards BSA than AgNPs which is evidenced in a higher binding constant of Ag⁺

[239]. BSA is a polymer of about 583 amino acids joined together by peptide linkage between two tryptophan residues. Each amino acid has two pH-sensitive functional groups, COOH and NH. The proposed binding mechanism was due to the electrostatic attraction between the ionized COO^- and the positive charge of Ag^+ at physiological pH ($\text{pH} = 7.4$). This was confirmed in the reported UV-vis spectra showing the peak intensity increasing with rising Ag^+ concentration. This correlates with our UV-vis spectra results for GCN/ Ag_2CrO_4 with and without royal blue LED irradiation where the BSA peak intensity increases indicating a rise in Ag^+ concentration with time in the reacting medium and therefore the increasing interaction between the COO^- and Ag^+ electrostatically. This interaction leads to denaturing, unfolding, aggregation, and the eventual inactivation of the protein. Jaiswar et al. investigated the binding interaction between protein and chromate ions and reported structural changes to protein, indicating successful interactions [240].

In [Figure 4.5](#), SARS-CoV-2 (Coronavirus) spike protein result is presented. It shows that GCN/ Ag_2CrO_4 also can degrade the spike protein under royal blue LED. A photocatalytic degradation efficiency of 77.5% was achieved in 30 minutes. The lower degradation efficiency observed for SARS-CoV-2 spike protein (SP) can be attributed to its heavier molecular weight and structure. SARS-CoV-2 SP is 135 kDa and 1213 amino residues which is twice the size of BSA protein which is 66 kDa and 583 amino acid residues.

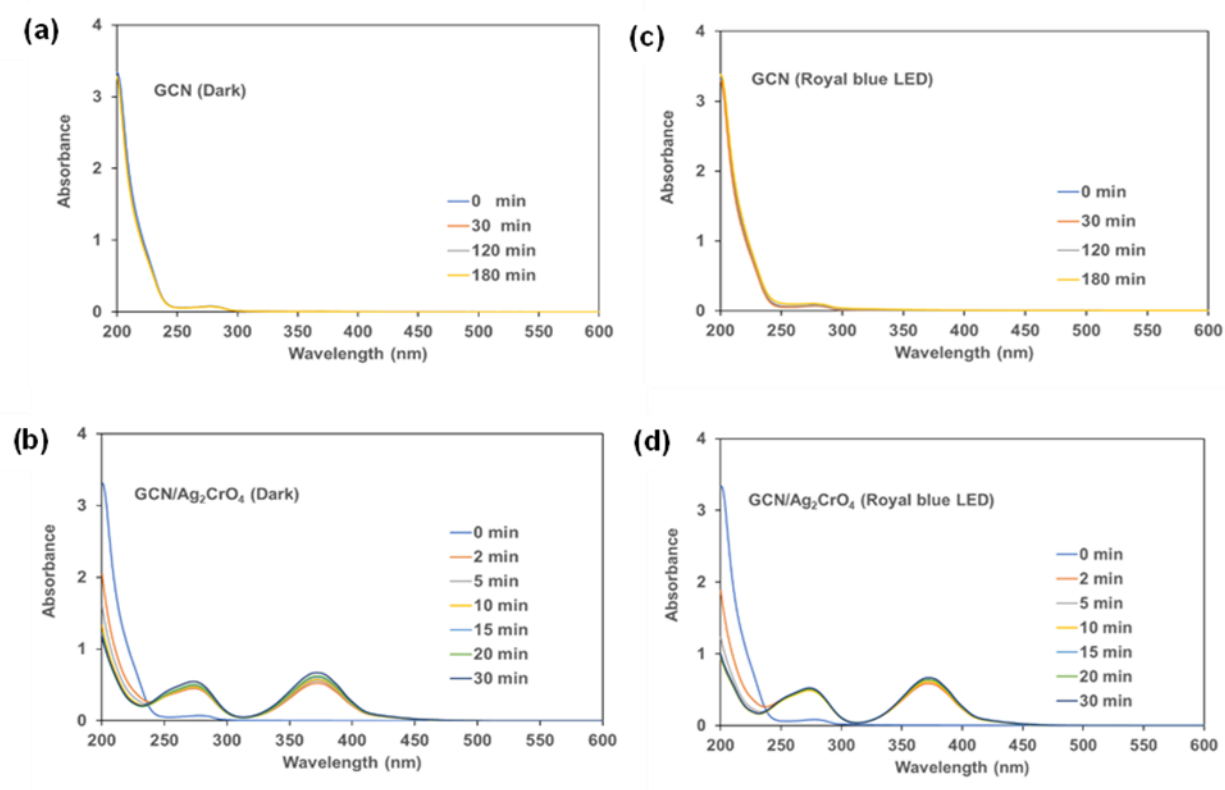


Figure 4. 4 UV-vis absorption spectra of BSA: Dark experiment (a and b) and Royal blue LED irradiation (c and d).

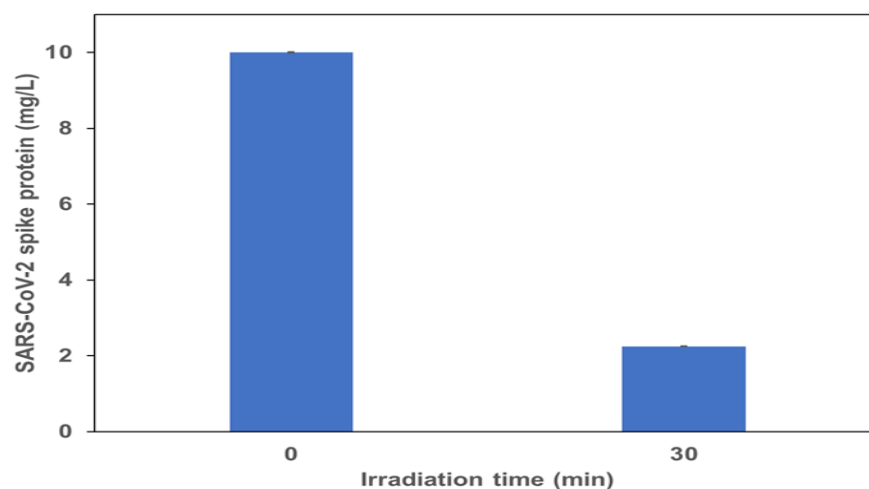


Figure 4. 5 Photocatalytic degradation of SARS-CoV-2 (Coronavirus) spike protein using GCN/Ag₂CrO₄. Under royal blue LED irradiation.

4.7.3 Photocatalytic disinfection of wastewater secondary effluent

Results on the disinfection of secondary effluent from a municipal wastewater treatment plant by GCN/Ag₂CrO₄ are presented in Figures 4.6 and 4.7. The log reduction of cellular Adenosine Triphosphate (cATP) is presented in Figure 6, while the log reduction of total coliforms and *E. coli* is presented in Figure 7. As shown in Figure 4.6, around 0.2 log reduction of cATP was observed after 60 minutes of royal blue LED irradiation or after 60 minutes of dark (control experiment). The presence of GCN/Ag₂CrO₄ in the dark or royal blue LED irradiation both increased the log reduction of cATP in wastewater. Moreover, a 1.2 log reduction was observed for cATP when wastewater was mixed with GCN/Ag₂CrO₄ in the dark for 60 minutes. An even higher log reduction (>1.7) was observed in the presence of GCN/Ag₂CrO₄ under royal blue LED irradiation for 60 minutes.

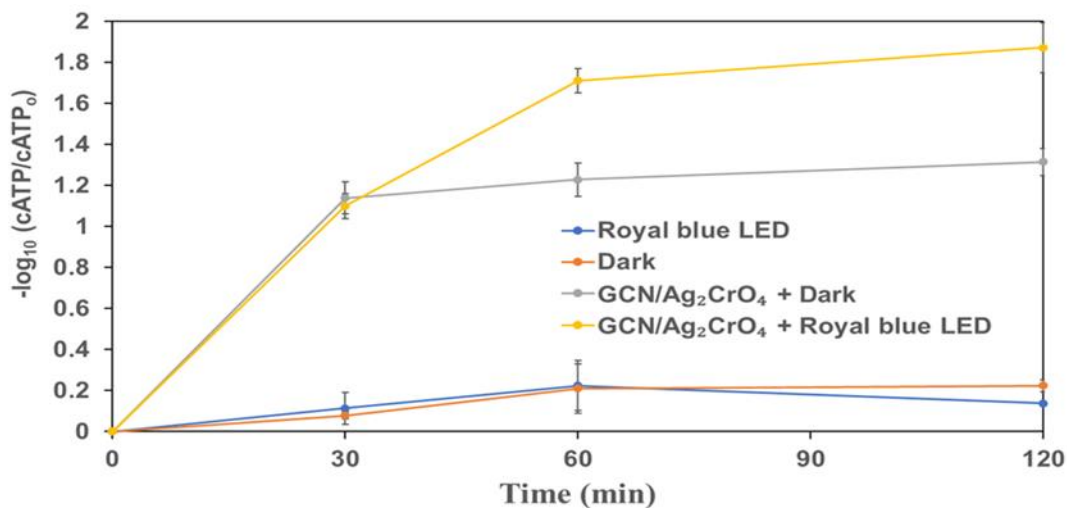


Figure 4. 6 The change of ATP in wastewater secondary effluent in the presence of GCN/Ag₂CrO₄ with and without royal blue LED irradiation.

In the control experiments of royal blue LED and GCN (dark experiment), the total coliforms and *E. coli* did not decrease during the experimental duration of 60 minutes. This indicates that the royal blue LED

irradiation and GCN (dark experiment) did not impact the total coliforms and *E. coli* counts in the wastewater. The dark control experiment of GCN/Ag₂CrO₄ and the use of GCN under royal blue LED both led to lower log reduction (<1) in 60 minutes for total coliforms and *E. coli*. However, the use of GCN/Ag₂CrO₄ under royal blue LED irradiation led to a higher log reduction (>1) in 60 minutes with a 2.43 log reduction of total coliforms and a 1.48 log reduction of *E. coli*. This result indicates that the disinfection rate of *E. coli* was slower than that of the total coliforms.

The interaction of silver compounds with the cell membrane of the bacteria is one of the important mechanisms of silver compound toxicity [223]. This can occur both in the dark and visible light irradiation. Over one log reduction was observed for ATP, total coliforms, and *E. coli* in 60 minutes during the photocatalytic degradation process. This indicates GCN/Ag₂CrO₄ can potentially photocatalytically inactivate, under royal blue LED irradiation, over 98% (1.7 log) of the microbial activity (ATP) in 60 minutes which includes inactivation of over 99.6% (2.43 log) of total coliforms.

The bind-and-damage model of protein oxidation, release of ions from the photocatalyst, and the ROS generation processes of protein degradation described in section 3.2 can be adopted for this disinfection process since it was used for protein degradation and bacterial disinfection by Shi et al. [231]. In [Figure 4.6](#), the GCN/Ag₂CrO₄ with and without royal blue LED irradiation showed a significant impact on the reduction of cATP of microorganisms. Without light (GCN/Ag₂CrO₄ + Dark), the release of Ag⁺ and CrO₄²⁻ contributed to the reduction of cATP by 1.2 log in 60 minutes. However, with irradiation (GCN/Ag₂CrO₄ + Royal blue LED), the ROS generation in addition to Ag⁺ and CrO₄²⁻ released resulted in a >1.7 log reduction of cATP in 60 minutes. With the marginal difference of >0.5 log reduction of cATP, it means the release of the two ions contributed far more than ROS generation in the overall reduction of cATP. In [Figure 4.7a](#), the GCN/Ag₂CrO₄ with and without royal blue LED irradiation showed a different response to the disinfection of total coliforms. Without light (GCN/Ag₂CrO₄ + Dark), the release of Ag⁺ and CrO₄²⁻ resulted in a 0.3 log reduction of total coliforms in 60 minutes while the irradiation (GCN/Ag₂CrO₄ + Royal blue LED), the ROS generation and the light-induced protein oxidation in addition to the released two ions

resulted in 2.4 log reduction of total coliforms in 60 minutes. The log reduction difference >2 log is largely due to the contributions of the generated ROS and the light-induced protein oxidation. In [Figure 4.7b](#), the GCN/Ag₂CrO₄, with and without royal blue LED irradiation showed a different response to E. coli disinfection. Without light (GCN/Ag₂CrO₄ + dark), the Ag⁺ and CrO₄²⁻ released resulted in a 0.1 log reduction of E. coli in 60 minutes while with irradiation (GCN/Ag₂CrO₄ + Royal blue LED), the generated ROS and light-induced protein oxidation in addition to the released ions resulted in 1.5 log reduction of E. coli in 60 minutes. The log reduction difference >1 log is largely due to the contributions of the ROS generated and the light-induced protein oxidation.

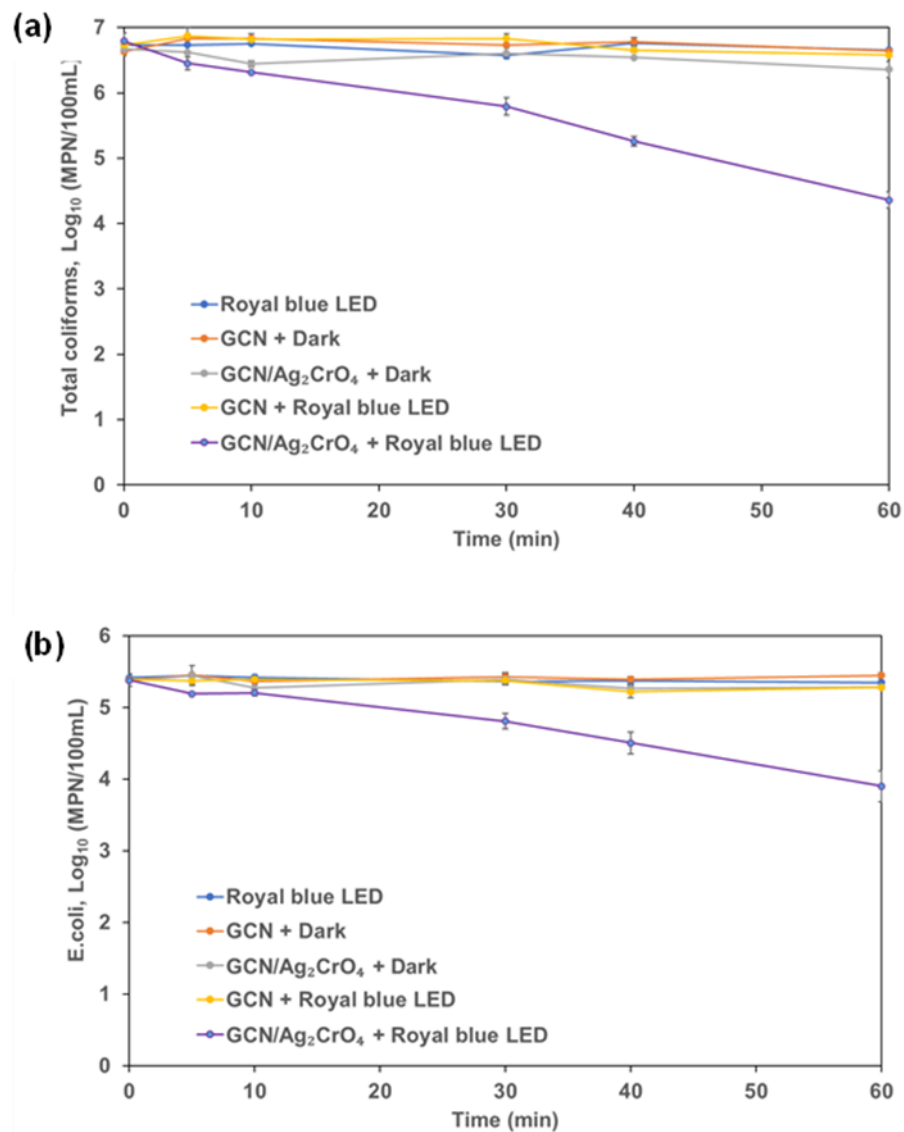


Figure 4. 7 Coliforms in wastewater secondary effluent: (a) total coliforms and (b) *E. coli*.

Zhang et al. investigated the impact of light irradiation on the reduction of Ag^+ to AgNPs by bacteria and reported that visible lights (monochromatic light at wavelengths 415 nm and 600 nm) accelerated the reduction of Ag^+ to AgNPs by bacteria and almost no AgNPs were formed in the dark [104]. Furthermore, the visible light irradiation reversibly can excite the AgNPs for their surface plasmon resonance (SPR) and accelerate the electrons from the bacteria to the adjacent Ag^+ . It reported that the bacteria can reduce Ag^+ and the process can be accelerated by light irradiation. Shi et al. focused on the bactericidal effect of AgNPs and identified a new antibacterial mechanism different from the ROS-induced photocatalyst [231]. AgNPs can penetrate the cell wall and membrane and gather in the cytosol and bind directly with the cytosol protein leading to the inducement of protein aggregation, an indication of protein degradation, caused by the bind-and-damage model of the light-induced protein oxidation. Deng et al. investigated the effects of silver ions, chromium VI, Cr(VI) , and ROS on the photocatalytic disinfection mechanism of *E. coli* [105]. The results show that the combined effects of the release of silver ions and the generation of ROS of holes (h^+) and hydroxyl ($\cdot\text{OH}$) radicals played important roles in the photocatalytic disinfection process. The silver ions interact with the thiol ($-\text{SH}$) functional group causing cell damage and the generated ROS could inactivate bacterial cells by interacting with the cell wall and destabilizing the membrane causing leakage of potassium ions (K^+). The interaction of Ag^+ with bacterial cell membranes can also lead to lower ATP readings caused by the leakage of potassium ions [223]. The addition of hexavalent chromium to the photocatalytic system enhanced the photocatalytic disinfection kinetics. This is because Cr(VI) can behave as an electron scavenger, directly reduces electron-hole recombination, enhances the amount of h^+ available for disinfection, and ultimately leads to better disinfection performance. Table 4.4 shows the photocatalytic disinfection of microorganisms by different photocatalysts.

Table 4. 4 Comparison of microorganism disinfection with the results of previously published articles.

S/N	Photocatalyst	Visible Light Source	Contaminant	Disinfection Time (min)	Concentration (CFU/mL)	Disinfection Efficiency (Log Reduction)	Ref.
1	BiOBr	Xenon lamp (1000 W/m ² , 300 W)	<i>E. coli</i>	24	10 ⁷	7	[115]
2	Ag/BiOI	Iodide lamp (400 W)	<i>E. coli</i>	20	10 ⁷	7	[117]
3	Ag/ZnO/GCN	Xenon lamp (300 W)	<i>E. coli</i>	120	10 ⁷	7	[118]
4	GCN/Ag ₂ CrO ₄	Royal blue LED (460 nm)	Total coliforms and <i>E. coli</i>	60 and 60	10 ^{6.7} and 10 ^{5.5}	2.43 and 1.48	Current study

4.8 Conclusions

A visible-light active photocatalyst, GCN/Ag₂CrO₄ nanocomposite was synthesized, and its performance was investigated in the degradation of organic pollutants (2,4-D and Mecoprop-P) in Killex^R, BSA protein, and SARS-CoV-2 spike protein) and the disinfection of WWTP secondary effluent, using a narrowband low-energy visible light source (royal blue LED at 460 nm). The results from this study highlight the following:

- Similar degradation rates and percentage removal visible light irradiation were observed for 2,4-D and Mecoprop-P.
- The degradation performance of a photocatalyst is dependent on the available surface area for absorption for photocatalytic activity and the bond energies of the chemical bonds that exist in the contaminant.
- Released Ag⁺ and CrO₄²⁻ from the GCN/Ag₂CrO₄ nanocomposite were largely responsible for the BSA degradation and cATP reduction.
- Generated ROS were largely responsible for the disinfection of total coliforms and *E. coli*.

- The lower percentage degradation (70%) of SARS-CoV-2 spike protein can be attributed to its large molecular weight and structure compared to BSA protein.
- The pathways for the degradation of proteins and the disinfection of microorganisms depend on any of the following: (1) the binding affinity of the released metal ions from GCN/Ag₂CrO₄ with the functional groups of proteins and ATP, (2) the amount of ROS generated, and (3) the quantum of emission light from the photocatalyst that is absorbed and quenched by the proteins because of the light-induced protein oxidation.
- Significant disinfection results observed in the reduction of microorganisms' cATP, total coliforms, and E. coli with GCN/Ag₂CrO₄ are also due to the reduction of the released Ag⁺ to AgNPs by bacteria which was accelerated by light irradiation.
- Over one log reduction of microorganisms' cATP, total coliforms, and E. coli in wastewater secondary effluent was achieved in 60 minutes.
- The combination of GCN/Ag₂CrO₄ and the narrowband low-energy light (royal blue LED at peak wavelength = 460 nm) holds promise in that it can be used in the wastewater treatment plant to degrade multiple recalcitrant organic pollutants and inactivate microorganisms.

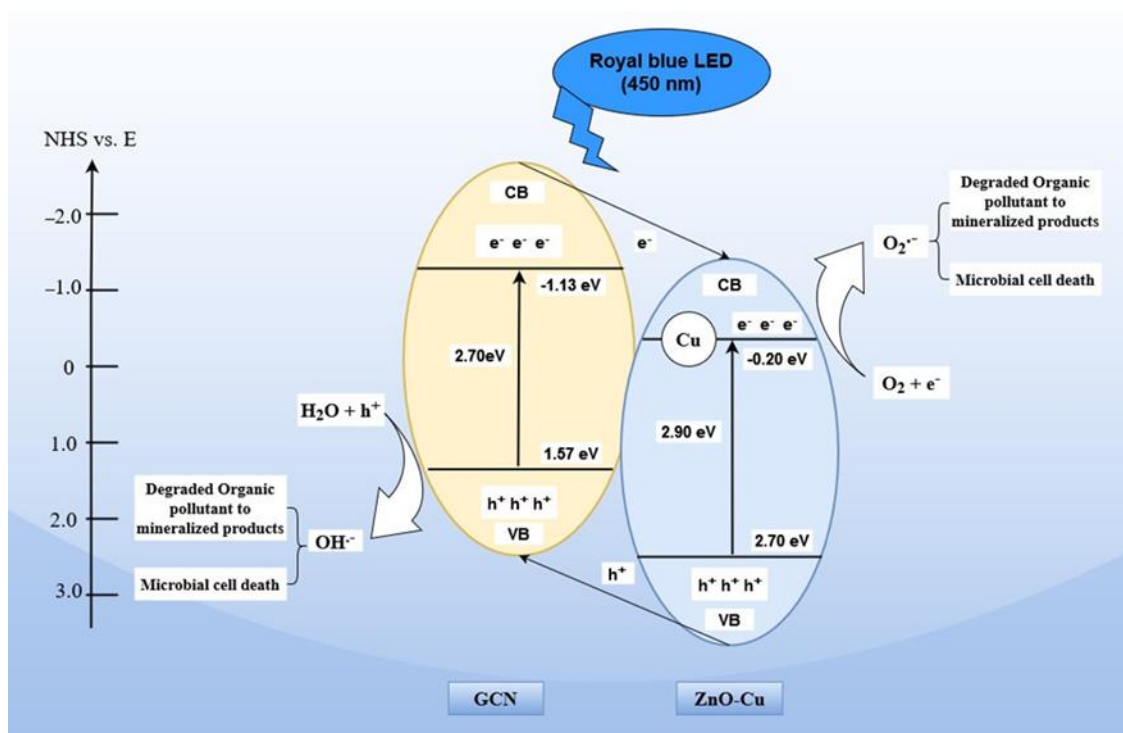
Chapter 5: A facile synthesis process of GCN/ZnO-Cu nanocomposite and the evaluation of the performance for the photocatalytic degradation of organic pollutants and the disinfection of wastewater under visible light³

5.1 Highlights

- ZnO-Cu3% nanoparticles showed the best photocatalytic degradation activity.
- GCN/0.1ZnO-Cu3% nanocomposite has the largest BET surface area and the lowest bandgap energy.
- GCN/0.1ZnO-Cu3% nanocomposite showed the best degradation of organic contaminant and the disinfection of wastewater.
- Hydroxyl radical (OH^\cdot) was observed to be the dominant reactive oxidation specie (ROS).

³ O.O. Akintunde, J. Hu, M.G. Kibria, S. Pogolian, G. Achari, A facile synthesis process of GCN/ZnO–Cu nanocomposite and the evaluation of the performance for the photocatalytic degradation of organic pollutants and the disinfection of wastewater under visible light, *Chemosphere*. 344 (2023) 140287. <https://doi.org/10.1016/j.chemosphere.2023.140287>.

5.2 Graphical abstract



5.3 Abstract

In this research, graphitic carbon nitride/zinc oxide-copper denoted as GCN/ZnO-Cu nanocomposite photocatalysts were synthesized using a novel facile synthesis process, the co-exfoliation method involving ultrasonic exfoliation of the mixture of GCN and ZnO-Cu in ethanol and then thermal exfoliation. Different characterization techniques such as X-ray diffraction (XRD), mean crystallite size (MCS), BET surface area, transmission electron microscopy (TEM), scanning electron microscopy (SEM), energy dispersive spectroscopy (EDS), particle size distribution (PSD), Fourier transform-infrared spectroscopy (FT-IR), photoluminescence (PL) spectra, and ultraviolet-visible diffuse reflectance spectroscopy (UV-Vis DRS) were conducted to study the crystallinity, morphology, elemental composition, chemical structure, and

optoelectronic properties. The band gap was estimated using the UV-Vis DRS results and Tauc plots. The photocatalytic activity of the GCN/ZnO-Cu3% nanocomposites was evaluated in the degradation of 4-chlorophenol (4-CP), and the disinfection of wastewater primary influent under a narrowband visible light source, royal blue LED ($\lambda = 450$ nm). GCN/0.1ZnO-Cu3% nanocomposite showed the best performance in the degradation of 4-CP and the disinfection of municipal wastewater primary influent. For 4-CP degradation, GCN/0.1ZnO-Cu3% was 2.2 times better than GCN, 9.4 times better than ZnO-Cu3%, and 1.8 times better than the sum of the individual GCN and ZnO-Cu3%. A 5.5 log reduction was achieved for the disinfection of total coliforms in wastewater primary influent in 360 minutes. This enhanced photocatalytic activity of GCN/ZnO-Cu3% nanocomposite can be attributed to the synergistic effect of GCN and the ZnO-Cu3%, resulting in a large surface area and improved bandgap.

5.4 Introduction

Rapid global industrialization has led to environmental challenges such as the release of toxic chemicals and microorganisms into the environment [241,242]. The wastewater generated after industrial processes is treated using conventional methods followed by disinfection. Chlorination, ozonation, and ultraviolet (UV) treatment are some of the disinfection methods. However, these treatment methods have limitations such as the chlorination of organics (phenolic compounds) to generate carcinogenic chlorophenols [243–245], and the generation of toxic disinfection by-products [246,247]. Other conventional treatment methods such as adsorption, membrane filtration, and precipitation are known to have high energy consumption [248–250]. Photocatalysis has shown to be an effective method of organic contaminant degradation and the disinfection of microorganisms in wastewater due to its low energy consumption and non-toxicity [251]. Photocatalysis is a process in which a photocatalyst is irradiated by photons with energy greater than or equal to its bandgap energy, causing the generation of electrons and holes on its surface. These photogenerated electrons and photogenerated holes react with the dissolved oxygen in the water and the

water molecules to form reactive oxidation species (ROS) such as superoxide and hydroxyl radicals, which in turn react with the target organics and microorganisms leading to their degradation and disinfection [194,251–253]. Semiconductor photocatalysts such as 2D polymeric graphitic carbon nitride (g-C₃N₄ or GCN) [254–256] and other various metal oxides (ZnO, TiO₂, WO₂, Bi₂WO₆, and CuO) [257–260] have been widely used in wastewater treatment due to their non-toxicity, ease of synthesis, and low cost.

ZnO, a metal oxide semiconductor photocatalyst has been a choice for degradation and disinfection because of its stability, high electron mobility, abundance, non-toxicity, antimicrobial properties, and bandgap (3.3 eV) [261,262] similar to TiO₂ (3.2 eV) [194,263]. However, ZnO has limitations due to its wide bandgap limiting its application mostly to the UV region of the electromagnetic spectrum as well as the fast recombination rate of the electron-hole pair [264]. Other drawbacks of ZnO include particle aggregation due to the strong van der Waals intermolecular forces of attraction between its particles and photocorrosion [265]. It has been reported that the photocatalytic activity of ZnO can increase by two factors, (a) the presence of oxygen vacancies in its structure and (b) by addition of carbonaceous materials such as GCN [266]. The presence of oxygen vacancies in the ZnO structure is a result of the introduction of a dopant. The dopant creates a sub-energy level below the conduction band thereby narrowing the bandgap. Doping with a transition metal increases its surface defects, narrows its bandgap, and invariably extends its use in the visible-light region [267]. ZnO can be doped with transition metals such as chromium, manganese, iron, and cobalt to enhance its visible light utilization [268]. Das et al. synthesized ZnO-Fe and the result shows a complete 7-log reduction of *E. coli* under visible light in 180 minutes [269]. Basu et al reported a complete 6-log reduction of *E. coli* using ZnO-Al under visible light in 240 minutes [270]. Carbonaceous materials such as graphene and GCN can act as both photo-sensitizers and stabilizers when added to ZnO.

GCN has been studied for environmental remediation in the degradation of organics and for disinfection due to its medium bandgap (2.7 eV to 2.8 eV), visible-light activity, non-toxicity, and ease of synthesis

[271]. However, GCN has limitations due to low photon utilization, fast electron-hole recombination, and poor charge separation [272]. Different modification techniques such as exfoliation, heterojunction, doping, and co-doping have been proposed to improve photocatalytic activity [273–276]. The combination of GCN with other semiconductor photocatalysts has been studied in the degradation of different organic contaminants and disinfection of wastewater [194,277]. ZnO is another semiconductor photocatalyst that has been suggested to enhance the photocatalytic activity of GCN. Jingyu et al. reported 96% degradation of methylene blue (MB) after 210 minutes using ZnO/GCN under visible light irradiation [278]. Wang et al. reported improved phenol degradation when GCN/ZnO was synthesized and used as a photoanode under visible light [279]. Qamar et al. reported the degradation of 60% and 35% of MB in 60 minutes and 90 minutes under visible light irradiation using Mn-ZnO and Fe-MnO respectively [280]. DeSouza et al. reported the degradation of 70% and 50% of 4-CP, both in 300 minutes under solar and visible light irradiation respectively when ZnO/GCN was used [281]. Qamar et al. and DeSouza et al. observed further improved photocatalytic activity of the ternary nanocomposites with the addition of GCN to Mn-doped ZnO (GCN/Mn-ZnO), GCN to Fe-doped ZnO (GCN/Fe-ZnO), and GCN to carbon xerogel-doped ZnO (XC/ZnO/GCN). Qamar et al. reported the degradation of 98% and 95% of MB after 60 minutes and 90 minutes under visible light irradiation for GCN/Mn-ZnO and GCN/Fe-MnO respectively [280,282] while DeSouza et al. reported the degradation of 4-CP of about 90% and 70% both in 300 minutes under solar and visible light irradiation respectively when XC/ZnO/GCN was used [281]. The observed enhanced photocatalytic activity of the ternary nanocomposites can be attributed to the coupling of the metal-doped ZnO/GCN and non-metal-doped ZnO/GCN to form heterostructures which inhibit the fast recombination of the electron-hole pairs and improves charge carrier separation.

In this research, GCN/ZnO-Cu ternary nanocomposites were synthesized using a novel facile synthesis process, the co-exfoliation method. The synthesized samples were characterized using different techniques. The photocatalytic activity of the synthesized photocatalysts was evaluated in the degradation of an organic

contaminant and the disinfection of municipal wastewater primary influent using a narrowband visible light source, royal blue LED ($\lambda = 450$ nm). Prior to this, most research reported the use of broadband visible light sources such as Xenon lamps (400 to 700 nm) or sunlight. The benefits and practical applications of narrowband light are longer lifetime, directionality, narrow beam width, and high photon flux meaning that a large number of photons generated can be used to drive the photocatalytic reaction. The contaminant of the study is 4-chlorophenol (4-CP) because of its frequent use in the synthesis of pharmaceuticals, dyes, pesticides, and herbicides, and its reported environmental hazards. The practical application of the synthesized photocatalyst was investigated by conducting reusability test experiments. The reactive oxidation species (ROS) was conducted to determine the active oxidative species involved in the photocatalytic reaction and a mechanism was proposed. The purpose of coupling ZnO and Cu with GCN is to improve the quantum efficiency of the GCN/ZnO-Cu nanocomposite (see section 3.6.3).

5.5 Materials and Methods

5.5.1 Chemicals

4-chlorophenol-ClCH₄OH (99%), urea-CH₄N₂O ($\geq 99.5\%$), isopropanol-C₃H₈O ($\geq 99.5\%$), p-benzoquinone-C₆H₄O₂ ($\geq 98\%$), potassium chromate-K₂CrO₄ ($\geq 99\%$), ammonium oxalate-(NH₄)₂C₂O₄, Methanol-CH₃OH ($\geq 99.9\%$), acetonitrile-C₂H₃N ($\geq 99.9\%$), and high-pressure liquid chromatography (HPLC) grade water were purchased from Sigma-Aldrich Co. (St. Louis MO, USA). Copper II nitrate hemi (pentahydrate)-Cu(NO₃)₂.2.5H₂O ($\geq 98\%$) was purchased from Alfar-Aesar (Ward Hill, MA, USA). Zinc sulfate heptahydrate-ZnSO₄.7H₂O was purchased from EM Science (Gibbstown, NJ, USA). Ethanol (absolute) was purchased from EMD Millipore Corp. (Burlington, MA, USA). Total coliforms/E.coli test kit was purchased from IDEXX laboratories Inc. (Westbrook, ME, USA). Sodium citrate tribasic-Na₃C₆H₅O₇ was purchased from CHEMCO (Port Louis, Mauritius). Municipal wastewater primary influent was obtained from Advanced Canadian Water Assets-ACWA (Calgary, AB, Canada), a full-scale testing facility embedded in a wastewater treatment plant in Calgary, Alberta.

5.5.2 Synthesis of GCN

Bulk graphitic carbon nitride (GCN) was synthesized from urea by direct pyrolysis [194], as shown in [Scheme 5.1a](#). Briefly, 70 g of urea was placed in a partially closed alumina crucible and then calcined in a muffle furnace (550-58, Fisher Scientific, Waltham, MA, USA) at 550 °C for 4 h. The muffle furnace was turned off after 4 h and the GCN was left to cool down in the muffle furnace to room temperature. The obtained pale-yellow material was ground to a powder and labeled GCN.

5.5.3 Synthesis of ZnO nanoparticles and ZnO-Cu nanoparticles

The ZnO and ZnO-Cu samples were synthesized using chemical co-precipitation [269,270], as shown in [Scheme 5.1b](#). ZnO-Cux samples were synthesized with different Cu ratios ($x = 1\%$, 3% , and 5%). 2.8756 g (50 mM) of zinc sulfate heptahydrate ($\text{ZnSO}_4 \cdot 7\text{H}_2\text{O}$) was added to 200 mL deionized (DI) water in different 400 mL beakers. An equivalent concentration of 50 mM (2.5806 g) of sodium tribasic- $\text{Na}_3\text{C}_6\text{H}_5\text{O}_7$ was added to the mixture as a stabilizing agent. While continuously stirring the solution, copper II nitrate hemi pentahydrate, $\text{Cu}(\text{NO}_3)_2 \cdot 2.5\text{H}_2\text{O}$ of different ratios [1% (0.029 g), 3% (0.086 g), and 5% (0.144 g)] as a function of the mass of $\text{ZnSO}_4 \cdot 7\text{H}_2\text{O}$ was added to the beakers. The solutions were heated while stirring on a hotplate at 70 °C for 15 minutes. This was followed by a dropwise addition of 100 mL of 200 mM NaOH. The solution was continuously stirred at 70 °C for 2 h as the colour changed from an initial pale blue to an opaque bluish milky slurry. The solution was allowed to cool down while being continuously stirred. It was then vacuum filtered using a 0.45 μm filter and washed thoroughly with DI water to remove excess NaOH. The samples were air-dried overnight and later calcined at 550 °C for 3 h. The calcined samples were left to cool down, ground, and labeled as ZnO-Cu1%, ZnO-Cu3%, and ZnO-Cu5%. The ZnO nanoparticles were synthesized using the same process of synthesizing ZnO-Cu nanoparticles except for the addition of copper II nitrate hemi pentahydrate, $\text{Cu}(\text{NO}_3)_2 \cdot 2.5\text{H}_2\text{O}$.

5.5.4 Synthesis of GCN/ZnO-Cu nanocomposites

GCN/ZnO-Cu samples were synthesized using the novel facile co-exfoliation method as shown in [Scheme 5.1c](#). GCN/xZnO-Cu3% samples were synthesized with different mass (g) of $x = 0.1, 0.3$, and 0.5 , based on the optimal ratio ZnO-Cu3% observed for the photocatalytic degradation of 4-chlorophenol (4-CP). 1 g of GCN was added to 50 mL of ethanol (absolute) in different quartz petri dishes and the mixtures were sonicated for 1 h to achieve uniform dispersion. With continuous stirring on a magnetic stirrer, different amounts of ZnO-Cu3% (0.1 g, 0.3 g, and 0.5 g) were added to the mixtures and afterward sonicated for another 0.5 h. The mixtures were continuously stirred for 2 h and then dried in the oven at 70 °C overnight. The dried samples were calcined in the muffle furnace at 550 °C for 4 h and left to cool down in the furnace to room temperature. The samples were then ground and labeled GCN/0.1ZnO-Cu3%, GCN/0.3ZnO-Cu3%, GCN/0.5ZnO-Cu3%, and stored for usage.

5.5.5 Characterization

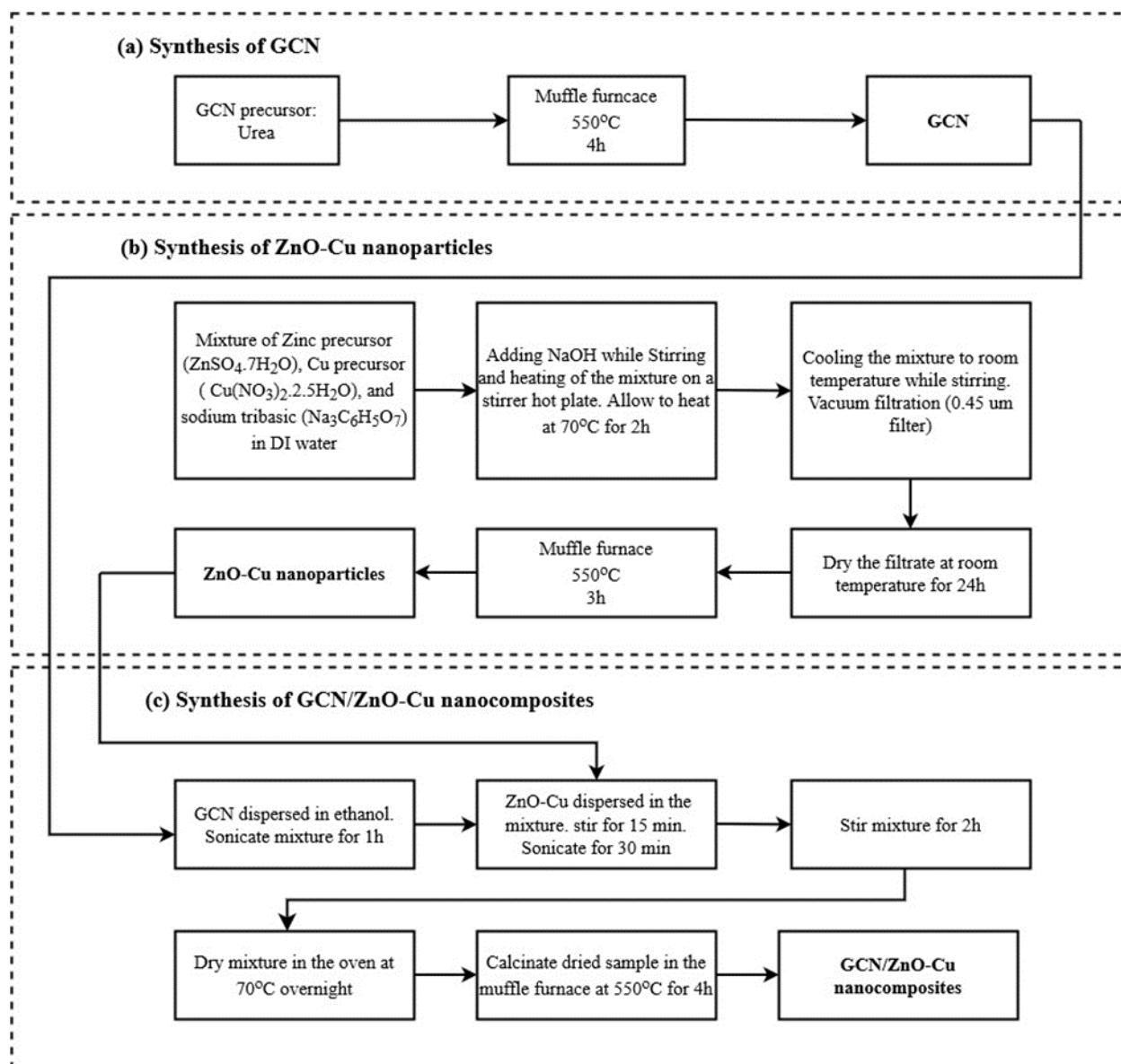
The crystal and phase structures and the crystallite size of the samples were studied using X-ray diffraction (XRD; Rigaku multiflex X-ray diffractometer) with Cu K α X-ray radiation, $\lambda = 1.5406 \text{ \AA}$. Particle size distribution (PSD) of the samples was measured using the dynamic light scattering (DLS) method (PSD; Malvern Zetasizer Nano ZS). The chemical and bonding structures of the samples were studied using Fourier transform-infrared spectroscopy (FT-IR; Bruker Vertex 70). The inner morphology of the samples was examined by transmission electron microscope (TEM; Tecnai F20). The outer morphology of the samples was examined by scanning electron microscope (SEM; Quanta FEG 250 FESEM). The elemental analysis of the samples was conducted using energy-dispersive X-ray spectroscopy (EDS; Bruker Quantum 5030 SDD X-ray spectrometer) with SVE III pulse processing electronics. The surface areas and pore volumes were obtained from N₂ sorption isotherm at 77K using automatic adsorption equipment (Tristar II; Micrometrics). The photoluminescence spectra of the samples were investigated using a

Spectrofluorimeter (PL spectra; Horiba FluoroMax-4). The UV-Visible (UV-VIS) diffuse reflectance spectroscopy (DRS) of the dry-pressed disk samples was measured using a spectrophotometer (UV-VIS DRS; UV-2600 Shimadzu spectrophotometer) with BaSO₄ as the reference sample. The UV-VIS DRS values of the samples were used in estimating the Kubelka-Munk function $[F(R)E]^2$ as shown in equation (5.1) and then the bandgap values of the samples were estimated from the Tauc plot of $[F(R)hv]^{1/Y}$ vs hv [55,194,283]:

$$[F(R)hv]^{1/Y} = \left(\frac{(1-R)^2}{2R} * hv \right)^{1/Y} \quad (5.1)$$

$$K = (1-R)^2; \quad S = 2R; \quad Y = \frac{1}{2} \text{ or } 2; \quad hv \equiv \text{eV}.$$

Where K is the molar absorption coefficient, S is the scattering factor; h is the Planck constant, v is the photon's frequency and Y is a factor dependent on the nature of the electron transition and it is either 1/2 or 2 for the direct and indirect band gaps respectively.

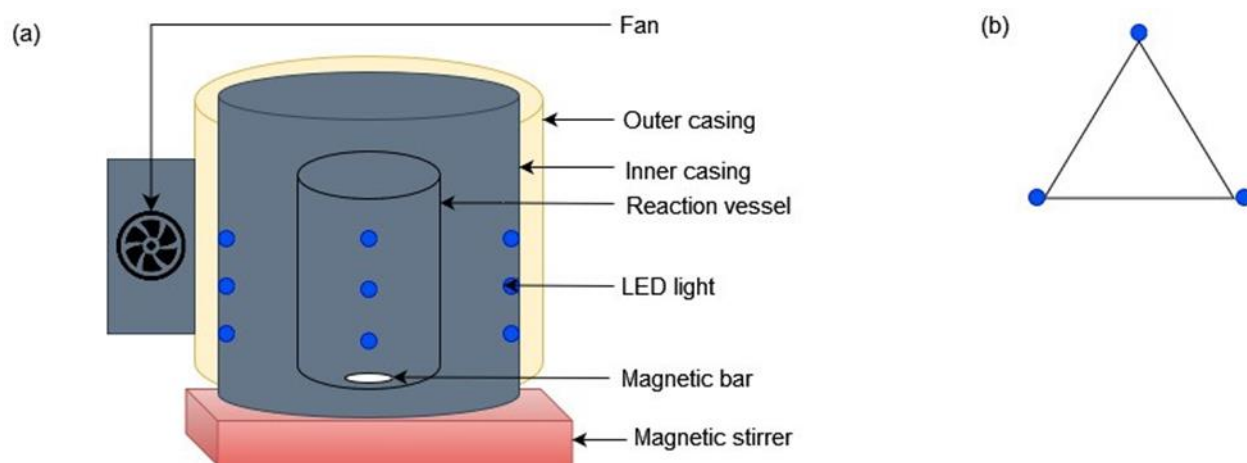


Scheme 5. 1 Synthesis process for GCN, ZnO-Cu nanoparticles, and GCN/ZnO-Cu nanocomposites.

5.5.6 Photoreactor

The royal blue LED photoreactor is fitted with LED lights in the blue region of the visible light as shown in [Scheme 5.2a](#). The LED lights are narrowband wavelength ($\lambda = 450$ nm) with a full-width half-maximum of 20 nm [194]. The outer casing is made of polyvinyl chloride (PVC) material while the inner casing is

made of reflective material that serves to minimize loss of light. A fan is fitted to the wall of the photoreactor in order to minimize temperature rise. There is a total of 9 LED lights that are arranged in groups of three vertically. The vertically arranged LED lights are of equal distance giving rise to a triangular pattern (Scheme 5.2b). This arrangement of the LED lights vertically and horizontally allows for uniform irradiation of the content in the reaction vessel.



Scheme 5. 2 Royal blue LED photoreactor

5.5.7 Photocatalytic degradation of 4-chlorophenol

The performance of the synthesized photocatalysts (GCN, ZnO, ZnO-Cu, and GCN/ZnO-Cu3%) was evaluated by testing the degradation of 4-chlorophenol (4-CP) under royal blue LED irradiation ($\lambda = 450\text{nm}$). In each experiment, 80 mg of the photocatalyst was dispersed in an 80 mL solution containing 5 mg/L 4-CP in a 100 mL beaker. Before irradiation, the solution/photocatalyst mixture was stirred continuously for 30 minutes in the dark to attain adsorption-desorption equilibrium. Immediately after, the light (royal blue LED) was turned on for the next 120 minutes while continuously stirring the mixture. The light intensity of royal blue LED entering the 80 mL solution was estimated to be 11.80×10^{17} photons/s using chemical ferrioxalate actinometry [149,194,277]. 3 mL of the mixture was taken at different irradiation intervals and filtered using a $0.45\ \mu\text{m}$ syringe filter (PTFE, Chromatographic Specialities Inc.,

Brockville, ON, Canada) to remove the photocatalyst particles. Control experiments were also conducted for all the synthesized photocatalysts for 120 minutes in the dark to determine the effect of the adsorption of 4-CP. Reusability experiments were conducted to determine the practical application of the synthesized photocatalyst using the optimal GCN/ZnO-Cu3% sample. At the end of each repeatability experiment, the photocatalyst was washed thoroughly with DI water and dried in the oven at 70 °C overnight for subsequent use.

The concentration of 4-CP was analyzed using high-performance liquid chromatography (HPLC; LC-2040C 3D Shimadzu Corporation, Japan) with UV absorbance detection at $\lambda = 280$ nm. The mobile phases were 0.1% phosphoric acid in HPLC-grade water and 0.1% phosphoric acid in acetonitrile at a 50:50 mixture with a flow rate of 1 mL/min. The measurements were conducted in duplicates and the detection limit was around 0.1 mg/L. The degradation efficiency and the rate constant using a pseudo-first-order equation were calculated as shown in equations (5.2) and (5.3) respectively:

$$\text{Degradation efficiency (\%)} = \left(\frac{C_o - C_t}{C_o} \right) * 100 \quad (5.2)$$

$$\ln \left(\frac{C_t}{C_o} \right) = -kt \quad (5.3)$$

Where C_o and C_t are the concentrations (mg/L) at time 0 and time t , k is the pseudo-first-order rate constant (min^{-1}) and t is time (min).

5.5.8 Photocatalytic disinfection of total coliforms in wastewater primary influent

Before conducting the disinfection experiment for total coliforms, the wastewater was first cultured. 50 mg of Luria broth was added to 1 L of wastewater sample in a 1 L jar. After inoculation, the jar was placed in an incubator at $35 \text{ }^{\circ}\text{C} \pm 0.5 \text{ }^{\circ}\text{C}$ for 24 h. The total coliforms cell density was determined by using the tray count procedure from IDEXX laboratories [284]. Briefly described, 0.5 mL of the incubated sample was

collected and added to 100 mL DI water in the 100 mL conical flask. 1 mL of the mixture in the conical flask was added to the mixture of DI water and colilert reagent in the colilert bottle. The mixture in the colilert bottle was poured in Quanti-tray/2000, sealed with IDEXX Quanti-tray sealer, and then placed in the incubator at $35\text{ }^{\circ}\text{C} \pm 0.5\text{ }^{\circ}\text{C}$ for 24 h. After 24 h, the result was read using the Most Probable Number (MPN) table. The total number of cells that turned yellow in the quanti-tray was counted which indicates the total coliforms in the wastewater. The initial cell density, that is average initial concentration, for total coliforms in the wastewater primary influent was calculated to be 2.8×10^5 MPN/100 mL.

For the disinfection experiment, 80 mg of the photocatalyst was added to 80 mL of wastewater and stirred with a magnetic stirrer while irradiating with royal blue LED. The light intensity of the royal blue LED entering 80 mL solution is the same as stated in section 2.7. 0.5 mL of the sample was collected at different time intervals and added to 100 mL DI water in the 100 mL conical flask. 1 mL was pipette from the mixture and added to the mixture of DI water and colilert reagent in the colilert bottle. The mixture in the colilert bottle was poured in Quanti-tray/2000, sealed with IDEXX Quanti-tray sealer, and then placed in the incubator at $35\text{ }^{\circ}\text{C} \pm 0.5\text{ }^{\circ}\text{C}$ for 24 h. After 24 h, the number of cells that turned yellow in the quantitrays was counted and read using the MPN table indicating the viable number of total coliforms in the wastewater.

Two types of control experiments were also conducted to estimate the concentration of the total coliforms, (a) in the dark using only photocatalysts, and (b) using royal blue LED only. For the total coliforms' experiments, the disinfection efficiency is expressed in log form was calculated from equation (5.4) as:

$$\text{Log reduction} = \log C_o - \log C_t \quad (5.4)$$

Where C_o and C_t are the concentrations of total coliforms at time 0 and time t, expressed as MPN/1000mL.

5.5.9 ROS identification

Radical trapping experiments were conducted to determine the active radicals involved in the photocatalytic degradation of 4-chlorophenol (4-CP). In the photocatalytic experiment, photogenerated electrons (e^-), photogenerated holes (h^+), superoxide radicals ($O_2^{\cdot-}$), and hydroxyl radicals (OH^{\cdot}) are generally believed to be generated and involved in a photocatalytic reaction. Four radical scavengers, potassium chromate (CrVI), ammonium oxalate (AO), p-benzoquinone (BQ), and isopropanol (IPA) were used as scavengers to quench e^- , h^+ , $O_2^{\cdot-}$, and OH^{\cdot} , respectively. During each experiment, 0.5 mM of the scavenger was added to the 80 mL solution containing 5 mg/L 4-CP before adding the photocatalyst and then the sample was collected as time $t = 0$. After the addition of the photocatalyst, the royal blue LED was turned on and samples were collected at different irradiation intervals. The concentrations of 4-CP in the samples were analyzed using HPLC to determine the effect of the reactive oxidation species (ROS) on 4-CP degradation.

5.5.10 Particle size distribution

Particle size analysis of the synthesized samples was determined by dispersing the samples in methanol. 10 mg of the sample was dispersed in 10 mL of methanol. The mixture was sonicated in an ultrasonic bath for 60 minutes and left to age by stabilizing for a day. The clear to opaque supernatant was collected using a pipette into a cuvette for particle size distribution analysis using Zetasizer ZS.

5.6 Results and discussions

5.6.1 XRD and Mean Crystallite Size (MCS)

The atomic and molecular structures of a crystal are determined using X-ray diffraction (XRD) analysis. The XRD patterns of the synthesized samples GCN, ZnO, ZnO-Cu3%, and GCN/0.1ZnO-Cu3% are presented in [Figure 5.1](#). Two typical peaks were observed for GCN. A dominant diffraction peak at 27.5°

corresponds to the 002 crystal plane and a weak diffraction peak at 13.3° corresponds to the 100 crystal plane. The presence of these two peaks indicates GCN nanosheet structure [285] while the 002 and 100 planes are associated with the interplanar stacking peak and the interlayer stacking of the conjugated hexagonal aromatic structure of GCN (JCPDS card number: 87-1526) [286]. The broad peaks observed on the 002 and 100 planes are due to the presence of strong electronegative heteroatom oxygen in the GCN structure caused by low polymerization [254]. The characteristic peaks of ZnO were observed at 32.2°, 34.8°, 36.6°, 48.0°, 57.0°, 63.4°, 68.4°, and 69.5° which correspond to 100, 002, 101, 102, 110, 103, 112, and 201 crystal planes. These diffraction peaks and planes are characteristic of the hexagonal wurtzite structure of ZnO (JCPDS card number: 36-1451) [287,288]. Slightly wide and shorter intensity peaks were observed for the ZnO-Cu3% XRD pattern compared to the ZnO peaks which can be attributed to the presence of Cu²⁺ in the ZnO structure. The presence of Cu as a dopant did not affect the ZnO crystalline structure because the ionic radius of Cu²⁺ which is 0.73 Å is similar to the ionic radius of Zn²⁺ which is 0.74 Å. Therefore, the peaks of ZnO and ZnO-Cu3% align as depicted by the dashed lines. In GCN/0.1ZnO-Cu3% XRD patterns, the ZnO-Cu3% peaks were observed but were greatly reduced and continued to reduce and eventually disappear at higher 2-Theta (degree). This shows the successful incorporation of the ZnO-Cu3% in the GCN structure and shows the significant quantity of GCN as opposed to ZnO-Cu3% in the GCN/0.1ZnO-Cu3% structure. The mean crystallite size of GCN, ZnO, ZnO-Cu3%, and GCN/0.1ZnO-Cu3% shown in Table 5.1 was calculated using the XRD patterns of the peaks and Scherrer's equation in equation (5.5). The crystallite size range for GCN/0.1ZnO-Cu3% nanocomposite is attributed to the presence of both GCN and ZnO-Cu3%. However, the reduced size of ZnO-Cu3% in the nanocomposite indicates that the ZnO-Cu3% is less agglomerated, indicating that the GCN provided stability to the ZnO-Cu3%. All the synthesized samples show that they are nanocrystals.

$$\tau = \frac{K\lambda}{\beta \cos\theta} \quad (5.5)$$

Where τ is the mean crystallite size (nm), K is a dimensionless shape factor which is typically 0.9, λ is the X-ray wavelength (nm), β is the broadening at half the maximum intensity also known as the full width at half maximum (FWHM), and Θ is the Bragg angle.

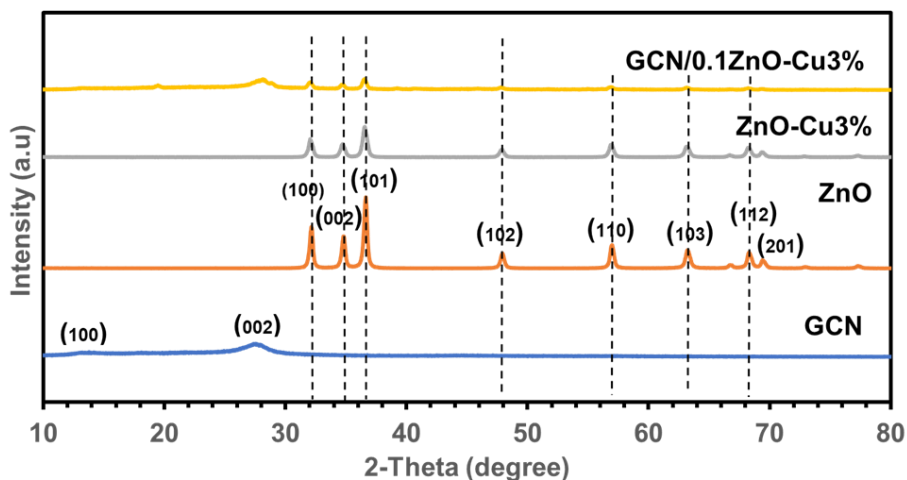


Figure 5. 1 XRD spectra patterns of GCN nanosheet, ZnO and ZnO-Cu3% nanoparticles, and GCN/0.1ZnO-Cu3% nanocomposite

Table 5. 1 Mean Crystallite Size (MCS) of GCN, ZnO and ZnO-Cu3% nanoparticles, and GCN/0.1ZnO-Cu3% nanocomposite.

Photocatalyst	Mean Crystallite Size (nm)
GCN	3.33
ZnO	34.23
ZnO-Cu3%	39.30
GCN/0.1ZnO-Cu3%	3.95 - 17.44

5.6.2 Average Particle Size (APS)

Particles are the result of the agglomeration of crystals. Particle size distribution and the average particle size were determined for GCN, ZnO, ZnO-Cu3%, and GCN/0.1ZnO-Cu3% as shown in Figure 5.2 and Table 5.2. All samples are observed to be in a nanoscale of less than 500 nm. GCN particles were distributed between 50 – 100 nm with 50% of the particles having a size of 68.43 nm. This confirms the widely reported 2D structure of GCN with one of its 3 dimensions in the x, y, and z planes less than 100 nm. The observed particle size distribution of ZnO is 150 – 400 nm with most of the particles (30%) having a size of 237.40 nm. This can be attributed to the aggregation of the ZnO particles due to the strong van der Waals intermolecular force of attraction usually exhibited by metal oxides [266]. The doping of ZnO with Cu in the ZnO-Cu showed a slight increase in the particle size with most particles (40%) at 263.50 nm. This increase in particle size is also reflected in the increase of the lower limit of particle size distribution between 200 – 400 nm. The incorporation of ZnO-Cu3% in the GCN/0.1ZnO-Cu3% resulted in the particle size distribution falling between that of GCN and ZnO-Cu3% at 125 – 225 nm with most particles (50%) being at 165.10 nm. The GCN stabilized the ZnO-Cu by inhibiting its aggregation and the formation of big particle sizes [266].

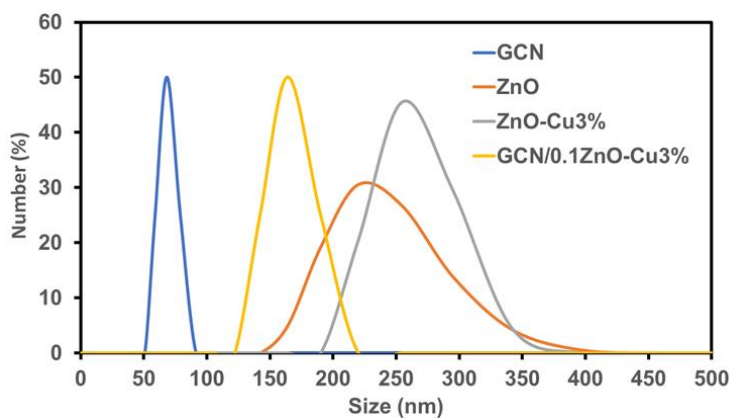


Figure 5. 2 Particle Size Distribution (PSD) of GCN nanosheet, ZnO and ZnO-Cu3% nanoparticles, and GCN/0.1ZnO-Cu3% nanocomposite.

Table 5. 2 Average Particle Size (APS) of GCN, ZnO and ZnO-Cu3% nanoparticles, and GCN/0.1ZnO-Cu3% nanocomposite

Photocatalyst	Average Particle Size (nm)
GCN	68.43
ZnO	237.40
ZnO-Cu3%	263.50
GCN/0.1ZnO-Cu3%	165.10

5.6.3 FT-IR

Fourier transform-infrared spectroscopy (FT-IR) was used as a technique to examine the functional groups and the chemical structure of the synthesized photocatalyst samples of GCN, ZnO, ZnO-Cu3%, and GCN/0.1ZnO-Cu3% as shown in [Figure 5.3](#). GCN shows three characteristic peaks at 3230 cm^{-1} , $1630 - 1230\text{ cm}^{-1}$, and 810 cm^{-1} . These peaks are indicative of the amine group (NH) stretching mode, C-N heterocycles stretching vibrational frequency, and triazine heterocycles vibrational mode, respectively [289,290]. Two distinctive peaks were observed for ZnO nanoparticles at 1034 cm^{-1} and 500 cm^{-1} which correspond to the stretching mode and the vibrational frequency respectively [289]. The doping of ZnO with Cu neither decreased the intensity nor altered the ZnO peaks in the ZnO-Cu3% nanoparticle. This is attributed to a very small fraction of Cu in the ZnO-Cu3% nanoparticles. All the peaks present in GCN were observed in the GCN/0.1ZnO-Cu3% nanocomposite. The peaks of ZnO-Cu3% were also observed in the nanocomposites but with reduced intensities which can be attributed to the small fraction in the GCN/0.1ZnO-Cu3% structure. The broadening and higher intensity of the peak at 3230 cm^{-1} of the nanocomposite as compared to GCN indicates a strong interaction between the GCN and the ZnO-Cu3% components of the nanocomposites [291].

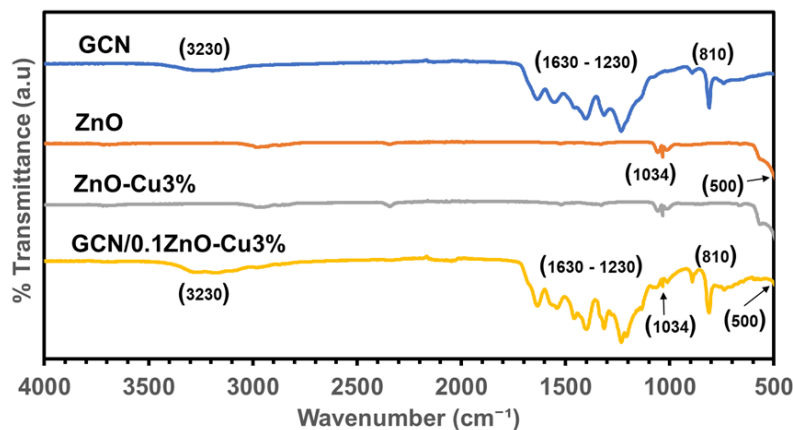


Figure 5. 3 FT-IR spectra patterns of GCN nanosheet, ZnO and ZnO-Cu3% nanoparticles, and GCN/0.1ZnO-Cu3% nanocomposite

5.6.4 SEM, TEM, and EDS

Scanning electron microscopy (SEM) is a morphology characterization technique that captures the surface image of a material. The SEM image of GCN, ZnO, ZnO-Cu3%, and GCN/0.1ZnO-Cu3% are given in [Figure 5.4](#). GCN displays sheet-like and flake-like structures rather than a particle. ZnO shows spherical-like structures of different sizes. The structure of the ZnO-Cu3% nanoparticle remained similar to ZnO due to the small amount of Cu in the nanoparticle. The GCN/0.1ZnO-Cu3% nanocomposite shows the presence of the sheet-like and flake-like structures of GCN and the sphere-like structure of the ZnO-Cu3% which is indicative of the successful interaction between GCN and ZnO-Cu3% components of the nanocomposite. Transmission electron microscopy (TEM) which is a technique used to probe the inside of a material was further used to validate the SEM morphology of the synthesized photocatalysts as shown in [Figure 5.5](#). GCN shows a thin-layered sheet-like structure. The ZnO and the ZnO-Cu3% nanoparticles show sphere-like shapes confirming what was observed in the SEM images. In the GCN/0.1ZnO-Cu3% nanocomposites, the sphere-like structure of the ZnO-Cu3% can be seen to be embedded in the thin-layered sheet-like structure of the GCN, indicating that the GCN served as a base for the ZnO-Cu3% and therefore a successful

formation of a nanocomposite. The elemental composition of the samples using electron dispersive x-ray spectroscopy (EDS) was conducted and the results are shown in [Figure 5.6](#). The EDS of GCN shows the presence of C, N, and O peaks which are indicative of a typical GCN derived from urea. The presence of strongly electronegative heteroatom oxygen in the GCN structure can serve to trap photogenerated electrons as a dopant thereby enhancing its photocatalytic activity when compared to other GCN derived from melamine and dicyandiamide [194,254,292]. The presence of Zn and O was confirmed for ZnO while for ZnO-Cu3% the elements of Zn, O, and Cu were confirmed. The C, N, O, Zn, and O peaks were confirmed for GCN/0.1ZnO-Cu3% nanocomposites. However, the peaks of C, N, and O in the nanocomposite were significantly reduced when compared to the bulk GCN. This is attributed to the presence of ZnO and Cu in the nanocomposite.

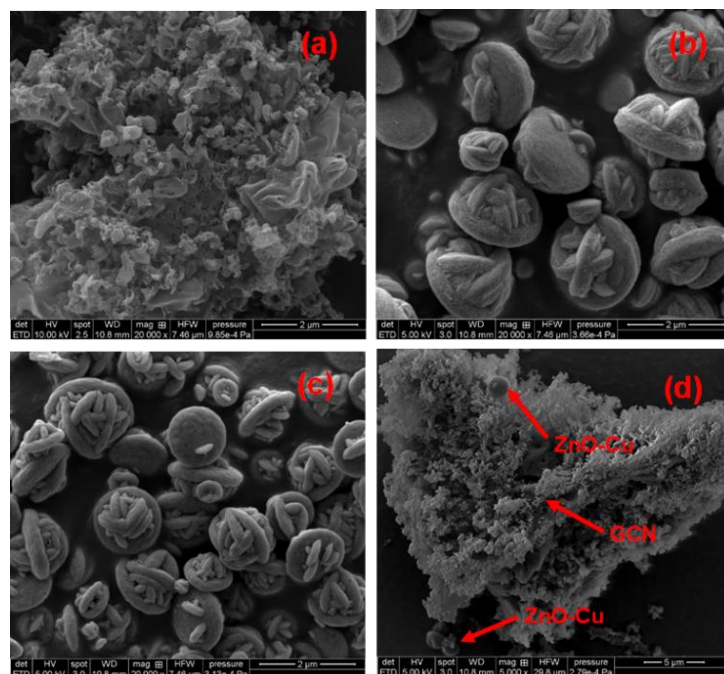


Figure 5. 4 SEM images: (a) GCN nanosheet, (b) ZnO nanoparticles, (c) ZnO-Cu3% nanoparticles, and (d) GCN/0.1ZnO-Cu3% nanocomposite

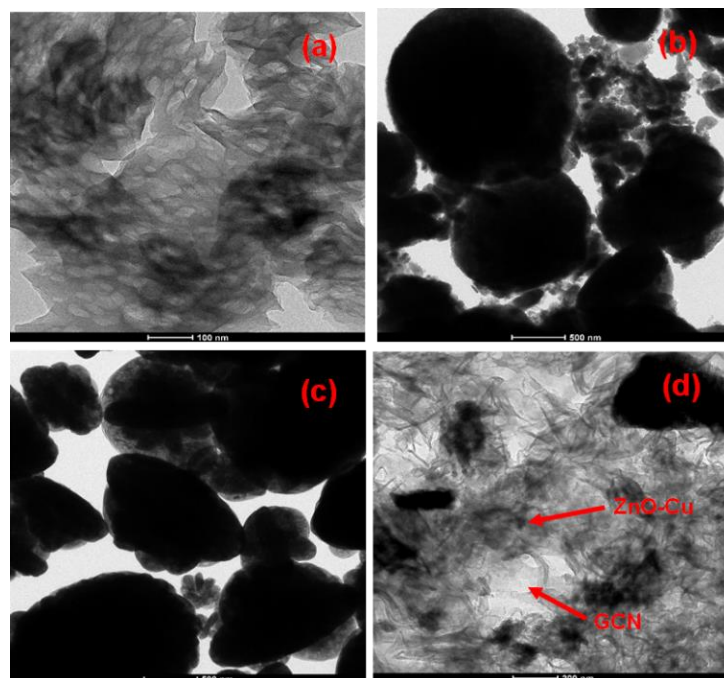


Figure 5. 5 TEM images: (a) GCN nanosheet, (b) ZnO nanoparticles, (c) ZnO-Cu3% nanoparticles, and (d) GCN/0.1ZnO-Cu3% nanocomposite

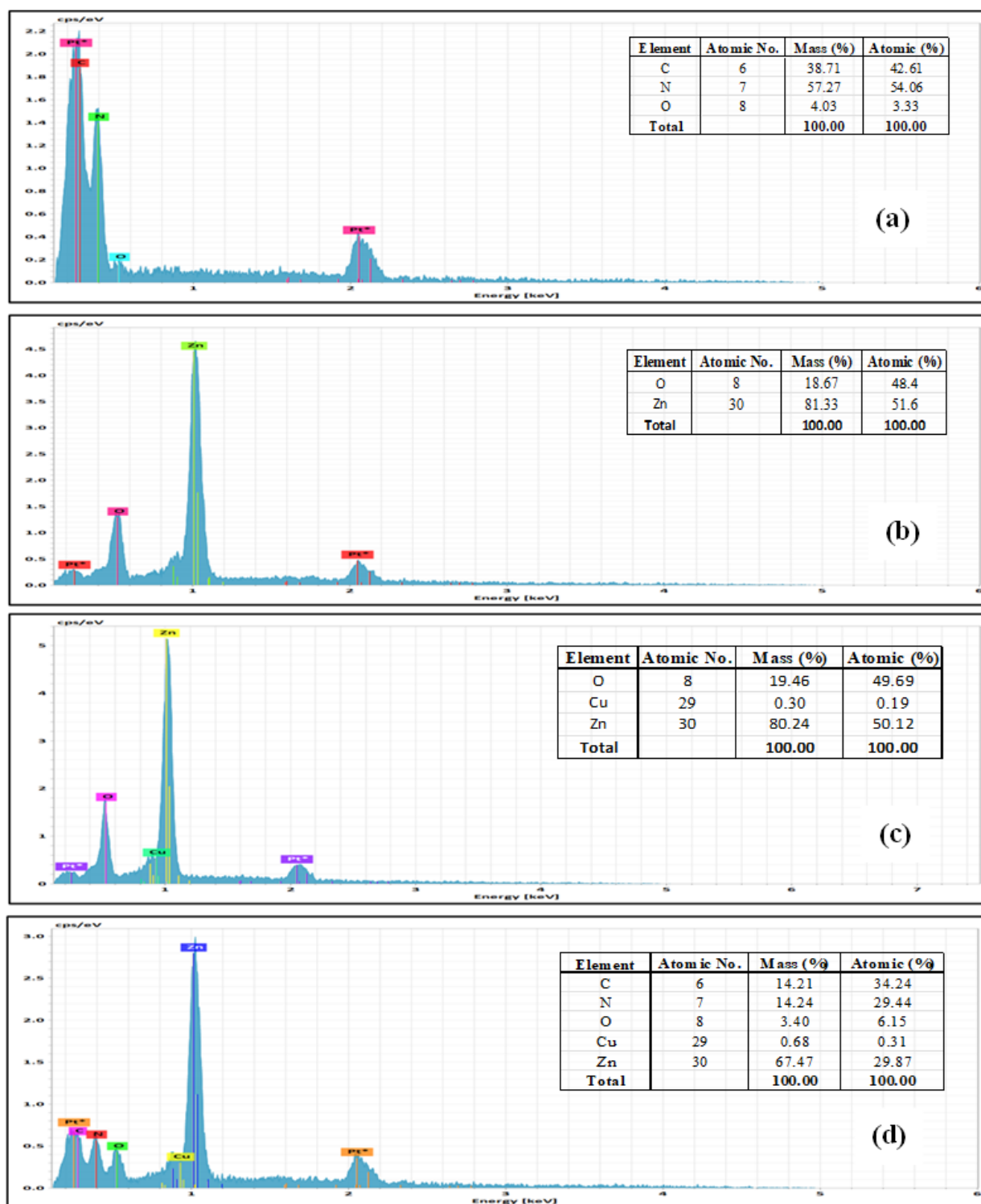


Figure 5. 6 EDS images: (a) GCN nanosheet, (b) ZnO nanoparticle, (c) ZnO-Cu3% nanoparticle, and (d) GCN/0.1ZnO-Cu3% nanocomposite.

5.6.5 BET surface area, BJH pore volume, and BJH average pore size

The N₂-adsorption analysis was carried out to determine the Brunauer-Emmett-Teller (BET) surface area, and the Barret-Joyner-Halenda (BJH) for pore volume and average pore size of the synthesized photocatalyst. The N₂ adsorption results of GCN, ZnO, ZnO-Cu3%, and GCN/0.1ZnO-Cu3% are shown in [Figure 5.7](#) and [Table 5.3](#). In [Figure 5.7a](#), all the photocatalysts display a type IV isotherm with an H3 hysteresis loop indicating a mesoporous structure according to the IUPAC classification [293,294]. In [Figure 5.7b](#), the mesoporous structure of the photocatalysts is confirmed with all of them having pore sizes less than 10 nm. The average pore size of the photocatalysts is shown in Table 3. From [Table 5.3](#), the GCN has a surface area of 57.17 m²/g as compared to the surface area of ZnO of 5.18 m²/g. This indicates that the GCN should be significantly more photocatalytically active than ZnO since the high surface area is an important component of photocatalytic reaction. The surface area of ZnO-Cu3% of 4.26 m²/g is slightly smaller than that of ZnO. This can be attributed to the incorporation of Cu in the ZnO lattice structure. The surface area of the GCN/0.1ZnO-Cu3% nanocomposite is the highest at 121.00 m²/g. This is attributed to the synthesis process involving calcination. With regards to the pore volume, the pore volumes of ZnO and ZnO-Cu3% are the same and this is attributed to the low fraction of Cu in the ZnO-Cu3% nanoparticles. The pore volume of GCN/0.1ZnO-Cu3% is 0.12 cm³/g as compared to GCN's 0.06 cm³/g showing that it doubled. The high surface area and high pore volume of GCN/0.1ZnO-Cu3% are expected to lead to greater photocatalytic activity than other photocatalysts.

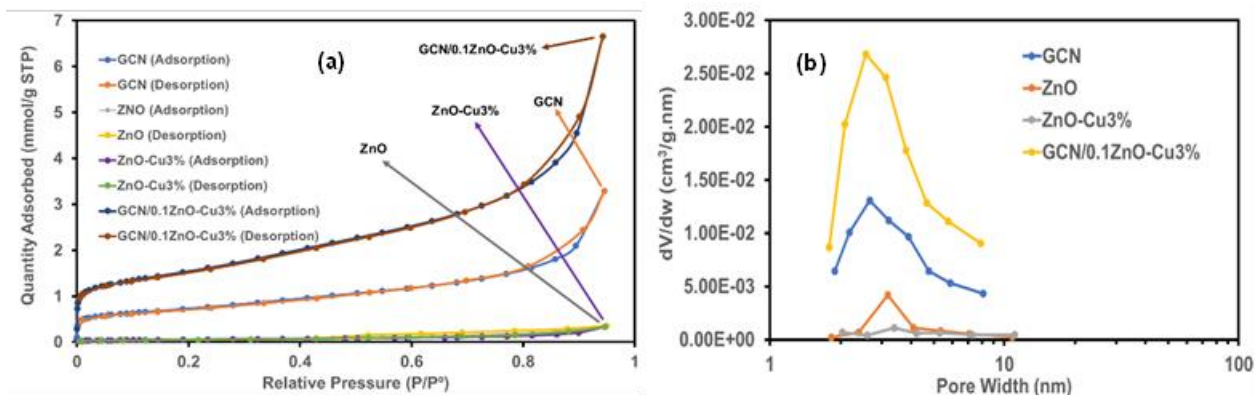


Figure 5. 7 (a) BET surface area and (b) BJH pore size distribution, of GCN nanosheet, ZnO and ZnO-Cu3% nanoparticles, and GCN/0.1ZnO-Cu3% nanocomposites

Table 5. 3 BET surface area, BJH pore volume, and BJH average pore size.

Photocatalyst	BET Surface Area (m^2/g)	BJH Pore Volume (cm^3/g)	BJH Average Pore Size (nm)
GCN	57.17	0.06	4.15
ZnO	5.18	0.01	4.41
ZnO-Cu3%	4.26	0.01	5.80
GCN/0.1ZnO-Cu3%	121.00	0.12	4.02

5.6.6 PL spectra

Photoluminescence (PL) spectral analysis is a technique used to determine the recombination intensity of the photogenerated electron-hole pair in a photocatalyst [295–297]. The PL spectra of GCN, ZnO, ZnO-Cu3%, and GCN/0.1ZnO-Cu3% were determined at an excitation wavelength of 360 nm and emission wavelengths in the visible region of the electromagnetic spectrum (400 – 650 nm) (see Figure 5.8). It is observed that ZnO nanoparticles did not show significant emission in the visible region. This is because ZnO is essentially a UV-sensitive photocatalyst [264]. The emission intensity of ZnO-Cu3% nanoparticles reduced slightly when compared to ZnO. This is attributed to the defects created by the incorporation of Cu in the ZnO lattice structure which serves as an electron-trapping agent by inhibiting the rate of electron-

hole pair recombination and promoting photocatalytic activity. The GCN was observed to show the highest emission intensity indicating a high rate of recombination of electron-hole pair. The heterostructure GCN/0.1ZnO-Cu3% nanocomposite showed a reduction in the emission intensity when compared to GCN. This can be attributed to the presence of ZnO-Cu3% in the nanocomposite structure which serves as a trapping agent to the photogenerated electrons from GCN. This reduced emission intensity means inhibition of the recombination of the electron-hole pair and therefore the nanocomposite is expected to have a better photocatalytic performance than GCN.

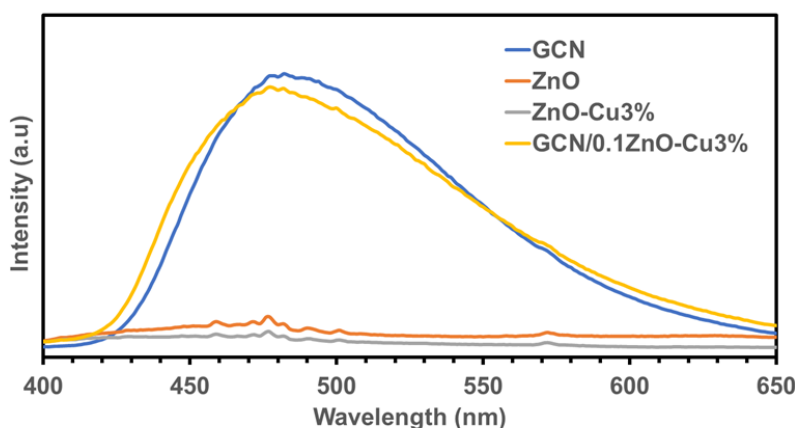


Figure 5. 8 PL spectra patterns of GCN nanosheets, ZnO and ZnO-Cu3% nanoparticles, and GCN/0.1ZnO-Cu3% nanocomposite.

5.6.7 UV-Vis DRS and Bandgap estimation

The ultraviolet-visible diffuse reflectance spectroscopy (UV-Vis DRS) was used to understand the optical behaviour of the photocatalyst. The bandgap was estimated using the UV-Vis DRS data and Tauc plot [283,298,299]. The results of UV-Vis DRS and bandgap estimation using Tauc plot for GCN, ZnO, ZnO-Cu3%, and GCN/0.1ZnO-Cu3% are presented in [Figure 5.9](#) and [Table 5.4](#). In [Figure 5.9a](#) and [Table 5.4](#), all the photocatalysts have their absorption edge below 480 nm which indicates that they can absorb light

in the visible region. ZnO and ZnO-Cu3% have absorptions at 428 nm and 435 nm as compared to GCN and GCN/0.1ZnO-Cu3% which have higher absorptions at 459 nm and 478 nm. This means that ZnO and ZnO-Cu3% can absorb lesser visible light energy. It was observed that the incorporation of ZnO-Cu3% into GCN to form the heterostructure GCN/0.1ZnO-Cu3% nanocomposites improved its visible light absorption capacity from 458 nm to 478 nm. Overall, this means that all the photocatalysts can absorb light energy (UV and visible) with a wavelength lower than their wavelength absorption edges. The proposed order of optical activity of the photocatalysts is $\text{GCN/0.1ZnO-Cu3\%} > \text{GCN} > \text{ZnO-Cu3\%} > \text{ZnO}$. The corresponding bandgaps of the wavelength adsorption edges estimated in [Figure 5.9b](#) are given in [Table 5.4](#). The ZnO with the highest bandgap of 2.90 eV indicates poor visible light utilization capacity. This is because the higher the bandgap the poorer the visible light sensitivity of the photocatalyst. The bandgap of ZnO-Cu3% improved slightly by reducing to 2.85 eV. The presence of Cu in the ZnO-Cu3% nanoparticles serves as a trapping agent for the photogenerated electrons from the ZnO. The bandgap of 2.70 eV recorded for GCN is typical as the bandgap of GCN is also reported by others to be between 2.70 eV – 2.80 eV [194,254,292]. The bandgap range of GCN indicates that it is visible light-sensitive. The heterostructure GCN/0.1ZnO-Cu3% showed even a smaller bandgap of 2.60 eV when compared to that of GCN. This indicates improved visible light energy utilization perhaps due to the synergistic effects of GCN and ZnO-Cu3%. Overall, it means that the photocatalysts can absorb energy from light (UV and visible) higher than their bandgap energy. The proposed order of optimal activity of the photocatalysts in terms of bandgap energy is $\text{GCN/0.1ZnO-Cu3\%} > \text{GCN} > \text{ZnO-Cu3\%} > \text{ZnO}$.

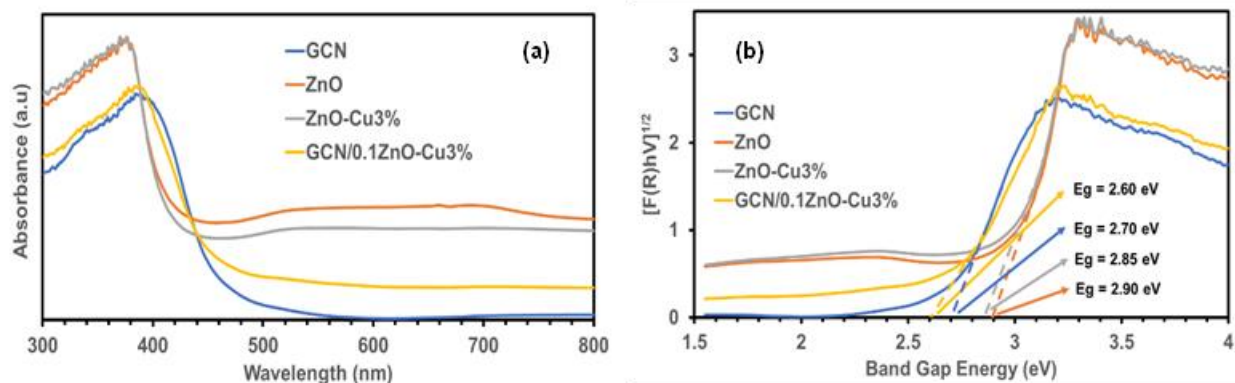


Figure 5. 9 (a) UV-Vis DRS and (b) Band gap, of GCN nanosheet, ZnO and ZnO-Cu3% nanoparticles, and GCN/0.1ZnO-Cu3% nanocomposite

Table 5. 4 Bandgaps and the corresponding wavelengths of GCN nanosheets, ZnO and ZnO-Cu3% nanoparticles, and GCN/0.1ZnO-Cu3% nanocomposite

Photocatalyst	Bandgap Energy (eV)	Wavelength (nm)
GCN	2.70	459
ZnO	2.90	428
ZnO-Cu3%	2.85	435
GCN/0.1ZnO-Cu3%	2.60	478

5.6.8 Photocatalytic degradation of 4-Chlorophenol

ZnO and ZnO-Cu nanoparticles were first synthesized, and their photocatalytic performance was evaluated against 4-chlorophenol (4-CP) under royal blue LED ($\lambda = 450$ nm) for 120 minutes as shown in [Figure 5.10a](#). The ZnO shows the least amount of 4-CP (2.06%) was photocatalytically degraded. The degradation of 4-CP was observed to increase and then decrease with the incorporation of Cu into the ZnO structure as follows: ZnO-Cu1% (6.99%), ZnO-Cu3% (9.13%), and ZnO-Cu5% (5.41%). The initial increase and subsequent decrease in 4-CP degradation as the Cu fraction increased can be attributed to the reduction of active sites available for photocatalytic activity beyond ZnO-Cu3% [300]. Another factor that contributed to the poor photocatalytic performance of ZnO and ZnO-Cu nanoparticles is the poor visible light sensitivity because of the wider bandgap ([Table 5.4](#)) [301]. To enhance the photocatalytic activity of ZnO-Cu nanoparticles such as surface area, active sites, and bandgap, the optimally performing ZnO-Cu3% was then coupled with a narrow bandgap, visible-light sensitive photocatalyst, GCN to form heterojunction GCN/ZnO-Cu3% nanocomposites.

The photocatalytic performance of the GCN/ZnO-Cu nanocomposites was evaluated (see [Figure 10b](#)). The GCN/ZnO-Cu3% nanocomposites showed better photocatalytic performance than ZnO, ZnO-Cu3%, and GCN. 36.88% of 4-CP was photocatalytically degraded by GCN and GCN performed better than ZnO and ZnO-Cu nanoparticles. The high photocatalytic performance of GCN compared to ZnO and ZnO-Cu nanoparticles is due to its high surface area and visible-light responsive bandgap ([Tables 5.3 and 5.4](#)) [302]. The photocatalytic performance of the GCN/ZnO-Cu3% nanocomposites was observed to decrease with an increasing fraction of ZnO-Cu3%. The amount of 4-CP photocatalytically degraded by these nanocomposites are GCN/0.1ZnO-Cu3% (65.1%), GCN/0.3ZnO-Cu3% (42.85%), and GCN/0.5ZnO-Cu3% (38.59%). This decrease in photocatalytic activity by the composites can be attributed to an increased fraction of ZnO-Cu3% and the agglomeration in the composite resulting in reduced surface area and active

sites [303,304]. The pseudo-first-order rate constants of all photocatalysts were calculated and included in [Figure 5.10c](#). The highest rate constant was observed for GCN/0.1ZnO-Cu3% among all photocatalysts and GCN/ZnO-Cu3% nanocomposites which is $0.85 \times 10^{-2} \text{ min}^{-1}$ while the lowest was ZnO which is $0.007 \times 10^{-2} \text{ min}^{-1}$. The ZnO-Cu3% has the highest rate constant of all the ZnO-Cu3% nanoparticles which is $0.09 \times 10^{-2} \text{ min}^{-1}$. The GCN also exhibited a high rate constant at $0.38 \times 10^{-2} \text{ min}^{-1}$. This infers that GCN/0.1ZnO-Cu3% is 2.2 times better than GCN, 9.4 times better than ZnO-Cu3%, 121 times better than ZnO, and 1.8 times better than the sum of the individual GCN and ZnO-Cu3%. Therefore, this indicates the synergistic effect of GCN/0.1ZnO-Cu3% nanocomposites as shown by the surface area and bandgap ([Tables 5.3 and 5.4](#)). The adsorption experiments for all photocatalysts were also conducted for 120 minutes in the dark and the results compared to that photocatalytic performance as shown in [Figure 5.10d](#). It shows that none of the photocatalysts adsorb 4-CP, indicating that the degradation of 4-CP was only due to photocatalysis [194].

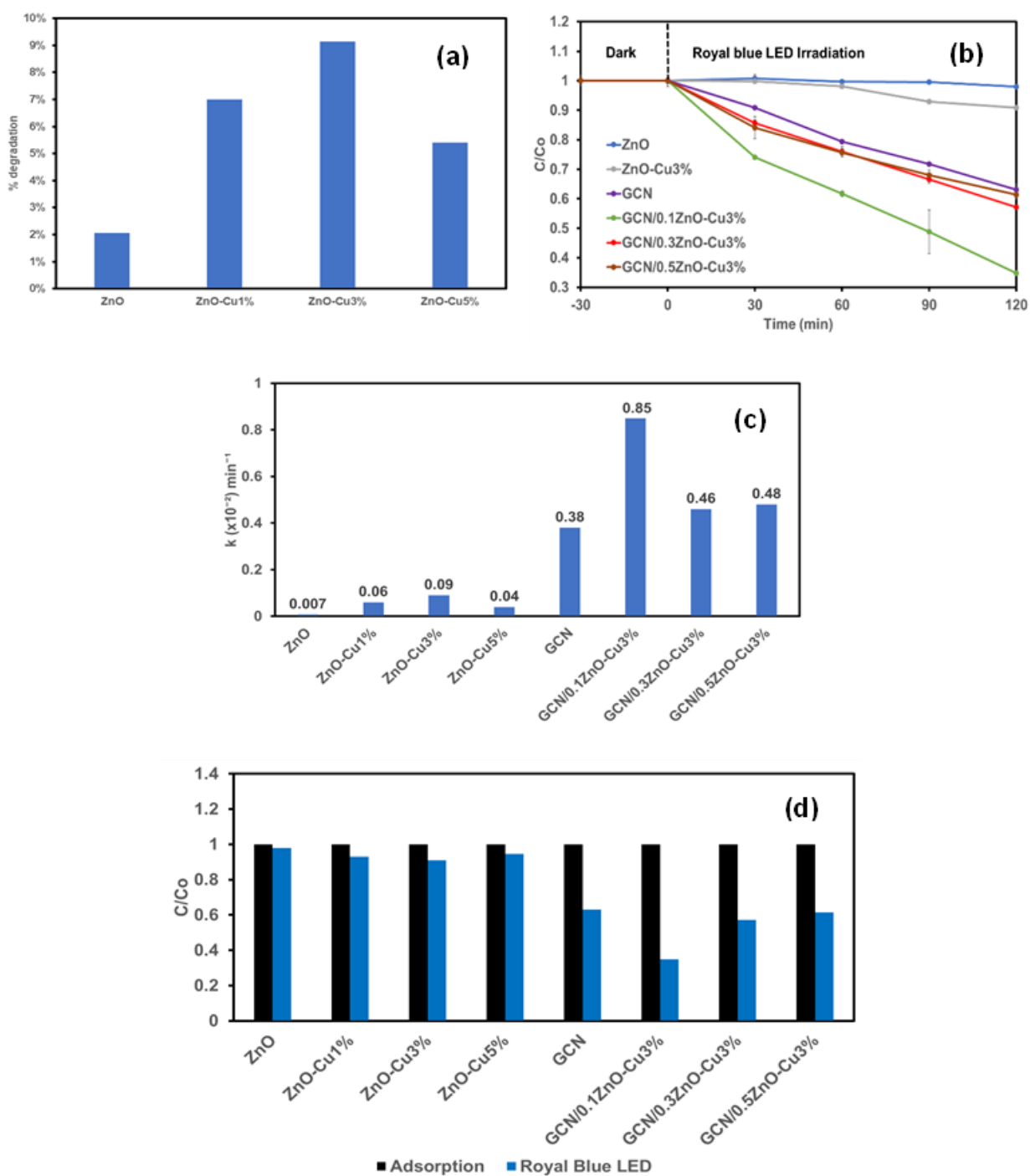


Figure 5. 10 (a) Photocatalytic degradation performance of ZnO and ZnO-Cu composites, (b) Photocatalytic degradation performance of GCN nanosheet, ZnO and ZnO-Cu nanoparticles, and GCN/ZnO-Cu nanocomposite, (c) Rate constant of all the synthesized photocatalysts, and (d) Comparison between photocatalytic degradation and adsorption (in the dark) performances of the synthesized photocatalysts.

5.6.9 Reactive Oxidation Species (ROS) trapping experiment

ROS experiments were to determine the active radicals that are responsible for the photocatalytic process. The ROS experiments for the commonly known radicals, e^- , h^+ , $O_2^{\cdot-}$, and OH^{\cdot} responsible for 4-CP degradation were conducted using the optimally performing photocatalyst GCN/0.1ZnO-Cu3% under royal blue LED irradiation. The results are presented in Figure 5.11. To determine these active radicals, the following scavengers were employed potassium chromate (Cr (VI)), ammonium oxalate (AO), p-benzoquinone (BQ), and isopropanol (IPA) for the following radicals, e^- , h^+ , $O_2^{\cdot-}$, and OH^{\cdot} , respectively. Scavengers are trapping agents used to remove the radicals (e^- , h^+ , $O_2^{\cdot-}$, and OH^{\cdot}) [305–308]. After 120 minutes, the IPA had the highest inhibition to the degradation of 4-CP giving a degradation of 24.48%. The lowest inhibition to 4-CP degradation was Cr (VI) with the most degradation of 45.78%. This indicates that the hydroxyl radical (OH^{\cdot}) which is scavenged by IPA is the dominant radical responsible for most of the photocatalytic degradation while e^- which is scavenged by Cr (VI) is the least involved. The order of reactivity from the most involved to the least involved in the photocatalytic degradation is $OH^{\cdot} > h^+ > O_2^{\cdot-} > e^-$.

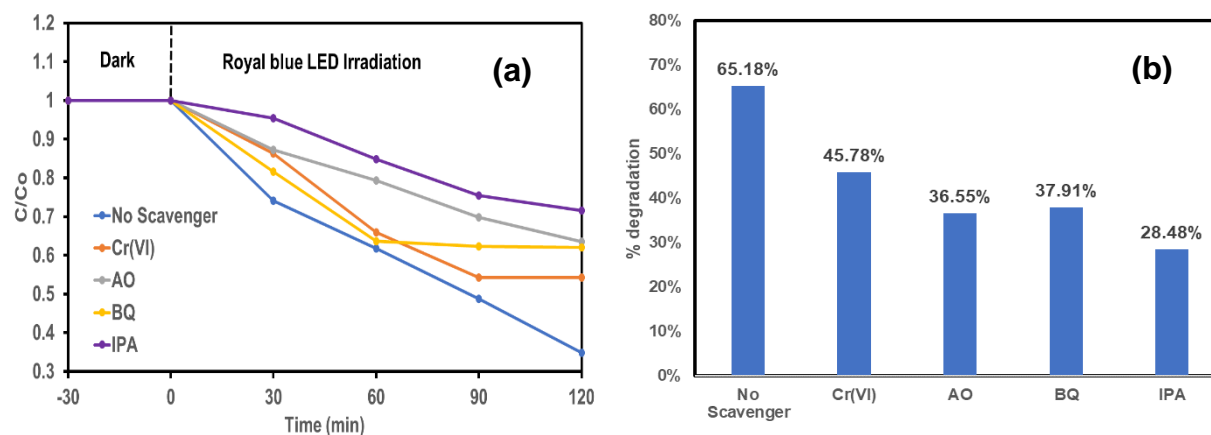


Figure 5. 11 ROS Experiment for the active species for the photocatalytic degradation of 4-CP by GCN/0.1ZnO-Cu nanocomposite.

5.6.10 Reusability experiment and stability test

The reusability experiment and stability test were conducted to determine the practical application of the synthesized photocatalyst. The optimally performing photocatalyst, GCN/0.1ZnO-Cu3% was used for these experiments on 4-chlorophenol (4-CP) degradation under royal blue LED irradiation, and 4 cycles were carried out as presented in Figure 5.12. In Figure 5.12a, the result shows a slight decline in 4-CP degradation between the 1st and 2nd cycles which is from 65.18% to 60.17%. However, no significant decline was observed for 4-CP degradation after the 2nd cycle. In the 3rd and the 4th cycles, 4-CP degradation was 60.03% and 59.09%. This decline between the 1st and the 4th cycles is because of the loss of photocatalyst mass during the process of washing several times with DI water and drying in the oven overnight at 70 °C between cycles. Further characterization of the used GCN/0.1ZnO-Cu3% was examined after the 4th cycle using XRD analysis to determine its stability (see Figure 5.12b). The XRD of the used and fresh GCN/0.1ZnO-Cu3% nanocomposites were compared. All peaks present in the fresh sample were observed in the used sample. No obvious shifts in peaks were observed. However, the peak intensities in the used samples appear stronger than in the fresh sample. This is indicative of higher crystallinity and more ordered structure which could be due to the washing and drying of the nanocomposite between each cycle of the experiment. Therefore, the GCN/0.1ZnO-Cu3% can be said to be stable and fit for practical application.

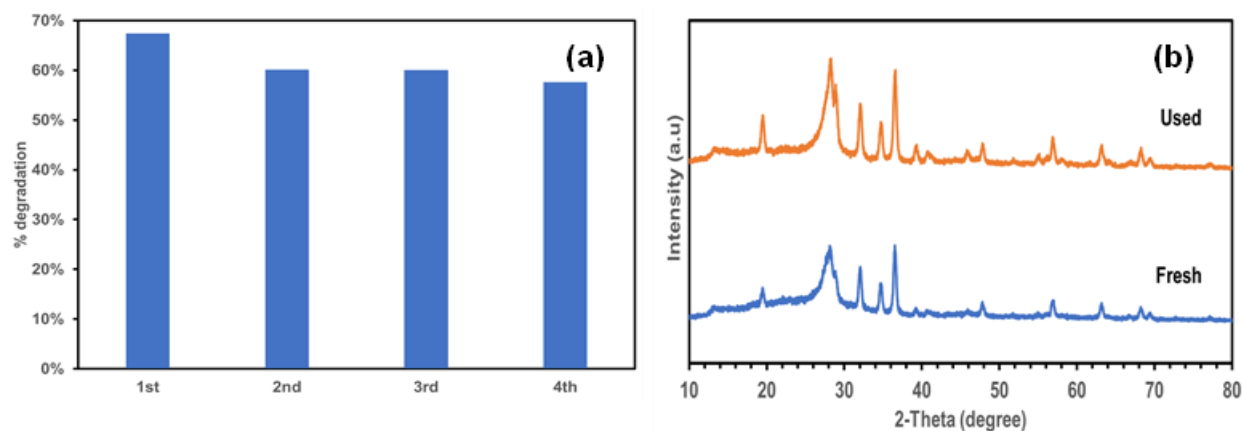


Figure 5. 12 (a) Reusability experiment and (b) Stability test (XRD analysis), of GCN/0.1ZnO-Cu3% after the 4th cycle.

5.6.11 Photocatalytic disinfection of wastewater primary influent

The antibacterial performance of GCN, ZnO, ZnO-Cu3%, and GCN/0.1ZnO-Cu3% in the dark and under royal blue LED irradiation were examined on wastewater primary influent for 360 minutes as shown in Figure 5.13. In Figure 5.13a, it was observed that the photocatalysts showed negligible disinfection in the dark during the adsorption experiments. This suggests that the synthesized photocatalysts show low cytotoxicity towards total coliforms present in the wastewater primary influent in the absence of visible light. ZnO, ZnO-Cu3%, and GCN/ZnO-Cu3% resulted in 0.19, 0.28, and 0.29 log reduction of total coliforms in the dark. This was expected because ZnO and Cu are known to have antimicrobial activity even without illumination [309,310]. GCN exhibited negligible disinfection in the dark. GCN is not known to have a cytotoxicity effect on bacteria in the dark as demonstrated in several publications including our previous work [277,311]. In Figure 5.13b, the royal blue LED had a negligible effect in disinfecting total coliforms. In our previous work, it was demonstrated that royal blue LED showed negligible disinfection effect on coliforms in the wastewater secondary effluent [277]. This is because royal blue LED, a narrowband visible light source ($\lambda = 450$ nm) does not possess sufficient energy that could significantly inactivate the coliforms. It is known that bacteria are largely disinfected in the UV region of the electromagnetic spectrum especially UV-C which is at a lower wavelength and very high photon energy [312,313]. GCN showed a slight log reduction of about 0.14 log which can be attributed to the photogenerated electrons and holes, and radical species thereby causing oxidative stress to the coliforms and loss of metabolic activity. As expected, ZnO showed a higher log reduction than GCN with a 0.45 log reduction of total coliforms under royal blue LED irradiation. This is attributed to the combined effects of ZnO cytotoxicity and the generation of radicals and photogenerated electrons and holes under royal blue LED irradiation that induced oxidative stress and loss of metabolic activity in the coliforms. The doping of ZnO with Cu in the ZnO-Cu3% nanoparticles slightly increased the disinfection of the total coliforms to a 0.49 log reduction. This slight increase even though small is attributed to the very small fraction of Cu in the nanoparticle. A complete 5.5 log reduction of total coliforms in the wastewater primary influent was

observed for GCN/0.1ZnO-Cu3% after 360 minutes. This significant response of total coliforms to disinfection can be attributed to the synergistic effect of the nanocomposite and the antimicrobial activity of ZnO and Cu. This synergistic effect is evident in the significant increase of the surface area, reduced bandgap of the nanocomposite, and improved visible light utilization. In the nanocomposite, more oxidative stress, and perturbation of the metabolic process of the coliforms developed because of the generation of more radicals, photoexcited electrons and holes, and the presence of cytotoxic ZnO and Cu. Radicals such as superoxide radicals ($O_2^{\cdot-}$) and hydroxyl radicals (OH^{\cdot}) are known to inhibit the metabolic process of microorganisms which eventually leads to the cause of inactivation [314]. Therefore, it indicates that the heterojunction structure of GCN/0.1ZnO-Cu3% under visible light irradiation can disinfect total coliforms in wastewater.

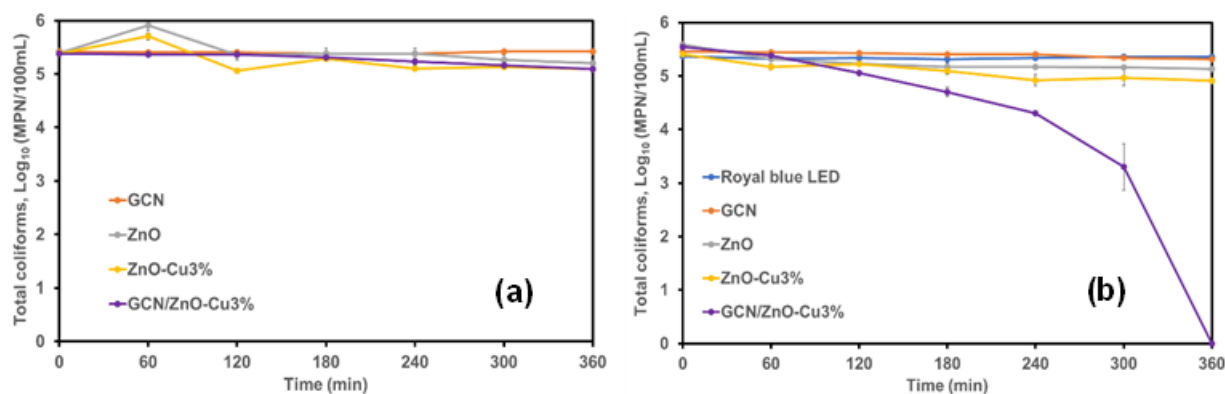


Figure 5. 13 (a) Disinfection of wastewater primary influent by the synthesized photocatalysts in the dark, (b) Photocatalytic disinfection of wastewater primary influent by the synthesized photocatalysts under visible light irradiation (Royal blue LED).

5.6.12 Proposed photocatalytic mechanism

The active species, e^- , h^+ , O_2^- , and OH^- have been identified to be involved in the photocatalytic degradation of 4-chlorophenol (4-CP) as described in section 3.9. [Scheme 5.3](#) depicts the proposed photocatalytic degradation mechanism of 4-CP using the optimally performing heterojunction GCN/0.1ZnO-Cu3% nanocomposite under royal blue LED irradiation based on the identified active species. It was observed that the mechanism is of type II heterojunction structure photocatalyst [315]. The sequence of the photocatalytic redox reactions involved in the mechanism is given in equations (5.8) to (5.14). The conduction band (CB) and the valence band (VB) potentials of GCN and ZnO were calculated based on equations (5.6) and (5.7) [194,316–318]:

$$E_{CB} = X - E^e - 0.5E_g \quad (5.6)$$

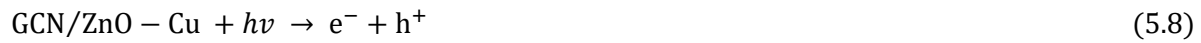
$$E_{VB} = E_{CB} + E_g \quad (5.7)$$

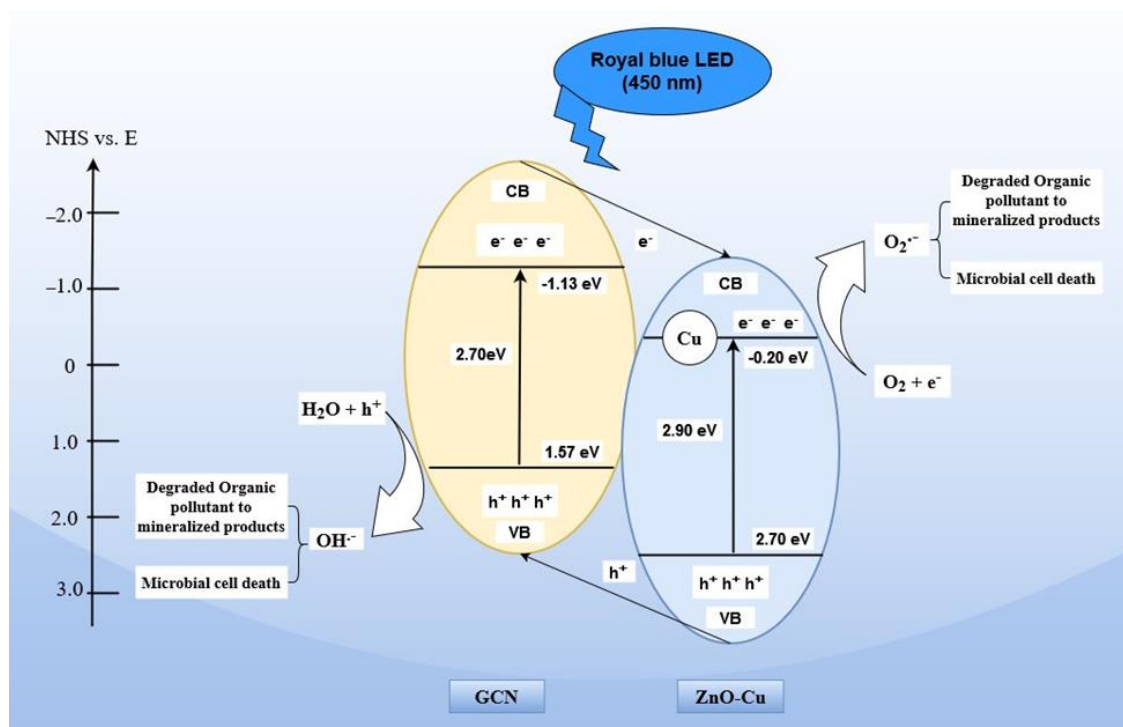
Where E_{CB} and E_{VB} are conduction band and valence band potentials, E^e is free electron energy on a hydrogen scale (~ 4.50 eV), E_g is the bandgap energy ([Table 5.4](#)), and X is the absolute electronegativity of the semiconductor, which is based on the geometric mean of the constituent atoms, which for GCN is 4.72 eV [194,319] and for ZnO is 5.75 eV [320]. Therefore, the calculated CB and VB for GCN are -1.13 eV and 1.57 eV while the calculated CB and VB of ZnO are -0.20 eV and 2.70 eV.

In the observed type II heterojunction structure photocatalytic mechanism, the irradiation of GCN/0.1ZnO-Cu3% generates photoexcited electron-hole (e-h) pairs on the GCN and ZnO-Cu3% components. The photogenerated electrons migrate from the valence band (VB) to the surface of the conduction band (CB) and thereby creating photogenerated holes in the VB. The electrons from the CB of GCN migrate toward

the CB of ZnO. This is because the CB of GCN has a higher negative potential (-1.13 eV) than the CB of ZnO-Cu3% (-0.20 eV). Similarly, the holes from the VB of ZnO migrate towards the VB of GCN because the VB of ZnO has a higher positive potential (2.70 eV) than the VB of GCN (1.57 eV). The Cu dopant in the ZnO acts as an interface and helps to facilitate electron transfer from GCN to ZnO thereby inhibiting the recombination rate of the electron-hole (e-h) pairs in the GCN. The electrons on the surface of the ZnO-Cu3% react and reduce the dissolved oxygen (O₂) in the mixture absorbed on its surface to generate a superoxide radical (O₂^{•-}). This is because the CB level of ZnO (-0.20 eV vs. NHS) is more negative than O₂/O₂^{•-} (-0.18 eV vs. NHS) [162,321]. Likewise, the holes on the surface of ZnO that migrate to the surface of GCN oxidize the absorbed water molecule on the GCN to generate hydroxyl radical (OH[•]). The reason is that the VB level of ZnO (2.70 eV vs. NHS) is more positive than the H₂O/OH[•] (2.40 eV vs. NHS) [162]. The photogenerated electrons and holes and the superoxide and the hydroxy radicals can react, oxidize, and degrade the 4-CP to mineralized products such as CO₂, H₂O, and HCl [194]. Various intermediates have been identified in the photocatalytic degradation of 4-CP to mineralized products using LC-MS analysis and they include hydroquinone, benzoquinone, phenol, and 4-chlorocatechol [88,171–173]. These by-products, which are hydroxylated intermediates, are formed during the oxidation of 4-CP.

A similar mechanism can be assumed and proposed for the photocatalytic disinfection of total coliforms in wastewater as also depicted in [Scheme 5.3](#). This is because the same light source and photocatalyst were used. The generated reactive oxygen species (ROS) and the cytotoxicity of ZnO-Cu in the nanocomposite can lead to oxidative stress by attaching and breaking up to the cell wall, reacting with and denaturing proteins, inhibiting metabolic processes and causing eventual bacterial death [309].





Scheme 5. 3 Schematic representation of the proposed mechanism for the photocatalytic degradation of 4-CP and the photocatalytic disinfection of total coliforms in wastewater primary influent.

5.7 Conclusions

GCN/ZnO-Cu nanocomposite was synthesized using a novel and facile synthesis process, the co-exfoliation method. The nanocomposite was characterized using different techniques such as XRD, FT-IR, BET, PL spectra, TEM, SEM, EDS, and UV-Vis DRS. The bandgap was calculated from the UV-Vis DRS data and estimated using the Tauc plot. The coupling of ZnO-Cu with GCN enhanced the performance of the

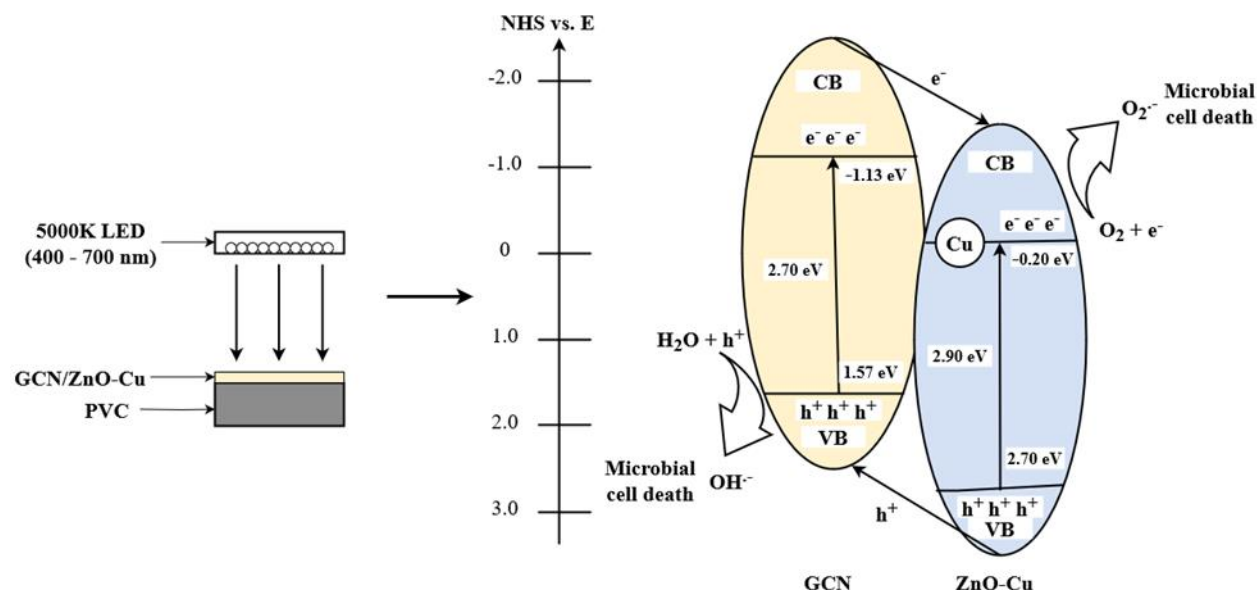
nanocomposite in the photocatalytic degradation of 4-CP and the photocatalytic disinfection of total coliforms. Of all the synthesized GCN/ZnO-Cu nanocomposites, the optimum ratio was achieved with GCN/0.1ZnO-Cu3%. The optimally performing photocatalyst, GCN/0.1ZnO-Cu3% was able to degrade 65.18% of 4-CP in 120 minutes when compared to GCN (36.88%), ZnO-Cu3% (9.13%), and ZnO (2.06%). The result shows that the doping of ZnO with Cu enhanced its photocatalytic activity in the ZnO-Cu3% nanoparticle. A complete 5.5 log reduction was achieved with GCN/0.1ZnO-Cu3% when compared to < 1 log reduction for GCN, ZnO, and ZnO-Cu3%. The characterization results validate these experimental results. The BET surface, Bandgap and PL spectra of the nanocomposite improved drastically which explains the improved photocatalytic activity. The BET surface area of the nanocomposite was 120 m²/g compared to GCN (57.17 m²/g) and ZnO-Cu3% (4.26 m²/g). The bandgap of the nanocomposite was (2.60 eV) compared to GCN (2.70 eV) and ZnO-Cu3% (2.85 eV). The PL spectra showed reduced emission intensity when compared to GCN. All these experimental and characterization observations and results indicate that the nanocomposite inhibited the rate of recombination of e-h pairs, improved charge separation, and ultimately enhanced its visible light response and utilization for the degradation of 4-CP and the disinfection of total coliforms in wastewater primary influent. The ROS experiment of the reactive species indicates that the hydroxyl radical (OH[•]) was the dominant species. The nanocomposite displayed stability in its practical application after the 4th cycle. Therefore, the GCN/ZnO-Cu nanocomposite can be used for practical applications in the disinfection of wastewater and the degradation of organic pollutants under sunlight, UV, and visible light.

Chapter 6: Evaluation of the performance of self-disinfecting coated surface with GCN/ZnO-Cu nanocomposite under 5000K LED visible light

6.1 Highlights

- Synthesis of GCN/ZnO-Cu nanocomposite by a novel facile synthesis method, co-exfoliation.
- Dip coating of PVC substrate using a novel facile mixture of nanocomposite, binder, and solvent.
- Use of 5000K LED visible light source used in commercial and industrial settings for photocatalysis experiments.
- Hydroxyl radical was determined to be the dominant reactive oxygen species (ROS) responsible for self-disinfecting photocatalysis.
- Reusability experiments showed that the coating was stable, and the efficiency of the disinfection depends on the light intensity and thickness of the coating layer.

6.2 Graphical abstract



6.3 Abstract

The search for low-cost and less labour-intensive self-disinfecting coated surfaces with minimal environmental impact is increasingly gaining attention. In this work, the GCN/ZnO-Cu₃% nanocomposite was synthesized by a novel facile co-exfoliation method. The coatings of the polyvinyl chloride (PVC) plastics were prepared by dipping the cleaned PVC substrate into a simple slurry mixture of the nanocomposite, ethanol, and adopted readily-available, cheap, environmentally friendly water-based polyurethane (PU) wood lacquer. Different characterization techniques such as XRD, SEM, EDS, FTIR, AFM, PL spectra, and UV-Vis DRS were conducted for the coated and uncoated PVC substrates to study the crystallinity, morphology, elemental composition, chemical structure, roughness, and optoelectronic properties. The band gap of the coated and uncoated PVC substrates was estimated from the UV-Vis DRS values and Tauc plots. The surface area of powered samples was also estimated. Under the visible light, 5000K LED (400–700 nm), the coated PVC denoted Coated PVC (GCN/ZnO-Cu₃%) showed excellent self-disinfecting performance of 2-log reduction (99% disinfection) of coliforms-containing wastewater

primary influent in 120 minutes. The ROS experiment showed that all the radicals (e^- , h^+ , O_2^- , and OH^\cdot) were strongly involved in the disinfection by the coated PVC surface but the OH radical was observed to be the dominant species and a plausible antibacterial mechanism was proposed on this basis. Reusability experiments were conducted and minimal loss in photocatalytic and antimicrobial activity of the coated surface was observed indicating the suitability of the coated surface for practical application.

6.4 Introduction

Pathogen infections have been identified to occur through the following transmission pathways namely, hands of health care practitioners (HCP), water, and air [322,323]. Dr. Weinstein, over 20 years ago, observed and estimated that the source of pathogens of health-care-related pathogens was cross infection via HCP is between 20% to 40% and the environment is 20% [324]. In the succeeding years, significant scientific evidence shows that contamination of environmental surfaces in the hospital now plays an important role in the transmission of health-care-related pathogens such as *Staphylococcus aureus* (*S. aureus*) and *Escherichia coli* (*E. coli*) [323,325].

The frequently used methods of decreasing the frequency and level of contamination of surfaces include the application of germicide (e.g., chitosan) [326] and the no-touch method (UV-C light, vaporized hydrogen peroxide) [327]. The limitation of chemical germicide is that it is labour intensive since it requires routine cleaning and disinfection of surfaces and less than 50% of the surfaces are adequately cleaned and disinfected [328,329]. The limitation of the no-touch method is that it can only be applied in rooms or places with no people and high room turnover [327].

Recently, self-disinfecting coated surfaces is increasingly gaining attention as an alternative method of decreasing the frequency of contaminated surfaces. The self-disinfecting coated surfaces are also referred

to as “contact killing” since microbial killing requires contact with the coated surface. Surfaces can either be impregnated or coated with heavy metals (specific gravity greater than 5) [330]. Since antiquity, some heavy metals are known to possess antimicrobial activity. Some of these heavy metals with antimicrobial activity are silver (Ag), gold (Au), Bismuth (Bi), Copper (Cu), Titanium (Ti), and Zinc (Zn). Semiconductors such as TiO_2 , ZnO , and MgO have been reported to have antimicrobial activity [331–333]. However, the drawback of these semiconductor photocatalysts is that it is essentially UV active due to their very wide bandgap ranging between 3.2 – 3.5 eV [194,253,261–263,334]. To overcome this drawback, these semiconductors can be doped with heavy metals to make them visible-light active and thus used as self-disinfecting coatings. Lin et al. coated TiO_2 on a polyvinyl chloride (PVC) substrate and the *E. coli* was completely disinfected under UV irradiation for 90 minutes [335]. Khan et al. coated Venetian blinds and glass substrates with Ag-TiO_2 to disinfect *P. aeruginosa* and *B. subtilis* under fluorescent light tubes and reported almost complete disinfection for both bacteria on the coated substrates in 120 minutes [336]. Liu et al. coated Cu-TiO_2 on a glass substrate and reported the 6.5-log reduction of a virus, bacteriophage under white light bulbs in 120 minutes [337].

Graphitic carbon nitride (GCN or $\text{g-C}_3\text{N}_4$), a 2D polymeric semiconductor photocatalyst is increasingly being used for research primarily due to its visible-light activity owing to its moderate bandgap of 2.7 – 2.8 eV [271]. GCN can be coupled with semiconductors such as ZnO and silver compounds to form GCN heterojunctions to enhance their visible light activity. While a lot of research has reported on the photocatalytic activity of GCN heterojunctions in disinfecting wastewater and microorganisms in synthetic water under visible light irradiation [277,338–341], few works have been done on coating surfaces with GCN or GCN heterojunctions for self-disinfecting purposes under the action of visible light irradiation. Hou et al. immersed coated stainless-steel substrate with PANI/GCN heterojunction in synthetic water containing *E. coli* and *S. aureus* under a Xenon lamp and reported 96.5% and 95.3% disinfection respectively in 30 minutes [342].

In this work, PVC coating with GCN/ZnO-Cu nanocomposite was developed by dip coating into a novel and simple mixture of GCN/ZnO-Cu nanocomposite, ethanol, and adopted, cheap, readily-available, environmentally-friendly, water-based polyurethane (PU) lacquer. The coated PVC substrates were characterized using different techniques to determine the structure and optoelectronic properties. The antimicrobial performance of the coated PVC substrates was evaluated under a visible light source, 5000K light-emitting diode (LED) (400 – 700 nm) for practical application and dropping a small quantity of coliforms-containing wastewater primary influent on the coated PVC substrate. 5000K LED, one of the LEDs, is expressed in Kelvin (K) which is a measure of colour temperature. It is used indoors such as in industrial spaces, factories, surgery, and exam rooms due to its brightness, compact size, low energy consumption, directionality, and extended lifetime. Reactive Oxygen Species (ROS) experiments were conducted to determine the dominant reactive species. For practical application, reusability experiments were also conducted.

6.5 Materials and Methods

6.5.1 Chemicals

Polyvinyl chloride (PVC)-($\text{C}_2\text{H}_3\text{Cl}$)_n was purchased from Grainger Canada (Calgary, AB, Canada). Polyurethane (water-based brand, Varathane) was purchased from Home Depot (Calgary, AB, Canada). Urea- $\text{CH}_4\text{N}_2\text{O}$ ($\geq 99.5\%$), isopropanol- $\text{C}_3\text{H}_8\text{O}$ ($\geq 99.5\%$), p-benzoquinone- $\text{C}_6\text{H}_4\text{O}_2$ ($\geq 98\%$), potassium chromate- K_2CrO_4 ($\geq 99\%$), and ammonium oxalate- $(\text{NH}_4)_2\text{C}_2\text{O}_4$, were purchased from Sigma-Aldrich Co. (St. Louis, MO, USA). Copper II nitrate hemi (pentahydrate)- $\text{Cu}(\text{NO}_3)_2 \cdot 2.5\text{H}_2\text{O}$ ($\geq 98\%$) was purchased from Alfa-Aesar (Ward Hill, MA, USA). Zinc sulfate heptahydrate- $\text{ZnSO}_4 \cdot 7\text{H}_2\text{O}$ was purchased from EM Science (Gibbstown, NJ, USA). Ethanol (absolute) was purchased from EMD Millipore Corp. (Burlington, MA, USA). Total coliforms/E.coli test kit was purchased from IDEXX laboratories Inc. (Westbrook, ME, USA). Sodium citrate tribasic- $\text{Na}_3\text{C}_6\text{H}_5\text{O}_7$ was purchased from CHEMCO (Port Louis, Mauritius).

Municipal wastewater primary influent was obtained from Advanced Canadian Water Assets-ACWA (Calgary, AB, Canada), a full-scale testing facility embedded in a wastewater treatment plant in Calgary, Alberta. Visible light (5000K LED) was provided by Nemalux Industrial (Calgary, AB, Canada).

6.5.2 Synthesis of GCN

Graphitic carbon nitride (GCN) was synthesized from urea by direct pyrolysis as described in our previous work [194]. In brief, 50 g of urea was placed in a crucible and calcined in a muffle furnace (550-58, Fisher Scientific, Waltham, MA, USA) for 4 h at 550 °C. The obtained pale-yellow material was labeled GCN.

6.5.3 Synthesis of GCN/ZnO-Cu nanocomposites

ZnO-Cu sample was synthesized using chemical co-precipitation [269,270]. 2.8756 g (50 mM) of zinc sulfate heptahydrate ($\text{ZnSO}_4 \cdot 7\text{H}_2\text{O}$) was added to 200 mL deionized (DI) water in different 400 mL beakers. An equivalent concentration of 50 mM (2.5806 g) of sodium tribasic- $\text{Na}_3\text{C}_6\text{H}_5\text{O}_7$ was added to the mixture as a stabilizing agent. While continuously stirring the solution, copper II nitrate hemi pentahydrate, $\text{Cu}(\text{NO}_3)_2 \cdot 2.5\text{H}_2\text{O}$ of 3% as a function of the mass of $\text{ZnSO}_4 \cdot 7\text{H}_2\text{O}$ was added to the beakers. The solution was heated while stirring on a hotplate at 70 °C for 15 minutes. This was followed by a dropwise addition of 100 mL of 200 mM NaOH. The solution was continuously stirred at 70 °C for 2 h as the colour changed from an initial pale blue to an opaque bluish milky slurry. The solution was allowed to cool down while being continuously stirred. It was then vacuum filtered using a 0.45 μm filter and washed thoroughly with DI water to remove excess NaOH. The sample was air-dried overnight and later calcined at 550 °C for 3 h. The calcined sample was left to cool down, ground, and labeled as ZnO-Cu3%.

The GCN/ZnO-Cu sample was synthesized using the novel facile co-exfoliation method as described in our previous work. Briefly, 1 g of GCN was added to 50 mL of ethanol (absolute) in a petri dish and then sonicated for 1 h to achieve uniform dispersion. While continuously stirring on a magnetic stirrer, 0.1 g of ZnO-Cu3% was added to the mixture and sonicated for another 0.5 h. The mixture was dried in the oven at

70 °C overnight after continuously stirring for 2 h. The dried sample was calcined at 550 °C for 4 h and left to cool down in the furnace to room temperature. The resulting pale-yellow sample was ground and labeled GCN/ZnO-Cu3%.

6.5.4 Fabrication of PVC coatings

PVC substrates of 2 x 2 cm² were prepared by cleaning with ethanol and deionized (DI) water for 15 min each in an ultrasonic bath and then dried in the air at room temperature. To prepare the novel and simple slurry mixture for the coating, 200 mg of GCN/ZnO-Cu3% nanocomposite photocatalyst was added to the mixture of 10 mL ethanol (absolute) and 3 mL of polyurethane (PU) water-based lacquer. The mixture was sonicated for 2 h for uniform dispersion of the photocatalyst in the mixture. The cleaned PVC substrates were dipped into the mixture 4 times to achieve a thicker and uniform spread, after which the coatings were allowed to dry in the air at room temperature and labeled Coated PVC (GCN/ZnO-Cu3%) as shown in [Scheme 6.1a](#). Coatings of PVC using GCN photocatalyst and PU (without photocatalysts) were also carried out and labeled Coated PVC (GCN) and Coated PVC (PU) respectively. The PU acts as a binding agent of the photocatalyst to the PVC substrate while the ethanol serves to reduce the thickness of the mixture to allow for uniform spread and a thin layer of the coat on the PVC substrate.

6.5.5 Characterization

Characterizations were conducted for coated and uncoated PVC substrates. The crystallinity of the coated and uncoated PVCs was studied using X-ray diffraction (XRD; Rigaku multiflex X-ray diffractometer) with Cu K α X-ray radiation, $\lambda = 1.5406 \text{ \AA}$. The chemical and bonding structures of the coated and uncoated PVCs were studied using Fourier transform-infrared spectroscopy (FT-IR; Bruker Vertex 70). The outer morphology of the coated and uncoated PVCs was examined by scanning electron microscope (SEM; Quanta FEG 250 FESEM). The elemental analysis of the coated and uncoated PVCs was conducted using energy-dispersive X-ray spectroscopy (EDS; Bruker Quantum 5030 SDD X-ray spectrometer) with SVE

III pulse processing electronics. The roughness of the coated and uncoated PVCs was examined using atomic force microscopy (AFM; Bruker Nano wizard IV). The photoluminescence spectra of the coated and uncoated PVCs were investigated using Spectrofluorimeter (PL spectra; Horiba FluoroMax-4). The UV-Visible (UV-VIS) diffuse reflectance spectroscopy (DRS) of coated and uncoated PVCs was measured using a spectrophotometer (UV-VIS DRS; UV-2600 Shimadzu spectrophotometer) with BaSO₄ as the reference sample. The Kubelka-Munk function was calculated from the UV-VIS DRS values and then the bandgap values were estimated from the Tauc plot. [194,283,343]. The surface areas (BET) of the powdered samples of GCN and GCN/ZnO-Cu3% were also conducted and obtained from N₂ sorption isotherm at 77K using automatic adsorption equipment (Tristar II; Micrometrics).

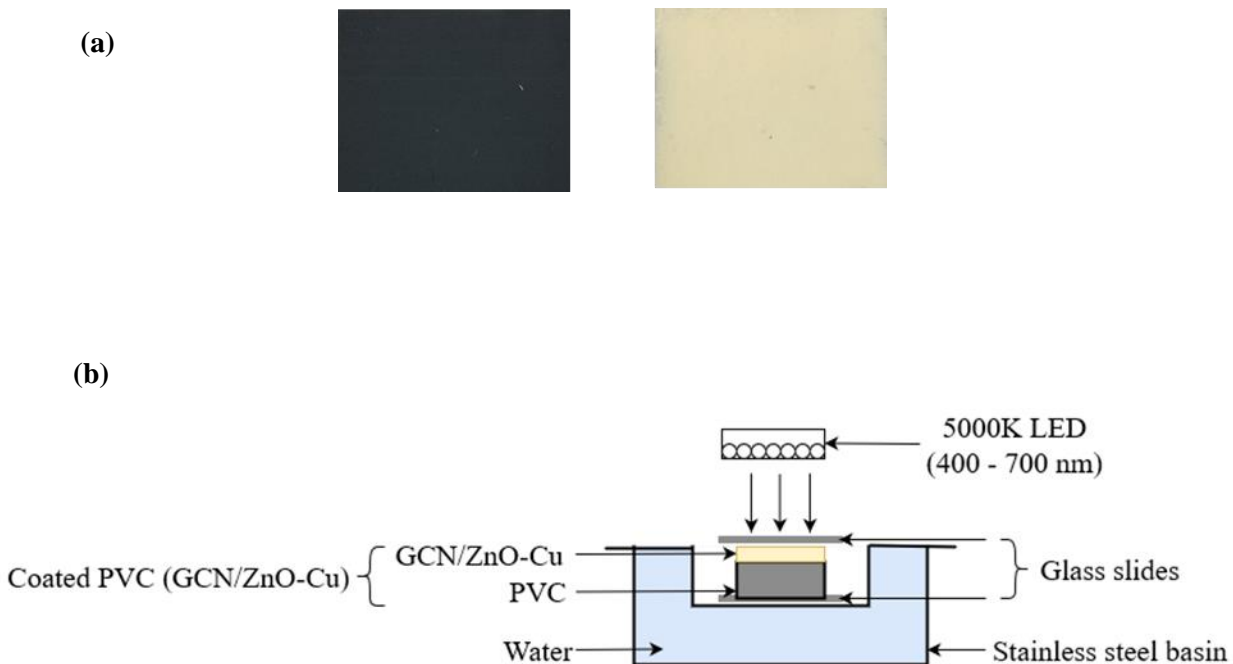
6.5.6 Photocatalytic self-disinfecting experiments of coated PVC

Before conducting experiments, 50 mg of Luria broth was added to 1 L of wastewater sample in a 1 L jar to culture the wastewater and then placed in an incubator at 35 °C ± 0.5 °C for 24 h. The total coliforms cell density was determined by using the tray count procedure from IDEXX laboratories [284]. Briefly described, the wastewater was serially diluted 50 times by taking 1 mL of the wastewater from the 1 L jar and adding it to 49 mL of deionized (DI) water in a 100 mL quartz beaker and then stirring to attain a homogenous mixture. 20 µL of the mixture was collected, dropped on a coated PVC, and further dropped into the mixture of 100 mL DI water and colilert reagent in a colilert bottle. The mixture was shaken to achieve homogeneity and poured in Quanti-tray/2000 without allowing the coated PVC to drop in the quantitrays, sealed with IDEXX Quanti-tray sealer, and then placed in the incubator at 35 °C ± 0.5 °C for 24 h. The result was read using the Most Probable Number (MPN) table. The total number of cells that turned yellow in the quanti-tray was counted which indicates the total coliforms in the wastewater. The initial cell density for total coliforms in the wastewater primary influent was calculated to be 2.2 x 10⁶ MPN/100 mL. For the self-disinfecting experiment, the coliforms-containing primary influent wastewater was serially diluted 50 times by taking 1 mL from the wastewater stock solution in the 1 L jar and adding it to 49 mL

of DI water in a 100 mL quartz beaker bottle. For the sample, 20 μ L was taken from the mixture and dropped on the Coated PVC (GCN/ZnO-Cu3%). [Scheme 6.1b](#) shows the experimental setup for the self-disinfecting experiment. The sample was placed between microscopic glass slides to allow for uniform spread and maximum contact of the coliforms-containing wastewater with the coated surface. The sample with the glass slides was placed in a stainless steel basin. This basin was placed in another stainless steel basin filled with water. This allows for uniform temperature throughout the experiment. The 5000K LED light (400 – 700 nm) at 10 cm to the PVC and estimated intensity of 16,800 Lux was turned on. The sample was collected at different irradiation interval and dropped in a mixture of 100 mL DI water and colilert reagent in a 100 mL colilert bottle and then shaken for homogeneity. The mixture was poured in a quantitray 2000 without allowing the coated PVC to drop in the quantitray, sealed with IDEXX Quantitray sealer, and then placed in the incubator at $35\text{ }^{\circ}\text{C} \pm 0.5\text{ }^{\circ}\text{C}$ for 24 h. After 24 h, the total number of cells that turned yellow in the quanti-tray was counted which indicates the total coliforms in the wastewater remaining. Several control experiments were also conducted to estimate the disinfection of the total coliforms, (a) in the dark using Coated PVC (GCN/ZnO-Cu3%), Coated PVC (GCN), Coated PVC (PU), and Uncoated PVC, and (b) under 5000K LED using Coated PVC (PU), Coated PVC (GCN), and Uncoated PVC. Reusability tests were conducted to determine the practical application of the coated PVC. The coated PVC was washed with DI water and allowed to dry in the air at room temperature overnight before reuse. For the self-disinfecting experiments, the disinfection efficiency is expressed in log form was calculated from equation (6.1) as:

$$\text{Log reduction} = \log C_o - \log C_t \quad (6.1)$$

Where C_o and C_t are the concentrations of total coliforms at time 0 and time t, expressed as MPN/1000mL.



Scheme 6. 1 (a) Uncoated PVC and Coated PVC (GCN/ZnO-Cu) and (b) Schematic representation of the experimental setup.

6.5.7 ROS identification

Reactive Oxygen Species (ROS) experiments were conducted to determine the active radicals involved in the self-disinfecting coated PVC substrate. Photogenerated electrons (e^-), photogenerated holes (h^+), superoxide radicals ($O_2^{\cdot-}$), and hydroxyl radicals (OH^{\cdot}) are generally believed to be involved in a photocatalytic reaction. Four radical scavengers, potassium chromate (CrVI), ammonium oxalate (AO), p-benzoquinone (BQ), and isopropanol (IPA) were used as scavengers to quench e^- , h^+ , $O_2^{\cdot-}$, and OH^{\cdot} , respectively. During each experiment, 0.5 mM of the scavenger was added to the 50 mL of the wastewater primary influent and then the mixture was stirred for homogeneity. 20 μ L was taken from the mixture and then dropped on the coated PVC substrate, Coated PVC (GCN/ZnO-Cu3%). The 5000K LED was turned on and the irradiated coated PVC was collected at different time intervals, treated, and analyzed to determine the ROS involved in the disinfection of the drop of coliforms-containing wastewater primary influent on the coated PVC based on the analytical process described in section 6.5.6.

6.6 Results and discussions

6.6.1 XRD

The X-ray diffraction (XRD) analysis of the uncoated PVC and coated PVC substrates were conducted to determine the molecular and atomic structures and is presented in [Figure 6.1](#). Uncoated PVC or pure PVC shows several peaks. Two sharp peaks at 27.5° (200) and 29.3° (210), and two weak peaks at 17.9° (110) and 47.5° (222) indicate its semi-crystalline or amorphous nature [344–347]. The peaks at 200 and 210 planes observed in Uncoated PVC were reduced in Coated PVC (PU) which is due to the coat of PU on the PVC. However, a weak peak was observed at 24.2° (111) confirming the semi-crystalline or amorphous structure of the polyurethane (PU) [348]. Two peaks were observed for Coated PVC (GCN). The sharp peak 27.5° (002) and the broad weak peak at 13.3° (100) correspond to the interplanar stacking and the interlayer stacking of the conjugated hexagonal aromatic structure of GCN (JCPDS card number: 87-1526) [286]. The presence of these two peaks indicates GCN nanosheet structure [285]. The broad peaks observed on the 002 and 100 planes are due to the presence of strong electronegative heteroatom oxygen in the GCN structure caused by low polymerization [254]. The ZnO peaks were observed at 32.2° (100), 34.8° (002), 36.6° (101), and 48.0° (102) in the Coated PVC (GCN/ZnO-Cu3%). These diffraction peaks and planes are characteristic of the hexagonal wurtzite structure of ZnO (JCPDS card number: 36-1451) [287,288]. No peak for Cu was observed in the ZnO-Cu because the ionic radius of Cu^{2+} which is 0.73 \AA is similar to the ionic radius of Zn^{2+} which is 0.74 \AA .

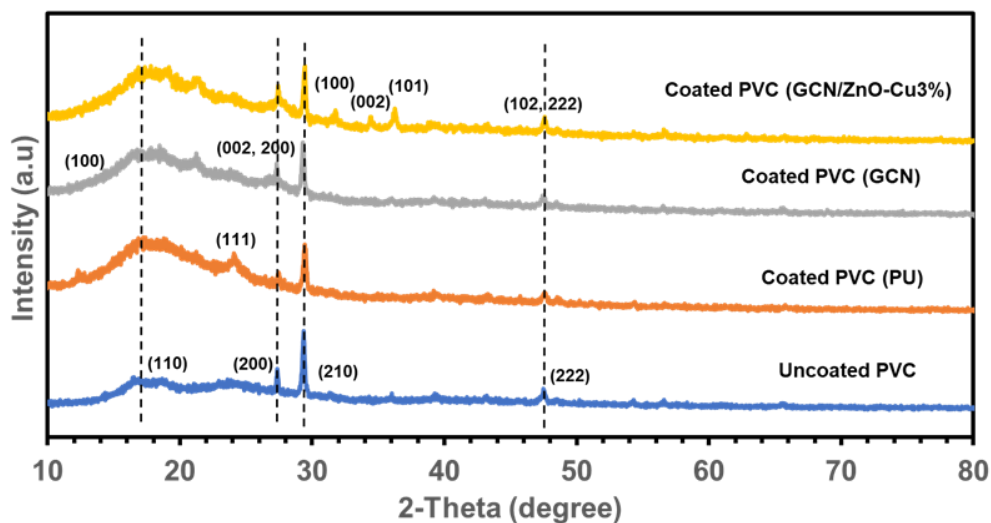


Figure 6. 1 XRD spectra patterns of Uncoated PVC, Coated PVC (PU), Coated PVC (GCN), and Coated PVC (GCN/ZnO-Cu3%).

6.6.2 FT-IR

The chemical structure and the functional groups of the Uncoated PVC and Coated PVCs were investigated using FTIR as shown in Figure 6.2. The Uncoated PVC shows several peaks at $2971 - 2850 \text{ cm}^{-1}$, 1428 cm^{-1} , 1254 cm^{-1} , 959 cm^{-1} , and $875 - 605 \text{ cm}^{-1}$. These peaks correspond to C-H stretching band vibration, angular deformation of the $\text{CH}_2\text{-Cl}$ bond, out-of-plane angular deformation of the CH-Cl bond, out-of-plane trans deformation of the C-H bond, and C-Cl stretching vibration, respectively [347]. Four peaks were observed for Coated PVC (PU) confirming the presence of the polyurethane (PU) chemical structure and functional groups at $3430 \text{ cm}^{-1} - 3230 \text{ cm}^{-1}$, 1728 cm^{-1} , $1235 - 1139 \text{ cm}^{-1}$, and 1040 cm^{-1} . These peaks represent the amine (NH) group vibration, CN group, and C-O-C bond vibration, respectively [349]. A peak was observed in the Coated PVC (GCN) at 810 cm^{-1} which is characteristic of GCN. This peak is the C-N heterocycles stretching vibrational frequency [289,290]. Coated PVC (GCN/ZnO-Cu3%) shows the 810 cm^{-1} peak observed in the Coated PVC (GCN) indicating the overwhelming presence and dominance of GCN in the GCN/ZnO-Cu3% nanocomposite. The peak at 500 cm^{-1} for the Coated PVC (GCN/ZnO-Cu3%)

is the vibrational frequency of ZnO [289]. It is worth noting that all the peaks observed in Uncoated PVC, Coated PVC (PU), and Coated PVC (GCN) were present in the Coated PVC (GCN/ZnO-Cu3%) in reduced form, indicating the bonding that exists in the Coated PVC (GCN/ZnO-Cu3%).

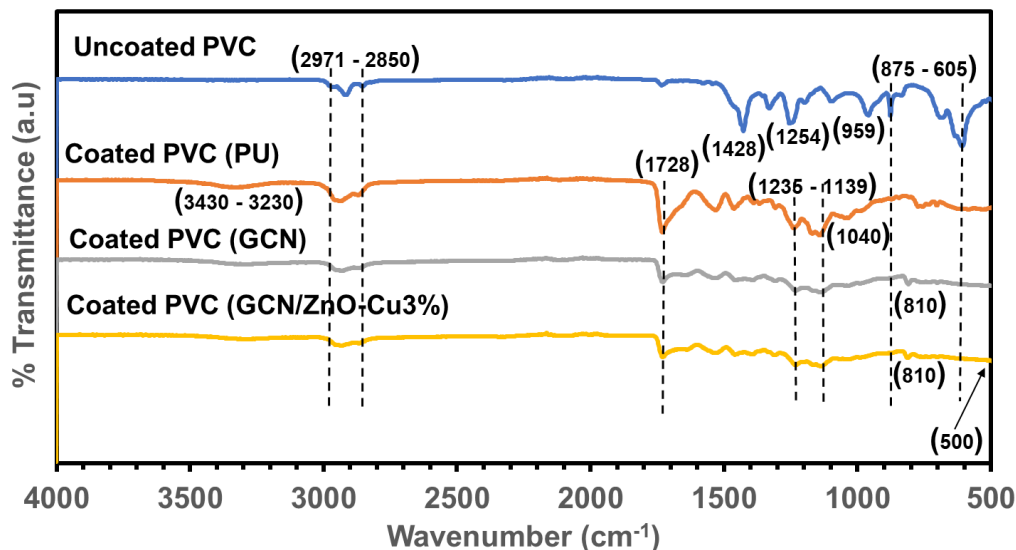


Figure 6. 2 FTIR spectra patterns of Uncoated PVC, Coated PVC (PU), Coated PVC (GCN), and Coated PVC (GCN/ZnO-Cu3%).

6.6.3 SEM, EDS, and AFM

The scanning electron microscopy (SEM) image of Uncoated PVC and Coated PVCs is shown in [Figure 6.3](#). The Uncoated PVC and Coated PVC (PU) show smooth surfaces however the surface of Coated PVC (PU) appeared darker which could be attributed to the presence of the polyurethane (PU) on the surface of PVC. The Coated PVC (GCN) shows the aggregation of the sheet-like structure of GCN. The Coated PVC (GCN/ZnO-Cu3%) shows less aggregation of the sheet-like structure of the GCN and spherical-like structure of the ZnO-Cu3%. The less aggregation observed in the Coated PVC (GCN/ZnO-Cu3%) can be attributed to the presence of ZnO-Cu3% in the GCN/ZnO-Cu3% coating mixture resulting in weak Van der

Waal's force of attraction, finer particles, and better dispersion of GCN and ZnO-Cu3%. This observation for Coated PVC (GCN/ZnO-Cu3%) is expected to yield a larger surface area and enhance its disinfection capacity.

The electron dispersive X-ray spectroscopy (EDS) was conducted, and the results are shown in [Figure 6.4](#). The Uncoated PVC shows the elements of Carbon (C), Oxygen (O), Calcium (Ca), titanium (Ti), and a huge presence of chlorine (Cl). The hydrogen atom which is part of the structure of PVC and PU was not detected due to its low atomic number. The huge presence of chlorine in the PVC shows that the PVC is richly chlorinated. The presence of Ti, Ca, and Cl in the PVC confers on it its antimicrobial properties since these elements are well known to have antimicrobial activity. In Coated PVC (PU), the peak intensity of Cl reduced drastically while Ti and Ca were no longer detected. This can be attributed to the coating layer of polyurethane (PU) over the PVC surface. Silicon (Si) and sodium (Na) elements were detected in trace amounts owing to the small peak intensities. The presence of Na and Cl in the PU can act as antimicrobial agents since Na and Cl are known to have antimicrobial properties. Other elements detected were carbon (C), Nitrogen, and Oxygen (O) which are part of the chemical structure of PU. All the elements detected in Coated PVC (PU) were observed in Coated PVC (GCN). In the Coated PVC (GCN/ZnO-Cu3%), Copper (Cu) and Zinc (Zn) elements were detected in addition to the expected C, N, and O elements of GCN. However, a very high peak intensity of Zn was observed indicating a huge presence of Zn in the GCN/ZnO-Cu3% nanocomposite. With the Coated PVC (GCN/ZnO-Cu3%), the presence of Na, Si, and Cl elements in trace amounts observed in Coated PVC (GCN) was no longer detected and this can be attributed to a huge amount of Zn in the Coated PVC (ZnO-Cu3%). The Zn and Cu elements are expected to play important roles in disinfection since they are known to have antimicrobial properties. The presence of strong electronegative heteroatom oxygen in all the EDS sample images can serve to trap photogenerated electrons thereby enhancing their photocatalytic activity [194].

The atomic force microscopy (AFM) topology of the Uncoated PVC and Coated PVCs are shown in [Figure 6.5](#). The average roughness (Ra) decreased from the Uncoated PVC at Ra = 5.54 μm , Coated PVC (PU) at Ra = 5.02 μm , to Coated PVC (GCN) at 3.19 μm . This indicates that the surface became increasingly smoother. However, it increased to 5.83 μm for Coated PVC (GCN/ZnO-Cu3% which is about two times higher than Coated PVC (GCN). This means that the Coated PVC (GCN/ZnO-Cu3%) became rougher. BET surface area of the powdered samples of GCN and GCN/ZnO-Cu3% were also investigated as shown in [Table 6.1](#). It shows that the surface area of GCN/ZnO-Cu3% is 121.00 m^2/g which is two times larger than GCN (57.17 m^2/g). A correlation between the Coated PVC (GCN), Coated PVC (GCN/ZnO-Cu3%), powdered GCN, and powdered GCN/ZnO-Cu3%) shows that the surface roughness increases with increasing surface area. The surface roughness and the BET surface area are related as shown in equation (6.2) [350,351]. A rough surface for bonding leads to stronger bonds for the following reasons, (1) roughness imparts additional surface area with which the adhesive can make contact when bonding and (2) A rough surface provides additional mechanical interlocking at the surface [352,353]. The rough surface also promotes wettability [354]. Therefore, the surface roughness and BET surface area properties are expected to enhance the adhesion, interaction, and disinfection performance of the Coated PVC (GCN/ZnO-Cu3%).

$$R_a = \frac{\rho \cdot D \cdot S_{BET}}{6} \quad (6.2)$$

Where ρ is the particle density (g/cm^3), D is the particle diameter (μm), S_{BET} is the BET surface area (m^2/g), and R_a is the surface roughness (dimensionless).

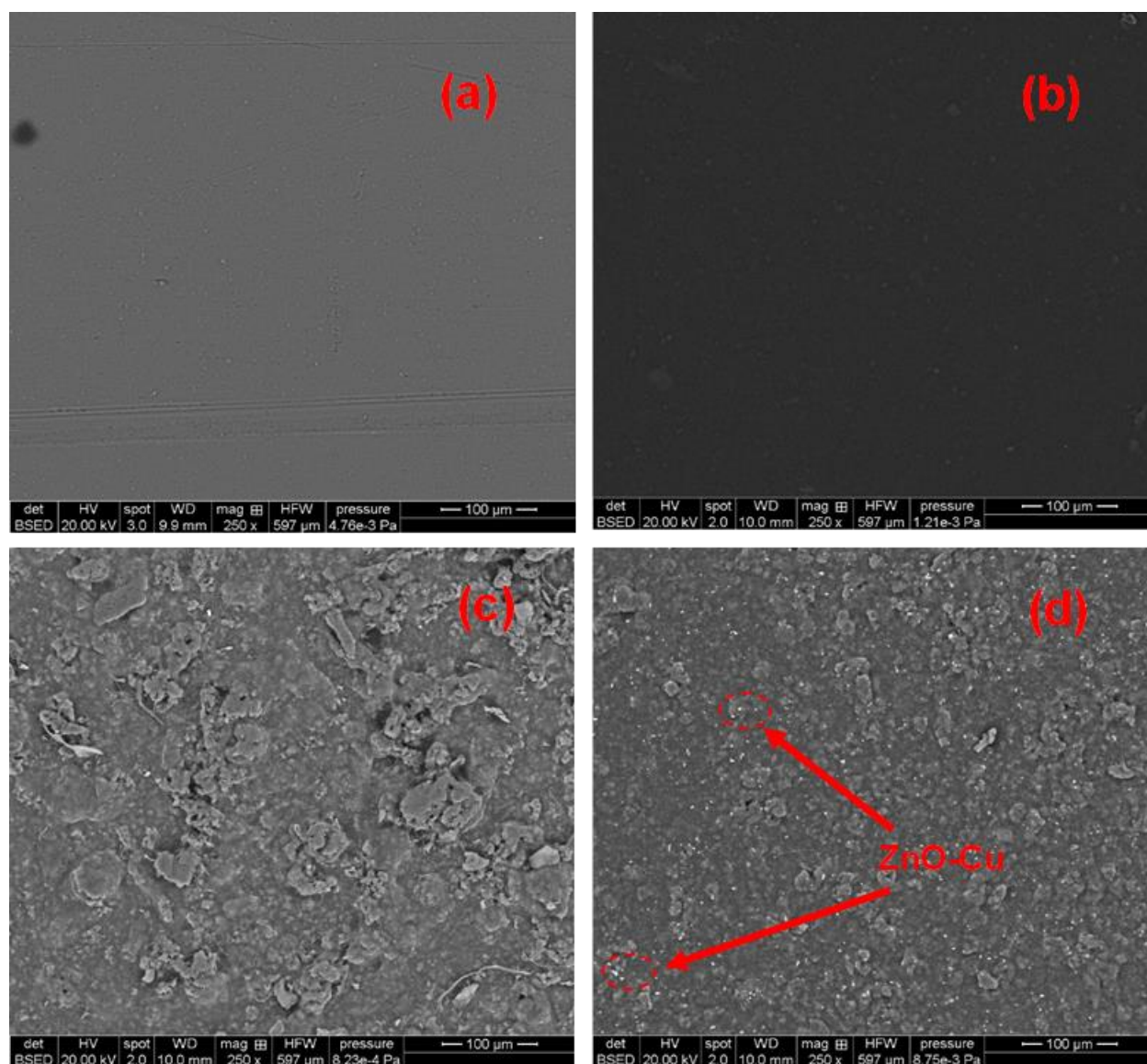


Figure 6. 3 SEM: (a) Uncoated PVC, (b) Coated PVC (PU), (c) Coated PVC (GCN), and (d) Coated PVC (GCN/ZnO-Cu3%).

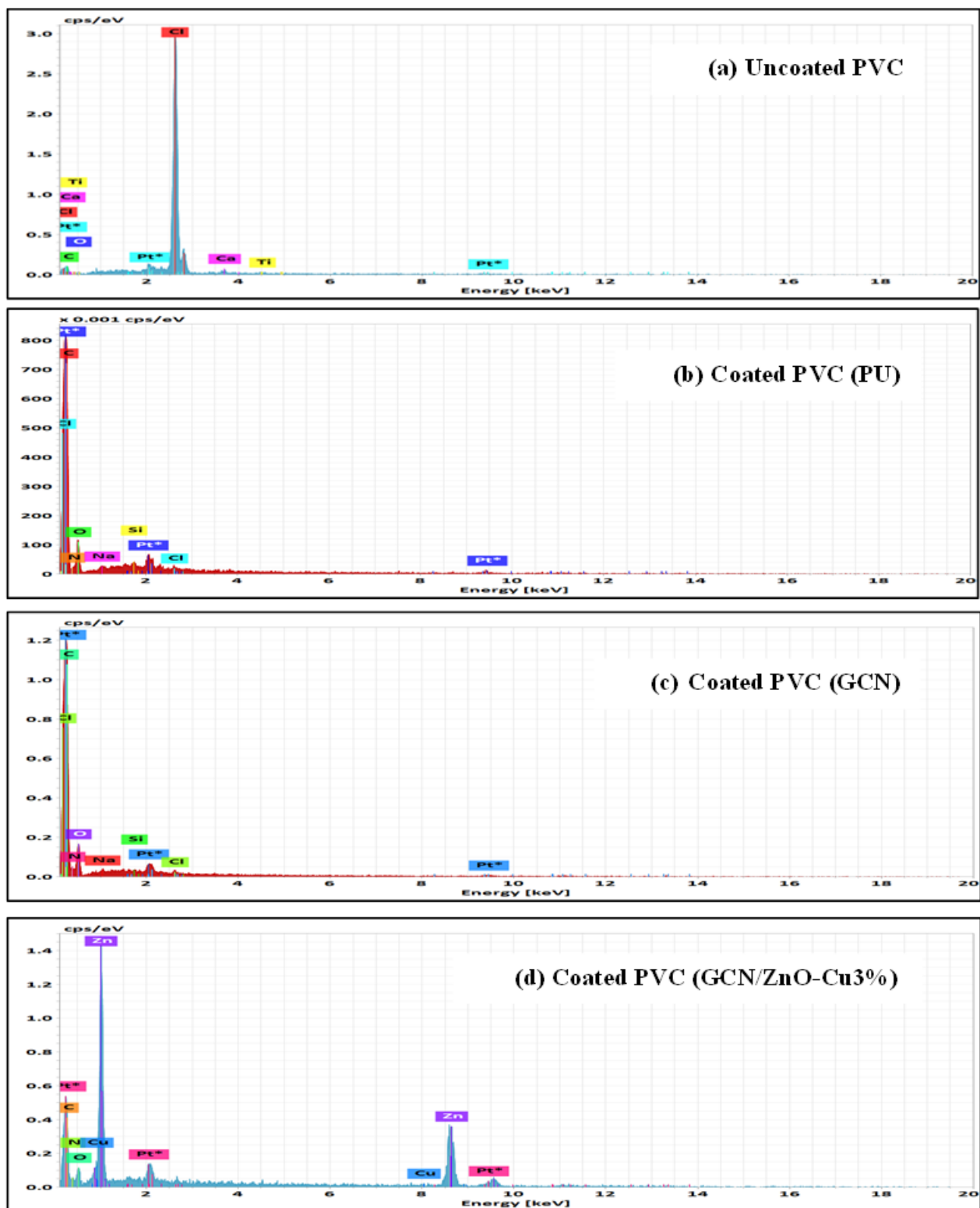
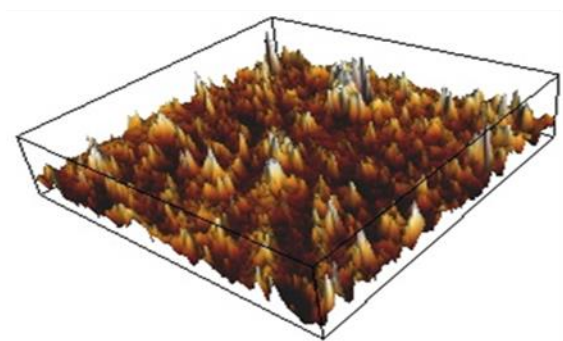
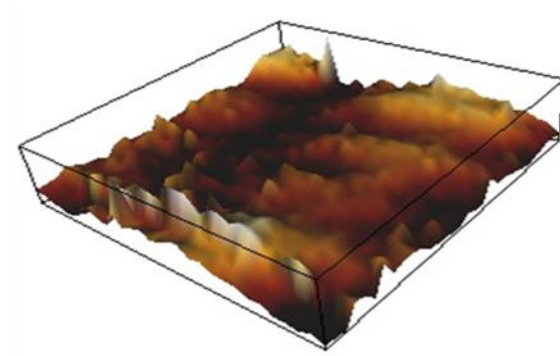


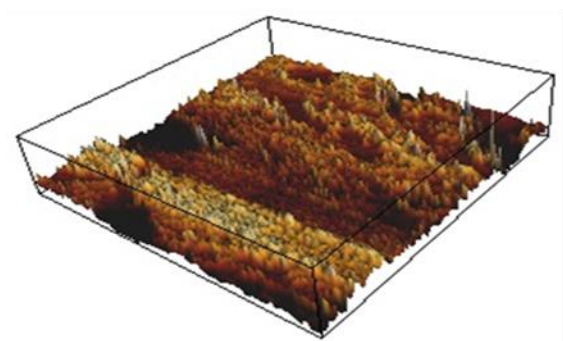
Figure 6. 4 EDS: (a) Uncoated PVC, (b) Coated PVC (PU), (c) Coated PVC (GCN), and (d) Coated PVC (GCN/ZnO-Cu3%).



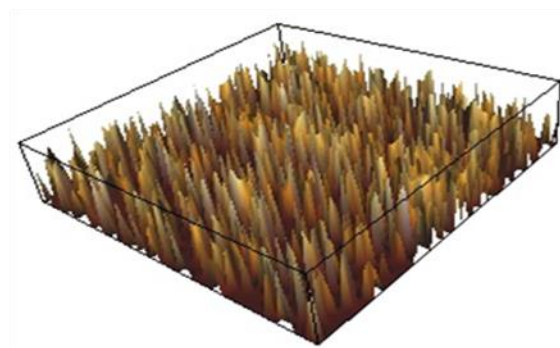
(a) $Ra = 5.54 \mu m$



(b) $Ra = 5.03 \mu m$



(c) $Ra = 3.19 \mu m$



(d) $Ra = 5.83 \mu m$

Figure 6. 5 AFM: (a) Uncoated PVC, (b) Coated PVC (PU), (c) Coated PVC (GCN), and (d) Coated PVC (GCN/ZnO-Cu3%).

Table 6. 1 BET surface area of powder GCN and GCN/ZnO-Cu3%

Photocatalyst	BET Surface Area (S_{BET}) (m^2/g)
GCN	57.17
GCN/0.1ZnO-Cu3%	121.00

6.6.4 UV-Vis DRS and Bandgap estimation

The ultraviolet-visible diffuse reflectance spectroscopy (UV-Vis DRS) was conducted for the Uncoated PVC and Coated PVCs and their bandgaps were estimated using the UV-Vis data, Kubelka-Munk function in equation (6.3) [55,194,283], and the Tauc plot. The UV-Vis DRS, Tauc plots, and bandgaps of the samples are presented in [Figure 6.6](#) and [Table 6.2](#). The Uncoated PVC and the Coated PVCs have their absorption edge below 620 nm, indicating that they can absorb light in the UV and visible regions. With the absorption edges of Uncoated PVC and Coated PVC (PU) at 620 nm and 428 nm, it means that they can also absorb IR and UV since they exist at the upper and lower boundaries of visible light. However, Uncoated PVC with 620 nm indicates that it can absorb more visible light energy than Coated PVC (PU) with 428 nm which should lead to a better photocatalytic activity. It was observed that the Coated PVC (GCN/ZnO-Cu3%) at 478 nm had improved visible light absorption capacity compared to Coated PVC (GCN) at 450 nm which is due to the presence of ZnO-Cu3% in the GCN/ZnO-Cu3% that serves to trap photogenerated electrons from the GCN. This also means that at 478 nm it can absorb more visible light energy thereby suggesting that it should lead to a better photocatalytic activity. The corresponding bandgaps of the wavelength absorption edges show that Coated PVC (PU) at 2.90 eV will have the least visible light utilization capacity while the Uncoated PVC at 2.00 eV will have the highest visible light utilization capacity. The absorption wavelength and the bandgaps of powdered samples of GCN and GCN/ZnO-Cu3% were conducted and estimated to be the same as the Coated PVC (GCN) and Coated PVC (GCN/ZnO-Cu3%), indicating that the presence of PU in the coat did not affect the optical properties of GCN and GCN/ZnO-Cu3%. The proposed order of visible light activity of the samples in terms of absorption edge and the bandgap energy is Uncoated PVC > Coated PVC (GCN/ZnO-Cu3%) > Coated PVC (GCN) > Coated PVC (PU).

$$[F(R)hv]^{\frac{1}{Y}} = \left(\frac{(1-R)^2}{2R} * hv \right)^{\frac{1}{Y}} \quad (6.3)$$

$$K = (1 - R)^2; \quad S = 2R; \quad Y = \frac{1}{2} \text{ or } 2; \quad hv \equiv \text{eV}.$$

Where K is the molar absorption coefficient, S is the scattering factor; h is the Planck constant, ν is the photon's frequency and γ is a factor dependent on the nature of the electron transition and it is either $\frac{1}{2}$ or 2 for the direct and indirect band gaps respectively.

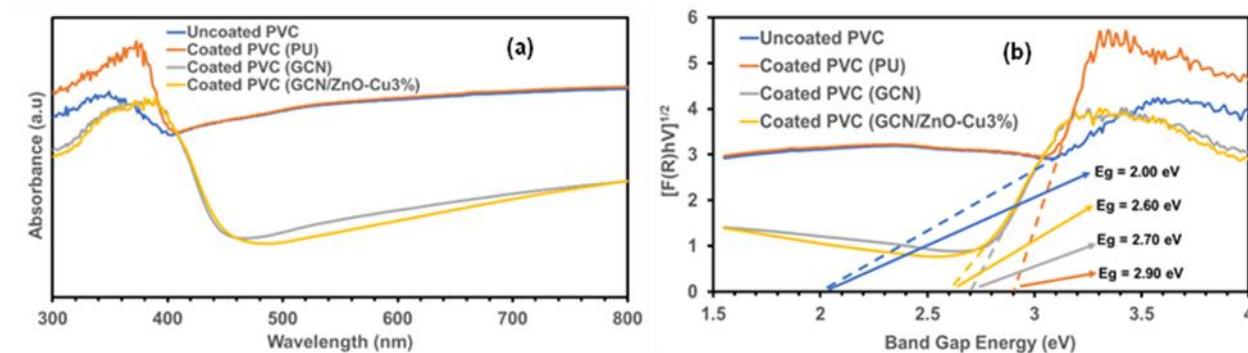


Figure 6. 6 (a) UV-Vis DRS and (b) Bandgap, of Uncoated PVC, Coated PVC (PU), Coated PVC (GCN), and Coated PVC (GCN/ZnO-Cu3%).

Table 6. 2 Bandgaps and the corresponding wavelengths of Uncoated PVC, Coated PVC (PU), Coated PVC (GCN), and Coated PVC (GCN/ZnO-Cu3%).

Photocatalyst	Bandgap Energy (eV)	Wavelength (nm)
Uncoated PVC	2.00	620
Coated PVC (PU)	2.90	428
Coated PVC (GCN)	2.70	450
Coated PVC (GCN/0.1ZnO-Cu3%)	2.60	478

6.6.5 PL spectra

Photoluminescence (PL) spectral analysis for Uncoated PVC and Coated PVCs is shown in Figure 6.7. It was determined at an excitation wavelength of 360 nm and emission wavelengths between 400 – 650 nm. The intensity of the PL peaks corresponds to the density of defects in the material [355]. These defects serve as electron trap sites that facilitate the inhibition of electron-hole pair recombination and enhance the

photocatalytic activity of the material. Therefore, PL spectra are a tool to measure the optical quality of a material. The figure shows that the Uncoated PVC, Coated PVC (PU), Coated PVC (GCN), and Coated PVC (GCN/ZnO-Cu3%) emitted between 450 – 500 nm, which is the blue region of the visible light spectrum. The Uncoated PVC and the Coated PVC (PU) both show a weak luminescence of around 478 nm, indicating that both emit blue light. The emission of the blue light is due to the recombination of the charge carriers after the trapping by gaps in defects in the material [355]. The Coated PVC (GCN) and Coated PVC (GCN/ZnO-Cu3%) show well-defined peaks with emission of blue light around 478 nm. The addition of GCN in the Coated PVC (GCN) raised the intensity of the peak when compared to the Coated PVC (PU). This means that the GCN contributed to the recombination rate of the electron-hole pair. GCN is known to have a high recombination rate due to its moderate bandgap of 2.7 – 2.8 eV [194,271]. However, the peak intensity of the Coated PVC (GCN/ZnO-Cu3%) reduced compared to the Coated PVC (GCN). This can be attributed to the inclusion of ZnO-Cu3% in the GCN/ZnO-Cu3% nanocomposite which serves as a site to trap the photogenerated electrons and photogenerated holes, reduce electron-hole pair recombination rate, and enhance the photocatalytic activity.

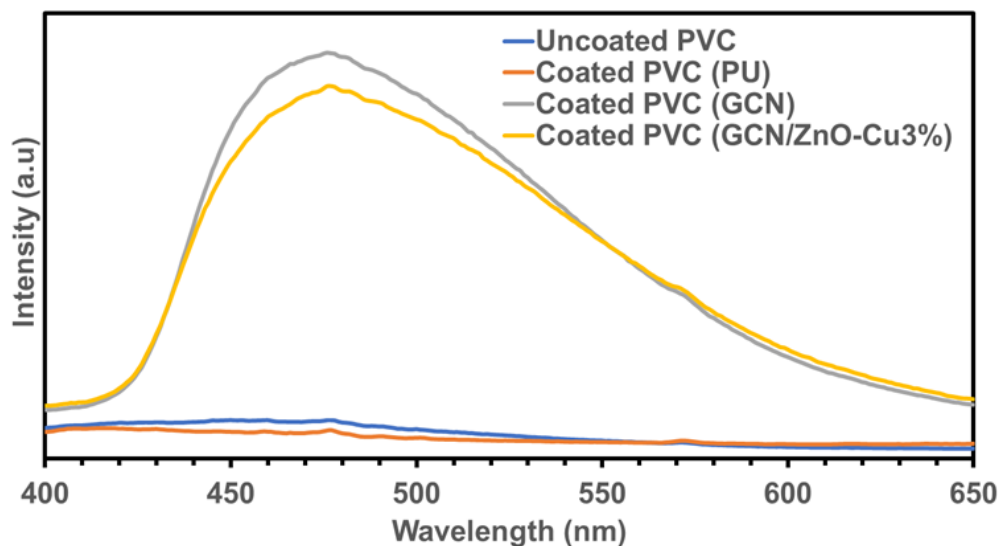


Figure 6. 7 PL spectral of Uncoated PVC, Coated PVC (PU), Coated PVC (GCN), and Coated PVC (GCN/ZnO-Cu3%).

6.6.6 Photocatalytic disinfection of coated PVC

The self-disinfecting performance of the Uncoated PVC and the Coated PVCs in the dark and under 5000K LED irradiation were examined on a drop of wastewater primary influent for 180 minutes as shown in Figures 6.8, 6.9, and 6.10. Figure 6.8 describes the effect of coat layer thickness on the self-disinfecting performance of coated PVC which was conducted at a 10 cm distance to the substrate with the corresponding light intensity of 16,800 Lux. PVC was coated with different coat layers of GCN/ZnO-Cu3%, Coated PVC (GCN/ZnO-Cu3%), as a 1-layer coat, 2-layer coat, and 4-layer coat. The self-disinfecting experiment of the 4-layer coat showed maximum disinfection of 2 log reduction (99%) while the 1-layer coat showed the least disinfection of less than 1 log reduction (65.47%) of total coliforms. This indicates that more disinfection is achieved with several layers of a thick coat. The optimal coat of 4-layer coat was used for the dark and self-disinfecting experiments (see Figures 6.9 and 6.10). In Figure 6.9a, very small disinfection was observed in the dark for Uncoated PVC and Coated PVCs. Uncoated PVC, Coated PVC (PU), Coated PVC (GCN), and Coated PVC (GCN/ZnO-Cu3%) results of 0.32, 0.22, 0.33, and 0.24

log reduction of total coliforms in the dark indicate low cytotoxicity. This was expected because the presence of Ti, Ca, Cl, Na, Zn, and Cu elements in the samples, as shown in the EDS image (see section 3.3), is known to have antimicrobial properties. In [Figure 6.9b](#), the experiment was conducted at a 10 cm distance to the substrate with the corresponding intensity of 16,800 Lux. The results for Uncoated PVC, Coated PVC (PU), and Coated PVC (GCN) of 0.33, 0.49, and 0.68 log reduction of total coliforms indicate that the visible light irradiation of 5000K LED improved slightly the cytotoxicity of the samples when compared to the corresponding dark experiments. This is due to the photogenerated electrons and holes, and ROS species. However, a drastic improvement was observed in the self-disinfecting performance of Coated PVC (GCN/ZnO-Cu3%) of 2 log reduction. This can be attributed to the presence of ZnO-Cu3% in the GCN/ZnO-Cu3% which serves to inhibit the recombination rate of electron-hole pair (see section 3.5), low bandgap (see section 3.4) and high surface roughness and large surface area (see section 3.3). [Figure 6.10](#) describes the effect of light intensity on the disinfection performance of the coated PVC using the optimally performing Coated PVC (GCN/ZnO-Cu3%) substrate. It was observed that at 10 cm of 5000K LED to the substrate with an intensity of 16,800 Lux, the highest disinfection of 2 log reduction (99% disinfection) of total coliforms was achieved but at 30 cm of 5000K LED to the substrate with an intensity of 3,500 Lux, the least disinfection of 0.72 log reduction (81.3%) of total coliforms was recorded. This suggests that disinfection efficiency is a function of distance and intensity.

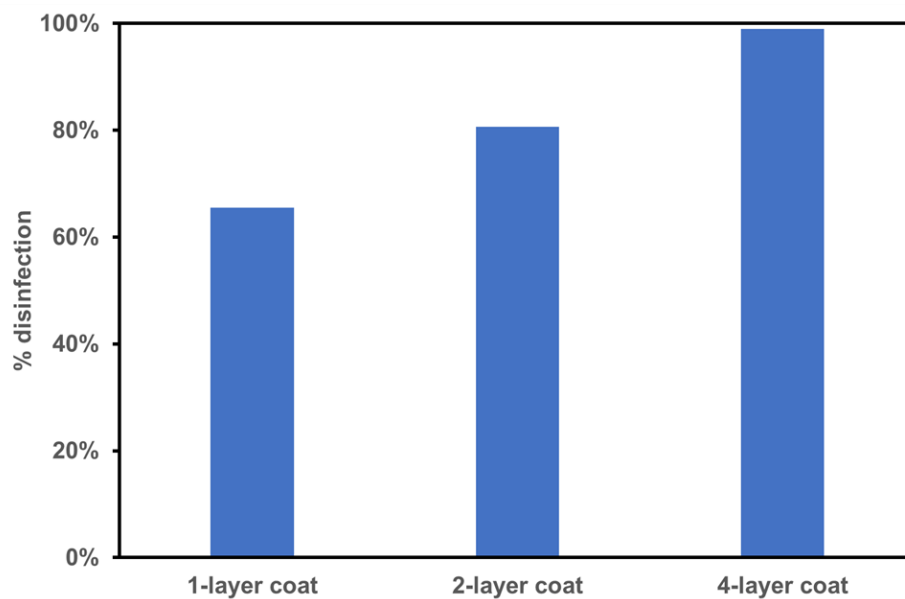


Figure 6. 8 Effect of coat layer on the self-disinfection performance of Coated PVC (GCN/ZnO-Cu3%) under 5000K LED (10 cm and 16,800 Lux).

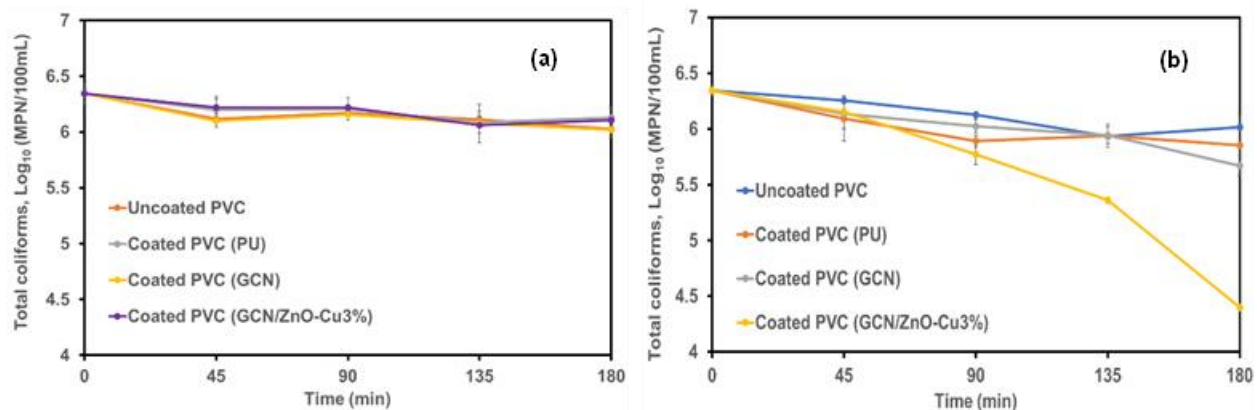


Figure 6. 9 Self-disinfecting experiments of Uncoated PVC, Coated PVC (PU), Coated PVC (GCN), and Coated PVC (GCN/ZnO-Cu3%), (a) in the dark and (b) under 5000K LED (10 cm and 16,800 Lux).

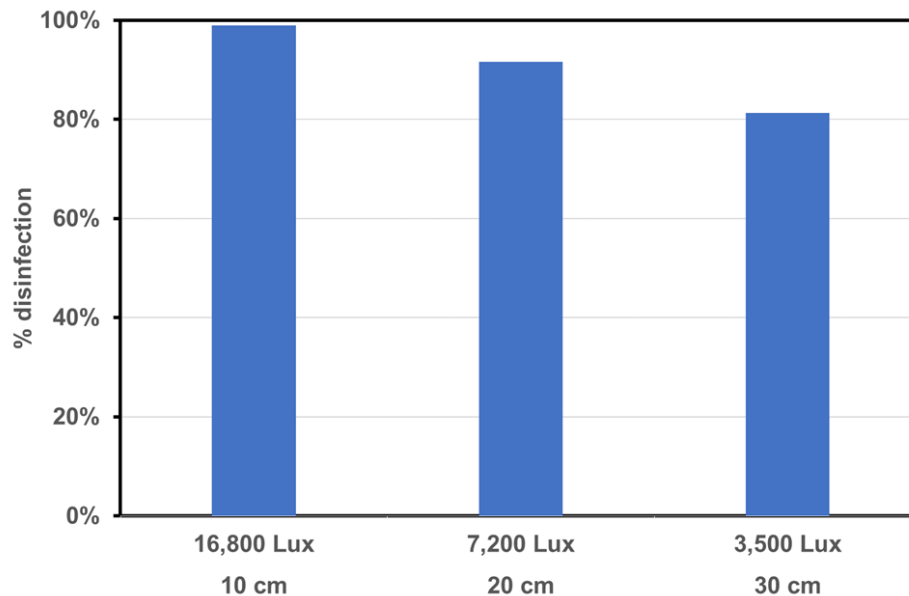


Figure 6. 10 Effect of light intensity on the self-disinfection performance of Coated PVC (GCN/ZnO-Cu3%) under 5000K LED.

6.6.7 Reactive Oxidation Species (ROS) trapping experiment

The ROS experiments for the commonly known radicals, e^- , h^+ , O_2^- , and OH^- responsible for disinfection were conducted using the optimally performing Coated PVC (GCN/ZnO-Cu3%) under 5000K LED irradiation (10 cm and 16,800 Lux). The results are presented in Figure 6.11. The following scavengers were employed potassium chromate (Cr (VI)), ammonium oxalate (AO), p-benzoquinone (BQ), and isopropanol (IPA) for the following radicals, e^- , h^+ , O_2^- , and OH^- , respectively. Scavengers are trapping agents used to remove the radicals (e^- , h^+ , O_2^- , and OH^-) [305–308]. All the radicals actively participated in the self-disinfection process after 180 minutes. However, the IPA, which is the OH^- scavenger, had the highest inhibition to the disinfection which gives the least disinfection of 76.44%. The lowest inhibition to disinfection was AO, which is the h^+ scavenger, with the most disinfection of 93.95%. This indicates that the hydroxyl radical (OH^-) is the dominant radical responsible for most of the disinfection while h^+ is the

least involved. The order of reactivity from the most involved to the least involved in the photocatalytic self-disinfection is $\text{OH}^\cdot > \text{e}^- > \text{O}_2^\cdot > \text{h}^+$.

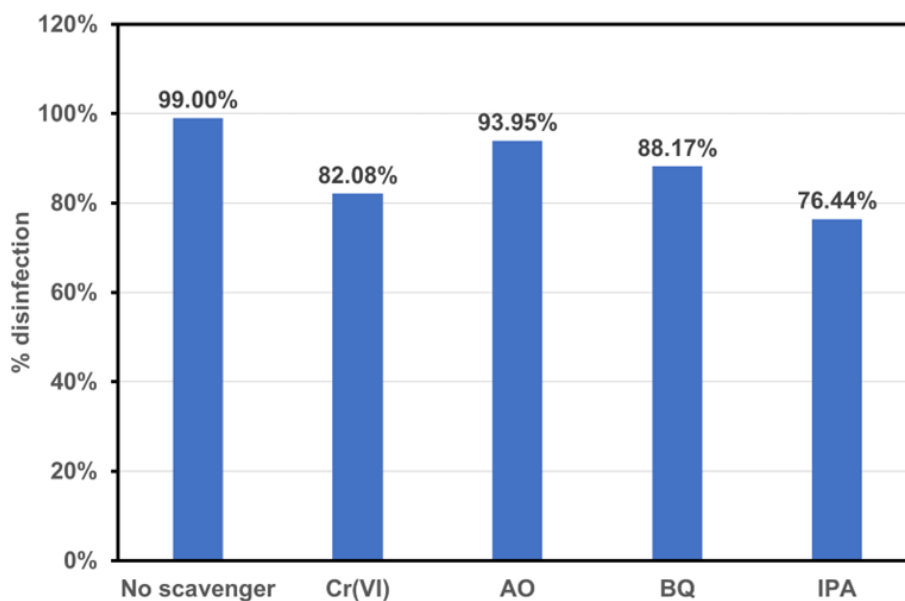


Figure 6. 11 ROS Experiment for the active species for the disinfection of Coated PVC (GCN/ZnO-Cu3%) under 5000K LED (10 cm and 16,800 Lux).

6.6.8 Reusability experiment and stability test

The reusability experiment and stability test were conducted to determine the practical application of the Coated PVC (GCN/ZnO-Cu3%) as presented in Figure 6.12. Between each cycle of the self-disinfecting experiment, the coated PVC was washed with DI water and air-dried overnight at room temperature. In Figure 6.12a, the result for the 1st, 2nd, 3rd, and 4th cycles is 99.0%, 97.3%, 96.4%, and 94.5% respectively, indicating less than 5% decline in the self-disinfecting performance of the Coated PVC (GCN/ZnO-Cu3%) and all cycles having a performance of over one log reduction in disinfecting total coliforms in the wastewater primary influent. The XRD pattern of the Coated PVC (GCN/ZnO-Cu3%) after the 4th cycle was examined and compared to a fresh Coated PVC (GCN/ZnO-Cu3%) to determine its stability (see Figure 6.12b). No obvious shift in the 2-theta (degree) of the fresh and used Co/ZnO-Cu3% ated PVC (GCN/ZnO-

Cu3%) was observed. The SEM images of the fresh and the used Coated PVC (GCN/ZnO-Cu3%) (see Figure 6.10 c and d) show that the uniform distribution of the spherical-like particles of the ZnO-Cu3% on the sheet-like structure of the GCN is the same. Therefore, the Coated PVC (GCN/0.1ZnO-Cu3%) can be said to be stable and fit for practical application.

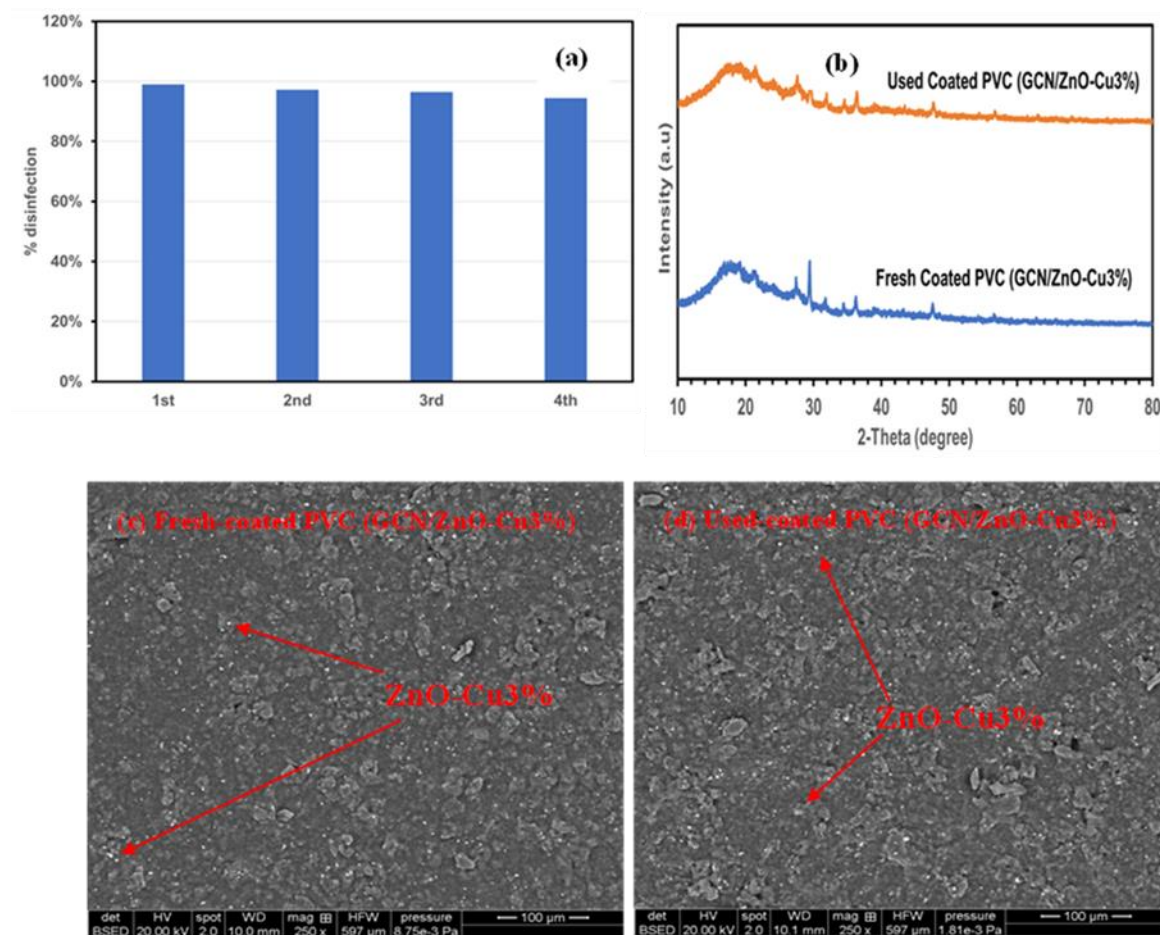


Figure 6. 12 Reusability experiment (a) and Stability tests for XRD pattern (b) and SEM image (c and d), of Coated PVC (GCN/ZnO-Cu3%) after the 4th cycle under 5000K LED (10 cm and 16,800 Lux).

6.6.9 Proposed photocatalytic mechanism

The conduction band (CB) and the valence band (VB) potentials of GCN and ZnO were calculated based on equations (6.4) and (6.5) [194,316–318]. The order of the photocatalytic redox reactions involved in the mechanism is given in equations (6.6) to (6.10) based on the participation of active radicals as described in section 6.6.7.

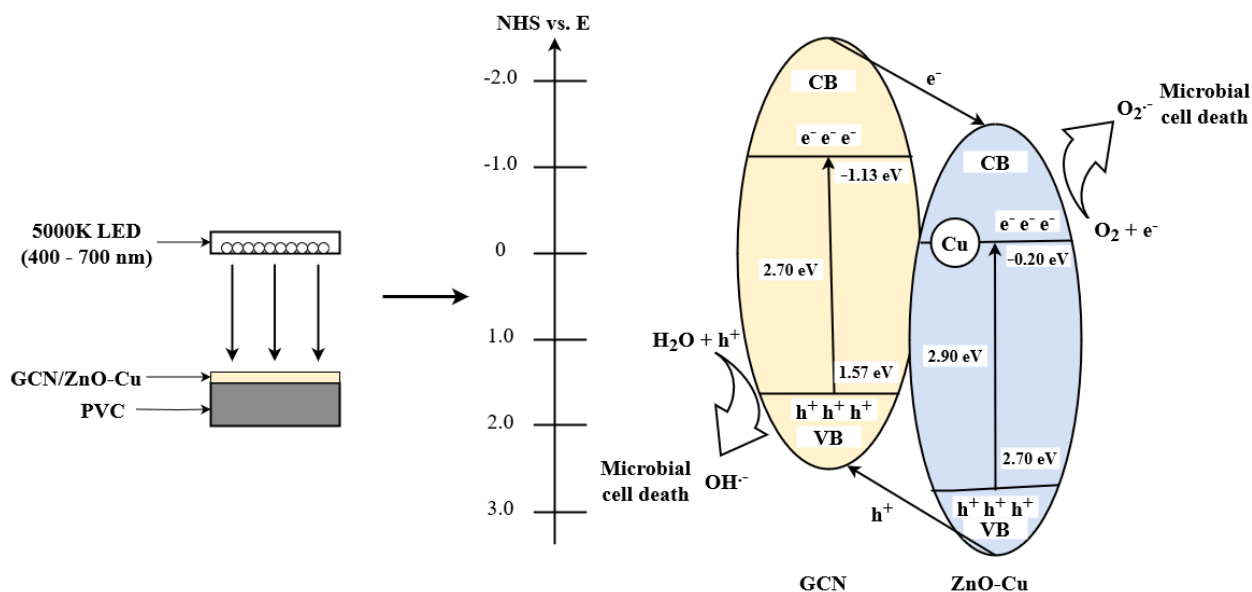
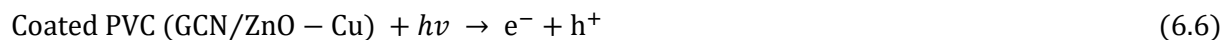
$$E_{CB} = X - E^e - 0.5E_g \quad (6.4)$$

$$E_{VB} = E_{CB} + E_g \quad (6.5)$$

Where E_{CB} and E_{VB} are conduction band and valence band potentials, E^e is free electron energy on a hydrogen scale (~ 4.50 eV), E_g is the bandgap energy and X is the absolute electronegativity of the semiconductor, which is based on the geometric mean of the constituent atoms, which for GCN is 4.72 eV [194,319] and for ZnO is 5.75 eV [320]. Therefore, the calculated CB and VB for GCN are -1.13 eV and 1.57 eV while the calculated CB and VB of ZnO are -0.20 eV and 2.70 eV.

[Scheme 6.2](#) depicts the proposed self-disinfecting mechanism of the microorganisms using the optimally performing Coated PVC (GCN/ZnO-Cu3%) under the irradiation of the visible light source, 5000K LED. The Photoexcited electron-hole (e-h) pairs on the GCN and ZnO-Cu3% components were generated upon irradiation of Coated PVC (GCN/ZnO-Cu3%). The photogenerated electrons move from the valence band (VB) to the surface of the conduction band (CB), creating photogenerated holes in the VB. The electrons from the CB of GCN move to the CB of ZnO. This is because the CB of GCN has a higher negative potential (-1.13 eV) than the CB of ZnO-Cu3% (-0.20 eV). Likewise, the holes from the VB of ZnO migrate towards the VB of GCN because the VB of ZnO has a higher positive potential (2.70 eV) than the VB of GCN (1.57 eV). The Cu dopant in the ZnO acts as an electron-trapping agent and inhibitor of the electron-hole pair recombination rate. The electrons on the surface of the ZnO-Cu3% react with the surrounding oxygen (O_2) on the surface of the coated PVC generating a superoxide radical ($O_2^{\cdot-}$). Likewise, the holes on the surface of GCN react with the wastewater molecule and moisture on the surface of the coated PVC to generate

hydroxyl radical (OH^\cdot). The photogenerated electrons and holes and the radicals (OH^\cdot , O_2^\cdot) can react, oxidize, and disinfect the wastewater leading to the cell death of the total coliforms by disrupting the metabolic cellular activities such as reproduction and respiratory functions as a result of oxidative stress [309].



Scheme 6. 2 Schematic representation of the proposed self-disinfecting mechanism of coliforms by Coated PVC (GCN/ZnO-Cu3%) under 5000K LED.

6.7 Conclusions

In this work, a novel facile mixing composition of GCN/ZnO-Cu nanocomposite, GCN, and polyurethane (PU) as a binding agent was prepared and used as a coat on polyvinyl chloride (PVC) substrates. Different characterization techniques were employed to understand the morphology, chemical structure, crystallinity, elemental composition, and optoelectronic properties of the coated materials. The PVC substrate coated with GCN/ZnO-Cu3% herein denoted as Coated PVC (GCN/ZnO-Cu3%) offered the optimum self-disinfecting performance. Two-log reduction of coliforms-containing wastewater primary influent was achieved in 180 minutes under the visible light source, 5000K LED (400 – 700 nm). The effects of coat layer thickness and light intensity of 5000K LED were also investigated for Coated PVC (GCN/ZnO-Cu3%) under 5000K LED. It was observed that the coat with the thickest layer achieved the optimum self-disinfecting performance of two log reduction of coliforms in 180 minutes. Similarly, the light intensity of 16,800 Lux at 10 cm to the coated PVC resulted in an optimal self-disinfection of 2 log reduction in 180 minutes. The ROS experiments of the reactive species for the optimally performing coated PVC, Coated PVC (GCN/ZnO-Cu3%), indicate that the hydroxyl radical (OH^\cdot) was the dominant species. The Coated PVC (GCN/ZnO-Cu3%) displayed stability in its practical application after the 4th cycle. Therefore, it is suggested that the Coated PVC (GCN/ZnO-Cu3%) can be used for practical applications in the self-disinfection of microorganisms under sunlight, UV, and visible light. The success of this coating shows that it can be further applied in cleaning ponds under natural sunlight irradiation by the dispersion of coated glass beads or coated plastic beads.

Chapter 7: Conclusions and Recommendations

7.1 Conclusions

The goal of this research was to develop practical visible light photocatalysts that can not only be used for treating organics but also for disinfection. To this end, the research focused on the following:

- (1) the synthesis of visible-light-driven photocatalysts and the evaluation of their photocatalytic performance in degrading organic contaminants and disinfection of wastewater,
- (2) the coating of the plastic substrate with the synthesized visible-light-driven photocatalyst to act as a self-disinfecting coated surface,
- (3) the ability to reuse the synthesized photocatalysts and self-disinfecting coated surface without losing their photocatalytic activity and structural stability after several cycles of experiments,
- (4) the effect of different light sources in degrading organic contaminants,
- (5) the effect of varying thickness (different coating layers) on disinfection performance of the coated surface,
- (6) the effect of light intensity on disinfection as a function of the distance of the light source from the coated surface,
- (7) the determination of the reactive oxygen species (ROS) involved in and the dominant ROS responsible for the photocatalytic activity of the photocatalysts and the self-disinfecting surface, and
- (8) Photocatalytic mechanisms for the visible-light photocatalysts and self-disinfecting coated surface.

The excerpts of the conclusions from each chapter of the research in this thesis are listed below.

1. Among different precursors of graphitic carbon nitride (GCN) which are melamine, dicyandiamide, and urea, the urea-derived GCN (U-GCN) showed the best photocatalytic performance due to its large surface area and pore volume.

2. The introduction of silver-based compounds such as AgBr, Ag₃PO₄, and Ag₂CrO₄ to the (U-GCN) to give U-GCN/AgBr, U-GCN/Ag₃PO₄, and U-GCN/Ag₂CrO₄ nanocomposites, enhanced the photocatalytic performance of U-GCN as they reduced U-GCN's recombination rate of the electron-hole pair and improved its charge separation.
3. The U-GCN/Ag₂CrO₄ nanocomposite showed the highest photocatalytic performance among the nanocomposites due to the very narrow bandgap and excellent visible-light responsiveness of Ag₂CrO₄.
4. The U-GCN/Ag₂CrO₄ (1:0.3) denoted U-GCN/0.3Ag₂CrO₄ showed the optimal photocatalytic performance in degrading an organic contaminant (4-CP) which may be attributed to the small size and homogeneous spread of Ag₂CrO₄ on U-GCN.
5. Among different light sources used such as royal blue LED (450 nm), UV-A LED (365 nm), cool white, fluorescent lamps (400 – 700 nm), and Solar simulator fitted with Xenon lamps (350 – 1800 nm), royal blue LED showed the optimal performance in degrading organic contaminant due to its very high light intensity.
6. Over 85% degradation was achieved in removing 2,4-D and MCPP simultaneously using U-GCN/0.3Ag₂CrO₄ and royal blue LED.
7. 100% and over 70% of BSA protein and SARS-CoV-2 spike protein were degraded by U-GCN/0.3Ag₂CrO₄ and royal blue LED.
8. Over one log reduction of microorganisms, total coliforms, and E. coli was achieved in disinfecting wastewater secondary effluent using U-GCN/0.3Ag₂CrO₄ and royal blue LED.
9. Novel facile synthesis of GCN/ZnO-Cu nanocomposite was proposed and conducted.
10. Over 65% of 4-CP was degraded and a complete 5.5 log reduction of total coliforms in wastewater primary influent was disinfected by GCN/ZnO-Cu nanocomposite and royal blue LED.
11. Novel facile mixing of GCN/ZnO-Cu nanocomposite, ethanol, and polyurethane binder for self-disinfecting surface was proposed and conducted.
12. The self-disinfecting surface was done using the dip coating method.

13. The effect of coat-layer thickness showed that the disinfection of the self-disinfecting coated surface increases with increasing coat layer.
14. The effect of light intensity for the self-disinfecting coated surface shows that the disinfection increases with decreasing light source distance to the coated substrate, that is increasing light intensity.
15. The light source 5000K LED used at 16,800 Lux shows that it can simulate sunlight illuminance at diffused light intensities (3,000 – 18,000 Lux) (see [section 2.4](#) on light sources and intensities) for outdoor application purposes especially in the dark such as a construction site at night time.
16. Over 2 log reduction was achieved for the self-disinfecting coated surface under 5000K LED (400 – 700 nm), a commercially and industrially available and widely used light source.
17. For practical application purposes, the reusability experiments of GCN/ZnO-Cu nanocomposite in degrading 4-CP and for disinfection surfaces show that the nanocomposite and the coated surface had a negligible loss in its photocatalytic activity and the structures show that there is stable. Therefore, they can be used after several cycles of photocatalytic experiments and washing.
18. The hydroxyl radical (OH^\cdot) was the dominant ROS for the GCN/ZnO-Cu nanocomposite and self-disinfecting coated surface. The photocatalytic mechanisms were proposed based on the dominant ROS.

7.2 Recommendations

The results from this research show that the synthesized visible-light-driven photocatalysts can degrade various organic contaminants, disinfection of microorganisms in wastewater, and on self-disinfecting coated surfaces. However, further research activities are recommended as thus:

- Development of versatile visible-light-driven photocatalysts that are low cost, non-toxic, large surface area, high quantum yield, and highly visible light active composite materials that can remove all forms of organic contaminants including emerging and forever chemicals such as Per-

and poly-fluoroalkyl substances (PFAS), and microorganisms in municipal, industrial, and produced wastewater.

- Development of visible-light-driven photocatalysts with reduced synthesis process time, reduced unit operations, and less energy consumption in terms of ultrasonication and heating time.
- The diffused light intensity of the light source and its application for both indoor and outdoor purposes (see [section 2.4](#) on light sources and intensities).
- Investigation of the use of the visible-light-driven photocatalyst as an electrocatalyst or electro-photocatalyst for wastewater treatment.
- Conduct more research in self-disinfecting coated surfaces on plastics and metals to understand the bonding between the photocatalyst and the substrate.
- Investigation of the application of photocatalyst as a dispersed coated glass beads or coated plastic beads in ponds to degrade contaminants and/or disinfect microorganisms under natural sunlight irradiation.
- Recommend more collaborative efforts between the industries such as material, paints, and lighting to scale up the successfully produced self-disinfecting coated surface at the laboratory scale to a pilot and industrial scale for day-to-day operations indoors and outdoors. The material industry serves to produce different types of plastics and metals, the paints industry incorporates the synthesized photocatalyst in their paints, and the lighting industry provides visible light sources of very high intensity for irradiation which Nemalux Industrial is already doing.

References

- [1] I.A. A., A.B. O., O.A. P., A.-A.T. A., D.A. O., O.T. A., Water Pollution: Effects, Prevention, and Climatic Impact, in: M. Glavan (Ed.), Water Challenges of an Urbanizing World, InTech, 2018.
<https://doi.org/10.5772/intechopen.72018>.
- [2] A.A. Inyinbor, F.A. Adekola, G.A. Olatunji, Liquid Phase Adsorption of Rhodamine B Dye onto Acid-treated *Raphia hookeri* Fruit Epicarp: Isotherms, Kinetics and Thermodynamics Studies, *S.Afr.j.Chem.* 69 (2016). <https://doi.org/10.17159/0379-4350/2016/v69a28>.
- [3] R.S. Rana, P. Singh, V. Kandari, R. Singh, R. Dobhal, S. Gupta, A review on characterization and bioremediation of pharmaceutical industries' wastewater: an Indian perspective, *Appl Water Sci* 7 (2017) 1–12. <https://doi.org/10.1007/s13201-014-0225-3>.
- [4] May 14, 2018 Melissa Denchak, Water Pollution: Everything You Need to Know, NRDC (n.d.).
<https://www.nrdc.org/stories/water-pollution-everything-you-need-know> (accessed April 9, 2022).
- [5] J. Gómez-Pastora, S. Dominguez, E. Bringas, M.J. Rivero, I. Ortiz, D.D. Dionysiou, Review and perspectives on the use of magnetic nanophotocatalysts (MNPCs) in water treatment, *Chemical Engineering Journal* 310 (2017) 407–427. <https://doi.org/10.1016/j.cej.2016.04.140>.
- [6] authorCorporate:UNESCO W.W.A. Programme, The United Nations world water development report 2020: water and climate change, (2020).
<https://unesdoc.unesco.org/ark:/48223/pf0000372985.locale=en> (accessed April 9, 2022).
- [7] J. Gamage, Z. Zhang, Applications of Photocatalytic Disinfection, *International Journal of Photoenergy* 2010 (2010) 1–11. <https://doi.org/10.1155/2010/764870>.
- [8] P.S.M. Dunlop, J.A. Byrne, N. Manga, B.R. Eggins, The photocatalytic removal of bacterial pollutants from drinking water, *Journal of Photochemistry and Photobiology A: Chemistry* 148 (2002) 355–363. [https://doi.org/10.1016/S1010-6030\(02\)00063-1](https://doi.org/10.1016/S1010-6030(02)00063-1).

- [9] R.D. Letterman, American Water Works Association, eds., Water quality and treatment: a handbook of community water supplies, 5th ed, McGraw-Hill, New York, 1999.
- [10] W.-J. Huang, G.-C. Fang, C.-C. Wang, The determination and fate of disinfection by-products from ozonation of polluted raw water, *Science of The Total Environment* 345 (2005) 261–272.
<https://doi.org/10.1016/j.scitotenv.2004.10.019>.
- [11] W.J. Masschelein, R.G. Rice, CRC Press (1973-2004), Ultraviolet light in water and wastewater sanitation, CRC Press/Taylor & Francis Group, Boca Raton; London; New York, 2018.
- [12] M.T. Yagub, T.K. Sen, S. Afroze, H.M. Ang, Dye and its removal from aqueous solution by adsorption: A review, *Advances in Colloid and Interface Science* 209 (2014) 172–184.
<https://doi.org/10.1016/j.cis.2014.04.002>.
- [13] A. Azimi, A. Azari, M. Rezakazemi, M. Ansarpour, Removal of Heavy Metals from Industrial Wastewaters: A Review, *ChemBioEng Reviews* 4 (2017) 37–59.
<https://doi.org/10.1002/cben.201600010>.
- [14] A.W. Zularisam, A.F. Ismail, R. Salim, Behaviours of natural organic matter in membrane filtration for surface water treatment — a review, *Desalination* 194 (2006) 211–231.
<https://doi.org/10.1016/j.desal.2005.10.030>.
- [15] S.M. Rodríguez, Waste water treatment by advanced oxidation processes (solar photocatalysis in degradation of industrial contaminants), (2007) 40.
- [16] M. Hincapié, M.I. Maldonado, I. Oller, W. Gernjak, J.A. Sánchez-Pérez, M.M. Ballesteros, S. Malato, Solar photocatalytic degradation and detoxification of EU priority substances, *Catalysis Today* 101 (2005) 203–210. <https://doi.org/10.1016/j.cattod.2005.03.004>.
- [17] J.M. Poyatos, M.M. Muñio, M.C. Almecija, J.C. Torres, E. Hontoria, F. Osorio, Advanced Oxidation Processes for Wastewater Treatment: State of the Art, *Water Air Soil Pollut* 205 (2010) 187–204.
<https://doi.org/10.1007/s11270-009-0065-1>.

- [18] R. Dewil, D. Mantzavinos, I. Poulios, M.A. Rodrigo, New perspectives for Advanced Oxidation Processes, *Journal of Environmental Management* 195 (2017) 93–99.
<https://doi.org/10.1016/j.jenvman.2017.04.010>.
- [19] L. Jing, B. Chen, D. Wen, J. Zheng, B. Zhang, The removal of COD and NH₃-N from atrazine production wastewater treatment using UV/O₃: experimental investigation and kinetic modeling, *Environ Sci Pollut Res* 25 (2018) 2691–2701. <https://doi.org/10.1007/s11356-017-0701-z>.
- [20] L. Yu, S. Iranmanesh, I. Keir, G. Achari, A Field Pilot Study on Treating Groundwater Contaminated with Sulfolane Using UV/H₂O₂, *Water* 12 (2020) 1200. <https://doi.org/10.3390/w12041200>.
- [21] L. Yu, G. Achari, C.H. Langford, I. Keir, A FEASIBILITY STUDY ON SULFOLANE DEGRADATION IN GROUNDWATER USING NEUTRAL FENTON CATALYSTS, (n.d.) 8.
- [22] M. Zhan, X. Yang, Q. Xian, L. Kong, Photosensitized degradation of bisphenol A involving reactive oxygen species in the presence of humic substances, *Chemosphere* 63 (2006) 378–386.
<https://doi.org/10.1016/j.chemosphere.2005.08.046>.
- [23] A.L. Boreen, W.A. Arnold, K. McNeill, Photodegradation of pharmaceuticals in the aquatic environment: A review, *Aquatic Sciences - Research Across Boundaries* 65 (2003) 320–341.
<https://doi.org/10.1007/s00027-003-0672-7>.
- [24] G.-A. Shin, K.G. Linden, M.J. Arrowood, M.D. Sobsey, Low-Pressure UV Inactivation and DNA Repair Potential of *Cryptosporidium parvum* Oocysts, *Appl Environ Microbiol* 67 (2001) 3029–3032.
<https://doi.org/10.1128/AEM.67.7.3029-3032.2001>.
- [25] H. Lu, Q. Li, W. Feng, Application Progress of O₃/UV Advanced Oxidation Technology in the Treatment of Organic Pollutants in Water, *Sustainability* 14 (2022) 1556.
<https://doi.org/10.3390/su14031556>.
- [26] C. Walling, Fenton's reagent revisited, *Acc. Chem. Res.* 8 (1975) 125–131.
<https://doi.org/10.1021/ar50088a003>.

- [27] L. Lin, W. Jiang, L. Chen, P. Xu, H. Wang, Treatment of Produced Water with Photocatalysis: Recent Advances, Affecting Factors and Future Research Prospects, *Catalysts* 10 (2020) 924. <https://doi.org/10.3390/catal10080924>.
- [28] L. Lin, H. Wang, H. Luo, P. Xu, Enhanced photocatalysis using side-glowing optical fibers coated with Fe-doped TiO₂ nanocomposite thin films, *Journal of Photochemistry and Photobiology A: Chemistry* 307–308 (2015) 88–98. <https://doi.org/10.1016/j.jphotochem.2015.04.010>.
- [29] A.E. Jacobsen, Titanium Dioxide Pigments: Correlation between Photochemical Reactivity and Chalking., *Ind. Eng. Chem.* 41 (1949) 523–526. <https://doi.org/10.1021/ie50471a018>.
- [30] H.A. Foster, I.B. Ditta, S. Varghese, A. Steele, Photocatalytic disinfection using titanium dioxide: spectrum and mechanism of antimicrobial activity, *Appl Microbiol Biotechnol* 90 (2011) 1847–1868. <https://doi.org/10.1007/s00253-011-3213-7>.
- [31] A. Fujishima, K. Honda, Electrochemical Photolysis of Water at a Semiconductor Electrode, *Nature* 238 (1972) 37–38. <https://doi.org/10.1038/238037a0>.
- [32] Y. Deng, R. Zhao, Advanced Oxidation Processes (AOPs) in Wastewater Treatment, *Curr Pollution Rep* 1 (2015) 167–176. <https://doi.org/10.1007/s40726-015-0015-z>.
- [33] W.H. Glaze, Drinking-water treatment with ozone, *Environ. Sci. Technol.* 21 (1987) 224–230. <https://doi.org/10.1021/es00157a001>.
- [34] W.H. Glaze, J.-W. Kang, D.H. Chapin, The Chemistry of Water Treatment Processes Involving Ozone, Hydrogen Peroxide and Ultraviolet Radiation, *Ozone: Science & Engineering* 9 (1987) 335–352. <https://doi.org/10.1080/01919518708552148>.
- [35] S. Lacombe, N. Keller, Photocatalysis: fundamentals and applications in JEP 2011, *Environ Sci Pollut Res* 19 (2012) 3651–3654. <https://doi.org/10.1007/s11356-012-1040-8>.

- [36] T. Lammel, P. Boisseaux, M.-L. Fernández-Cruz, J.M. Navas, Internalization and cytotoxicity of graphene oxide and carboxyl graphene nanoplatelets in the human hepatocellular carcinoma cell line Hep G2, *Part Fibre Toxicol* 10 (2013) 27. <https://doi.org/10.1186/1743-8977-10-27>.
- [37] L.A.V. de Luna, A.C.M. de Moraes, S.R. Consonni, C.D. Pereira, S. Cadore, S. Giorgio, O.L. Alves, Comparative in vitro toxicity of a graphene oxide-silver nanocomposite and the pristine counterparts toward macrophages, *J Nanobiotechnol* 14 (2016) 12. <https://doi.org/10.1186/s12951-016-0165-1>.
- [38] G. Ren, H. Han, Y. Wang, S. Liu, J. Zhao, X. Meng, Z. Li, Recent Advances of Photocatalytic Application in Water Treatment: A Review, *Nanomaterials* 11 (2021) 1804. <https://doi.org/10.3390/nano11071804>.
- [39] R. Li, C. Li, Photocatalytic Water Splitting on Semiconductor-Based Photocatalysts, in: *Advances in Catalysis*, Elsevier, 2017: pp. 1–57. <https://doi.org/10.1016/bs.acat.2017.09.001>.
- [40] Hydroxyl Radicals Reactivity | Hydrogen Link, (n.d.). <https://www.hydrogenlink.com/hydroxylradicalsreactivity> (accessed July 22, 2022).
- [41] Standard Reduction Potential, Chemistry LibreTexts (2013). [https://chem.libretexts.org/Bookshelves/Analytical_Chemistry/Supplemental_Modules_\(Analytical_Chemistry\)/Electrochemistry/Redox_Chemistry/Standard_Reduction_Potential](https://chem.libretexts.org/Bookshelves/Analytical_Chemistry/Supplemental_Modules_(Analytical_Chemistry)/Electrochemistry/Redox_Chemistry/Standard_Reduction_Potential) (accessed July 22, 2022).
- [42] G. Carré, E. Hamon, S. Ennahar, M. Estner, M.-C. Lett, P. Horvatovich, J.-P. Gies, V. Keller, N. Keller, P. Andre, TiO₂ Photocatalysis Damages Lipids and Proteins in Escherichia coli, *Appl Environ Microbiol* 80 (2014) 2573–2581. <https://doi.org/10.1128/AEM.03995-13>.
- [43] Centre international de recherche sur le cancer, ed., A review of human carcinogens, International agency for research on cancer, Lyon, 2012.

- [44] Solar Driven Photocatalysis – an Efficient Method for Removal of Pesticides from Water and Wastewater, *Biointerface Res Appl Chem* 11 (2020) 9071–9084.
<https://doi.org/10.33263/BRIAC112.90719084>.
- [45] Unit Conversions, (n.d.). <https://halas.rice.edu/unit-conversions> (accessed June 30, 2022).
- [46] Y. Lin, G. Yuan, R. Liu, S. Zhou, S.W. Sheehan, D. Wang, Semiconductor nanostructure-based photoelectrochemical water splitting: A brief review, *Chemical Physics Letters* 507 (2011) 209–215.
<https://doi.org/10.1016/j.cplett.2011.03.074>.
- [47] A. Mills, S. Le Hunte, An overview of semiconductor photocatalysis, *Journal of Photochemistry and Photobiology A: Chemistry* 108 (1997) 1–35. [https://doi.org/10.1016/S1010-6030\(97\)00118-4](https://doi.org/10.1016/S1010-6030(97)00118-4).
- [48] A. Janotti, C.G. Van de Walle, Fundamentals of zinc oxide as a semiconductor, *Rep. Prog. Phys.* 72 (2009) 126501. <https://doi.org/10.1088/0034-4885/72/12/126501>.
- [49] A.A. Kashale, A.S. Rasal, G.P. Kamble, V.H. Ingole, P.K. Dwivedi, S.J. Rajoba, L.D. Jadhav, Y.-C. Ling, J.-Y. Chang, A.V. Ghule, Biosynthesized Co-doped TiO₂ nanoparticles based anode for lithium-ion battery application and investigating the influence of dopant concentrations on its performance, *Composites Part B: Engineering* 167 (2019) 44–50.
<https://doi.org/10.1016/j.compositesb.2018.12.001>.
- [50] Z. Liu, B. Shao, G. Zeng, M. Chen, Z. Li, Y. Liu, Y. Jiang, H. Zhong, Y. Liu, M. Yan, Effects of rhamnolipids on the removal of 2,4,2,4-tetrabrominated biphenyl ether (BDE-47) by *Phanerochaete chrysosporium* analyzed with a combined approach of experiments and molecular docking, *Chemosphere* 210 (2018) 922–930. <https://doi.org/10.1016/j.chemosphere.2018.07.114>.
- [51] C. Zhang, Y. Li, D. Shuai, Y. Shen, W. Xiong, L. Wang, Graphitic carbon nitride (g-C₃N₄)-based photocatalysts for water disinfection and microbial control: A review, *Chemosphere* 214 (2019) 462–479. <https://doi.org/10.1016/j.chemosphere.2018.09.137>.

- [52] L. Shi, L. Liang, J. Ma, F. Wang, J. Sun, Remarkably enhanced photocatalytic activity of ordered mesoporous carbon/g-C₃N₄ composite photocatalysts under visible light, *Dalton Trans.* 43 (2014) 7236–7244. <https://doi.org/10.1039/C4DT00087K>.
- [53] M. Tanveer, C. Cao, Z. Ali, I. Aslam, F. Idrees, W.S. Khan, F.K. But, M. Tahir, N. Mahmood, Template free synthesis of CuS nanosheet-based hierarchical microspheres: an efficient natural light driven photocatalyst, *CrystEngComm* 16 (2014) 5290. <https://doi.org/10.1039/c4ce00090k>.
- [54] S.P. Adhikari, H.R. Pant, J.H. Kim, H.J. Kim, C.H. Park, C.S. Kim, One pot synthesis and characterization of Ag-ZnO/g-C₃N₄ photocatalyst with improved photoactivity and antibacterial properties, *Colloids and Surfaces A: Physicochemical and Engineering Aspects* 482 (2015) 477–484. <https://doi.org/10.1016/j.colsurfa.2015.07.003>.
- [55] M. Faisal, A.A. Ismail, F.A. Harraz, S.A. Al-Sayari, A.M. El-Toni, M.S. Al-Assiri, Synthesis of highly dispersed silver doped g-C₃N₄ nanocomposites with enhanced visible-light photocatalytic activity, *Materials & Design* 98 (2016) 223–230. <https://doi.org/10.1016/j.matdes.2016.03.019>.
- [56] P. Murugesan, J.A. Moses, C. Anandharamakrishnan, Photocatalytic disinfection efficiency of 2D structure graphitic carbon nitride-based nanocomposites: a review, *J Mater Sci* 54 (2019) 12206–12235. <https://doi.org/10.1007/s10853-019-03695-2>.
- [57] L. Jiang, X. Yuan, Y. Pan, J. Liang, G. Zeng, Z. Wu, H. Wang, Doping of graphitic carbon nitride for photocatalysis: A reveiw, *Applied Catalysis B: Environmental* 217 (2017) 388–406. <https://doi.org/10.1016/j.apcatb.2017.06.003>.
- [58] Y. Zheng, L. Lin, B. Wang, X. Wang, Graphitic Carbon Nitride Polymers toward Sustainable Photoredox Catalysis, *Angew. Chem. Int. Ed.* 54 (2015) 12868–12884. <https://doi.org/10.1002/anie.201501788>.
- [59] Y. Wang, S. Zhao, Y. Zhang, J. Fang, Y. Zhou, S. Yuan, C. Zhang, W. Chen, One-pot synthesis of K-doped g-C₃N₄ nanosheets with enhanced photocatalytic hydrogen production under visible-light

- irradiation, *Applied Surface Science* 440 (2018) 258–265.
<https://doi.org/10.1016/j.apsusc.2018.01.091>.
- [60] Y. Li, S. Wu, L. Huang, J. Wang, H. Xu, H. Li, Synthesis of carbon-doped g-C₃N₄ composites with enhanced visible-light photocatalytic activity, *Materials Letters* 137 (2014) 281–284.
<https://doi.org/10.1016/j.matlet.2014.08.142>.
- [61] S. Das, S. Sinha, B. Das, R. Jayabalan, M. Suar, A. Mishra, A.J. Tamhankar, C. Stålsby Lundborg, S.K. Tripathy, Disinfection of Multidrug Resistant *Escherichia coli* by Solar-Photocatalysis using Fe-doped ZnO Nanoparticles, *Sci Rep* 7 (2017) 104. <https://doi.org/10.1038/s41598-017-00173-0>.
- [62] A. Basu, A.J. Misra, M. Behera, S.K. Behera, A.K. Nayak, N.K. Dhal, A. Mishra, B.K. Satpathy, C.S. Lundborg, S.K. Tripathy, Photocatalytic disinfection of extended-spectrum beta-lactamase producing *Escherichia coli* using Alumina/ZnO heterostructures, *Journal of Environmental Chemical Engineering* 9 (2021) 106334. <https://doi.org/10.1016/j.jece.2021.106334>.
- [63] J. Fu, B. Zhu, C. Jiang, B. Cheng, W. You, J. Yu, Hierarchical Porous O-Doped g-C₃N₄ with Enhanced Photocatalytic CO₂ Reduction Activity, *Small* 13 (2017) 1603938.
<https://doi.org/10.1002/sml.201603938>.
- [64] S. Le, T. Jiang, Q. Zhao, X. Liu, Y. Li, B. Fang, M. Gong, Cu-doped mesoporous graphitic carbon nitride for enhanced visible-light driven photocatalysis, *RSC Adv.* 6 (2016) 38811–38819.
<https://doi.org/10.1039/C6RA03982K>.
- [65] W.-D. Oh, V.W.C. Chang, Z.-T. Hu, R. Goei, T.-T. Lim, Enhancing the catalytic activity of g-C₃N₄ through Me doping (Me = Cu, Co and Fe) for selective sulfathiazole degradation via redox-based advanced oxidation process, *Chemical Engineering Journal* 323 (2017) 260–269.
<https://doi.org/10.1016/j.cej.2017.04.107>.

- [66] C.H. Nguyen, C.-C. Fu, R.-S. Juang, Degradation of methylene blue and methyl orange by palladium-doped TiO₂ photocatalysis for water reuse: Efficiency and degradation pathways, *Journal of Cleaner Production* 202 (2018) 413–427. <https://doi.org/10.1016/j.jclepro.2018.08.110>.
- [67] G. Dong, K. Zhao, L. Zhang, Carbon self-doping induced high electronic conductivity and photoreactivity of g-C₃N₄, *Chem. Commun.* 48 (2012) 6178. <https://doi.org/10.1039/c2cc32181e>.
- [68] X. She, L. Liu, H. Ji, Z. Mo, Y. Li, L. Huang, D. Du, H. Xu, H. Li, Template-free synthesis of 2D porous ultrathin nonmetal-doped g-C₃N₄ nanosheets with highly efficient photocatalytic H₂ evolution from water under visible light, *Applied Catalysis B: Environmental* 187 (2016) 144–153. <https://doi.org/10.1016/j.apcatb.2015.12.046>.
- [69] L. Cao, R. Wang, D. Wang, Synthesis and characterization of sulfur self-doped g-C₃N₄ with efficient visible-light photocatalytic activity, *Materials Letters* 149 (2015) 50–53. <https://doi.org/10.1016/j.matlet.2015.02.119>.
- [70] J. Zhao, L. Ma, H. Wang, Y. Zhao, J. Zhang, S. Hu, Novel band gap-tunable K–Na co-doped graphitic carbon nitride prepared by molten salt method, *Applied Surface Science* 332 (2015) 625–630. <https://doi.org/10.1016/j.apsusc.2015.01.233>.
- [71] S. Hu, L. Ma, J. You, F. Li, Z. Fan, G. Lu, D. Liu, J. Gui, Enhanced visible light photocatalytic performance of g-C₃N₄ photocatalysts co-doped with iron and phosphorus, *Applied Surface Science* 311 (2014) 164–171. <https://doi.org/10.1016/j.apsusc.2014.05.036>.
- [72] Z. Lin, X. Wang, Ionic Liquid Promoted Synthesis of Conjugated Carbon Nitride Photocatalysts from Urea, *ChemSusChem* 7 (2014) 1547–1550. <https://doi.org/10.1002/cssc.201400016>.
- [73] H. Wang, X. Yuan, H. Wang, X. Chen, Z. Wu, L. Jiang, W. Xiong, G. Zeng, Facile synthesis of Sb₂S₃/ultrathin g-C₃N₄ sheets heterostructures embedded with g-C₃N₄ quantum dots with enhanced NIR-light photocatalytic performance, *Applied Catalysis B: Environmental* 193 (2016) 36–46. <https://doi.org/10.1016/j.apcatb.2016.03.075>.

- [74] J. Zhang, M. Zhang, R.-Q. Sun, X. Wang, A Facile Band Alignment of Polymeric Carbon Nitride Semiconductors to Construct Isotype Heterojunctions, *Angew. Chem. Int. Ed.* 51 (2012) 10145–10149. <https://doi.org/10.1002/anie.201205333>.
- [75] J. Luo, G. Dong, Y. Zhu, Z. Yang, C. Wang, Switching of semiconducting behavior from n -type to p -type induced high photocatalytic NO removal activity in g-C₃N₄, *Applied Catalysis B: Environmental* 214 (2017) 46–56. <https://doi.org/10.1016/j.apcatb.2017.05.016>.
- [76] X.-F. Wu, C.-X. Zhang, Y.-D. Wang, J.-Z. Su, J.-R. Zhang, Y.-M. Feng, M. Zhang, X. Tong, W.-G. Zhang, X.-G. Sun, Synthesis of Ag₂CrO₄/SnO₂ n–n type heterojunction as a visible light photocatalyst for degradation of rhodamine B, *J Mater Sci: Mater Electron* 29 (2018) 20959–20967. <https://doi.org/10.1007/s10854-018-0240-5>.
- [77] H. Jiang, Y. Li, D. Wang, X. Hong, B. Liang, Recent Advances in Heteroatom Doped Graphitic Carbon Nitride (g-C₃N₄) and g-C₃N₄/Metal Oxide Composite Photocatalysts, *COC* 24 (2020) 673–693. <https://doi.org/10.2174/1385272824666200309151648>.
- [78] S.I. Sinar Mashuri, M.L. Ibrahim, M.F. Kasim, M.S. Mastuli, U. Rashid, A.H. Abdullah, A. Islam, N. Asikin Mijan, Y.H. Tan, N. Mansir, N.H. Mohd Kaus, T.-Y. Yun Hin, Photocatalysis for Organic Wastewater Treatment: From the Basis to Current Challenges for Society, *Catalysts* 10 (2020) 1260. <https://doi.org/10.3390/catal10111260>.
- [79] S.P. Adhikari, G.P. Awasthi, H.J. Kim, C.H. Park, C.S. Kim, Electrospinning Directly Synthesized Porous TiO₂ Nanofibers Modified by Graphitic Carbon Nitride Sheets for Enhanced Photocatalytic Degradation Activity under Solar Light Irradiation, *Langmuir* 32 (2016) 6163–6175. <https://doi.org/10.1021/acs.langmuir.6b01085>.
- [80] I.M. Sundaram, S. Kalimuthu, G. Ponniah, Highly active ZnO modified g-C₃N₄ Nanocomposite for dye degradation under UV and Visible Light with enhanced stability and antimicrobial activity, *Composites Communications* 5 (2017) 64–71. <https://doi.org/10.1016/j.coco.2017.07.003>.

- [81] J. Tang, R. Guo, W. Zhou, C. Huang, W. Pan, Ball-flower like NiO/g-C₃N₄ heterojunction for efficient visible light photocatalytic CO₂ reduction, *Applied Catalysis B: Environmental* 237 (2018) 802–810. <https://doi.org/10.1016/j.apcatb.2018.06.042>.
- [82] V. Vaiano, Visible-Light-Active Photocatalysts for Environmental Remediation and Organic Synthesis, *Photochem* 1 (2021) 460–461. <https://doi.org/10.3390/photochem1030029>.
- [83] G. Ren, H. Han, Y. Wang, S. Liu, J. Zhao, X. Meng, Z. Li, Recent Advances of Photocatalytic Application in Water Treatment: A Review, *Nanomaterials* 11 (2021) 1804. <https://doi.org/10.3390/nano11071804>.
- [84] Z. Li, X. Meng, Z. Zhang, Equilibrium and kinetic modelling of adsorption of Rhodamine B on MoS₂, *Materials Research Bulletin* 111 (2019) 238–244. <https://doi.org/10.1016/j.materresbull.2018.11.012>.
- [85] C.-C. Wang, J.-R. Li, X.-L. Lv, Y.-Q. Zhang, G. Guo, Photocatalytic organic pollutants degradation in metal–organic frameworks, *Energy Environ. Sci.* 7 (2014) 2831–2867. <https://doi.org/10.1039/C4EE01299B>.
- [86] X. Ni, C. Chen, Q. Wang, Z. Li, One-step hydrothermal synthesis of SnO₂-MoS₂ composite heterostructure for improved visible light photocatalytic performance, *Chemical Physics* 525 (2019) 110398. <https://doi.org/10.1016/j.chemphys.2019.110398>.
- [87] A.M. Maszenan, Y. Liu, W.J. Ng, Bioremediation of wastewaters with recalcitrant organic compounds and metals by aerobic granules, *Biotechnology Advances* 29 (2011) 111–123. <https://doi.org/10.1016/j.biotechadv.2010.09.004>.
- [88] X. Li, J.W. Cubbage, T.A. Tetzlaff, W.S. Jenks, Photocatalytic Degradation of 4-Chlorophenol. 1. The Hydroquinone Pathway, *J. Org. Chem.* 64 (1999) 8509–8524. <https://doi.org/10.1021/jo990820y>.

- [89] R.A. Hamza, O.T. Iorhemen, J.H. Tay, Occurrence, impacts and removal of emerging substances of concern from wastewater, *Environmental Technology & Innovation* 5 (2016) 161–175.
<https://doi.org/10.1016/j.eti.2016.02.003>.
- [90] Factsheet on 2,4-D by US EPA.pdf, (n.d.).
- [91] H. Canada, Guidelines for Canadian Drinking Water Quality - Summary Table, (2014).
<https://www.canada.ca/en/health-canada/services/environmental-workplace-health/reports-publications/water-quality/guidelines-canadian-drinking-water-quality-summary-table.html>
(accessed June 30, 2021).
- [92] G. Heydari, C.H. Langford, G. Achari, Passive Solar Photocatalytic Treatment of Emerging Contaminants in Water: A Field Study, *Catalysts* 9 (2019) 1045.
<https://doi.org/10.3390/catal9121045>.
- [93] D. Wu, M. Long, Visible light assisted photocatalytic degradation of methyl orange using Ag/N–TiO₂ photocatalysts, *Water Science and Technology* 65 (2012) 1027–1032.
<https://doi.org/10.2166/wst.2012.926>.
- [94] J.G.M. de Sousa, T.V.C. da Silva, N.P. de Moraes, M.L. Caetano Pinto da Silva, R. da Silva Rocha, R. Landers, L.A. Rodrigues, Visible light-driven ZnO/g-C₃N₄/carbon xerogel ternary photocatalyst with enhanced activity for 4-chlorophenol degradation, *Materials Chemistry and Physics* 256 (2020) 123651. <https://doi.org/10.1016/j.matchemphys.2020.123651>.
- [95] D.A.K. Alenazi, M. Aslam, S. Chandrasekaran, M.T. Soomro, S. Ali, E.Y. Danish, I.M.I. Ismail, A. Hameed, Facile fabrication of MoO₃/g-C₃N₄ p-n junction for boosted photocatalytic elimination of 2,4-D under natural sunlight exposure, *Journal of Environmental Chemical Engineering* 9 (2021) 106304. <https://doi.org/10.1016/j.jece.2021.106304>.
- [96] J. Zhong, H. Jiang, Z. Wang, Z. Yu, L. Wang, J.F. Mueller, J. Guo, Efficient photocatalytic destruction of recalcitrant micropollutants using graphitic carbon nitride under simulated sunlight irradiation,

- Environmental Science and Ecotechnology 5 (2021) 100079.
<https://doi.org/10.1016/j.es.2021.100079>.
- [97] T. Matsunaga, R. Tomoda, T. Nakajima, H. Wake, Photoelectrochemical sterilization of microbial cells by semiconductor powders, *FEMS Microbiology Letters* 29 (1985) 211–214.
<https://doi.org/10.1111/j.1574-6968.1985.tb00864.x>.
- [98] P. Wu, J.A. Imlay, J.K. Shang, Mechanism of *Escherichia coli* inactivation on palladium-modified nitrogen-doped titanium dioxide, *Biomaterials* 31 (2010) 7526–7533.
<https://doi.org/10.1016/j.biomaterials.2010.06.032>.
- [99] I.X. Yin, J. Zhang, I.S. Zhao, M.L. Mei, Q. Li, C.H. Chu, The Antibacterial Mechanism of Silver Nanoparticles and Its Application in Dentistry, *IJN Volume* 15 (2020) 2555–2562.
<https://doi.org/10.2147/IJN.S246764>.
- [100] D.J. Weber, W.A. Rutala, Self-disinfecting surfaces: Review of current methodologies and future prospects, *American Journal of Infection Control* 41 (2013) S31–S35.
<https://doi.org/10.1016/j.ajic.2012.12.005>.
- [101] K.S. Siddiqi, A. ur Rahman, Tajuddin, A. Husen, Properties of Zinc Oxide Nanoparticles and Their Activity Against Microbes, *Nanoscale Res Lett* 13 (2018) 141. <https://doi.org/10.1186/s11671-018-2532-3>.
- [102] I. Salah, I.P. Parkin, E. Allan, Copper as an antimicrobial agent: recent advances, *RSC Adv.* 11 (2021) 18179–18186. <https://doi.org/10.1039/D1RA02149D>.
- [103] C. Regmi, B. Joshi, S.K. Ray, G. Gyawali, R.P. Pandey, Understanding Mechanism of Photocatalytic Microbial Decontamination of Environmental Wastewater, *Front. Chem.* 6 (2018) 33.
<https://doi.org/10.3389/fchem.2018.00033>.

- [104] X. Zhang, C.-W. Yang, H.-Q. Yu, G.-P. Sheng, Light-induced reduction of silver ions to silver nanoparticles in aquatic environments by microbial extracellular polymeric substances (EPS), *Water Research* 106 (2016) 242–248. <https://doi.org/10.1016/j.watres.2016.10.004>.
- [105] J. Deng, J. Liang, M. Li, M. Tong, Enhanced visible-light-driven photocatalytic bacteria disinfection by g-C₃N₄-AgBr, *Colloids and Surfaces B: Biointerfaces* 152 (2017) 49–57. <https://doi.org/10.1016/j.colsurfb.2017.01.003>.
- [106] C. Karunakaran, G. Abiramasundari, P. Gomathisankar, G. Manikandan, V. Anandi, Preparation and characterization of ZnO–TiO₂ nanocomposite for photocatalytic disinfection of bacteria and detoxification of cyanide under visible light, *Materials Research Bulletin* 46 (2011) 1586–1592. <https://doi.org/10.1016/j.materresbull.2011.06.019>.
- [107] W. Zhang, C. Yu, Z. Sun, S. Zheng, Visible-Light-Driven Catalytic Disinfection of *Staphylococcus aureus* Using Sandwich Structure g-C₃N₄/ZnO/Stellerite Hybrid Photocatalyst, *Journal of Microbiology and Biotechnology* 28 (2018) 957–967. <https://doi.org/10.4014/jmb.1712.12057>.
- [108] T.W. Ng, L. Zhang, J. Liu, G. Huang, W. Wang, P.K. Wong, Visible-light-driven photocatalytic inactivation of *Escherichia coli* by magnetic Fe₂O₃-AgBr, *Water Research* 90 (2016) 111–118. <https://doi.org/10.1016/j.watres.2015.12.022>.
- [109] Y. Li, C. Zhang, D. Shuai, S. Naraginti, D. Wang, W. Zhang, Visible-light-driven photocatalytic inactivation of MS2 by metal-free g-C₃N₄: Virucidal performance and mechanism, *Water Research* 106 (2016) 249–258. <https://doi.org/10.1016/j.watres.2016.10.009>.
- [110] A.R. Badireddy, J.F. Budarz, S. Chellam, M.R. Wiesner, Bacteriophage Inactivation by UV-A Illuminated Fullerenes: Role of Nanoparticle-Virus Association and Biological Targets, *Environ. Sci. Technol.* 46 (2012) 5963–5970. <https://doi.org/10.1021/es300340u>.

- [111] P. Kelly, G. West, M. Ratova, L. Fisher, S. Ostovarpour, J. Verran, Structural Formation and Photocatalytic Activity of Magnetron Sputtered Titania and Doped-Titania Coatings, *Molecules* 19 (2014) 16327–16348. <https://doi.org/10.3390/molecules191016327>.
- [112] S. Khan, I.A. Qazi, I. Hashmi, M.A. Awan, N.-S.S. Zaidi, Synthesis of Silver-Doped Titanium TiO_2 Powder-Coated Surfaces and Its Ability to Inactivate *Pseudomonas aeruginosa* and *Bacillus subtilis*, *Journal of Nanomaterials* 2013 (2013) 1–8. <https://doi.org/10.1155/2013/531010>.
- [113] M. Liu, K. Sunada, K. Hashimoto, M. Miyauchi, Visible-light sensitive $\text{Cu}(\text{II})$ - TiO_2 with sustained anti-viral activity for efficient indoor environmental remediation, *J. Mater. Chem. A* 3 (2015) 17312–17319. <https://doi.org/10.1039/C5TA03756E>.
- [114] B. Lallo da Silva, M.P. Abuçafy, E. Berbel Manaia, J.A. Oshiro Junior, B.G. Chiari-Andréo, R.C.R. Pietro, L.A. Chiavacci, Relationship Between Structure And Antimicrobial Activity Of Zinc Oxide Nanoparticles: An Overview, *IJN Volume* 14 (2019) 9395–9410. <https://doi.org/10.2147/IJN.S216204>.
- [115] T. Feng, J. Liang, Z. Ma, M. Li, M. Tong, Bactericidal activity and mechanisms of BiOBr-AgBr under both dark and visible light irradiation conditions, *Colloids and Surfaces B: Biointerfaces* 167 (2018) 275–283. <https://doi.org/10.1016/j.colsurfb.2018.04.022>.
- [116] W. Zhang, C. Yu, Z. Sun, S. Zheng, Visible-Light-Driven Catalytic Disinfection of *Staphylococcus aureus* Using Sandwich Structure $\text{g-C}_3\text{N}_4/\text{ZnO}/\text{Stellerite}$ Hybrid Photocatalyst, *Journal of Microbiology and Biotechnology* 28 (2018) 957–967. <https://doi.org/10.4014/jmb.1712.12057>.
- [117] L. Zhu, C. He, Y. Huang, Z. Chen, D. Xia, M. Su, Y. Xiong, S. Li, D. Shu, Enhanced photocatalytic disinfection of *E. coli* 8099 using Ag/BiOI composite under visible light irradiation, *Separation and Purification Technology* 91 (2012) 59–66. <https://doi.org/10.1016/j.seppur.2011.10.026>.

- [118] S. Ma, S. Zhan, Y. Xia, P. Wang, Q. Hou, Q. Zhou, Enhanced photocatalytic bactericidal performance and mechanism with novel Ag/ZnO/g-C₃N₄ composite under visible light, *Catalysis Today* 330 (2019) 179–188. <https://doi.org/10.1016/j.cattod.2018.04.014>.
- [119] M.A. Qamar, S. Shahid, M. Javed, M. Sher, S. Iqbal, A. Bahadur, D. Li, Fabricated novel g-C₃N₄/Mn doped ZnO nanocomposite as highly active photocatalyst for the disinfection of pathogens and degradation of the organic pollutants from wastewater under sunlight radiations, *Colloids and Surfaces A: Physicochemical and Engineering Aspects* 611 (2021) 125863. <https://doi.org/10.1016/j.colsurfa.2020.125863>.
- [120] Strunk, 2021 (txtbook) - Heterogeneous Photocatalysis..... (Monochromatic vs polychromatic lights).pdf, (n.d.).
- [121] NEMALUX-SPEC-SL-A10.pdf, (n.d.).
- [122] 21.1 Planck and Quantum Nature of Light | Texas Gateway, (n.d.). <https://www.texasgateway.org/resource/211-planck-and-quantum-nature-light> (accessed September 8, 2023).
- [123] Lux and Kelvin - An Overlooked Relationship Between Illuminance and Color Temperature | Waveform Lighting, (n.d.). <https://www.waveformlighting.com/home-residential/lux-and-kelvin-an-overlooked-relationship-between-illuminance-and-color-temperature> (accessed September 8, 2023).
- [124] how to evaluate daylight(1).pdf, (n.d.).
- [125] M. Jin, X. Chen, B. Pan, Simultaneous determination of 19 Chlorophenols in water by Liquid Chromatography-Mass Spectrometry with solid-phase extraction, *Journal of Liquid Chromatography & Related Technologies* 29 (2006) 1369–1380. <https://doi.org/10.1080/10826070600598944>.

- [126] S.K. Khetan, T.J. Collins, Human pharmaceuticals in the aquatic environment: A Challenge to green chemistry, *Chem. Rev.* 107 (2007) 2319–2364. <https://doi.org/10.1021/cr020441w>.
- [127] H. Canada, Chlorophenols, (2015). <https://www.canada.ca/en/health-canada/services/publications/healthy-living/chlorophenols.html> (accessed June 18, 2021).
- [128] M. Gómez, M.D. Murcia, R. Dams, N. Christofi, E. Gómez, J.L. Gómez, Removal efficiency and toxicity reduction of 4-chlorophenol with physical, chemical and biochemical methods, *Environmental Technology* 33 (2012) 1055–1064. <https://doi.org/10.1080/09593330.2011.606847>.
- [129] K. Kuśmierk, A. Świątkowski, Removal of chlorophenols from aqueous solutions by sorption onto walnut, pistachio and hazelnut shells, *Polish Journal of Chemical Technology* 17 (2015) 23–31. <https://doi.org/10.1515/pjct-2015-0005>.
- [130] G. L, C. I, C. P, S. A, Treatment Options for Reclaiming Wastewater Produced by the Pesticide Industry, *Int J Water Wastewater Treat* 4 (2018) 1–15. <https://doi.org/10.16966/2381-5299.149>.
- [131] L.G.C. Villegas, N. Mashhadi, M. Chen, D. Mukherjee, K.E. Taylor, N. Biswas, A Short Review of Techniques for Phenol Removal from Wastewater, *Curr Pollution Rep* 2 (2016) 157–167. <https://doi.org/10.1007/s40726-016-0035-3>.
- [132] Y. Yang, X. Li, C. Zhou, W. Xiong, G. Zeng, D. Huang, C. Zhang, W. Wang, B. Song, X. Tang, X. Li, H. Guo, Recent advances in application of graphitic carbon nitride-based catalysts for degrading organic contaminants in water through advanced oxidation processes beyond photocatalysis: A critical review, *Water Research* 184 (2020) 116200. <https://doi.org/10.1016/j.watres.2020.116200>.
- [133] N. Suriyachai, S. Chuangchote, N. Laosiripojana, V. Champreda, T. Sagawa, Synergistic Effects of Co-Doping on Photocatalytic Activity of Titanium Dioxide on Glucose Conversion to Value-Added Chemicals, *ACS Omega* 5 (2020) 20373–20381. <https://doi.org/10.1021/acsomega.0c02334>.

- [134] A. Nashim, S. Martha, K.M. Parida, Gd₂/Ti₂O₇/In₂O₃: Efficient visible-light-driven heterojunction-based composite photocatalysts for hydrogen production, *Chem. Cat. Chem* 5 (2013) 2352–2359. <https://doi.org/10.1002/cctc.201300037>.
- [135] C. Zhou, Z. Zeng, G. Zeng, D. Huang, R. Xiao, M. Cheng, C. Zhang, W. Xiong, C. Lai, Y. Yang, W. Wang, H. Yi, B. Li, Visible-light-driven photocatalytic degradation of sulfamethazine by surface engineering of carbon nitride : Properties, degradation pathway and mechanisms, *Journal of Hazardous Materials* 380 (2019) 120815. <https://doi.org/10.1016/j.jhazmat.2019.120815>.
- [136] Y. Wang, X. Wang, M. Antonietti, Polymeric Graphitic Carbon Nitride as a Heterogeneous Organocatalyst: From Photochemistry to Multipurpose Catalysis to Sustainable Chemistry, *Angew. Chem. Int. Ed.* 51 (2012) 68–89. <https://doi.org/10.1002/anie.201101182>.
- [137] Y. Zheng, Z. Zhang, C. Li, A comparison of graphitic carbon nitrides synthesized from different precursors through pyrolysis, *Journal of Photochemistry and Photobiology A: Chemistry* 332 (2017) 32–44. <https://doi.org/10.1016/j.jphotochem.2016.08.005>.
- [138] W. Zhang, Q. Zhang, F. Dong, Z. Zhao, The Multiple Effects of Precursors on the Properties of Polymeric Carbon Nitride, *International Journal of Photoenergy* 2013 (2013) 1–9. <https://doi.org/10.1155/2013/685038>.
- [139] S.C. Yan, Z.S. Li, Z.G. Zou, Photodegradation Performance of g-C₃N₄ Fabricated by Directly Heating Melamine, *Langmuir* 25 (2009) 10397–10401. <https://doi.org/10.1021/la900923z>.
- [140] S.-Z. Wu, C.-H. Chen, W.-D. Zhang, Etching graphitic carbon nitride by acid for enhanced photocatalytic activity toward degradation of 4-nitrophenol, *Chinese Chemical Letters* 25 (2014) 1247–1251. <https://doi.org/10.1016/j.cclet.2014.05.017>.
- [141] Y. Li, H. Zhang, P. Liu, D. Wang, Y. Li, H. Zhao, Cross-Linked g-C₃N₄ /rGO nanocomposites with tunable band structure and enhanced visible light photocatalytic activity, *Small* (2013). <https://doi.org/10.1002/sml.201203135>.

- [142] Z. Zhang, J. Huang, M. Zhang, Q. Yuan, B. Dong, Ultrathin hexagonal SnS₂ nanosheets coupled with g-C₃N₄ nanosheets as 2D/2D heterojunction photocatalysts toward high photocatalytic activity, *Applied Catalysis B: Environmental* 163 (2015) 298–305.
<https://doi.org/10.1016/j.apcatb.2014.08.013>.
- [143] Y. Ren, Q. Zhao, X. Li, W. Xiong, M. Tade, L. Liu, 2D Porous graphitic C₃N₄ nanosheets/Ag₃PO₄ nanocomposites for enhanced visible-light photocatalytic degradation of 4-chlorophenol, *J Nanopart Res* (2014) 8.
- [144] J. Xu, Y. Li, S. Peng, G. Lu, S. Li, Eosin Y-sensitized graphitic carbon nitride fabricated by heating urea for visible light photocatalytic hydrogen evolution: the effect of the pyrolysis temperature of urea, *Phys. Chem. Chem. Phys.* 15 (2013) 7657. <https://doi.org/10.1039/c3cp44687e>.
- [145] N. Kumar, N.S. Chauhan, A. Mittal, S. Sharma, TiO₂ and its composites as promising biomaterials: a review, *Biomaterials* 31 (2018) 147–159. <https://doi.org/10.1007/s10534-018-0078-6>.
- [146] M. Faisal, A.A. Ismail, F.A. Harraz, S.A. Al-Sayari, A.M. El-Toni, M.S. Al-Assiri, Synthesis of highly dispersed silver doped g-C₃N₄ nanocomposites with enhanced visible-light photocatalytic activity, *Materials & Design* 98 (2016) 223–230. <https://doi.org/10.1016/j.matdes.2016.03.019>.
- [147] P. Makuła, M. Pacia, W. Macyk, How to correctly determine the band gap energy of modified semiconductor photocatalysts based on UV–Vis spectra, *J. Phys. Chem. Lett.* 9 (2018) 6814–6817. <https://doi.org/10.1021/acs.jpclett.8b02892>.
- [148] L. Yu, G. Achari, C.H. Langford, LED-Based Photocatalytic Treatment of Pesticides and Chlorophenols, *J. Environ. Eng.* 139 (2013) 1146–1151. [https://doi.org/10.1061/\(ASCE\)EE.1943-7870.0000730](https://doi.org/10.1061/(ASCE)EE.1943-7870.0000730).
- [149] K. Watanabe, S. Matsuda, C.A. Cuevas, A. Saiz-Lopez, A. Yabushita, Y. Nakano, Experimental Determination of the Photooxidation of Aqueous I[–] as a Source of Atmospheric I₂, *ACS Earth Space Chem.* 3 (2019) 669–679. <https://doi.org/10.1021/acsearthspacechem.9b00007>.

- [150] M. Thommes, K. Kaneko, A.V. Neimark, J.P. Olivier, F. Rodriguez-Reinoso, J. Rouquerol, K.S.W. Sing, Physisorption of gases, with special reference to the evaluation of surface area and pore size distribution (IUPAC Technical Report), *Pure and Applied Chemistry* 87 (2015) 1051–1069.
<https://doi.org/10.1515/pac-2014-1117>.
- [151] Y. Zhang, J. Liu, G. Wu, W. Chen, Porous graphitic carbon nitride synthesized via direct polymerization of urea for efficient sunlight-driven photocatalytic hydrogen production, *Nanoscale* 4 (2012) 5300. <https://doi.org/10.1039/c2nr30948c>.
- [152] G. Zhang, J. Zhang, M. Zhang, X. Wang, Polycondensation of thiourea into carbon nitride semiconductors as visible light photocatalysts, *J. Mater. Chem.* 22 (2012) 8083.
<https://doi.org/10.1039/c2jm00097k>.
- [153] Y. Cui, J. Huang, X. Fu, X. Wang, Metal-free photocatalytic degradation of 4-chlorophenol in water by mesoporous carbon nitride semiconductors, *Catal. Sci. Technol.* 2 (2012) 1396.
<https://doi.org/10.1039/c2cy20036h>.
- [154] H. Ji, F. Chang, X. Hu, W. Qin, J. Shen, Photocatalytic degradation of 2,4,6-trichlorophenol over g-C₃N₄ under visible light irradiation, *Chemical Engineering Journal* 218 (2013) 183–190.
<https://doi.org/10.1016/j.cej.2012.12.033>.
- [155] L. Shi, L. Liang, F. Wang, M. Liu, J. Sun, Ag₂CrO₄ nanoparticles loaded on two-dimensional large surface area graphite-like carbon nitride sheets: simple synthesis and excellent photocatalytic performance, *Dalton Trans.* 45 (2016) 5815–5824. <https://doi.org/10.1039/C5DT04644K>.
- [156] J. Shen, Y. Lu, J.-K. Liu, X.-H. Yang, Photocatalytic activity of silver chromate materials by various synthesis methods, *Journal of Experimental Nanoscience* 11 (2016) 650–659.
<https://doi.org/10.1080/17458080.2015.1110624>.
- [157] Z. Zhao, Y. Ma, J. Fan, Y. Xue, H. Chang, Y. Masubuchi, S. Yin, Synthesis of graphitic carbon nitride from different precursors by fractional thermal polymerization method and their visible light

- induced photocatalytic activities, *Journal of Alloys and Compounds* 735 (2018) 1297–1305.
<https://doi.org/10.1016/j.jallcom.2017.11.033>.
- [158] D. Xu, S. Cao, J. Zhang, B. Cheng, J. Yu, Effects of the preparation method on the structure and the visible-light photocatalytic activity of Ag_2CrO_4 , *Beilstein J. Nanotechnol.* 5 (2014) 658–666.
<https://doi.org/10.3762/bjnano.5.77>.
- [159] F. Soofivand, F. Mohandes, M. Salavati-Niasari, Silver chromate and silver dichromate nanostructures: Sonochemical synthesis, characterization, and photocatalytic properties, *Materials Research Bulletin* 48 (2013) 2084–2094. <https://doi.org/10.1016/j.materresbull.2013.02.025>.
- [160] Y. Shen, A.J. Dos santos-Garcia, M.J. Martín de Vidales, Graphitic Carbon Nitride-Based Composite in Advanced Oxidation Processes for Aqueous Organic Pollutants Removal: A Review, *Processes* 9 (2020) 66. <https://doi.org/10.3390/pr9010066>.
- [161] P. Yang, J. Wang, G. Yue, R. Yang, P. Zhao, L. Yang, X. Zhao, D. Astruc, Constructing mesoporous g-C₃N₄/ZnO nanosheets catalyst for enhanced visible-light driven photocatalytic activity, *Journal of Photochemistry and Photobiology A: Chemistry* 388 (2020) 112169.
<https://doi.org/10.1016/j.jphotochem.2019.112169>.
- [162] Z. Liu, Y. Jiang, X. Liu, G. Zeng, B. Shao, Y. Liu, Y. Liu, W. Zhang, W. Zhang, M. Yan, X. He, Silver chromate modified sulfur doped graphitic carbon nitride microrod composites with enhanced visible-light photoactivity towards organic pollutants degradation, *Composites Part B: Engineering* 173 (2019) 106918. <https://doi.org/10.1016/j.compositesb.2019.106918>.
- [163] S.K. Padmanabhan, S. Pal, A. Licciulli, Diatomite/silver phosphate composite for efficient degradation of organic dyes under solar radiation, *Bull Mater Sci* 43 (2020) 295.
<https://doi.org/10.1007/s12034-020-02269-2>.
- [164] S. Ghattavi, A. Nezamzadeh-Ejhieh, GC-MASS detection of methyl orange degradation intermediates by AgBr/g-C₃N₄: Experimental design, bandgap study, and characterization of the

- catalyst, *International Journal of Hydrogen Energy* 45 (2020) 24636–24656.
<https://doi.org/10.1016/j.ijhydene.2020.06.207>.
- [165] D.R. Paul, R. Sharma, P. Panchal, S.P. Nehra, A.P. Gupta, A. Sharma, Synthesis, characterization and application of silver doped graphitic carbon nitride as photocatalyst towards visible light photocatalytic hydrogen evolution, *International Journal of Hydrogen Energy* 45 (2020) 23937–23946. <https://doi.org/10.1016/j.ijhydene.2019.06.061>.
- [166] M. Zarei, Ultrasonic-assisted preparation of ZrO₂/g-C₃N₄ nanocomposites with high visible-light photocatalytic activity for degradation of 4-chlorophenol in water, *Water-Energy Nexus* 3 (2020) 135–142. <https://doi.org/10.1016/j.wen.2020.08.002>.
- [167] Z. Huang, Z. Chen, A. Qayum, X. Zhao, H. Xia, F. Lu, L. Hu, Enhanced photocatalytic degradation of 4-chlorophenol under visible light over carbon nitride nanosheets with carbon vacancies, *Nanotechnology* 32 (2021) 415704. <https://doi.org/10.1088/1361-6528/ac0eac>.
- [168] UV LEDs ramp up the quiet side of the LED market (MAGAZINE), *LEDs Magazine* (2012).
<https://www.ledsmagazine.com/manufacturing-services-testing/research-development/article/16695464/uv-leds-ramp-up-the-quiet-side-of-the-led-market-magazine>
 (accessed September 2, 2021).
- [169] Y. Muramoto, M. Kimura, S. Nouda, Development and future of ultraviolet light-emitting diodes: UV-LED will replace the UV lamp, *Semicond. Sci. Technol.* (2014) 9.
- [170] H. Bahruji, H. Maarof, N. Abdul Rahman, Quantum efficiency of Pd/TiO₂ catalyst for photocatalytic reforming of methanol in ultra violet region, *Chem. Pap.* 73 (2019) 2707–2714.
<https://doi.org/10.1007/s11696-019-00822-w>.
- [171] K. Elghniji, O. Hentati, N. Mlaik, A. Mahfoudh, M. Ksibi, Photocatalytic degradation of 4-chlorophenol under P-modified TiO₂/UV system: Kinetics, intermediates, phytotoxicity and acute

- toxicity, *Journal of Environmental Sciences* 24 (2012) 479–487. [https://doi.org/10.1016/S1001-0742\(10\)60659-6](https://doi.org/10.1016/S1001-0742(10)60659-6).
- [172] X. Li, J.W. Cubbage, W.S. Jenks, Photocatalytic Degradation of 4-Chlorophenol. 2. The 4-Chlorocatechol Pathway, *J. Org. Chem.* 64 (1999) 8525–8536. <https://doi.org/10.1021/jo990912n>.
- [173] A.M. Abeish, H.M. Ang, H. Znad, Solar photocatalytic degradation of 4-chlorophenol: mechanism and kinetic modelling, *Desalination and Water Treatment* 53 (2015) 2915–2923. <https://doi.org/10.1080/19443994.2013.869665>.
- [174] L. Shi, L. Liang, F. Wang, M. Liu, J. Sun, Facile synthesis of a g-C₃N₄ isotype composite with enhanced visible-light photocatalytic activity, *RSC Adv.* 5 (2015) 101843–101849. <https://doi.org/10.1039/C5RA19833J>.
- [175] W. Zhang, Y. Sun, F. Dong, W. Zhang, S. Duan, Q. Zhang, Facile synthesis of organic–inorganic layered nanojunctions of g-C₃N₄/(BiO)₂CO₃ as efficient visible light photocatalyst, *Dalton Trans.* 43 (2014) 12026–12036. <https://doi.org/10.1039/C4DT00513A>.
- [176] Y. Che, B. Lu, Q. Qi, H. Chang, J. Zhai, K. Wang, Z. Liu, Bio-inspired Z-scheme g-C₃N₄/Ag₂CrO₄ for efficient visible-light photocatalytic hydrogen generation, *Sci Rep* 8 (2018) 16504. <https://doi.org/10.1038/s41598-018-34287-w>.
- [177] P. Dong, Y. Wang, B. Cao, S. Xin, L. Guo, J. Zhang, F. Li, Ag₃PO₄/reduced graphite oxide sheets nanocomposites with highly enhanced visible light photocatalytic activity and stability, *Applied Catalysis B: Environmental* 132–133 (2013) 45–53. <https://doi.org/10.1016/j.apcatb.2012.11.022>.
- [178] S. Obregón, Improved H₂ production of Pt-TiO₂/g-C₃N₄-MnOx composites by an efficient handling of photogenerated charge pairs, (2014) 8.
- [179] Y. Jiang, Z. Liu, G. Zeng, Y. Liu, B. Shao, Z. Li, Y. Liu, W. Zhang, Q. He, Polyaniline-based adsorbents for removal of hexavalent chromium from aqueous solution: a mini review, *Environ Sci Pollut Res* 25 (2018) 6158–6174. <https://doi.org/10.1007/s11356-017-1188-3>.

- [180] Y. Liu, Z. Liu, G. Zeng, M. Chen, Y. Jiang, B. Shao, Z. Li, Y. Liu, Effect of surfactants on the interaction of phenol with laccase: Molecular docking and molecular dynamics simulation studies, *Journal of Hazardous Materials* 357 (2018) 10–18. <https://doi.org/10.1016/j.jhazmat.2018.05.042>.
- [181] Y. Liu, Z. Liu, D. Huang, M. Cheng, G. Zeng, C. Lai, C. Zhang, C. Zhou, W. Wang, D. Jiang, H. Wang, B. Shao, Metal or metal-containing nanoparticle@MOF nanocomposites as a promising type of photocatalyst, *Coordination Chemistry Reviews* 388 (2019) 63–78. <https://doi.org/10.1016/j.ccr.2019.02.031>.
- [182] S. Ahmadian-Fard-Fini, D. Ghanbari, M. Salavati-Niasari, Photoluminescence carbon dot as a sensor for detecting of *Pseudomonas aeruginosa* bacteria: Hydrothermal synthesis of magnetic hollow NiFe₂O₄-carbon dots nanocomposite material, *Composites Part B: Engineering* 161 (2019) 564–577. <https://doi.org/10.1016/j.compositesb.2018.12.131>.
- [183] G. Mamba, A.K. Mishra, Graphitic carbon nitride (g-C₃N₄) nanocomposites: A new and exciting generation of visible light driven photocatalysts for environmental pollution remediation, *Applied Catalysis B: Environmental* 198 (2016) 347–377. <https://doi.org/10.1016/j.apcatb.2016.05.052>.
- [184] T. Zhang, B. Jiang, Y. Huang, UV-curable photosensitive silicone resins based on a novel polymerizable photoinitiator and GO-modified TiO₂ nanoparticles, *Composites Part B: Engineering* 140 (2018) 214–222. <https://doi.org/10.1016/j.compositesb.2017.12.006>.
- [185] H. Fu, C. Pan, W. Yao, Y. Zhu, Visible-Light-Induced Degradation of Rhodamine B by Nanosized Bi₂WO₆, *J. Phys. Chem. B* 109 (2005) 22432–22439. <https://doi.org/10.1021/jp052995j>.
- [186] S. Liu, J. Tian, L. Wang, Y. Luo, X. Sun, One-pot synthesis of CuO nanoflower-decorated reduced graphene oxide and its application to photocatalytic degradation of dyes, *Catal. Sci. Technol.* 2 (2012) 339–344. <https://doi.org/10.1039/C1CY00374G>.

- [187] N. Bao, L. Shen, T. Takata, K. Domen, Self-Templated Synthesis of Nanoporous CdS Nanostructures for Highly Efficient Photocatalytic Hydrogen Production under Visible Light, *Chem. Mater.* 20 (2008) 110–117. <https://doi.org/10.1021/cm7029344>.
- [188] M. Izadifard, G. Achari, C. Langford, Application of Photocatalysts and LED Light Sources in Drinking Water Treatment, *Catalysts* 3 (2013) 726–743. <https://doi.org/10.3390/catal3030726>.
- [189] M. Izadifard, C.H. Langford, G. Achari, Photocatalytic dechlorination of PCB 138 using leucomethylene blue and visible light; reaction conditions and mechanisms, *Journal of Hazardous Materials* 181 (2010) 393–398. <https://doi.org/10.1016/j.jhazmat.2010.05.023>.
- [190] J.P. Ghosh, C.H. Langford, G. Achari, Characterization of an LED Based Photoreactor to Degrade 4-Chlorophenol in an Aqueous Medium Using Coumarin (C-343) Sensitized TiO₂, *J. Phys. Chem. A* 112 (2008) 10310–10314. <https://doi.org/10.1021/jp804356w>.
- [191] A.Y.S. Malkhasian, M. Izadifard, G. Achari, C.H. Langford, Photocatalytic degradation of agricultural antibiotics using a UV-LED light source, *Journal of Environmental Science and Health, Part B* 49 (2014) 35–40. <https://doi.org/10.1080/03601234.2013.836871>.
- [192] C. Langford, M. Izadifard, E. Radwan, G. Achari, Some Observations on the Development of Superior Photocatalytic Systems for Application to Water Purification by the “Adsorb and Shuttle” or the Interphase Charge Transfer Mechanisms, *Molecules* 19 (2014) 19557–19572. <https://doi.org/10.3390/molecules191219557>.
- [193] S.P. Adhikari, H.R. Pant, J.H. Kim, H.J. Kim, C.H. Park, C.S. Kim, One pot synthesis and characterization of Ag-ZnO/g-C₃N₄ photocatalyst with improved photoactivity and antibacterial properties, *Colloids and Surfaces A: Physicochemical and Engineering Aspects* 482 (2015) 477–484. <https://doi.org/10.1016/j.colsurfa.2015.07.003>.

- [194] O.O. Akintunde, L. Yu, J. Hu, M.G. Kibria, G. Achari, Visible-light driven photocatalytic degradation of 4-chlorophenol using Graphitic Carbon Nitride-based nanocomposites, *Catalysts* 12 (2022) 281. <https://doi.org/10.3390/catal12030281>.
- [195] M. Jourshabani, J.A. Dominic, G. Achari, Z. Shariatnia, Synergetic photocatalytic ozonation using modified graphitic carbon nitride for treatment of emerging contaminants under UVC, UVA and visible irradiation, *Chemical Engineering Science* 209 (2019) 115181. <https://doi.org/10.1016/j.ces.2019.115181>.
- [196] D. Wang, Y. Duan, Q. Luo, X. Li, L. Bao, Visible light photocatalytic activities of plasmonic Ag/AgBr particles synthesized by a double jet method, *Desalination* 270 (2011) 174–180. <https://doi.org/10.1016/j.desal.2010.11.042>.
- [197] P. Wang, B. Huang, X. Qin, X. Zhang, Y. Dai, J. Wei, M.-H. Whangbo, Ag@AgCl: A Highly Efficient and Stable Photocatalyst Active under Visible Light, *Angew. Chem. Int. Ed.* 47 (2008) 7931–7933. <https://doi.org/10.1002/anie.200802483>.
- [198] Y. Bi, S. Ouyang, N. Umezawa, J. Cao, J. Ye, Facet Effect of Single-Crystalline Ag₃PO₄ Sub-microcrystals on Photocatalytic Properties, *J. Am. Chem. Soc.* 133 (2011) 6490–6492. <https://doi.org/10.1021/ja2002132>.
- [199] Y. Liu, H. Yu, M. Cai, J. Sun, Microwave hydrothermal synthesis of Ag₂CrO₄ photocatalyst for fast degradation of PCP-Na under visible light irradiation, *Catalysis Communications* 26 (2012) 63–67. <https://doi.org/10.1016/j.catcom.2012.04.017>.
- [200] D. Xu, S. Cao, J. Zhang, B. Cheng, J. Yu, Effects of the preparation method on the structure and the visible-light photocatalytic activity of Ag₂CrO₄, *Beilstein J. Nanotechnol.* 5 (2014) 658–666. <https://doi.org/10.3762/bjnano.5.77>.
- [201] Z. Liu, Y. Jiang, X. Liu, G. Zeng, B. Shao, Y. Liu, Y. Liu, W. Zhang, W. Zhang, M. Yan, X. He, Silver chromate modified sulfur doped graphitic carbon nitride microrod composites with enhanced

- visible-light photoactivity towards organic pollutants degradation, *Composites Part B: Engineering* 173 (2019) 106918. <https://doi.org/10.1016/j.compositesb.2019.106918>.
- [202] 2,4-D Technical Fact Sheet, (2008). <http://npic.orst.edu/factsheets/archive/2,4-DTech.html> (accessed March 5, 2022).
- [203] H. Canada, Re-evaluation Note REV2016-08, Special Review of 2,4-D: Proposed Decision for Consultation, (2017). <https://www.canada.ca/en/health-canada/services/consumer-product-safety/pesticides-pest-management/public/consultations/re-evaluation-note/2016/special-review-2-4-d/document.html> (accessed April 2, 2022).
- [204] A. Anderson, G. Byrtus, J. Thompson, D. Humphries, B. Hill, M. Bilyk, Baseline pesticide data for semi-permanent wetlands in the Aspen Parkland of Alberta - Open Government, (2002). <https://open.alberta.ca/publications/0778524426> (accessed April 2, 2022).
- [205] N.F. Gray, *Drinking Water Quality*, Second Edition, (2008) 538.
- [206] C. Flox, J.A. Garrido, R.M. Rodríguez, P.-L. Cabot, F. Centellas, C. Arias, E. Brillas, Mineralization of herbicide mecoprop by photoelectro-Fenton with UVA and solar light, *Catalysis Today* 129 (2007) 29–36. <https://doi.org/10.1016/j.cattod.2007.06.049>.
- [207] WHO Coronavirus (COVID-19) Dashboard, (2021). <https://covid19.who.int> (accessed December 31, 2021).
- [208] CDC, National Wastewater Surveillance System, Centers for Disease Control and Prevention (2022). <https://www.cdc.gov/healthywater/surveillance/wastewater-surveillance/wastewater-surveillance.html> (accessed April 5, 2022).
- [209] Wastewater Technology Fact Sheet: Bacterial Source Tracking, U.E. Environmental Protection Agency (2002) 12.

- [210] L. Yu, G. Achari, C.H. Langford, Design and Evaluation of a Novel Light-Emitting Diode Photocatalytic Reactor for Water Treatment, *J. Environ. Eng.* 144 (2018) 04018014.
[https://doi.org/10.1061/\(ASCE\)EE.1943-7870.0001356](https://doi.org/10.1061/(ASCE)EE.1943-7870.0001356).
- [211] E.K. Radwan, L. Yu, G. Achari, C.H. Langford, Photocatalytic ozonation of pesticides in a fixed bed flow through UVA-LED photoreactor, *Environ Sci Pollut Res* 23 (2016) 21313–21318.
<https://doi.org/10.1007/s11356-016-7346-1>.
- [212] S.A. Abubshait, S. Iqbal, H.A. Abubshait, A.A. AlObaid, T.I. Al-Muhimeed, H.S.M. Abd-Rabboh, A. Bahadur, W. Li, Effective heterointerface combination of 1D/2D Co-NiS/S-g-C₃N₄ heterojunction for boosting spatial charge separation with enhanced photocatalytic degradation of organic pollutants and disinfection of pathogens, *Colloids and Surfaces A: Physicochemical and Engineering Aspects* 628 (2021) 127390. <https://doi.org/10.1016/j.colsurfa.2021.127390>.
- [213] S. Iqbal, A. Amjad, M. Javed, M. Alfakeer, M. Mushtaq, S. Rabea, E.B. Elkaeed, R.A. Pashameah, E. Alzahrani, A.-E. Farouk, Boosted spatial charge carrier separation of binary ZnFe₂O₄/S-g-C₃N₄ heterojunction for visible-light-driven photocatalytic activity and antimicrobial performance, *Front. Chem.* 10 (2022) 975355. <https://doi.org/10.3389/fchem.2022.975355>.
- [214] A. Baral, L. Satish, D.P. Das, H. Sahoo, M.K. Ghosh, Construing the interactions between MnO₂ nanoparticle and bovine serum albumin: insight into the structure and stability of a protein–nanoparticle complex, *New J. Chem.* 41 (2017) 8130–8139. <https://doi.org/10.1039/C7NJ01227F>.
- [215] P. Huang, Z. Li, H. Hu, D. Cui, Synthesis and Characterization of Bovine Serum Albumin-Conjugated Copper Sulfide Nanocomposites, *Journal of Nanomaterials* 2010 (2010) 1–6.
<https://doi.org/10.1155/2010/641545>.
- [216] D. Ballottin, S. Fulaz, M.L. Souza, P. Corio, A.G. Rodrigues, A.O. Souza, P.M. Gaspari, A.F. Gomes, F. Gozzo, L. Tasic, Elucidating Protein Involvement in the Stabilization of the Biogenic Silver Nanoparticles, *Nanoscale Res Lett* 11 (2016) 313. <https://doi.org/10.1186/s11671-016-1538-y>.

- [217] V. Banerjee, K.P. Das, Interaction of silver nanoparticles with proteins: A characteristic protein concentration dependent profile of SPR signal, *Colloids and Surfaces B: Biointerfaces* 111 (2013) 71–79. <https://doi.org/10.1016/j.colsurfb.2013.04.052>.
- [218] What Is the Difference Between Ordinary Light and Laser Light?, *Lighting Portal* (2021). <https://www.aydinlatma.org/en/what-is-the-difference-between-ordinary-light-and-laser-light.html> (accessed May 7, 2022).
- [219] C.G. Hatchard, C.A. Parker, E.J. Bowen, A new sensitive chemical actinometer - II. Potassium ferrioxalate as a standard chemical actinometer, *Proceedings of the Royal Society of London. Series A. Mathematical and Physical Sciences* 235 (1956) 518–536. <https://doi.org/10.1098/rspa.1956.0102>.
- [220] Quick Start™ Bradford Protein Assay, Bio-Rad Laboratories (2022). <https://www.bio-rad.com/en-ca/product/quick-start-bradford-protein-assay?ID=5ec149ee-0cd1-468b-8651-a2fe9de6944d> (accessed June 19, 2022).
- [221] P. Whalen, LuminUltra Technologies Ltd.: Cellular Adenosine Triphosphate (cATP) assay procedure, (2012) 10.
- [222] Colilert - IDEXX US, (2022). <https://www.idexx.com/en/water/water-products-services/colilert/> (accessed June 19, 2022).
- [223] A. Kędziora, M. Speruda, E. Krzyżewska, J. Rybka, A. Łukowiak, G. Bugła-Płoskońska, Similarities and Differences between Silver Ions and Silver in Nanoforms as Antibacterial Agents, *IJMS* 19 (2018) 444. <https://doi.org/10.3390/ijms19020444>.
- [224] General Chemistry, (2022) 1417.
- [225] K. Djebbar, A. Zertal, T. Sehili, Photocatalytic Degradation of 2,4-Dichlorophenoxyacetic Acid and 4-Chloro-2-Methylphenoxyacetic Acid in Water by using TiO₂, *Environmental Technology* 27 (2006) 1191–1197. <https://doi.org/10.1080/09593332708618732>.

- [226] G.R. Helz, R.G. Zepp, D.G. Crosby, eds., Aquatic and surface photochemistry, Lewis Publishers, Boca Raton, 1994.
- [227] A. Kumar, G. Sharma, Mu. Naushad, A.H. Al-Muhtaseb, A. Kumar, I. Hira, T. Ahamad, A.A. Ghfar, F.J. Stadler, Visible photodegradation of ibuprofen and 2,4-D in simulated waste water using sustainable metal free-hybrids based on carbon nitride and biochar, *Journal of Environmental Management* 231 (2019) 1164–1175. <https://doi.org/10.1016/j.jenvman.2018.11.015>.
- [228] S.Y. Ejeta, T. Imae, Photodegradation of pollutant pesticide by oxidized graphitic carbon nitride catalysts, *Journal of Photochemistry and Photobiology A: Chemistry* 404 (2021) 112955. <https://doi.org/10.1016/j.jphotochem.2020.112955>.
- [229] J. Gu, H. Chen, F. Jiang, X. Wang, L. Li, All-solid-state Z-scheme Co₉S₈/graphitic carbon nitride photocatalysts for simultaneous reduction of Cr(VI) and oxidation of 2,4-dichlorophenoxyacetic acid under simulated solar irradiation, *Chemical Engineering Journal* 360 (2019) 1188–1198. <https://doi.org/10.1016/j.cej.2018.10.137>.
- [230] J. Zhong, Y. Ahmed, G. Carvalho, Z. Wang, L. Wang, J.F. Mueller, J. Guo, Simultaneous removal of micropollutants, antibiotic resistant bacteria, and antibiotic resistance genes using graphitic carbon nitride under simulated solar irradiation, *Chemical Engineering Journal* (2021) 133839. <https://doi.org/10.1016/j.cej.2021.133839>.
- [231] T. Shi, Q. Wei, Z. Wang, G. Zhang, X. Sun, Q.-Y. He, Photocatalytic Protein Damage by Silver Nanoparticles Circumvents Bacterial Stress Response and Multidrug Resistance, *MSphere* 4 (2019) e00175-19. <https://doi.org/10.1128/mSphere.00175-19>.
- [232] V.D. Suryawanshi, L.S. Walekar, A.H. Gore, P.V. Anbhule, G.B. Kolekar, Spectroscopic analysis on the binding interaction of biologically active pyrimidine derivative with bovine serum albumin, *Journal of Pharmaceutical Analysis* 6 (2016) 56–63. <https://doi.org/10.1016/j.jpha.2015.07.001>.

- [233] V.D. Jaiswal, P.M. Dongre, Biophysical interactions between silver nanoparticle-albumin interface and curcumin, *Journal of Pharmaceutical Analysis* 10 (2020) 164–177.
<https://doi.org/10.1016/j.jpha.2020.02.004>.
- [234] V. Ershov, N. Tarasova, B. Ershov, Evolution of Electronic State and Properties of Silver Nanoparticles during Their Formation in Aqueous Solution, *IJMS* 22 (2021) 10673.
<https://doi.org/10.3390/ijms221910673>.
- [235] U. Klueh, V. Wagner, S. Kelly, A. Johnson, J.D. Bryers, Efficacy of silver-coated fabric to prevent bacterial colonization and subsequent device-based biofilm formation, *J. Biomed. Mater. Res.* 53 (2000) 621–631. [https://doi.org/10.1002/1097-4636\(2000\)53:6<621::AID-JBM2>3.0.CO;2-Q](https://doi.org/10.1002/1097-4636(2000)53:6<621::AID-JBM2>3.0.CO;2-Q).
- [236] T.C. Dakal, A. Kumar, R.S. Majumdar, V. Yadav, Mechanistic Basis of Antimicrobial Actions of Silver Nanoparticles, *Front. Microbiol.* 7 (2016). <https://doi.org/10.3389/fmicb.2016.01831>.
- [237] M.K. Rai, S.D. Deshmukh, A.P. Ingle, A.K. Gade, Silver nanoparticles: the powerful nanoweapon against multidrug-resistant bacteria: Activity of silver nanoparticles against MDR bacteria, *Journal of Applied Microbiology* 112 (2012) 841–852. <https://doi.org/10.1111/j.1365-2672.2012.05253.x>.
- [238] G. Franci, A. Falanga, S. Galdiero, L. Palomba, M. Rai, G. Morelli, M. Galdiero, Silver Nanoparticles as Potential Antibacterial Agents, *Molecules* 20 (2015) 8856–8874.
<https://doi.org/10.3390/molecules20058856>.
- [239] Z. Zaheer, S.A. Kosa, M. Akram, Interactions of Ag⁺ ions and Ag-nanoparticles with protein. A comparative and multi spectroscopic investigation, *Journal of Molecular Liquids* 335 (2021) 116226. <https://doi.org/10.1016/j.molliq.2021.116226>.
- [240] A. Jaiswar, D. Varshney, A. Adholeya, P. Prasad, Do environmentally induced DNA variations mediate adaptation in *Aspergillus flavus* exposed to chromium stress in tannery sludge?, *BMC Genomics* 19 (2018) 868. <https://doi.org/10.1186/s12864-018-5244-2>.

- [241] R.S. Rana, P. Singh, V. Kandari, R. Singh, R. Dobhal, S. Gupta, A review on characterization and bioremediation of pharmaceutical industries' wastewater: an Indian perspective, *Appl Water Sci* 7 (2017) 1–12. <https://doi.org/10.1007/s13201-014-0225-3>.
- [242] A.A. Inyinbor, F.A. Adekola, G.A. Olatunji, Liquid Phase Adsorption of Rhodamine B Dye onto Acid-treated *Raphia hookeri* Fruit Epicarp: Isotherms, Kinetics and Thermodynamics Studies, *S.Afr.j.Chem.* 69 (2016). <https://doi.org/10.17159/0379-4350/2016/v69a28>.
- [243] J. Gamage, Z. Zhang, Applications of Photocatalytic Disinfection, *International Journal of Photoenergy* 2010 (2010) 1–11. <https://doi.org/10.1155/2010/764870>.
- [244] P.S.M. Dunlop, J.A. Byrne, N. Manga, B.R. Eggins, The photocatalytic removal of bacterial pollutants from drinking water, *Journal of Photochemistry and Photobiology A: Chemistry* 148 (2002) 355–363. [https://doi.org/10.1016/S1010-6030\(02\)00063-1](https://doi.org/10.1016/S1010-6030(02)00063-1).
- [245] R.D. Letterman, American Water Works Association, eds., *Water quality and treatment: a handbook of community water supplies*, 5th ed, McGraw-Hill, New York, 1999.
- [246] W.-J. Huang, G.-C. Fang, C.-C. Wang, The determination and fate of disinfection by-products from ozonation of polluted raw water, *Science of The Total Environment* 345 (2005) 261–272. <https://doi.org/10.1016/j.scitotenv.2004.10.019>.
- [247] W. Masschelein, *Ultraviolet light in water and wastewater sanitation*, CRC Press, Boca Raton, FL, 2018.
- [248] A.W. Zularisam, A.F. Ismail, R. Salim, Behaviours of natural organic matter in membrane filtration for surface water treatment — a review, *Desalination* 194 (2006) 211–231. <https://doi.org/10.1016/j.desal.2005.10.030>.
- [249] M.T. Yagub, T.K. Sen, S. Afroze, H.M. Ang, Dye and its removal from aqueous solution by adsorption: A review, *Advances in Colloid and Interface Science* 209 (2014) 172–184. <https://doi.org/10.1016/j.cis.2014.04.002>.

- [250] A. Azimi, A. Azari, M. Rezakazemi, M. Ansarpour, Removal of Heavy Metals from Industrial Wastewaters: A Review, *ChemBioEng Reviews* 4 (2017) 37–59.
<https://doi.org/10.1002/cben.201600010>.
- [251] Y. Yang, X. Li, C. Zhou, W. Xiong, G. Zeng, D. Huang, C. Zhang, W. Wang, B. Song, X. Tang, X. Li, H. Guo, Recent advances in application of graphitic carbon nitride-based catalysts for degrading organic contaminants in water through advanced oxidation processes beyond photocatalysis: A critical review, *Water Research* 184 (2020) 116200. <https://doi.org/10.1016/j.watres.2020.116200>.
- [252] J.M. Poyatos, M.M. Muñio, M.C. Almecija, J.C. Torres, E. Hontoria, F. Osorio, Advanced Oxidation Processes for Wastewater Treatment: State of the Art, *Water Air Soil Pollut* 205 (2010) 187–204.
<https://doi.org/10.1007/s11270-009-0065-1>.
- [253] R. Dewil, D. Mantzavinos, I. Poulios, M.A. Rodrigo, New perspectives for Advanced Oxidation Processes, *Journal of Environmental Management* 195 (2017) 93–99.
<https://doi.org/10.1016/j.jenvman.2017.04.010>.
- [254] Y. Zheng, Z. Zhang, C. Li, A comparison of graphitic carbon nitrides synthesized from different precursors through pyrolysis, *Journal of Photochemistry and Photobiology A: Chemistry* 332 (2017) 32–44. <https://doi.org/10.1016/j.jphotochem.2016.08.005>.
- [255] J. Zhong, H. Jiang, Z. Wang, Z. Yu, L. Wang, J.F. Mueller, J. Guo, Efficient photocatalytic destruction of recalcitrant micropollutants using graphitic carbon nitride under simulated sunlight irradiation, *Environmental Science and Ecotechnology* 5 (2021) 100079.
<https://doi.org/10.1016/j.es.2021.100079>.
- [256] J. Zhong, Y. Ahmed, G. Carvalho, Z. Wang, L. Wang, J.F. Mueller, J. Guo, Simultaneous removal of micropollutants, antibiotic resistant bacteria, and antibiotic resistance genes using graphitic carbon nitride under simulated solar irradiation, *Chemical Engineering Journal* 433 (2022) 133839.
<https://doi.org/10.1016/j.cej.2021.133839>.

- [257] 2013 - ICheaP11- Special ISSUE 11th International Confere.pdf, (n.d.).
- [258] Y. Lv, J. Lin, S. Peng, L. Zhang, L. Yu, Effective ways to enhance the photocatalytic activity of ZnO nanopowders: high crystalline degree, more oxygen vacancies, and preferential growth, *New J. Chem.* 43 (2019) 19223–19231. <https://doi.org/10.1039/C9NJ04767K>.
- [259] H. Fu, C. Pan, W. Yao, Y. Zhu, Visible-Light-Induced Degradation of Rhodamine B by Nanosized Bi₂WO₆, *J. Phys. Chem. B* 109 (2005) 22432–22439. <https://doi.org/10.1021/jp052995j>.
- [260] S. Liu, J. Tian, L. Wang, Y. Luo, X. Sun, One-pot synthesis of CuO nanoflower-decorated reduced graphene oxide and its application to photocatalytic degradation of dyes, *Catal. Sci. Technol.* 2 (2012) 339–344. <https://doi.org/10.1039/C1CY00374G>.
- [261] A. Walsh, J. Buckeridge, C.R.A. Catlow, A.J. Jackson, T.W. Keal, M. Miskufova, P. Sherwood, S.A. Shevlin, M.B. Watkins, S.M. Woodley, A.A. Sokol, Limits to Doping of Wide Band Gap Semiconductors, *Chem. Mater.* 25 (2013) 2924–2926. <https://doi.org/10.1021/cm402237s>.
- [262] H. Yin, J. Chen, Y. Wang, J. Wang, H. Guo, Composition dependent band offsets of ZnO and its ternary alloys, *Sci Rep* 7 (2017) 41567. <https://doi.org/10.1038/srep41567>.
- [263] N. Suriyachai, S. Chuangchote, N. Laosiripojana, V. Champreda, T. Sagawa, Synergistic Effects of Co-Doping on Photocatalytic Activity of Titanium Dioxide on Glucose Conversion to Value-Added Chemicals, *ACS Omega* 5 (2020) 20373–20381. <https://doi.org/10.1021/acsomega.0c02334>.
- [264] S. Liang, K. Xiao, Y. Mo, X. Huang, A novel ZnO nanoparticle blended polyvinylidene fluoride membrane for anti-irreversible fouling, *Journal of Membrane Science* 394–395 (2012) 184–192. <https://doi.org/10.1016/j.memsci.2011.12.040>.
- [265] S. Zhang, C. Su, H. Ren, M. Li, L. Zhu, S. Ge, M. Wang, Z. Zhang, L. Li, X. Cao, In-Situ Fabrication of g-C₃N₄/ZnO Nanocomposites for Photocatalytic Degradation of Methylene Blue: Synthesis Procedure Does Matter, *Nanomaterials* 9 (2019) 215. <https://doi.org/10.3390/nano9020215>.

- [266] M. Samadi, H.A. Shivaee, A. Pourjavadi, A.Z. Moshfegh, Synergism of oxygen vacancy and carbonaceous species on enhanced photocatalytic activity of electrospun ZnO-carbon nanofibers: Charge carrier scavengers mechanism, *Applied Catalysis A: General* 466 (2013) 153–160. <https://doi.org/10.1016/j.apcata.2013.06.024>.
- [267] I. Djerdj, Z. Jagličić, D. Arčon, M. Niederberger, Co-Doped ZnO nanoparticles: Minireview, *Nanoscale* 2 (2010) 1096. <https://doi.org/10.1039/c0nr00148a>.
- [268] M.A. Qamar, M. Javed, S. Shahid, M. Sher, Fabrication of g-C₃N₄/transition metal (Fe, Co, Ni, Mn and Cr)-doped ZnO ternary composites: Excellent visible light active photocatalysts for the degradation of organic pollutants from wastewater, *Materials Research Bulletin* 147 (2022) 111630. <https://doi.org/10.1016/j.materresbull.2021.111630>.
- [269] S. Das, S. Sinha, B. Das, R. Jayabalan, M. Suar, A. Mishra, A.J. Tamhankar, C. Stålsby Lundborg, S.K. Tripathy, Disinfection of Multidrug Resistant *Escherichia coli* by Solar-Photocatalysis using Fe-doped ZnO Nanoparticles, *Sci Rep* 7 (2017) 104. <https://doi.org/10.1038/s41598-017-00173-0>.
- [270] A. Basu, A.J. Misra, M. Behera, S.K. Behera, A.K. Nayak, N.K. Dhal, A. Mishra, B.K. Satpathy, C.S. Lundborg, S.K. Tripathy, Photocatalytic disinfection of extended-spectrum beta-lactamase producing *Escherichia coli* using Alumina/ZnO heterostructures, *Journal of Environmental Chemical Engineering* 9 (2021) 106334. <https://doi.org/10.1016/j.jece.2021.106334>.
- [271] C. Zhou, Z. Zeng, G. Zeng, D. Huang, R. Xiao, M. Cheng, C. Zhang, W. Xiong, C. Lai, Y. Yang, W. Wang, H. Yi, B. Li, Visible-light-driven photocatalytic degradation of sulfamethazine by surface engineering of carbon nitride : Properties, degradation pathway and mechanisms, *Journal of Hazardous Materials* 380 (2019) 120815. <https://doi.org/10.1016/j.jhazmat.2019.120815>.
- [272] Y. Wang, X. Wang, M. Antonietti, Polymeric Graphitic Carbon Nitride as a Heterogeneous Organocatalyst: From Photochemistry to Multipurpose Catalysis to Sustainable Chemistry, *Angew. Chem. Int. Ed.* 51 (2012) 68–89. <https://doi.org/10.1002/anie.201101182>.

- [273] A.O. Idris, E.O. Oseghe, T.A.M. Msagati, A.T. Kuvarega, U. Feleni, B. Mamba, Graphitic Carbon Nitride: A Highly Electroactive Nanomaterial for Environmental and Clinical Sensing, *Sensors* 20 (2020) 5743. <https://doi.org/10.3390/s20205743>.
- [274] J. Zhu, P. Xiao, H. Li, S.A.C. Carabineiro, Graphitic Carbon Nitride: Synthesis, Properties, and Applications in Catalysis, *ACS Appl. Mater. Interfaces* 6 (2014) 16449–16465. <https://doi.org/10.1021/am502925j>.
- [275] H. Jiang, Y. Li, D. Wang, X. Hong, B. Liang, Recent Advances in Heteroatom Doped Graphitic Carbon Nitride (g-C₃N₄) and g-C₃N₄/Metal Oxide Composite Photocatalysts, *COC* 24 (2020) 673–693. <https://doi.org/10.2174/1385272824666200309151648>.
- [276] L. Jiang, X. Yuan, Y. Pan, J. Liang, G. Zeng, Z. Wu, H. Wang, Doping of graphitic carbon nitride for photocatalysis: A review, *Applied Catalysis B: Environmental* 217 (2017) 388–406. <https://doi.org/10.1016/j.apcatb.2017.06.003>.
- [277] O.O. Akintunde, L. Yu, J. Hu, M.G. Kibria, C.R.J. Hubert, S. Pogolian, G. Achari, Disinfection and photocatalytic degradation of organic Contaminants using visible light-activated GCN/Ag₂CrO₄ nanocomposites, *Catalysts* 12 (2022) 943. <https://doi.org/10.3390/catal12090943>.
- [278] H. Jingyu, Y. Ran, L. Zhaohui, S. Yuanqiang, Q. Lingbo, A. Nti Kani, In-situ growth of ZnO globular on g-C₃N₄ to fabrication binary heterojunctions and their photocatalytic degradation activity on tetracyclines, *Solid State Sciences* 92 (2019) 60–67. <https://doi.org/10.1016/j.solidstatesciences.2019.02.009>.
- [279] J. Wang, Z. Yang, X. Gao, W. Yao, W. Wei, X. Chen, R. Zong, Y. Zhu, Core-shell g-C₃N₄@ZnO composites as photoanodes with double synergistic effects for enhanced visible-light photoelectrocatalytic activities, *Applied Catalysis B: Environmental* 217 (2017) 169–180. <https://doi.org/10.1016/j.apcatb.2017.05.034>.

- [280] M.A. Qamar, S. Shahid, M. Javed, M. Sher, S. Iqbal, A. Bahadur, D. Li, Fabricated novel g-C₃N₄/Mn doped ZnO nanocomposite as highly active photocatalyst for the disinfection of pathogens and degradation of the organic pollutants from wastewater under sunlight radiations, *Colloids and Surfaces A: Physicochemical and Engineering Aspects* 611 (2021) 125863.
<https://doi.org/10.1016/j.colsurfa.2020.125863>.
- [281] J.G.M. de Sousa, T.V.C. da Silva, N.P. de Moraes, M.L. Caetano Pinto da Silva, R. da Silva Rocha, R. Landers, L.A. Rodrigues, Visible light-driven ZnO/g-C₃N₄/carbon xerogel ternary photocatalyst with enhanced activity for 4-chlorophenol degradation, *Materials Chemistry and Physics* 256 (2020) 123651. <https://doi.org/10.1016/j.matchemphys.2020.123651>.
- [282] M.A. Qamar, S. Shahid, M. Javed, Synthesis of dynamic g-C₃N₄/Fe@ZnO nanocomposites for environmental remediation applications, *Ceramics International* 46 (2020) 22171–22180.
<https://doi.org/10.1016/j.ceramint.2020.05.294>.
- [283] Makuła et al. - 2018 - How To Correctly Determine the Band Gap Energy of Modified Semiconductor Photocatalysts Based on UV-Vis Spectra, (n.d.).
- [284] IDEXX Laboratories Total coliforms and E. coli assay procedure using Colilert Defined Substrate Technology (DST) and Quanti-tray. (2019)..pdf, (n.d.).
- [285] L.-S. Lin, Z.-X. Cong, J. Li, K.-M. Ke, S.-S. Guo, H.-H. Yang, G.-N. Chen, Graphitic-phase C₃N₄ nanosheets as efficient photosensitizers and pH-responsive drug nanocarriers for cancer imaging and therapy, *J. Mater. Chem. B* 2 (2014) 1031. <https://doi.org/10.1039/c3tb21479f>.
- [286] L. Shi, L. Liang, F. Wang, M. Liu, J. Sun, Ag₂CrO₄ nanoparticles loaded on two-dimensional large surface area graphite-like carbon nitride sheets: simple synthesis and excellent photocatalytic performance, *Dalton Trans.* 45 (2016) 5815–5824. <https://doi.org/10.1039/C5DT04644K>.

- [287] X. Wu, Z. Wei, L. Zhang, X. Wang, H. Yang, J. Jiang, Optical and Magnetic Properties of Fe Doped ZnO Nanoparticles Obtained by Hydrothermal Synthesis, *Journal of Nanomaterials* 2014 (2014) 1–6. <https://doi.org/10.1155/2014/792102>.
- [288] K.V.A. Kumar, S.R. Amanchi, B. Sreedhar, P. Ghosal, Ch. Subrahmanyam, Phenol and Cr(VI) degradation with Mn ion doped ZnO under visible light photocatalysis, *RSC Adv.* 7 (2017) 43030–43039. <https://doi.org/10.1039/C7RA08172C>.
- [289] Z. Wang, X. Zhan, Y. Wang, S. Muhammad, Y. Huang, J. He, A flexible UV nanosensor based on reduced graphene oxide decorated ZnO nanostructures, *Nanoscale* 4 (2012) 2678. <https://doi.org/10.1039/c2nr30354j>.
- [290] S.C. Yan, Z.S. Li, Z.G. Zou, Photodegradation Performance of g-C₃N₄ Fabricated by Directly Heating Melamine, *Langmuir* 25 (2009) 10397–10401. <https://doi.org/10.1021/la900923z>.
- [291] N. Kumaresan, M.M.A. Sinthiya, M. Sarathbavan, K. Ramamurthi, K. Sethuraman, R.R. Babu, Synergetic effect of g-C₃N₄/ZnO binary nanocomposites heterojunction on improving charge carrier separation through 2D/1D nanostructures for effective photocatalytic activity under the sunlight irradiation, *Separation and Purification Technology* 244 (2020) 116356. <https://doi.org/10.1016/j.seppur.2019.116356>.
- [292] W. Zhang, Q. Zhang, F. Dong, Z. Zhao, The Multiple Effects of Precursors on the Properties of Polymeric Carbon Nitride, *International Journal of Photoenergy* 2013 (2013) 1–9. <https://doi.org/10.1155/2013/685038>.
- [293] M. Thommes, K. Kaneko, A.V. Neimark, J.P. Olivier, F. Rodriguez-Reinoso, J. Rouquerol, K.S.W. Sing, Physisorption of gases, with special reference to the evaluation of surface area and pore size distribution (IUPAC Technical Report), *Pure and Applied Chemistry* 87 (2015) 1051–1069. <https://doi.org/10.1515/pac-2014-1117>.

- [294] J. Zhou, M. Zhang, Y. Zhu, Preparation of visible light-driven g-C₃N₄@ZnO hybrid photocatalyst via mechanochemistry, *Phys. Chem. Chem. Phys.* 16 (2014) 17627–17633.
<https://doi.org/10.1039/C4CP02061H>.
- [295] N. Kumaresan, M.M.A. Sinthiya, M. Praveen Kumar, S. Ravichandran, R. Ramesh Babu, K. Sethurman, K. Ramamurthi, Investigation on the g-C₃N₄ encapsulated ZnO nanorods heterojunction coupled with GO for effective photocatalytic activity under visible light irradiation, *Arabian Journal of Chemistry* 13 (2020) 2826–2843. <https://doi.org/10.1016/j.arabjc.2018.07.013>.
- [296] Y.-A. Chen, Y.-T. Wang, H.S. Moon, K. Yong, Y.-J. Hsu, Yolk-shell nanostructures: synthesis, photocatalysis and interfacial charge dynamics, *RSC Adv.* 11 (2021) 12288–12305.
<https://doi.org/10.1039/D1RA00803J>.
- [297] Q.T.H. Ta, G. Namgung, J.-S. Noh, Facile synthesis of porous metal-doped ZnO/g-C₃N₄ composites for highly efficient photocatalysts, *Journal of Photochemistry and Photobiology A: Chemistry* 368 (2019) 110–119. <https://doi.org/10.1016/j.jphotochem.2018.09.049>.
- [298] M.A.M. Khan, S. Kumar, T. Ahamad, A.N. Alhazaa, Enhancement of photocatalytic and electrochemical properties of hydrothermally synthesized WO₃ nanoparticles via Ag loading, *Journal of Alloys and Compounds* 743 (2018) 485–493.
<https://doi.org/10.1016/j.jallcom.2018.01.343>.
- [299] Y. Habba, M. Capochichi-Gnambodoe, Y. Leprince-Wang, Enhanced Photocatalytic Activity of Iron-Doped ZnO Nanowires for Water Purification, *Applied Sciences* 7 (2017) 1185.
<https://doi.org/10.3390/app7111185>.
- [300] Y. Matsukawa, S. Hirata, M. Inada, N. Enomoto, J. Hojo, K. Hayashi, Kinetic effects of polymorphs and surface areas on adsorption and photocatalytic decomposition of acetaldehyde on titania, *Chemical Engineering Journal* 397 (2020) 125422. <https://doi.org/10.1016/j.cej.2020.125422>.

- [301] L.-N. Tong, T. Cheng, H.-B. Han, J.-L. Hu, X.-M. He, Y. Tong, C.M. Schneider, Photoluminescence studies on structural defects and room temperature ferromagnetism in Ni and Ni-H doped ZnO nanoparticles, *Journal of Applied Physics* 108 (2010) 023906. <https://doi.org/10.1063/1.3460644>.
- [302] T.-H. Lai, K. Katsumata, Y.-J. Hsu, In situ charge carrier dynamics of semiconductor nanostructures for advanced photoelectrochemical and photocatalytic applications, *Nanophotonics* 10 (2020) 777–795. <https://doi.org/10.1515/nanoph-2020-0472>.
- [303] Y.-H. Chiu, T.-F. Chang, C.-Y. Chen, M. Sone, Y.-J. Hsu, Mechanistic Insights into Photodegradation of Organic Dyes Using Heterostructure Photocatalysts, *Catalysts* 9 (2019) 430. <https://doi.org/10.3390/catal9050430>.
- [304] Y.-F. Lin, Y.-J. Hsu, Interfacial charge carrier dynamics of type-II semiconductor nanoheterostructures, *Applied Catalysis B: Environmental* 130–131 (2013) 93–98. <https://doi.org/10.1016/j.apcatb.2012.10.024>.
- [305] X. Zheng, J. Yuan, J. Shen, J. Liang, J. Che, B. Tang, G. He, H. Chen, A carnation-like rGO/Bi₂O₂CO₃/BiOCl composite: efficient photocatalyst for the degradation of ciprofloxacin, *J Mater Sci: Mater Electron* 30 (2019) 5986–5994. <https://doi.org/10.1007/s10854-019-00898-w>.
- [306] S. Zhang, C. Su, H. Ren, M. Li, L. Zhu, S. Ge, M. Wang, Z. Zhang, L. Li, X. Cao, In-Situ Fabrication of g-C₃N₄/ZnO Nanocomposites for Photocatalytic Degradation of Methylene Blue: Synthesis Procedure Does Matter, *Nanomaterials* 9 (2019) 215. <https://doi.org/10.3390/nano9020215>.
- [307] Y. Wu, Y. Zhou, H. Xu, Q. Liu, Y. Li, L. Zhang, H. Liu, Z. Tu, X. Cheng, J. Yang, Highly Active, Superstable, and Biocompatible Ag/Polydopamine/g-C₃N₄ Bactericidal Photocatalyst: Synthesis, Characterization, and Mechanism, *ACS Sustainable Chem. Eng.* 6 (2018) 14082–14094. <https://doi.org/10.1021/acssuschemeng.8b02620>.
- [308] S. Iqbal, N. Ahmad, M. Javed, M.A. Qamar, A. Bahadur, S. Ali, Z. Ahmad, R.M. Irfan, G. Liu, M.B. Akbar, M.A. Qayyum, Designing highly potential photocatalytic comprising silver deposited ZnO

- NPs with sulfurized graphitic carbon nitride (Ag/ZnO/S-g-C₃N₄) ternary composite, *Journal of Environmental Chemical Engineering* 9 (2021) 104919.
<https://doi.org/10.1016/j.jece.2020.104919>.
- [309] Y.N. Slavin, J. Asnis, U.O. Häfeli, H. Bach, Metal nanoparticles: understanding the mechanisms behind antibacterial activity, *J Nanobiotechnol* 15 (2017) 65. <https://doi.org/10.1186/s12951-017-0308-z>.
- [310] A. Kessler, J. Hedberg, E. Blomberg, I. Odnevall, Reactive Oxygen Species Formed by Metal and Metal Oxide Nanoparticles in Physiological Media—A Review of Reactions of Importance to Nanotoxicity and Proposal for Categorization, *Nanomaterials* 12 (2022) 1922.
<https://doi.org/10.3390/nano12111922>.
- [311] S. Ma, S. Zhan, Y. Xia, P. Wang, Q. Hou, Q. Zhou, Enhanced photocatalytic bactericidal performance and mechanism with novel Ag/ZnO/g-C₃N₄ composite under visible light, *Catalysis Today* 330 (2019) 179–188. <https://doi.org/10.1016/j.cattod.2018.04.014>.
- [312] G.-A. Shin, K.G. Linden, M.J. Arrowood, M.D. Sobsey, Low-Pressure UV Inactivation and DNA Repair Potential of *Cryptosporidium parvum* Oocysts, *Appl Environ Microbiol* 67 (2001) 3029–3032.
<https://doi.org/10.1128/AEM.67.7.3029-3032.2001>.
- [313] M. Zhan, X. Yang, Q. Xian, L. Kong, Photosensitized degradation of bisphenol A involving reactive oxygen species in the presence of humic substances, *Chemosphere* 63 (2006) 378–386.
<https://doi.org/10.1016/j.chemosphere.2005.08.046>.
- [314] S.Lj. Tomić, J.S. Vuković, Antimicrobial Activity of Silver, Copper, and Zinc Ions/Poly(Acrylate/Itaconic Acid) Hydrogel Matrices, *Inorganics* 10 (2022) 38.
<https://doi.org/10.3390/inorganics10030038>.

- [315] G. Liao, C. Li, X. Li, B. Fang, Emerging polymeric carbon nitride Z-scheme systems for photocatalysis, *Cell Reports Physical Science* 2 (2021) 100355.
<https://doi.org/10.1016/j.xcrp.2021.100355>.
- [316] L. Shi, L. Liang, F. Wang, M. Liu, J. Sun, Facile synthesis of a g-C₃N₄ isotype composite with enhanced visible-light photocatalytic activity, *RSC Adv.* 5 (2015) 101843–101849.
<https://doi.org/10.1039/C5RA19833J>.
- [317] W. Zhang, Y. Sun, F. Dong, W. Zhang, S. Duan, Q. Zhang, Facile synthesis of organic–inorganic layered nanojunctions of g-C₃N₄/(BiO)₂CO₃ as efficient visible light photocatalyst, *Dalton Trans.* 43 (2014) 12026–12036. <https://doi.org/10.1039/C4DT00513A>.
- [318] D. Xu, S. Cao, J. Zhang, B. Cheng, J. Yu, Effects of the preparation method on the structure and the visible-light photocatalytic activity of Ag₂CrO₄, *Beilstein J. Nanotechnol.* 5 (2014) 658–666.
<https://doi.org/10.3762/bjnano.5.77>.
- [319] Y. Che, B. Lu, Q. Qi, H. Chang, J. Zhai, K. Wang, Z. Liu, Bio-inspired Z-scheme g-C₃N₄/Ag₂CrO₄ for efficient visible-light photocatalytic hydrogen generation, *Sci Rep* 8 (2018) 16504.
<https://doi.org/10.1038/s41598-018-34287-w>.
- [320] C. Chen, W. Bi, Z. Xia, W. Yuan, L. Li, Hydrothermal Synthesis of the CuWO₄/ZnO Composites with Enhanced Photocatalytic Performance, *ACS Omega* 5 (2020) 13185–13195.
<https://doi.org/10.1021/acsomega.0c01220>.
- [321] D.A. Armstrong, R.E. Huie, S. Lyman, W.H. Koppenol, G. Merényi, P. Neta, D.M. Stanbury, S. Steenken, P. Wardman, Standard electrode potentials involving radicals in aqueous solution: inorganic radicals, *Bioinorganic Reaction Mechanisms* 9 (2013). <https://doi.org/10.1515/irm-2013-0005>.

- [322] W.A. Rutala, D.J. Weber, Sterilization, High-Level Disinfection, and Environmental Cleaning, *Infectious Disease Clinics of North America* 25 (2011) 45–76.
<https://doi.org/10.1016/j.idc.2010.11.009>.
- [323] J.A. Otter, S. Yezli, G.L. French, The Role Played by Contaminated Surfaces in the Transmission of Nosocomial Pathogens, *Infect. Control Hosp. Epidemiol.* 32 (2011) 687–699.
<https://doi.org/10.1086/660363>.
- [324] R.A. Weinstein, Epidemiology and Control of Nosocomial Infections in Adult Intensive Care Units, 91 (1991).
- [325] J.M. Boyce, Environmental contamination makes an important contribution to hospital infection, *Journal of Hospital Infection* 65 (2007) 50–54. [https://doi.org/10.1016/S0195-6701\(07\)60015-2](https://doi.org/10.1016/S0195-6701(07)60015-2).
- [326] W.A. Rutala, Guideline for Disinfection and Sterilization in Healthcare Facilities, 2008, (2008).
- [327] W.A. Rutala, D.J. Weber, Are Room Decontamination Units Needed to Prevent Transmission of Environmental Pathogens?, *Infect. Control Hosp. Epidemiol.* 32 (2011) 743–747.
<https://doi.org/10.1086/661226>.
- [328] P.C. Carling, M.F. Parry, S.M. Von Behren, Healthcare Environmental Hygiene Study Group, Identifying Opportunities to Enhance Environmental Cleaning in 23 Acute Care Hospitals, *Infect. Control Hosp. Epidemiol.* 29 (2008) 1–7. <https://doi.org/10.1086/524329>.
- [329] E.R. Goodman, R. Piatt, R. Bass, A.B. Onderdonk, D.S. Yokoe, S.S. Huang, Impact of an Environmental Cleaning Intervention on the Presence of Methicillin-Resistant *Staphylococcus aureus* and Vancomycin-Resistant Enterococci on Surfaces in Intensive Care Unit Rooms, *Infect. Control Hosp. Epidemiol.* 29 (2008) 593–599. <https://doi.org/10.1086/588566>.
- [330] D.J. Weber, W.A. Rutala, Use of metals and microbicides in the prevention of nosocomial infections, *Disinfection, Sterilization, and Antisepsis in Healthcare*. Champlain, New York: Polyscience Publications (1995) 271–85.

- [331] S. Makhluaf, R. Dror, Y. Nitzan, Y. Abramovich, R. Jelinek, A. Gedanken, Microwave-Assisted Synthesis of Nanocrystalline MgO and Its Use as a Bactericide, *Adv. Funct. Mater.* 15 (2005) 1708–1715. <https://doi.org/10.1002/adfm.200500029>.
- [332] K. Ghule, A.V. Ghule, B.-J. Chen, Y.-C. Ling, Preparation and characterization of ZnO nanoparticles coated paper and its antibacterial activity study, *Green Chem.* 8 (2006) 1034. <https://doi.org/10.1039/b605623g>.
- [333] W.A. Daoud, J.H. Xin, Y.-H. Zhang, Surface functionalization of cellulose fibers with titanium dioxide nanoparticles and their combined bactericidal activities, *Surface Science* 599 (2005) 69–75. <https://doi.org/10.1016/j.susc.2005.09.038>.
- [334] D.M. Hoat, V. Van On, D.K. Nguyen, M. Naseri, R. Ponce-Pérez, T.V. Vu, J.F. Rivas-Silva, N.N. Hieu, G.H. Coccoletzi, Structural, electronic and optical properties of pristine and functionalized MgO monolayers: a first principles study, *RSC Adv.* 10 (2020) 40411–40420. <https://doi.org/10.1039/D0RA05030J>.
- [335] H. Lin, Z. Xu, X. Wang, J. Long, W. Su, X. Fu, Q. Lin, Photocatalytic and antibacterial properties of medical-grade PVC material coated with TiO₂ film, *J. Biomed. Mater. Res.* 87B (2008) 425–431. <https://doi.org/10.1002/jbm.b.31120>.
- [336] S. Khan, I.A. Qazi, I. Hashmi, M.A. Awan, N.-S.S. Zaidi, Synthesis of Silver-Doped Titanium TiO₂ Powder-Coated Surfaces and Its Ability to Inactivate *Pseudomonas aeruginosa* and *Bacillus subtilis*, *Journal of Nanomaterials* 2013 (2013) 1–8. <https://doi.org/10.1155/2013/531010>.
- [337] M. Liu, K. Sunada, K. Hashimoto, M. Miyauchi, Visible-light sensitive Cu(II)–TiO₂ with sustained anti-viral activity for efficient indoor environmental remediation, *J. Mater. Chem. A* 3 (2015) 17312–17319. <https://doi.org/10.1039/C5TA03756E>.

- [338] S. Ma, S. Zhan, Y. Xia, P. Wang, Q. Hou, Q. Zhou, Enhanced photocatalytic bactericidal performance and mechanism with novel Ag/ZnO/g-C₃N₄ composite under visible light, *Catalysis Today* 330 (2019) 179–188. <https://doi.org/10.1016/j.cattod.2018.04.014>.
- [339] J. Deng, J. Liang, M. Li, M. Tong, Enhanced visible-light-driven photocatalytic bacteria disinfection by g-C₃N₄-AgBr, *Colloids and Surfaces B: Biointerfaces* 152 (2017) 49–57. <https://doi.org/10.1016/j.colsurfb.2017.01.003>.
- [340] Y. Li, Y. Li, S. Ma, P. Wang, Q. Hou, J. Han, S. Zhan, Efficient water disinfection with Ag₂WO₄-doped mesoporous g-C₃N₄ under visible light, *Journal of Hazardous Materials* 338 (2017) 33–46. <https://doi.org/10.1016/j.jhazmat.2017.05.011>.
- [341] Y. Xu, Q. Liu, C. Liu, Y. Zhai, M. Xie, L. Huang, H. Xu, H. Li, J. Jing, Visible-light-driven Ag/AgBr/ZnFe₂O₄ composites with excellent photocatalytic activity for E. coli disinfection and organic pollutant degradation, *Journal of Colloid and Interface Science* 512 (2018) 555–566. <https://doi.org/10.1016/j.jcis.2017.10.077>.
- [342] J. Hou, S. Liu, X. Jiang, G.I.N. Waterhouse, Z.-M. Zhang, L. Yu, Polyaniline/graphite carbon nitride composite coatings with outstanding photo-induced anodic antifouling and antibacterial properties under visible light, *Progress in Organic Coatings* 154 (2021) 106203. <https://doi.org/10.1016/j.porgcoat.2021.106203>.
- [343] M. Faisal, A.A. Ismail, F.A. Harraz, S.A. Al-Sayari, A.M. El-Toni, M.S. Al-Assiri, Synthesis of highly dispersed silver doped g-C₃N₄ nanocomposites with enhanced visible-light photocatalytic activity, *Materials & Design* 98 (2016) 223–230. <https://doi.org/10.1016/j.matdes.2016.03.019>.
- [344] E.M. Allam, T.A. Lashen, S.A. Abou El-Enein, M.A. Hassanin, A.K. Sakr, M.Y. Hanfi, M.I. Sayyed, J.S. Al-Otaibi, M.F. Cheira, Cetylpyridinium Bromide/Polyvinyl Chloride for Substantially Efficient Capture of Rare Earth Elements from Chloride Solution, *Polymers* 14 (2022) 954. <https://doi.org/10.3390/polym14050954>.

- [345] M. Pandey, G.M. Joshi, A. Mukherjee, P. Thomas, Electrical properties and thermal degradation of poly(vinyl chloride)/polyvinylidene fluoride/ZnO polymer nanocomposites: PVC/PVDF/ZnO polymer nano-composites, *Polym. Int.* 65 (2016) 1098–1106. <https://doi.org/10.1002/pi.5161>.
- [346] R. Arunkumar, R.S. Babu, M. Usha Rani, Investigation on Al₂O₃ doped PVC–PBMA blend polymer electrolytes, *J Mater Sci: Mater Electron* 28 (2017) 3309–3316. <https://doi.org/10.1007/s10854-016-5924-0>.
- [347] A.M. Abdelghany, M.S. Meikhail, N. Asker, Synthesis and structural-biological correlation of PVC/PVAc polymer blends, *Journal of Materials Research and Technology* 8 (2019) 3908–3916. <https://doi.org/10.1016/j.jmrt.2019.06.053>.
- [348] J.-T. Sun, J.-W. Li, C.-H. Tsou, J.-C. Pang, R.-J. Chung, C.-W. Chiu, Polyurethane/Nanosilver-Doped Halloysite Nanocomposites: Thermal, Mechanical Properties, and Antibacterial Properties, *Polymers* 12 (2020) 2729. <https://doi.org/10.3390/polym12112729>.
- [349] A. Asefnejad, Khorasani, Behnamghader, Bonakdar, Manufacturing of biodegradable polyurethane scaffolds based on polycaprolactone using a phase separation method: physical properties and in vitro assay, *IJN* (2011) 2375. <https://doi.org/10.2147/IJN.S15586>.
- [350] M. Rahimi, M.R. Aslani, B. Rezai, Influence of surface roughness on flotation kinetics of quartz, *J. Cent. South Univ. Technol.* 19 (2012) 1206–1211. <https://doi.org/10.1007/s11771-012-1130-2>.
- [351] C. Hicyilmaz, U. Ulusoy, S. Bilgen, M. Yekeler, Flotation responses to the morphological properties of particles measured with three-dimensional approach, *International Journal of Mineral Processing* 75 (2005) 229–236. <https://doi.org/10.1016/j.minpro.2004.08.019>.
- [352] Influence of Surface Roughness | 3M Science of Adhesion Educational Series, (n.d.). https://www.3m.com/3M/en_US/bonding-and-assembly-us/resources/science-of-adhesion/influence-surface-roughness/ (accessed June 26, 2023).

[353] J.P.B. van Dam, S.T. Abrahams, A. Yilmaz, Y. Gonzalez-Garcia, H. Terryn, J.M.C. Mol, Effect of surface roughness and chemistry on the adhesion and durability of a steel-epoxy adhesive interface, *International Journal of Adhesion and Adhesives* 96 (2020) 102450. <https://doi.org/10.1016/j.ijadhadh.2019.102450>.

[354] Surface Roughness | Measurements, (n.d.).

<https://www.biolinscientific.com/measurements/surface-roughness> (accessed June 26, 2023).

[355] aimane guedri, M. Zaabat, B. Boudine, A. Hafdallah, Effect of sample thickness on the structural and optical properties of Polyvinyl Chloride/Zinc Oxide Nanocomposite Films for photocatalysis application, *In Review*, 2021. <https://doi.org/10.21203/rs.3.rs-811397/v1>.

Appendices

Appendix A: Copyright Form

SPRINGER NATURE LICENSE

TERMS AND CONDITIONS

Oct 08, 2023

This Agreement between University of Calgary -- Olufemi Akintunde ("You") and Springer Nature ("Springer Nature") consists of your license details and the terms and conditions provided by Springer Nature and Copyright Clearance Center.

License Number	5644080169506
License date	Oct 08, 2023
Licensed Content Publisher	Springer Nature
Licensed Content Publication	Journal of Materials Science
Licensed Content Title	Photocatalytic disinfection efficiency of 2D structure graphitic carbon nitride-based nanocomposites: a review
Licensed Content Author	Pramila Murugesan et al
Licensed Content Date	May 28, 2019
Type of Use	Thesis/Dissertation
Requestor type	academic/university or research institute
Format	print and electronic
Portion	figures/tables/illustrations
Number of figures/tables/illustrations	1
Will you be translating?	no
Circulation/distribution	1 - 29
Author of this Springer Nature content	no
Title	Olufemi Akintunde
Institution name	University of Calgary
Expected presentation date	Dec 2023
Portions	Figure 5
	University of Calgary
	2500 University Dr. NW
Requestor Location	Calgary, AB T2N 1N4
	Canada
	Attn: University of Calgary

Appendix B: Copyright Form

ELSEVIER LICENSE
TERMS AND CONDITIONS
Oct 08, 2023

This Agreement between University of Calgary -- Olufemi Akintunde ("You") and Elsevier ("Elsevier") consists of your license details and the terms and conditions provided by Elsevier and Copyright Clearance Center.

License Number	5644070890614
License date	Oct 08, 2023
Licensed Content Publisher	Elsevier
Licensed Content Publication	Journal of Cleaner Production
Licensed Content Title	Degradation of methylene blue and methyl orange by palladium-doped TiO ₂ photocatalysis for water reuse: Efficiency and degradation pathways
Licensed Content Author	Chi Hieu Nguyen, Chun-Chieh Fu, Ruey-Shin Juang
Licensed Content Date	Nov 20, 2018
Licensed Content Volume	202
Licensed Content Issue	n/a
Licensed Content Pages	15
Start Page	413
End Page	427
Type of Use	reuse in a thesis/dissertation
Portion	figures/tables/illustrations
Number of figures/tables/illustrations	1
Format	both print and electronic
Are you the author of this Elsevier article?	No
Will you be translating?	No
Title	Olufemi Akintunde
Institution name	University of Calgary
Expected presentation date	Dec 2023
Portions	Figure 14
	University of Calgary 2500 University Dr. NW
Requestor Location	Calgary, AB T2N 1N4 Canada Attn: University of Calgary

Appendix C: Copyright Form

Photocatalytic Degradation of 4-Chlorophenol. 1. The Hydroquinone Pathway

Author: Xiaojing Li, Jerry W. Cubbage, Troy A. Tetzlaff, et al

Publication: The Journal of Organic Chemistry

Publisher: American Chemical Society

Date: Nov 1, 1999

Copyright © 1999, American Chemical Society



PERMISSION/LICENSE IS GRANTED FOR YOUR ORDER AT NO CHARGE

This type of permission/license, instead of the standard Terms and Conditions, is sent to you because no fee is being charged for your order. Please note the following:

- Permission is granted for your request in both print and electronic formats, and translations.
- If figures and/or tables were requested, they may be adapted or used in part.
- Please print this page for your records and send a copy of it to your publisher/graduate school.
- Appropriate credit for the requested material should be given as follows: "Reprinted (adapted) with permission from {COMPLETE REFERENCE CITATION}. Copyright {YEAR} American Chemical Society." Insert appropriate information in place of the capitalized words.
- One-time permission is granted only for the use specified in your RightsLink request. No additional uses are granted (such as derivative works or other editions). For any uses, please submit a new request.

If credit is given to another source for the material you requested from RightsLink, permission must be obtained from that source.

BACK

CLOSE WINDOW

Appendix D: Copyright Form

This is a License Agreement between Olufemi Akintunde ("User") and Copyright Clearance Center, Inc. ("CCC") on behalf of the Rightsholder identified in the order details below. The license consists of the order details, the Marketplace Permissions General Terms and Conditions below, and any Rightsholder Terms and Conditions which are included below. All payments must be made in full to CCC in accordance with the Marketplace Permissions General Terms and Conditions below.

Order Date	08-Oct-2023	Type of Use	Republish in a thesis/dissertation
Order License ID	1404408-1	Publisher	RSC Publishing
ISSN	2046-2069	Portion	Chart/graph/table/figure

LICENSED CONTENT

Publication Title	RSC advances	Publication Type	e-Journal
Article Title	Copper as an antimicrobial agent: recent advances	Start Page	18179
		End Page	18186
Date	01/01/2011	Issue	30
Language	English	Volume	11
Country	United Kingdom of Great Britain and Northern Ireland	URL	http://pubs.rsc.org/en/Journals/Journalss...
Rightsholder	Royal Society of Chemistry		

REQUEST DETAILS

Portion Type	Chart/graph/table/figure	Distribution	Worldwide
Number of Charts / Graphs / Tables / Figures Requested	1	Translation	Original language of publication
Format (select all that apply)	Print, Electronic	Copies for the Disabled?	No
Who Will Republish the Content?	Academic institution	Minor Editing Privileges?	No
Duration of Use	Life of current edition	Incidental Promotional Use?	No
Lifetime Unit Quantity	Up to 499	Currency	CAD
Rights Requested	Main product		

NEW WORK DETAILS

Title	Olufemi Akintunde	Institution Name	University of Calgary
Instructor Name	Olufemi Akintunde	Expected Presentation Date	2023-12-07

Appendix E: Supplementary materials for Chapter 3 (Paper 1)

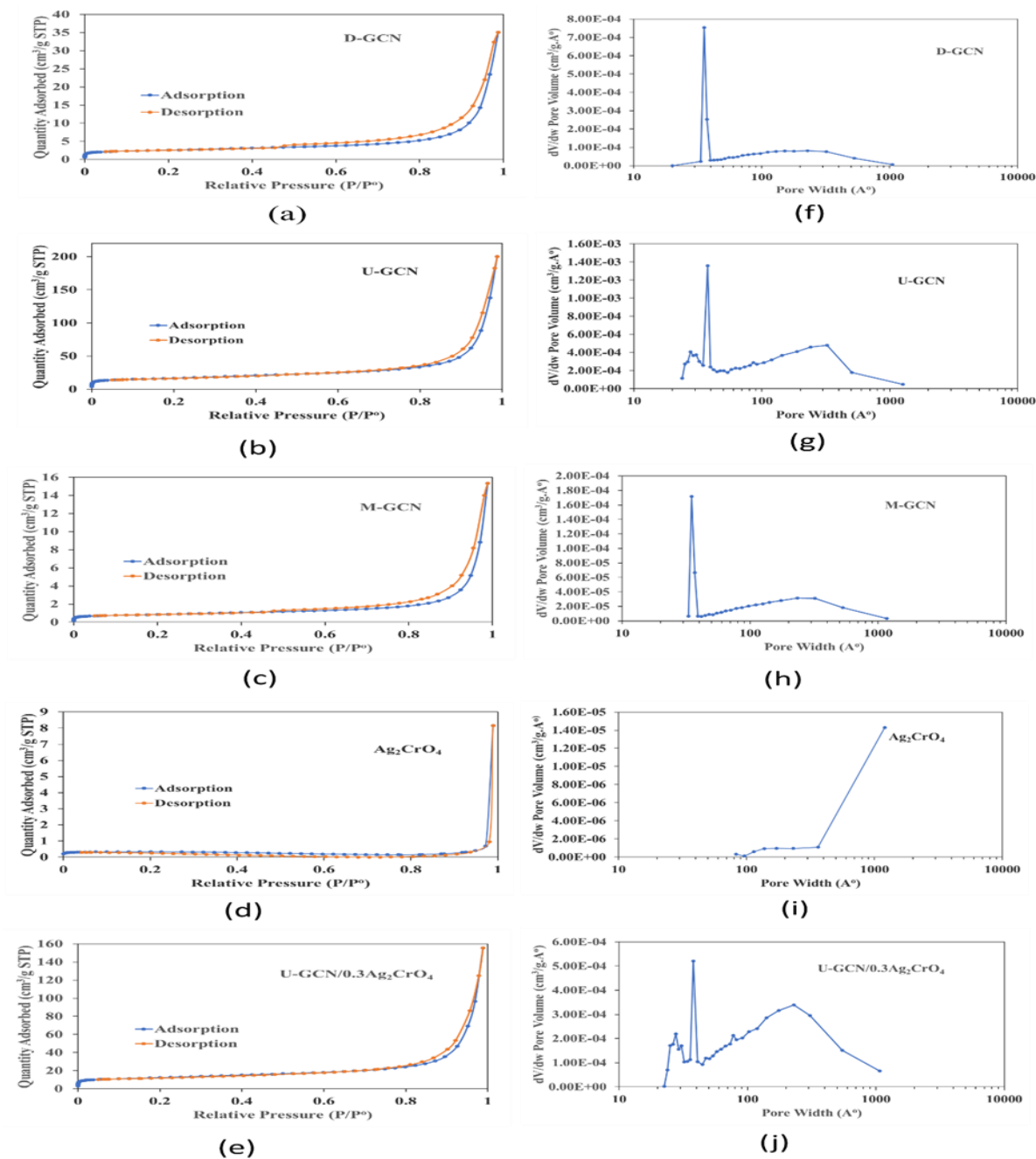


Figure S3. 1 N_2 adsorption-desorption isotherms and their corresponding pore size distribution curves for the photocatalysts: D-GCN, U-GCN, M-GCN, Ag_2CrO_4 , and U-GCN/0.3 Ag_2CrO_4

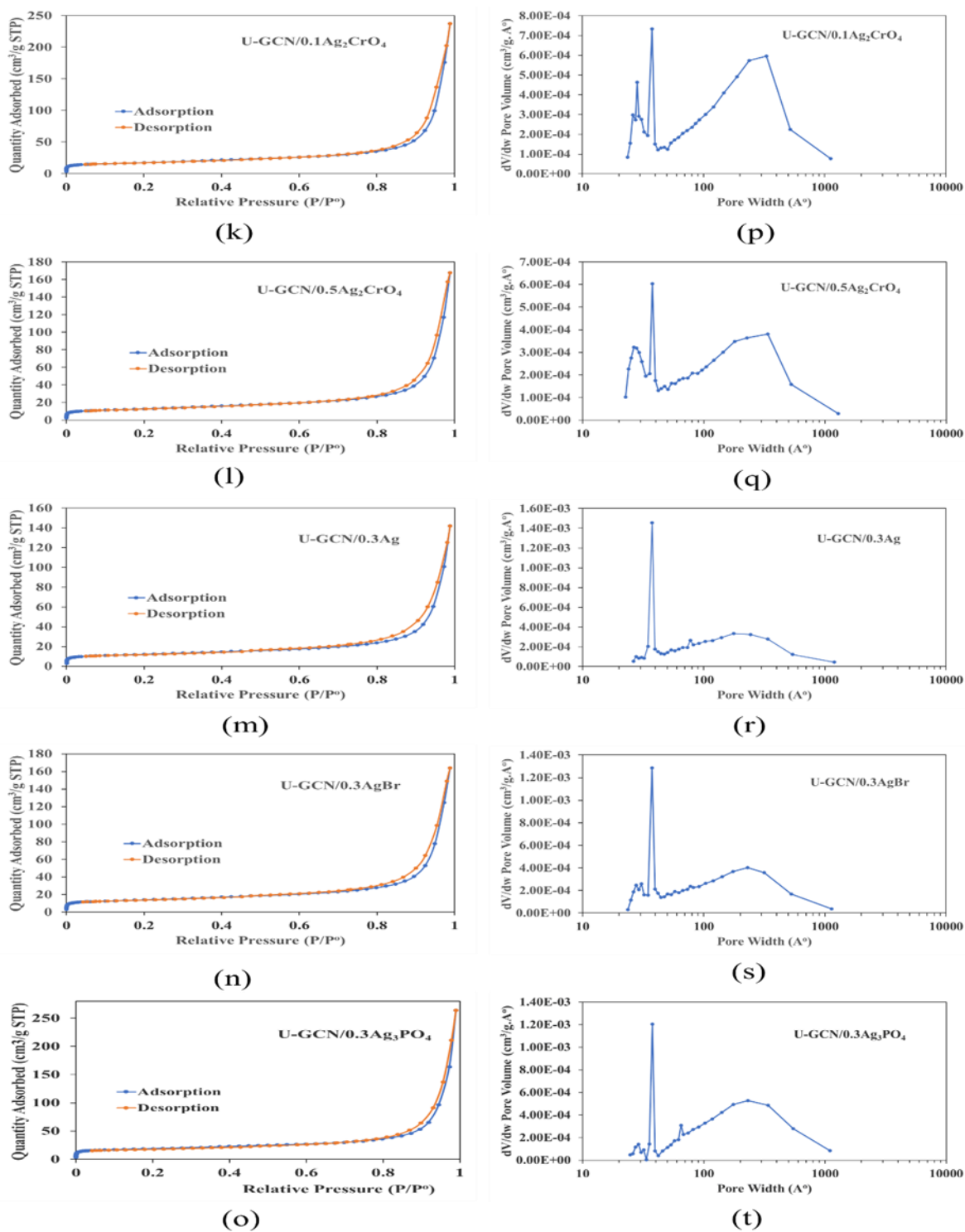


Figure S3. 2 N_2 adsorption-desorption isotherms and their corresponding pore size distribution curves for the photocatalysts: U-GCN/0.1Ag₂CrO₄, U-GCN/0.5Ag₂CrO₄, U-GCN/0.3Ag, U-GCN/0.3AgBr, and U-GCN/0.3Ag₃PO₄

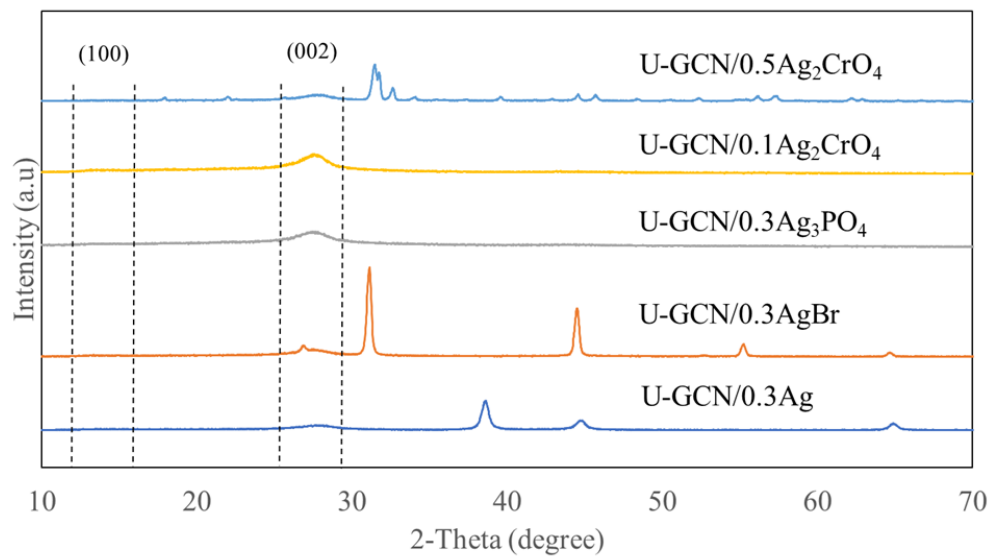


Figure S3. 3 XRD patterns for the photocatalysts: U-GCN/silver-based composites and U-GCN/silver chromate composites.

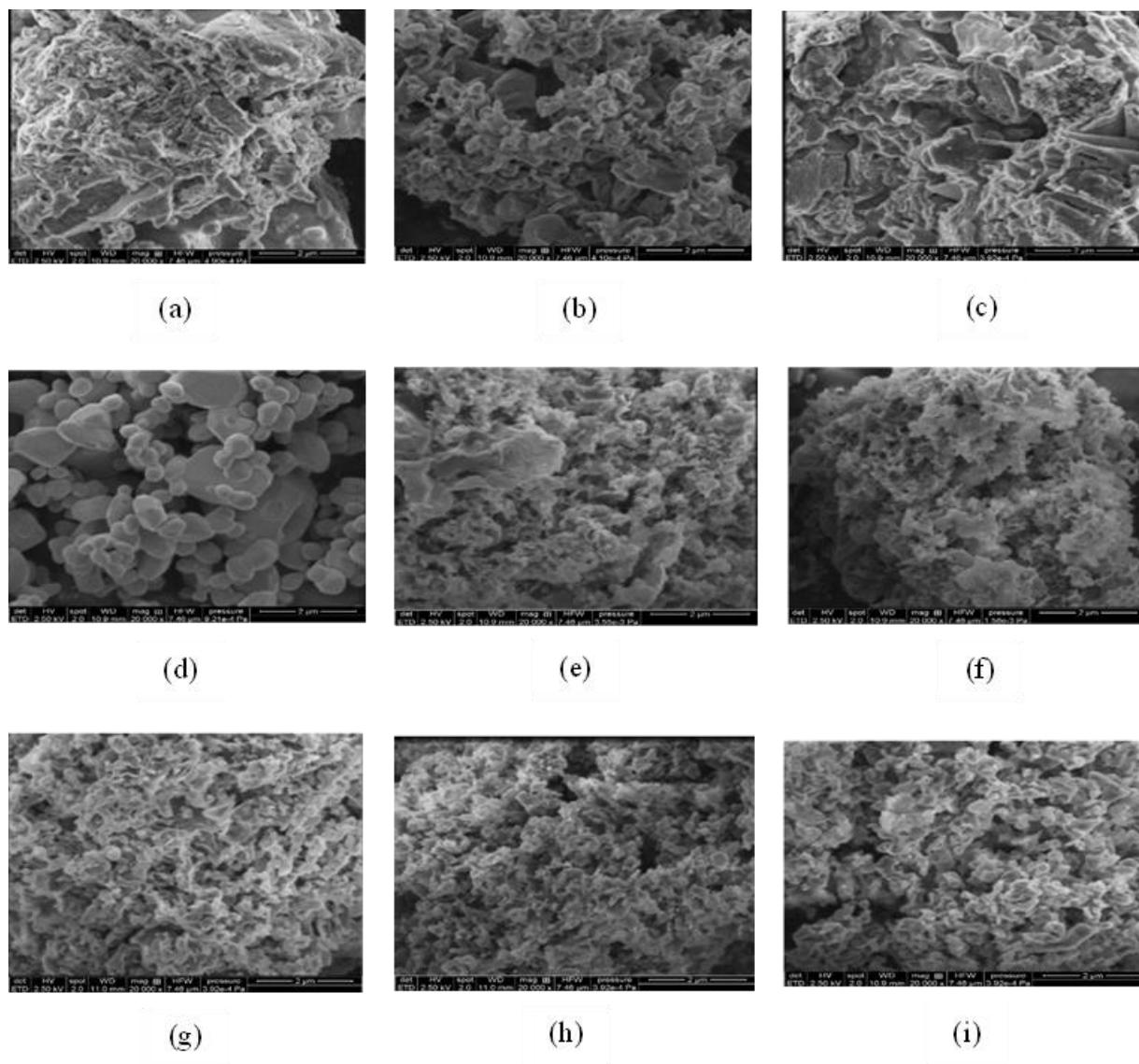


Figure S3. 4 SEM images for the photocatalysts: (a) D-GCN, (b) U-GCN, (c) M-GCN, (d) Ag_2CrO_4 , (e) U-GCN/ $0.1\text{Ag}_2\text{CrO}_4$, (f) U-GCN/ $0.5\text{Ag}_2\text{CrO}_4$, (g) U-GCN/ 0.3Ag , (h) U-GCN/ 0.3AgBr , and (i) U-GCN/ $0.3\text{Ag}_3\text{PO}_4$

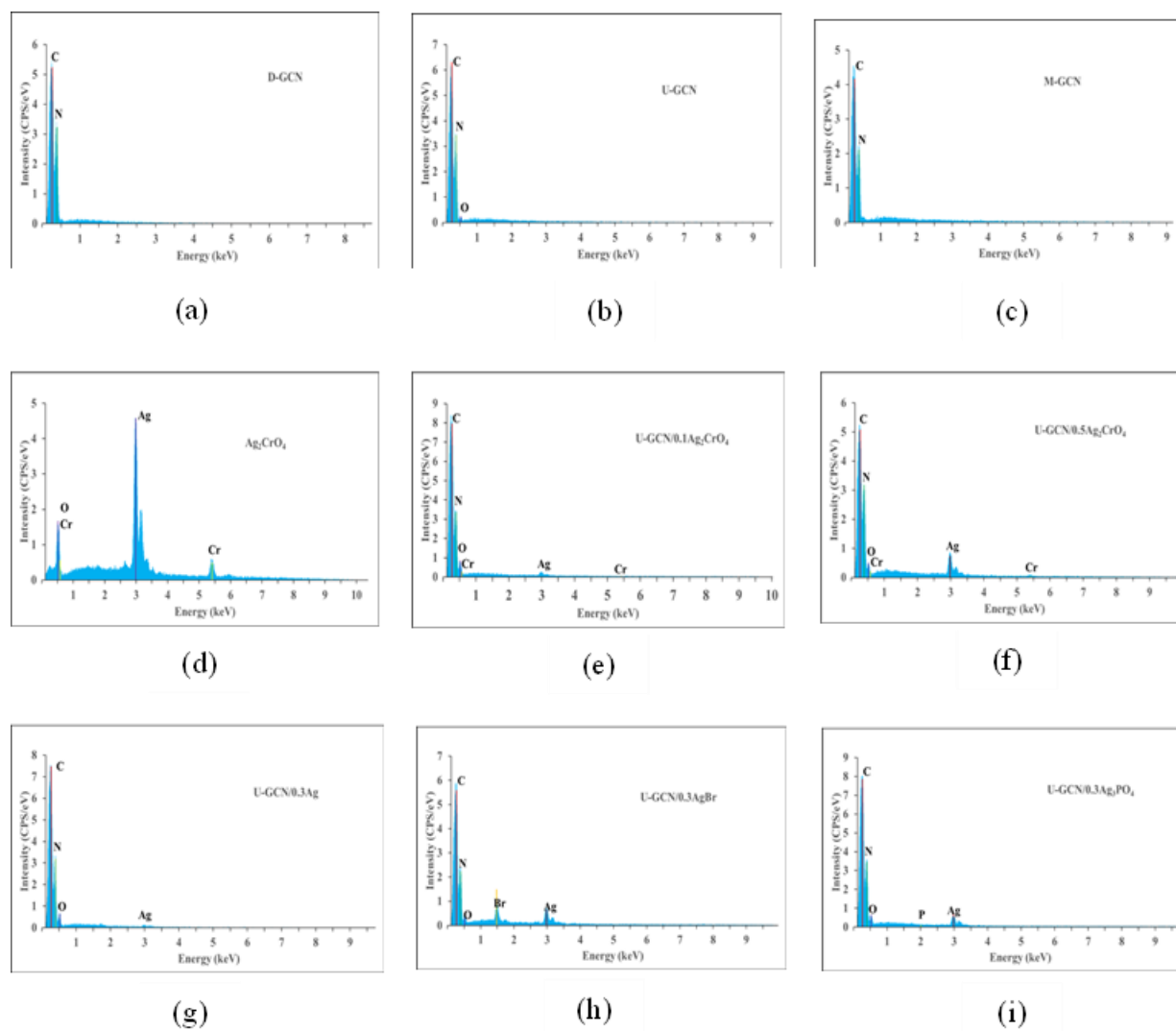


Figure S3. 5 EDS images for the photocatalysts: (a) D-GCN, (b) U-GCN, (c) M-GCN, (d) Ag_2CrO_4 , (e) U-GCN/0.1 Ag_2CrO_4 , (f) U-GCN/0.5 Ag_2CrO_4 , (g) U-GCN/0.3Ag, (h) U-GCN/0.3AgBr, and (i) U-GCN/0.3 Ag_3PO_4

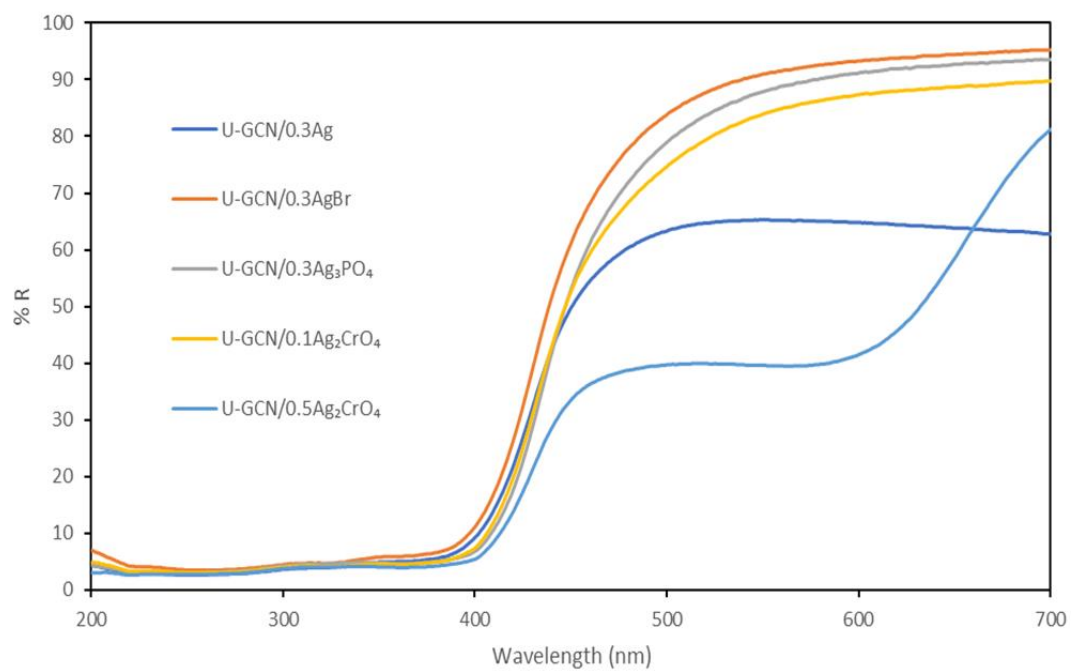


Figure S3. 6 UV-Vis DRS for the photocatalysts: U-GCN/silver-based composites and U-GCN/silver chromate composites

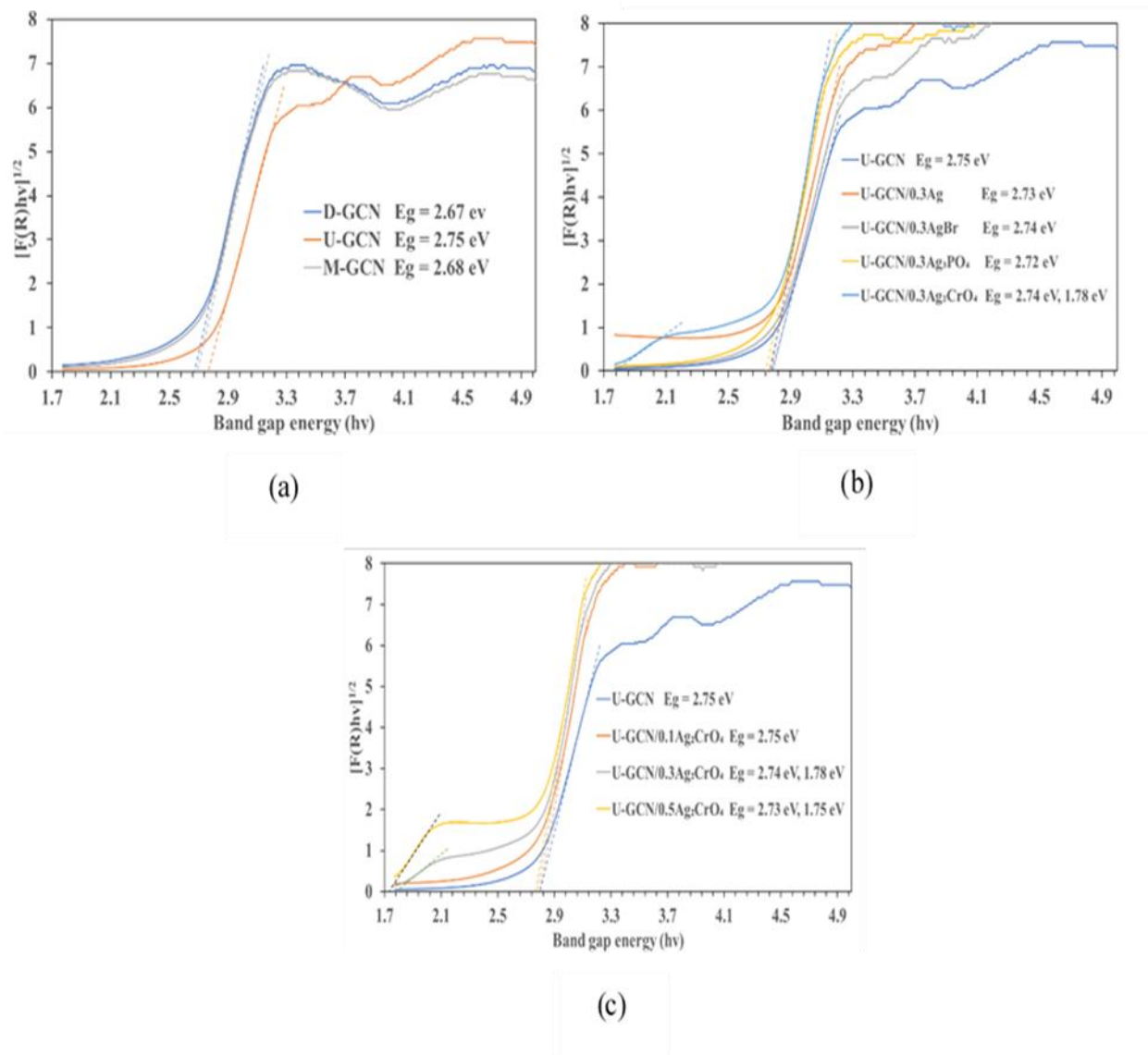


Figure S3. 7 Bandgap energies of the photocatalysts: (a) GCNs derived from different precursors of dicyandiamide (D), urea (U), and melamine (M), (b) U-GCN/silver-based compounds, all in the same ratio of 1:0.3 and (c) U-GCN/ $x\text{Ag}_2\text{CrO}_4$ where $x = 0.1, 0.3$ and 0.5 .

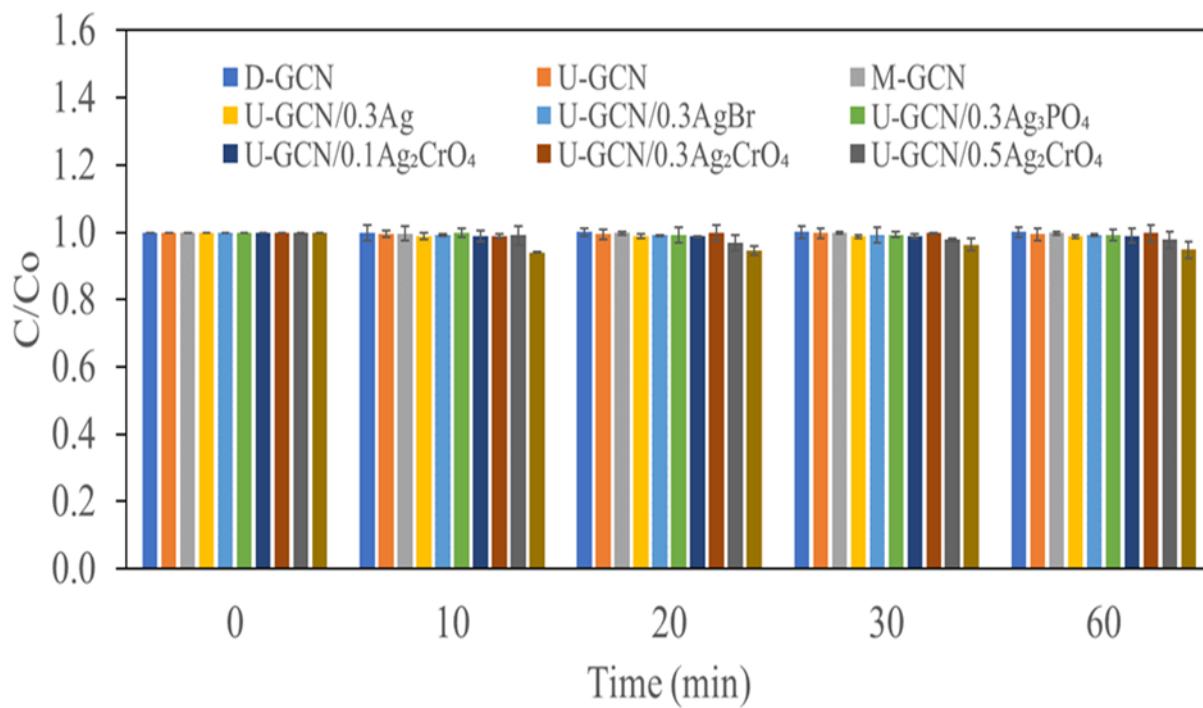


Figure S3. 8 Adsorption performance of the synthesized photocatalysts on 4-CP in dark condition

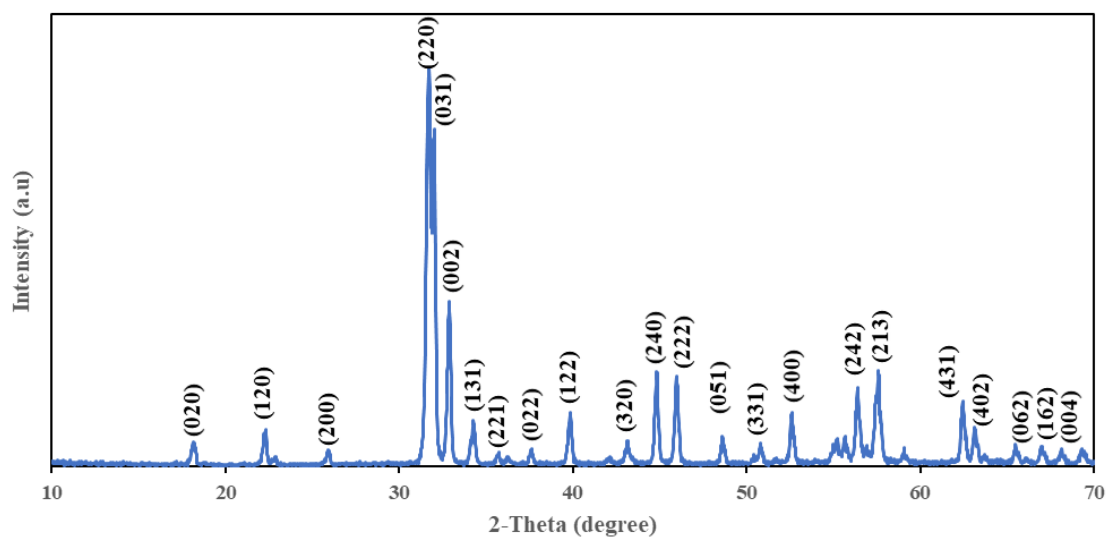


Figure S3. 9 XRD pattern for Ag₂CrO₄

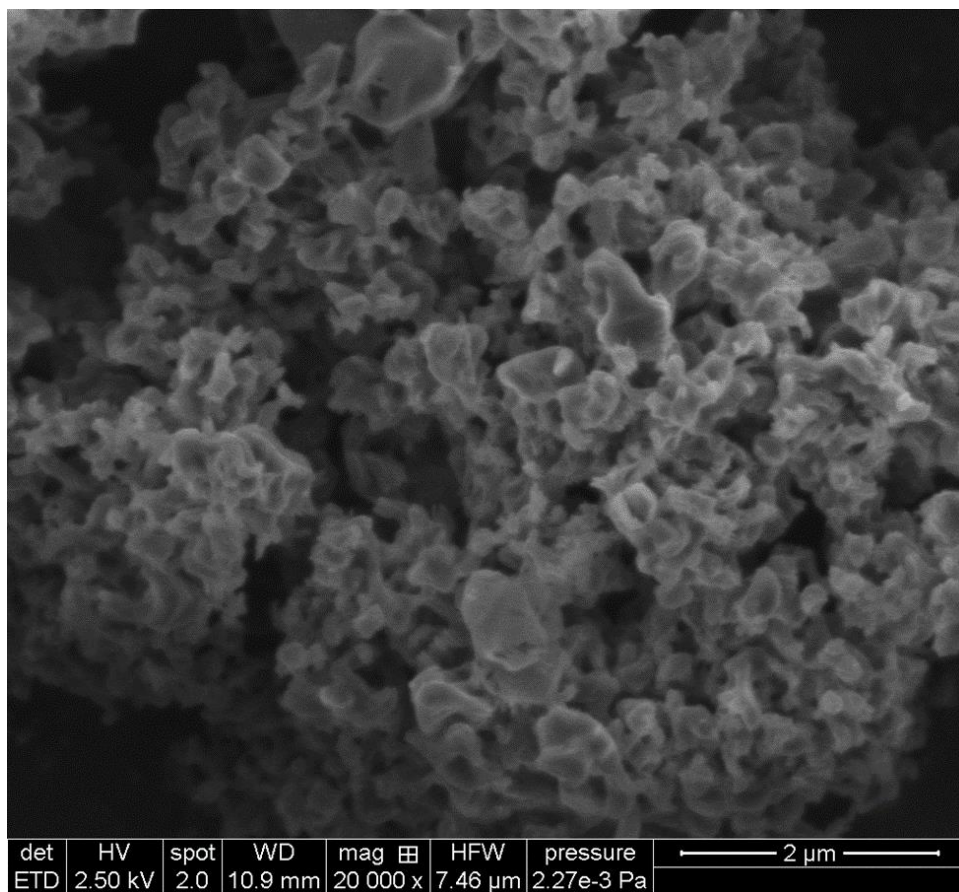


Figure S3. 10 High-resolution SEM image of U-GCN/Ag₂CrO₄